Synthesis, Structure and Property of Polyoxometalate-based Novel Microporous Crystalline Oxides

Zhenxin Zhang

2014

Graduate School of Chemical Sciences and Engineering
Hokkaido University

CONTENT

Chapter 1. General introduction

1.1. Polyoxometalate

Polyoxometalates (POMs) are anionic metal-oxygen clusters comprised of mainly early transition metals such as W, Mo, Nb, and V, which are one of the most important materials with interesting properties. Nowadays, POM chemistry is a key emerging field that allows the development of new molecule-based materials and devices that can be applied to the development in instrumentation, nanoscalescience, and material fabrication methods. POMs have attracted much attention because they are applicable to functional materials such as catalysts, electrode materials, optical materials, and magnetic materials. [1–5] Furthermore, their molecular properties such as multi-electron transfer properties, strong acidic properties, and magnetic properties are tunable by changing their structures and incorporating metal components in the structures. POM clusters possess many different physical and chemical properties, which can act as well-defined building blocks that can be utilized in the formation of various new materials. So far many kinds of POM and POM-based materials with interesting properties have been synthesized, leading to variety of research bunches based on POM, from fundamental researches to practical applications.

1.1.1 Structure chemistry of polyoxometalate

There are many compounds which can be classified to POM compounds, and they come in a vast range of shapes and sizes with a seemingly endless number of structure types. Therefore, it is essential to understand the relationships between the different cluster types. However, to broadly classify POM is possible, which can help in the conceptualization and understanding of the many structural types. In general, the class of compounds known as POMs are based upon metal oxide building blocks with a general formula $\{MO_x\}_n$, where M = Mo, W, V, and sometimes Nb and x = 4-7. The structures of POM are quite diverse. Basically, POMs are comprised of metal-oxygen octahedra in a contain arrangement to form a molecular cluster of the material. There are hundreds and thousands POM structures are found, including Keggin and

well-Dawson structures, which are famous and have been applied to many fields. Today, an increasing number of novel POM molecules have been reported, which not only differ on the chemical composition of POM but also the structure of POM molecule.

1.1.2 Keggin structure and *ε*-Keggin structure

One of the most important structures of POM is Keggin structure. The first *α*-Keggin POM, ammonium phosphomolybdate ($(NH_4)_3[\alpha\text{-}PMo_{12}O_{40}]$), was reported by Berzelius in 1826. In 1934, the structure of *α*-Keggin was experimentally determined with the use of X-ray diffraction. Keggin POM formed by assembly of one metal-oxygen tetrahedron with 12 surrounding metal oxygen octahedra (Figure 1. 1a). In most cases, central tetrahedron is occupied with some elements such as P and Si. In some cases, the central site is not occupied by heavy elements but protons. *α*-Keggin has other four isomers that are named *β*-Keggin, *γ*-Keggin, *δ*-Keggin, and *ε*-Keggin, which are formed by rotation of tri-metal-oxygen cluster of the Keggin unit (Figure 1. 1b-e).

In the case of *ε*-Keggin POM, all of the tri-metal-oxygen clusters in *α*-Keggin POM are rotated for 60 degree, which forms four hexagonal faces that can coordinate to other metal ions (capping metal ions) in a tetrahedral fashion. These capping metal ions are normally in the structure of *ε*-Keggin POM and can stabilize the *ε*-Keggin unit. One *ε*-Keggin unit always has 4 capping metal ions. So far, many *ε*-Keggin POM molecules have been successfully synthesized, most of which are polyoxomolybdate (Table 1. 1). However, aluminate or vanadate can also form the *ε*-Keggin structure in some cases. For *ε*-Keggin polyoxomolybdate, most of the molybdenum ions in the structure are reduced. There are three sites in *ε*-Keggin anion structure: surrounding 12 sites, central metal site, and capping metal site (Figure 1. 1f).

To obtain *ε*-Keggin POM, some starting chemicals or synthesis processes are needed. There are three starting materials for formation of *ε*-Keggin POM in most cases: molybdenum source, reducing agent, and capping metal source. Several molybdates,

such as ammonium heptamolybdate and sodium molybdate, can be used as molybdenum source. N_2H_4 and $Na_2S_2O_4$ are popular to use for reduction of molybdates to form ε-Keggin POM. After addition of capping metal ions, the crystallization of the material is always conducted at room temperature or with mild heating.

ε-Keggin POM offers advantages, because there are four hexagonal faces in its structure, which can coordinate to other metal ions (capping metal ions) in a tetrahedral fashion. The capping metal ions can connect to other organic ligands or other metal coordination compounds, forming some extended structures based on POM. Therefore, many kinds of new materials based on different ε-Keggin POMs can be synthesized.

1.2. Polyoxometalate-based material

POMs can act as ideal building blocks for various materials, because the oxygen-rich surface of POMs can make them as excellent inorganic ligands for oxophilic metals, which cannot only interact with various organic ligands but also with many inorganic ions. Furthermore, POM is normally anionic metal-oxygen clusters, and the negatively charged molecule can easily interact with organic ammonium ligands or other ammonium modified solid. The unique properties of POMs lead to a wide variety of complex compounds based on POM. POMs offer advantages that their structures as well as the chemical compositions can be easily modified and tuned, and their properties can be tuned with changing the structures and chemical composition. Thus, the properties of POM-based materials can be changed with altering POM moiety of the material.

1.2.1. Crystalline materials based on polyoxometalate

Among POM-based materials, ordered crystalline material is a large family. Generally, there are five strategies to form POM-based crystalline materials, showing in Figure 1. 2. The first way (type I approach) is based on electrostatic interaction between POMs and cationic species that include alkaline metal ions, alkaline earth metal ions,

ammonium (organic ammonium) cations, and newly developed metal-organic complex cations, because POMs are mostly anionic materials (Figure 1. 2a). Many kinds of classic POM-based materials and newly-developed materials have been designed and successfully synthesized based on this approach. The second approach (type II approach) uses the size effect of POMs and micropores of metal-organic frameworks (MOFs). Size of the POM anions is around 1 nm, which is similar to or smaller than size of the micropore aperture of MOFs, and therefore some POMs can be incorporated in the micropores of MOFs to form POM-based MOF materials (Figure 1. 2b). The third and fourth approaches (type III and IV approaches) use the coordination chemistry of POMs with transition metal ions and organic ligands. POM building blocks would connect with transition metal ions and organic linkers, leading to synthesis of various organic-POM hybrid frameworks (Figure 1. 2c,d). Using the fifth method (type V approach) to obtain POM-based material receives more and more attention because so formed materials would have a purely-inorganic framework based on POM (Figure 1. 2e). However, the materials obtained so far by using this strategy are very rare.

1.2.1.1 Ionic polyoxometalate material

POMs are anionic molecular metal oxides, which can easily react with some cationic species to form materials based on POM. These POM-based crystalline materials are designed and synthesized based on the type I approach (Figure 1. 2a). Typical materials here are ammonium and cesium salts of α-Keggin POMs. [6–11] After heat treatment, water and ammonium desorb from the structure, and the process makes some micropores and mesopores for the materials. The micropores and mesorpore of the materials are derived from nanometer-sized crystalline particle aggregation (Figure 1. 3). The porous aggregates of $(NH_4)_3PW_{12}O_{40}$ and $Cs_3PW_{12}O_{40}$ nanocrystallites are formed by controlling the preparation conditions. BET surface area of the materials of ammonium and cesium POM are calculated to be 197 m^2/g (the highest case). [6,11] The materials are thermally stable. Thermal stability of the materials is mainly dependent on

the POM anions, and the stability sequence of the POM anion is $H_3PW_{12}O_{40}$ > $H_3PMo_{12}O_{40}$ > $H_4SiMo_{12}O_{40}$. The materials are found to have many applications such as adsorption and catalysis.

1.2.1.2. Macrocation-POM material

POMs are nanometer-sized metal-oxygen macroanions and suitable building blocks of ionic crystals with nano-structures in combination with appropriate macrocations. POM anions show unique redox or acidic properties, which can be controlled at atomic or molecular levels and have been applied to many fields such as catalysis.

A recent achievement on the material that is comprised of a macrocation and a POM unit is also on the basis of the type I approach (Figure 1. 2a). The macrocation molecule, a kind of organic coordination compound with positive charge, are composed of three chromium cations and six organic carboxylate such as $[Cr_3O\{RCO_2\}_6L_3]^+$ (L = ligand). The macrocation assembles with the POM units to form a crystalline material based on POM with intrinsic micropores in its crystal structure (Figure 1. 4). Mizuno's group successfully developed a method to use variety of macrocation molecules and different POM units to synthesize a serial of porous POM materials. Structures of the materials are diverse by altering the structures of both organic macrocation moiety and inorganic POM moiety. Different POM anions can interact with different macrocation to obtained different kinds of hybrid materials with tunable properties (Table 1. 2).

The material of macrocation POM material is synthesized by mixing POM units with macrocation, and some other cation species is added into the system to make charge balance of the material. Crystallization process is always conducted at room temperature.

The macrocation-POM materials show interesting, properties including adsorption, separation, and catalysis. After removal of the present solvent molecules, micropores of the materials can be opened. The material shows selective adsorption properties such as

adsorption of carbon dioxide form carbon dioxide and methane mixture. The properties of the materials can be tuned by altering the components of either organic macrocation moiety or POM moiety.

1.2.1.3. POM-based MOF material

One of the most important topics of coordination chemistry is the combination of metal centers and divergent polydentate ligands, leading to self-assembly processes to access infinite extended structures. The resulting materials of coordination polymers or MOFs can display not only the physical and chemical properties of organic and inorganic building blocks, but also some additional properties associated with their fixed arrangement in the hybrid material. Polynuclear metal complexes are superior to single-metal centers in the design and synthesis of coordination polymers, which can provide more sites for organic linkers. These building blocks can be either synthesized in situ or preformed, and should be robust complexes with divergent binding sites. POMs are polynuclear metal-oxygen clusters of early transition metals and often have heteroatoms incorporated within the structure. POM-based metal organic frameworks represent another kind of POM-based crystalline material.

Most of POM-based MOFs are obtained by using the strategy of type II~IV approaches. According to different sites that POM occupied, POM-based MOF materials can be classified to two kinds, which can be synthesized by different synthesis strategies and processes. One is POM occupies the micropore position of MOF, so called POM@MOF, [12] and the other is POM occupies the framework position of MOF, so called POMOF. [13]

POM@MOF materials. MOF materials that incorporate POM units in their pores are called POM@MOF materials. The size of POM is 1 nm or less in one diameter, which is similar to the size of micropores of MOF materials. Introduction of POM anions into the pores of MOF material can modify the properties of MOF materials, which leads to many kinds of applications and potential applications. A typical example

of the material is incorporation of α-Keggin POM in the micropores of $Cu_3(BTC)_2$ (Figure 1. 5). Structure analysis shows that the POM units are inserted into the micropores of the material of $Cu_3(BTC)_2$ noncontinously. It is found that the different kinds of POM units can be introduced into different kinds of MOF materials (Table 1. 3), and so formed materials display interesting properties, including adsorption and catalysis. POM acts as a key role in the hybrid material of POM@MOF, and the material possesses some properties that are derived from POM.

POMOF materials. Although POM-based extended systems can be accessed by serendipity, pathfinding studies from the Versailles group of Dolbecq and co-workers have made it clear that the network-based approach, typically employed for crystal engineering of conventional metal organic frameworks, is also applicable for POM-based metal organic frameworks, so called POMOF.

One of the most popular inorganic building blocks of POMOF materials is ε-Keggin POM. ε-Keggin formed by assembly of 12 metal-oxygen octahedra with a central metal-oxygen tetrahedron. There are four hexagonal faces of one ε-Keggin unit which can coordinate to other metal ions (capping metal ions) in a tetrahedral fashion (Figure 1. 1 and Figure 1. 6). In the case of POMOF, the capping metal ions further connect to some organic ligands that act as linkers to combine the POM units together tetrahedrally, and thus a network-based POM material can be formed.

To obtain POMOF material, different synthesis processes are needed. The materials can form either in an in situ synthesis condition or an ex situ synthesis condition. In the case of using in situ synthesis, the formation of ε-Keggin POM and assembly of POM unit with linker to form the hybrid material proceed spontaneously in the synthesis. In this case, hydrothermal reaction is always applied for the preparation. Furthermore, the material also can be synthesized under ex situ condition, in which ε-Keggin POM units are prepared before formation of the hybrid materials. In this case, soluble POM units are always welcome as starting materials, which would assemble with the organic linker in solution at room temperature.

It is found that using different linkers produces different resulting extended structures of POMOF materials (Table 1. 4). The connection fashion of the POM units with organic linkers is very similar with the PO_4 or SiO_4 tetrahedra in zeolite. Therefore, many proposed structures based on tetrahedral connection of POM with organic linker are predicted. [13] Many kinds of structures are found based on connection of organic linker with ε-Keggin POM, which forms 0 dimension, 1 dimension, 2 dimension, and 3 dimension structures. Some metal complexes also can be a linker for connection of ε-Keggen POM to be a framework type material. It is found that iron cyanometalate compound can connect ε-Keggin. The CN ligands can coordinate to both iron ions and POM building blocks. In this case, the water soluble POM, $[PMo_{12}O_{36}(OH)_4\{La(H_2O)_4\}_4]$, is used as a building block for the material.

POMOF materials are found to be redox active, indicating that their application potentials in the electrochemistry field. Because of the organic containing structure, POMOF materials are not so stable under thermal conditions, and heat treatment over 473 K would collapse the materials.

1.2.1.4. Assembly of POM with transition metal ions

POMs are very easy to react with transition metal ions in solution, which would form precipitation quickly after mixed them together. [14] The resulting solids are always amorphous due to too fast material formation process. To avoid this problem, some organic ligands are added to the synthesis system to “protect” the transition metal ions and to slowly release the transition metal ions into solution so that POM would react with the transition metal ions slower, and thus well-crystallized materials might be obtained. [15] However, applying this strategy (this is the type III or IV approach in Figure 1. 2) would make some organic compounds left in or constructed the framework of POM-based materials. Therefore, it is very rare that a fully-inorganic framework based on POM that is linked with transition metal ions can be found by using the type V approach (Figure 1. 2e).

Cronin group reported an interesting material that is formed by assembly of a wheel-like POM, $[Mn_8(H_2O)_{48}P_8W_{48}O_{184}]^{242-}$ with manganese ions (Figure 1. 7). [15] Structure analysis shows that six wheel-like POM units construct a cubic chamber by connecting with manganese ions. The cubic chamber surrounded by the POM units are accessible to some small metal ions such as copper ions, and the existed cation species in the original material allows the material to show ion-exchange property with other cations. The aperture of the chamber can be closed by exchange with some large organic cations that can block the aperture of the material. It is also found that using different synthesis conditions can produce the material with different structures. [16] In this case, no organic ligands are used for material synthesis, and thus fully-inorganic material can be obtained.

Another example from Wang group shows that using organic ligands in a certain condition can avoid the incorporation of organic ligand to construct the framework of the POM-based material. [14] In the case of the material synthesized with this process, the material is assembled by POM with La ions to form a fully-inorganic POM-based framework. After removal of the occupied solvent molecules, the micropores of the materials can be opened. The material can adsorb different kinds of molecules, including water and ethanol.

1.2.1.5. Porous complex metal oxides based on polyoxometalate

Crystalline complex metal oxide formed mostly metal-oxygen octahedra so called octahedral molecular sieve (OMS). The first octahedral molecular sieve material is manganese oxide that is formed by manganese oxygen octahedra. [17] The example of octahedral molecule sieve is very rare. POM is found to be a well-defined unit for formation of octahedral molecular sieve materials.

A pentagonal POM building block of $\{Mo_6O_{21}\}$ is found to be an ideal unit for construction of crystalline microporous complex metal oxides. Mo and V-based complex metal oxides are formed by linking the pentagonal POM units with other metal

oxygen octahedra that act as linker. There are three different Mo–V oxide with different symmetry, orthorhombic Mo–V oxide, trigonal Mo–V oxide, and tetragonal Mo–V oxide (Figure 1. 8). [5,9,18–35] The structures of the materials are solved by powder XRD with Rietveld refinement. In the case of orthorhombic Mo–Sb–V oxide, an iso-structural material of orthorhombic Mo–V oxide, the structure is solved with X-ray single crystal analysis for the first time. Mo–V oxide is formed by connecting pentagonal POM units ($\{Mo_6O_{21}\}$) with other metal oxygen octahedra in a-b plane that is grown in c direction.

Water and ammonium cations existed in the as-synthesized material of orthorhombic Mo–V oxide and trigonal Mo–V oxide, which can be removed with heat treatment. After this process, the materials with opening micropores exhibit zeolite-like properties. The materials can adsorb some small molecules such as carbon dioxide, methane, and ethane. Size of the micropores of the materials is determined with molecular probe method. It is found that the porosity of the material is redox active. Size of the micropores can be tuned by changing the element oxidation state of the material.

The materials have many application and application potentials in various fields. The materials can be used as effective catalysts for selective oxidation including ethane, propane, acrolein, and alcohol. Furthermore, it is interesting that the orthorhombic Mo–V oxide can be used as an electrode material for lithium battery.

Another porous complex metal oxide based on POM units is found by Hwu. [36] In this case, the material formed by high temperature solid state reaction of the mixture of starting materials, which produces a material based on polyoxovanadate. Structure analysis of the material shows that the material is comprised of POM unit of $[V_4O_{16}]$, which is linked with As-O tetrahedron. The framework of the material surrounds a void space for the material which is originally occupied by countercations and water. After removal of water molecule, the material shows adsorption property, and the surface area is calculated by the BET method to be 90 m^2/g.

1.2.2. Amorphous material

POMs are anionic materials that can connect with other cationic species, including organic and inorganic compounds, to assemble various organic-inorganic hybrid materials. Organic ammonium cation with different structures can connect to POM units. One example is connecting cationic dendrimer with different kinds of POM units to form dendrimer-POM hybrid materials. [37–47] So formed materials can be acted as heterogeneous catalysts. The materials are efficient catalysts for olefin epoxidation and alcohol oxidation with hydrogen peroxide under mild condition. The material can be recovered from solution by filtration or centrifugation.

POM also can be connected to ammonium-cation-based polymer material, which forms POM-organic hybrid materials. [48–50] These materials show property of temperature sensitivity, and the materials can dissolve in organic solvents at high temperature, whereas when the temperature of the system deceases to a lower temperature, the material would precipitate from the solvent again.

There are other types of hybrid materials based on POM. Connection of POM to ammonia modified solids, such as mesoporous silica and Fe_3O_4, forms hybrid materials which can be used for catalytic reaction. [51–56]

1.3. Structure determination with powder XRD

Structure determination is of great importance. Once a new material is synthesized, structure information of the material is desirable to be understood. In most case, high quality crystal of the new material is required to perform single crystal X-ray analysis. However, it is quite difficult to obtain high quality single crystal of the material even obtaining a well-crystallized material is somewhat difficult. Therefore, understanding an unknown structure is a challenge of material chemists. When only micrometer-sized or submicrometer-sized crystals can be obtained, structure determination with powder diffraction method is a good choice for structure analysis.

The structure determination with powder diffraction data has developed rapidly

over the last twenty years. [57–60] Before 1990, very few new materials had been determined directly from powder diffraction data. Today, the situation is quite different and numerous crystal structures of organic and inorganic compounds have been solved from powder diffraction data. The recent progress in structure determination with powder X-ray diffraction is highly dependent on the developments in instrumentation, computer technology, and powder diffraction methodology. However, the route to a successful structure determination is still by no means as straightforward and routine as it is with single crystal X-ray diffraction data. One of the most important progresses on powder diffraction structure determination is Rietveld method. Based on Rietveld method, structure can be refined with powder diffraction data. Therefore, Rietveld method receives more and more and attention, and so far it is a widely used method for refinement the structures of new materials to obtain the correct structure information of the materials.

Compared with single crystal X-ray analysis, Rietveld method is a structure refinement method, which means a correct initial structure, in a certain extent, should be provide for this refinement. However, it is difficult to set up an initial model. There are several methods so far applied to address this problem. One is using other characterization methods, such as NMR and high resolution electron microscopy, to obtain some structure information of the material and set up the initial structure for refinement. The other method is using Le Bail fitting or Pawley fitting to extract the intensity of powder data, and the extracted structure factors can be used for solving the initial structure of the materials, so called ab initio structure determination with powder diffraction data.

1.3.1 Structure determination with powder XRD combined with TEM

Rietveld method is strong and effective to refine structures with powder diffraction data, but an initial structure for refinement is necessary before starting the refinement. One way to set up the initial structure is to use atomic resolution electron microscopy

technic such as high resolution TEM (HRTEM) and high angle annular dark Field STEM (HAADF-STEM). Partial structure information, such as heavy metal distribution in a contain plane of the material, can be obtained, based on which an initial structure of the material can be built up. Then Rietveld refinement can be conducted on the material.

Several new materials, including zeolites [61] and complex metal oxides, [20,32,34] have been solved by using Rietveld refinement combined with high resolution electron microscopy. The typical example is the structure determination of Mo and V based metal oxides. In the case of the structure determination of orthorhombic Mo–V oxide and trigonal Mo–V oxide, high resolution TEM measurement is applied to obtain the structure information of heavy metal distribution in a-b plane of both materials first (Figure 1. 9). The oxygen atoms of the material are added chemical-logically. The initial structures of the materials are refined by Rietveld method.

1.3.2. Ab initio structure determination with powder diffraction

In the case of the material which is very weak against the electron beam, HRTEM measurement is not easy to get a clear atomic resolution image for obtaining the structure information. The ab initio structure determination with powder X-ray diffraction patterns is another choice to get structure information of new material. Powder X-ray diffraction data loses some information for structure determination compared with single crystal X-ray analysis, because a 3D diffraction data in X-ray single crystal analysis displays a 1D data in powder diffraction, which causes the peak overlap in powder diffraction. To overcome this problem, Pawley fitting or Le Bail fitting is applied to decompose the powder diffraction profile, and to recover a 3 D data from powder diffraction data. However, the data recovered using Pawley fitting or Le Bail fitting [62] is not exact single crystal X-ray data. Moreover, the data from powder diffraction would be affected by other measurement conditions or samples. Therefore, quality of the powder diffraction data is much worse than that of single crystal X-ray data, which would make the structure determination process with plenty of difficulties.

The general process of this method is a high quality powder diffraction profile would be obtained first. Powder indexing would be performed to get correct lattice parameter and possible space group. Then Pawley fitting or Le Bail fitting is applied to extract the structure factors from the XRD profile. Several methods including direct method, Patterson method, and charge flipping method [63,64] are applied to solve the initial structures of the materials. After obtaining a reasonable initial structure, the model is refined with Rietveld method to obtain a finial structure. The process is shown in Figure 1. 10.

As a newly obtained material with unknown structure, in the case that researcher cannot obtain single crystal for structure analysis, plenty of other characterization methods should performed to obtain as much information of the material as possible, and this would provide great help for structure determination.

1.4. Outline of the thesis

This thesis mainly focuses on synthesis, structure characterization, and property investigation of novel POM-based crystalline materials, ε-Keggin POM-based microporous material and one dimensional POM-based material.

In chapter 2, synthesis of well-crystallized material based on Mo, V, and Bi were presented. Structure of the material was determined by single crystal X-ray analysis combined with XPS, redox titration, and elemental analysis. Single crystal X-ray analysis showed that the material was constructed by connecting ε-Keggin units, $[VMo_{9.4}V_{2.6}O_{40}]$, with Bi ions as linkers in a tetrahedral fashion. Heat treatment could open the microporous of the material, which were accessible to some small molecules such as methane, ethane, and carbon dioxide.

In chapter 3, iso-structrual materials of Mo–V–Bi oxide, X–Mo–Y oxide (X = Na or NH_4, Y = Zn, Mn, Fe, or Co), were synthesized. Structures of the materials were determined with powder X-ray diffraction with Rietveld method. The materials were characterized with XPS, FT-IR, and elemental analysis, which showed that the building

blocks of the materials were ε-Keggin POM, and POM units were connected with transition metal ions in a tetrahedral fashion. The occupied guest molecule could be removed by heating without collapse of the structures.

The detailed condition for synthesis of Mo–V–Bi oxide and formation process of the material were presented in chapter 4. The starting materials, synthesis temperature, precursor concentration, and pH of solution were investigated. It was found that using all soluble precursor compounds could produce nanometer-sized Mo–V–Bi oxide, which was characterized with powder diffraction, FT-IR, and electron microscopy. The formation process of the material was investigated with Raman spectroscopy, which indicated that the transformation of a ball-type POM, $\{Mo_{72}V_{30}\}$, to ε-Keggin in solution.

In chapter 5, the adsorption property of the ε-Keggin POM-based microporous material, Mo–Zn oxide, were investigated. It was found that the adsorption properties of carbon dioxide and methane were different on the material. The material showed higher adsorption capacity for carbon dioxide than methane, and adsorption entropy of carbon dioxide was higher than that of methane. Co-adsorption of methane and carbon dioxide showed that Na–Mo–Zn oxide had better performance of NH_4–Mo–Zn oxide on selective adsorption of methane and carbon dioxide mixture. The material was applied to gas chromatographically separate carbon dioxide and methane effectively.

In chapter 6, ion-exchange property was studied on ε-Keggin POM-based materials of Mo–V–Bi oxide, Na–Mo–Zn oxide, and NH_4–Mo–Mn oxide. The countercation species in the original materials, such as Na^+ and NH_4^+, could be easily exchanged with other cations such as alkaline metal ions in aqueous solution. The ion-exchange efficiency of cations was varied. Generally, large cations showed high ion-exchange ability, while small cations showed low ion-exchange ability.

In chapter 7, a new POM compound, $[TeMo_6O_{24}]_x$, with one dimensional polyanions structure was successfully synthesized. The material was characterized with powder diffraction, electron microscopy, FT-IR, redox-titration, UV-Vis, TG-DTA, and

elemental analysis, which showed that the material was constructed with a one dimensional POM that was connected by some weak interactions with water and ammonium cations. The structure of the material was confirmed by single crystal X-ray analysis. Stability of the material was tested.

In chapter 8, conclusions were drawn for every chapter.

References

(1) Pope, M. T. *Heteropoly and Isopoly Oxometalates*; Springer-Verlag: Berlin, 1983.

(2) Special thematic issue on polyoxometalates. Cronin, L.; Müller, A.; Ed.; *Chem. Soc. Rev.* **2012**, *41*, 7325–7648.

(3) Special thematic issue on polyoxometalates. Hill, C. L.; Ed.; *Chem. Rev.* **1998**, *98*, 1–390.

(4) Kamiya, Y.; Sadakane, M.; Ueda, W. Heteropoly Compounds. In *Comprehensive Inorganic Chemistry II*; Reedijk, J., Poeppelmeier, K., Ed.; Oxford: Elsevier, 2013; Vol. 7, pp. 185–204.

(5) Long, D.-L.; Tsunashima, R.; Cronin, L. *Angew. Chem. Int. Ed.* **2010**, *49*, 1736–1758.

(6) Inumaru, K. *Catal. Surv. Asia* **2006**, *10*, 151–160.

(7) Mizuno, N.; Misono, M. *Chem. Rev.* **1998**, *98*, 199–218.

(8) Okamoto, K.; Uchida, S.; Ito, T.; Mizuno, N. *J. Am. Chem. Soc.* **2007**, *129*, 7378–7384.

(9) Sahiro, K.; Ide, Y.; Sano, T.; Sadakane, M. *Acta Chim. Slov.* **2014**, *61*, 177–184.

(10) Taylor, D. B.; McMonagle, J. B.; Moffat, J. B. *J. Colloid Interface Sci.* **1985**, *108*, 278–284.

(11) Sahiro, K.; Ide, Y.; Sano, T.; Sadakane, M. *Mater. Res. Bull.* **2005**, *48*, 4157–4162.

(12) Canioni, R.; Roch-Marchal, C.; Sécheresse, F.; Horcajada, P.; Serre, C.; Hardi-Dan, M.; Férey, G.; Grenèche, J.-M.; Lefebvre, F.; Chang, J.-S.; Hwang, Y.-K.; Lebedev, O.; Turner, S.; Van Tendeloo, G. *J. Mater. Chem.* **2011**, *21*, 1226–1233.

(13) Rodriguez-Albelo, L. M.; Rabdel Ruiz-Salvador, A.; Sampieri, A.; Lewis, D. W.; Gomez, A.; Nohra, B.; Mialane, P.; Marrot, J.; Secheresse, F.; Mellot-Draznieks, C.; Biboum, R. N.; Keita, B.; Nadjo, L.; Dolbecq, A. *J. Am. Chem. Soc.* **2009**, *131*, 16078–16087.

(14) Liu, D.; Lu, Y.; Tan, H.-Q.; Chen, W.-L.; Zhang, Z.-M.; Li, Y.-G.; Wang, E.-B. *Chem. Commun.* **2013**, 3673–3675.

(15) Mitchell, S. G.; Streb, C.; Miras, H. N.; Boyd, T.; Long, D.-L.; Cronin, L. *Nature Chem.* **2010**, *2*, 308–312.

(16) Mitchell, S. G.; Boyd, T.; Miras, H. N.; Long, D.-L.; Cronin, L. *Inorg. Chem.* **2011**, *50*, 136–143.

(17) Suib, S. L. *Acc. Chem. Res.* **2008**, *41*, 479–487.

(18) Todea, A. M.; Merca, A.; Bögge, H.; Glaser, T.; Pigga, J. M.; Langston, M. L. K.; Liu, T.; Prozorov, R.; Luban, M.; Schröder, C.; Casey, W. H.; Müller, A. *Angew. Chem. Int. Ed.* **2010**, *49*, 514–519.

(19) Tagami, H.; Uchida, S.; Mizuno, N. *Angew. Chem. Int. Ed.* **2009**, *48*, 6160–6164.

(20) Sadakane, M.; Kodato, K.; Kuranishi, T.; Nodasaka, Y.; Sugawara, K.; Sakaguchi, N.; Nagai, T.; Matsui, Y.; Ueda, W. *Angew. Chem. Int. Ed.* **2008**, *47*, 2493–2496.
(21) Sadakane, M.; Ohmura, S.; Kodato, K.; Fujisawa, T.; Kato, K.; Shimidzu, K.; Murayama, T.; Ueda, W. *Chem. Commun.* **2011**, 10812–10814.
(22) Sadakane, M.; Endo, K.; Kodato, K.; Ishikawa, S.; Murayama, T.; Ueda, W. *Eur. J. Inorg. Chem.* **2013**, 1731–1736.
(23) Kortz, U.; Müller, A.; van Slageren, J.; Schnack, J.; Dalal, N. S.; Dressel, M. *Coord. Chem. Rev.* **2009**, *253*, 2315–2327.
(24) Inman, C.; Knaust, J. M.; Keller, S. W. *Chem. Commun.* **2002**, 156–157.
(25) Sadakane, M.; Ueda, W. Ordered Crystalline Transition Metal Oxides. In *Porous Materials*; Bruce, D. W.; O'Hare, D.; Walton, R. I., Eds.; Wiley, 2011; Vol. 11, pp. 147–216.
(26) Tao, W.; Li, Z.; Pan, D.; Nie, L.; Yao, S. *J. Phys. Chem. B* **2005**, *109*, 2666–2672.
(27) Liu, X.; Jia, Y.; Zhang, Y.; Huang, R. *Eur. J. Inorg. Chem.* **2010**, 4027–4033.
(28) Feng, X.-J.; Yao, W.; Luo, M.-F.; Ma, R.-Y.; Xie, H.-W.; Yu, Y.; Li, Y.-G.; Wang, E.-B. *Inorganic Chim. Acta* **2011**, *368*, 29–36.
(29) Compain, J.-D.; Nakabayashi, K.; Ohkoshi, S. *Polyhedron* **2013**, *66*, 116–122.
(30) Dolbecq, A.; Mialane, P.; Lisnars, L.; Marrot, J.; Sécheresse, F. *Chem. Eur. J.* **2003**, *9*, 2914–2920.
(31) Ishikawa, S.; Yi, X.; Murayama, T.; Ueda, W. *Appl. Catal. A Gen.* **2013**, *474*, 10–17.
(32) Sadakane, M.; Watanabe, N.; Katou, T.; Nodasaka, Y.; Ueda, W. *Angew. Chem. Int. Ed.* **2007**, *46*, 1493–1496.
(33) Konya, T.; Katou, T.; Murayama, T.; Ishikawa, S.; Sadakane, M.; Buttrey, D.; Ueda, W. *Catal. Sci. & Technol.* **2013**, *3*, 380–387.
(34) Sadakane, M.; Yamagata, K.; Kodato, K.; Endo, K.; Toriumi, K.; Ozawa, Y.; Ozeki, T.; Nagai, T.; Matsui, Y.; Sakaguchi, N.; Pyrz, W. D.; Buttrey, D. J.; Blom, D. A.; Vogt, T.; Ueda, W. *Angew. Chem. Int. Ed.* **2009**, *48*, 3782–3786.
(35) Schäffer, C.; Merca, A.; Bögge, H.; Todea, A. M.; Kistler, M. L.; Liu, T.; Thouvenot, R.; Gouzerh, P.; Müller, A. *Angew. Chem. Int. Ed.* **2009**, *48*, 149–153.
(36) Queen, W. L.; Hwu, S.-J.; Reighard, S. *Inorg. Chem.* **2010**, *49*, 1316–1318.
(37) Vasylyev, M. V; Astruc, D. *Adv. Synth. Catal.* **2005**, *347*, 39–44.
(38) Vasylyev, M. V; Neumann, R. *J. Am. Chem. Soc.* **2004**, *10*, 884–890.
(39) Vasylyev, M. V; Gatard, S.; Bar-nahum, I.; Konstantinovski, L.; Wachtel, E. J.; Neumann, R. *J. Clust. Sci.* **2006**, *17*, 235–243.
(40) Vasylyev, M. V; Wachtel, E. J.; Popovitz-biro, R.; Neumann, R. *Chem. Eur. J.* **2006**, *12*, 3507–3514.
(41) Nlate, S.; Plault, L.; Astruc, D. *New J. Chem.* **2007**, *31*, 1264–1274.

(42) Astruc, D.; Ruiz, J.; Gatard, S.; Neumann, R. *Angew. Chem. Int. Ed.* **2004**, *43*, 2924–2928.
(43) Yang, Y.; Wang, Y.; Li, H.; Li, W.; Wu, L. *Chem. Eur. J.* **2010**, *16*, 8062–8071.
(44) Nlate, S.; Astruc, D.; Neumann, R. *Adv. Synth. Catal.* **2004**, *346*, 1445–1448.
(45) Nlate, S.; Plault, L.; Astruc, D. *Chem. Eur. J.* **2006**, *12*, 903–914.
(46) Jahier, C.; Mal, S.; Kortz, U.; Nlate, S. *Eur. J. Inorg. Chem.* **2010**, 1559–1566.
(47) Zhang, Z.; Zhao, W.; Ma, B.; Ding, Y. *Catal. Commun.* **2010**, *12*, 318–322.
(48) Qi, W.; Wu, L. *Polym. Int.* **2009**, *58*, 1217–1225.
(49) Haimov, A.; Neumann, R. *J. Am. Chem. Soc.* **2006**, *128*, 15697–15700.
(50) Raj, G.; Swalus, C.; Guillet, A.; Devillers, M.; Nysten, B.; Gaigneaux, E. M. *Langmuir* **2013**, *29*, 4388–4395.
(51) Zhang, Z.; Zhang, F.; Zhu, Q.; Zhao, W.; Ma, B.; Ding, Y. *J. Colloid Interface Sci.* **2011**, *360*, 189–194.
(52) Kumar, D.; Landry, C. C. *Microporous Mesoporous Mater.* **2007**, *98*, 309–316.
(53) Liu, P.; Wang, H.; Feng, Z.; Ying, P.; Li, C. *J. Catal.* **2008**, *256*, 345–348.
(54) Liu, P.; Wang, C.; Li, C. *J. Catal.* **2009**, *262*, 159–168.
(55) Maksimchuk, N. V.; Melgunov, M. S.; Chesalov, Y. A.; Mrowiecbialon, J.; Jarzebski, A. B.; Kholdeeva, O. A. *J. Catal.* **2007**, *246*, 241–248.
(56) Zhou, Y.; Bao, R.; Yue, B.; Gu, M.; Pei, S.; He, H. *J. Mol. Catal. A: Chem.* **2007**, *270*, 50–55.
(57) *Structure Determination from Powder Diffraction Data*; David, W. i. f.; Shankland, K.; McCusker, L. b.; Baerlocher, C., Eds.; Oxford University Press, 2006; Vol. 47.
(58) Young, R. A. *The Rietveld Method*; Young, R. A., Ed.; Oxford University Press: Oxford, 1995.
(59) Jenkins, R.; Snyder, R. L. *Introduction to X-ray Powder Diffractometry*; Winefordner, J. D., Ed.; wiley-interscience, 1996; Vol. 27.
(60) Bish, D. L.; Post, J. e. *Modern Powder Diffraction*; Mineralogical Society of America, 1989; Vol. 27.
(61) Gramm, F.; Baerlocher, C.; McCusker, L. B.; Warrender, S. J.; Wright, P. A.; Han, B.; Hong, S. B.; Liu, Z.; Ohsuna, T.; Terasaki, O. *Nature* **2006**, *444*, 79–81.
(62) Le Bail, A. *Powder Diffr.* **2008**, *23*, S5–S12.
(63) Palatinus, L.; Chapuis, G. *J. Appl. Crystallogr.* **2007**, *40*, 786–790.
(64) Ryu, J.; Park, R.; Kim, D.-S. *J. Comput. Sci. Technol.* **2006**, *21*, 225–260.
(65) Mialane, P.; Dolbecq, A.; Lisnard, L.; Mallard, A. *Angew. Chem. Int. Ed.* **2002**, *36*, 2504–2507.
(66) Müller, A.; Beugholt, C.; Kögerler, P.; Bögge, H.; Bud'ko, S.; Luban, M. *Inorg. Chem.* **2000**, *39*, 5176–5177.
(67) Sloboda-Rozner, D.; Neimann, K.; Neumann, R. *J. Mol. Catal. A: Chem.* **2007**, *262*, 109–113.
(68) Ellern, A.; Kögerler, P. *Acta Crystallogr. Sect. C* **2012**, *68*, i17–i19.

(69) Cui, X.-B.; Zheng, S.-T.; Yang, G.-Y. *Z. Anorg. Allg. Chem.* **2005**, *631*, 642–644.
(70) Chae, H. K.; Klemperer, W. G.; Paez Loyo, D. E. *Inorg. Chem.* **1992**, *8*, 3187–3189.
(71) Nohra, B.; El Moll, H.; Rodriguez Albelo, L. M.; Mialane, P.; Marrot, J.; Mellot-Draznieks, C.; O'Keeffe, M.; Biboum, R. N.; Lemaire, J.; Keita, B.; Nadjo, L.; Dolbecq, A. *J. Am. Chem. Soc.* **2011**, *133*, 13363–13374.
(72) Wang, W.; Xu, L.; Gao, G.; Liu, L.; Liu, X. *CrystEngComm* **2009**, *11*, 2488–2493.
(73) Son, J.-H.; Kwon, Y.-U. *Inorg. Chem.* **2004**, *43*, 1929–1932.
(74) Tucher, J.; Nye, L. C.; Ivanovic-Burmazovic, I.; Notarnicola, A.; Streb, C. *Chem. Eur. J.* **2012**, *18*, 10949–10953.
(75) Yamase, T.; Makino, H.; Naruke, H. *Chem. Lett.* **2000**, *27*, 1350–1351.
(76) Ishaque, M.; Chen, Q.; Zubieta, J.; Goshorn, D. *Inorganic Chim. Acta* **1992**, *191*, 97–102.
(77) Eguchi, R.; Uchida, S.; Mizuno, N. *J. Phys. Chem. C* **2012**, *116*, 16105–16110.
(78) Eguchi, R.; Uchida, S.; Mizuno, N. *Angew. Chem. Int. Ed.* **2012**, *51*, 1635–1639.
(79) Uchida, S.; Mizuno, N. *J. Am. Chem. Soc.* **2004**, *6*, 1602–1603.
(80) Mizuno, N.; Uchida, S. *Chem. Lett.* **2006**, *35*, 688–693.
(81) Uchida, S.; Hashimoto, M.; Mizuno, N. *Angew. Chem. Int. Ed.* **2002**, *6*, 2814–2817.
(82) Uchida, S.; Hikichi, S.; Akatsuka, T.; Tanaka, T.; Kawamoto, R.; Lesbani, A.; Nakagawa, Y.; Uehara, K.; Mizuno, N. *Chem. Mater.* **2007**, *19*, 4694–4701.
(83) Ogasawara, Y.; Uchida, S.; Mizuno, N. *J. Phys. Chem. C* **2007**, *6*, 8218–8227.
(84) Uchida, S.; Eguchi, R.; Mizuno, N. *Angew. Chem. Int. Ed.* **2010**, *49*, 9930–9934.
(85) Song, J.; Luo, Z.; Britt, D. K.; Furukawa, H.; Yaghi, O. M.; Hardcastle, K. I.; Hill, C. L. *J. Am. Chem. Soc.* **2011**, *133*, 16839–16846.
(86) Zhang, Y.; Degirmenci, V.; Li, C.; Hensen, E. J. M. *ChemSusChem* **2011**, *4*, 59–64.
(87) Juan-Alcañiz, J.; Ramos-Fernandez, E. V.; Lafont, U.; Gascon, J.; Kapteijn, F. *J. Catal.* **2010**, *269*, 229–241.
(88) Maksimchuk, N. V.; Timofeeva, M. N.; Melgunov, M. S.; Shmakov, A. N.; Chesalov, Y. A.; Dybtsev, D. N.; Fedin, V. P.; Kholdeeva, O. A. *J. Catal.* **2008**, *257*, 315–323.
(89) Kuang, X.; Wu, X.; Zhang, J.; Lu, A. *Chem. Commun.* **2011**, 4150–4152.
(90) Kuang, X.; Wu, X.; Yu, R.; Donahue, J. P.; Huang, J.; Lu, C.-Z. *Nature Chem.* **2010**, *2*, 461–465.
(91) Li, C.-H.; Huang, K.-L.; Chi, Y.-N.; Liu, X.; Han, Z.-G.; Shen, L.; Hu, C.-W. *Inorg. Chem.* **2009**, *48*, 2010–2017.
(92) Duan, C.; Wei, M.; Guo, D.; He, C.; Meng, Q. *J. Am. Chem. Soc.* **2010**, *132*, 3321–3330.

(93) Bajpe, S. R.; Breynaert, E.; Mustafa, D.; Jobbágy, M.; Maes, A.; Martens, J.; Kirschhock, C. E. *J. Mater. Chem.* **2011**, *21*, 9768–9771.
(94) Mustafa, D.; Breynaert, E.; Bajpe, S. R.; Martens, J. A.; Kirschhock, C. E. A. *Chem. Commun.* **2011**, 8037–8039.
(95) Yang, L.; Naruke, H.; Yamase, T. *Inorg. Chem. Commun.* **2003**, *6*, 1020–1024.
(96) Wee, L. H.; Bajpe, S. R.; Janssens, N.; Hermans, I.; Houthoofd, K.; Kirschhock, C. E. A.; Martens, J. A. *Chem. Commun.* **2010**, 8186–8188.
(97) Bajpe, S. R.; Kirschhock, C. E. A.; Aerts, A.; Breynaert, E.; Absillis, G.; Parac-Vogt, T. N.; Giebeler, L.; Martens, J. A. *Chem. Eur. J.* **2010**, *16*, 3926–3932.
(98) Ma, F.; Liu, S.; Liang, D.; Ren, G.; Zhang, C.; Wei, F.; Su, Z. *Eur. J. Inorg. Chem.* **2010**, *2010*, 3756–3761.
(99) Liang, D.-D.; Liu, S.-X.; Ma, F.-J.; Wei, F.; Chen, Y.-G. *Adv. Synth. Catal.* **2011**, *353*, 733–742.
(100) Sun, C.-Y.; Liu, S.-X.; Liang, D.-D.; Shao, K.-Z.; Ren, Y.-H.; Su, Z.-M. *J. Am. Chem. Soc.* **2009**, *131*, 1883–1888.
(101) Férey, G.; Mellot-Draznieks, C.; Serre, C.; Millange, F.; Dutour, J.; Surblé, S.; Margiolaki, I. *Science* **2005**, *309*, 2040–2042.
(102) Zheng, S.-T.; Yang, G.-Y. *Dalton Trans.* **2010**, *39*, 700–703.
(103) Long, G. E. D.; Cronin, L.; Zhu, G.; Geletii, Y. V; Zhao, C.; Musaev, D. G.; Song, J.; Hill, C. L. *Dalton Trans.* **2012**, *41*, 9989–9999.
(104) Dolbecq, A.; Mellot-Draznieks, C.; Mialane, P.; Marrot, J.; Férey, G.; Sécheresse, F. *Eur. J. Inorg. Chem.* **2005**, 3009–3018.

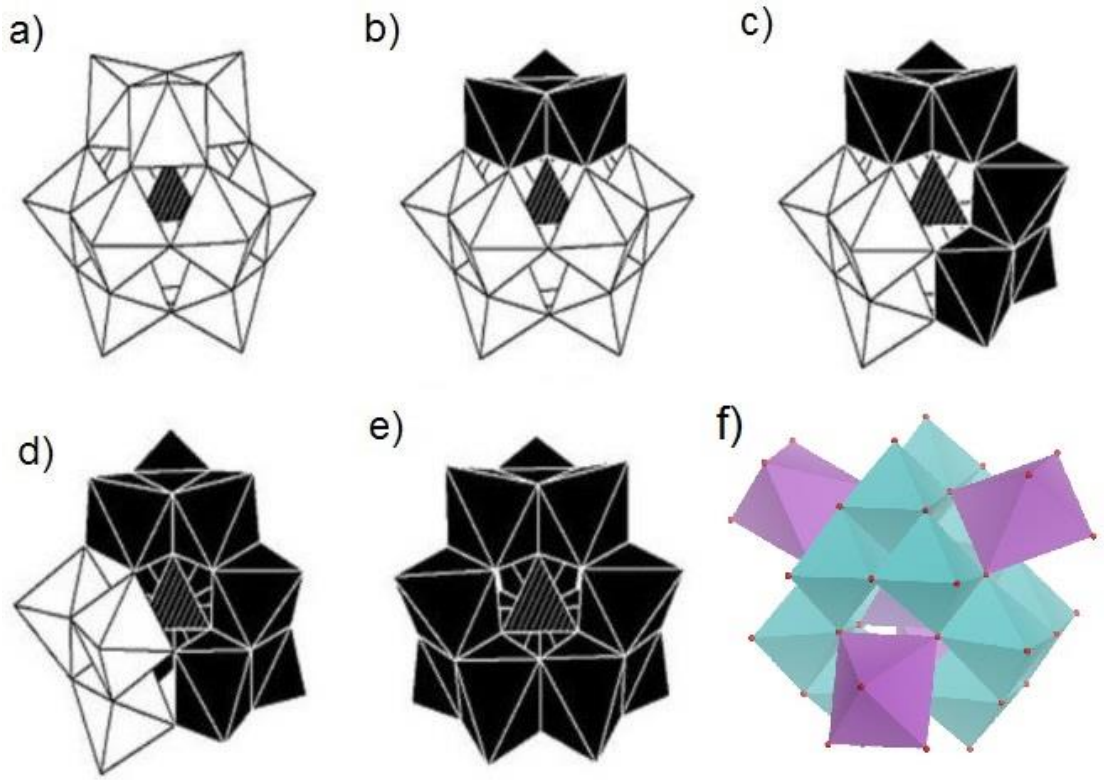

Figure 1. 1. Polyhedral presentations of a) α-Keggin, b) β-Keggin, c) γ-Keggin, d) δ-Keggin, e) ε-Keggin, and f) ε-Keggin core with four capping metal ions, central site (purple tetrahedron), capping metal site (purple octahedron), surrounding metal sites (blue octahedron).

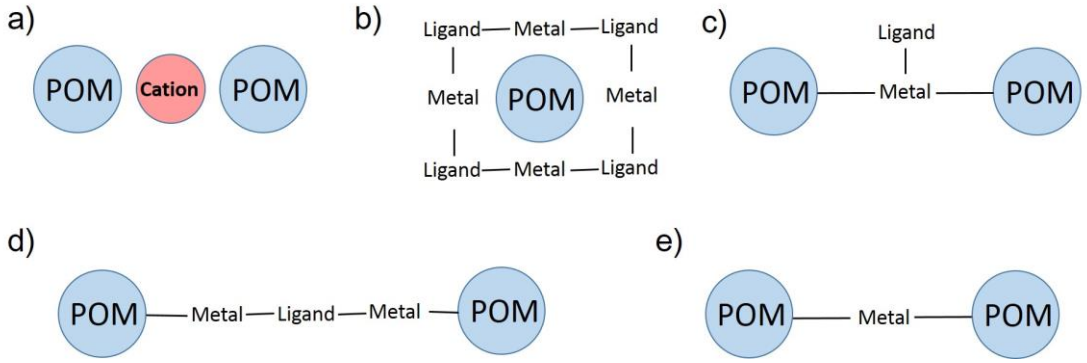

Figure 1. 2. Representations of formation of POM-based materials: a) type I approach, b) type II approach, c) type III approach, d) type IV approach, and e) type V approach.

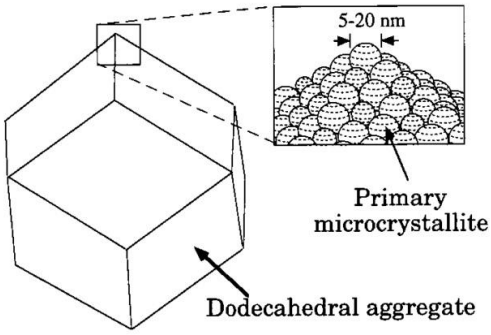

Figure 1. 3. Representation of cesium or ammonium salt of POMs.

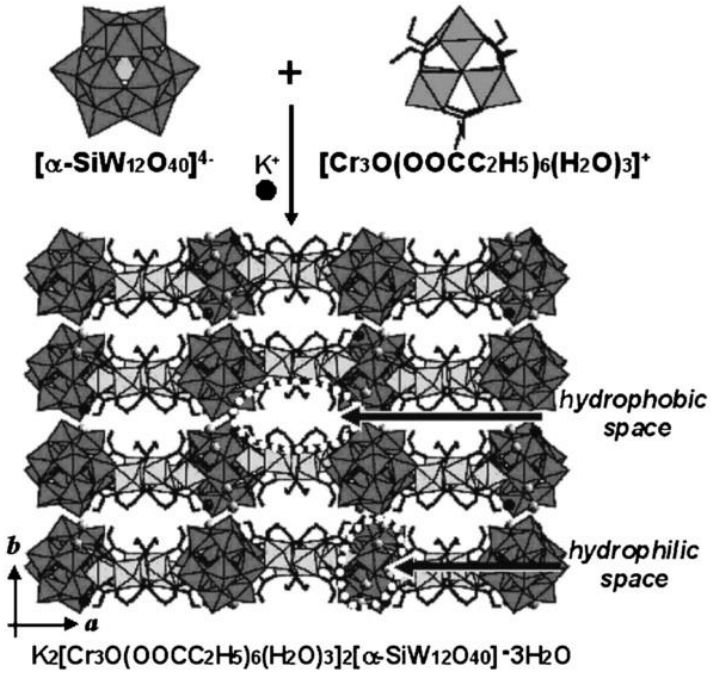

Figure 1. 4. Presentation of POM-macrocation material

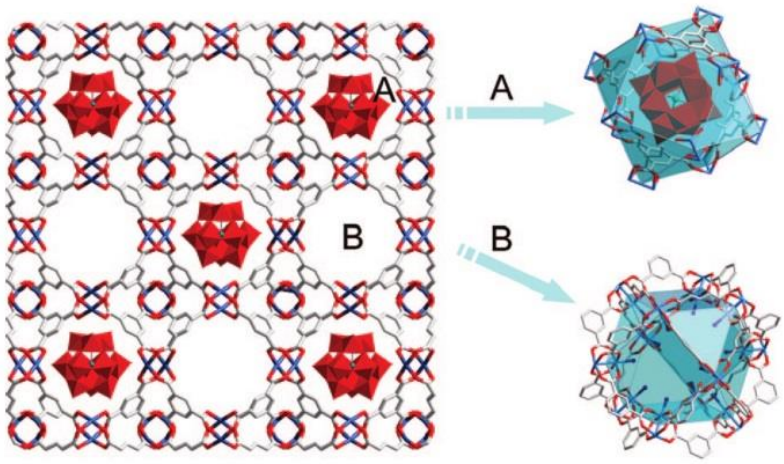

Figure 1. 5. Stick representation (MOF framework) and polyhedral repesentation (POM units) of Cu-BTC framework and Keggin polyanions, Cu, O, and C (Blue, red, and gray).

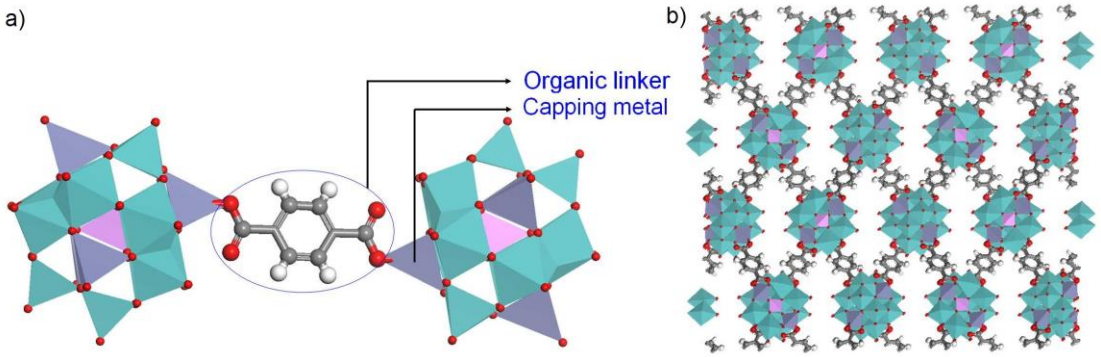

Figure 1. 6. Polyhedral representations of a) linkage of POM units with organic linker and b) crystal structure of POMOF material, MoO_6 (blue octahedron), PO_4 (pink tetrahedron), ZnO_4 (purple tetrahedron), O (red sphere), C (gray sphere), H (white sphere).

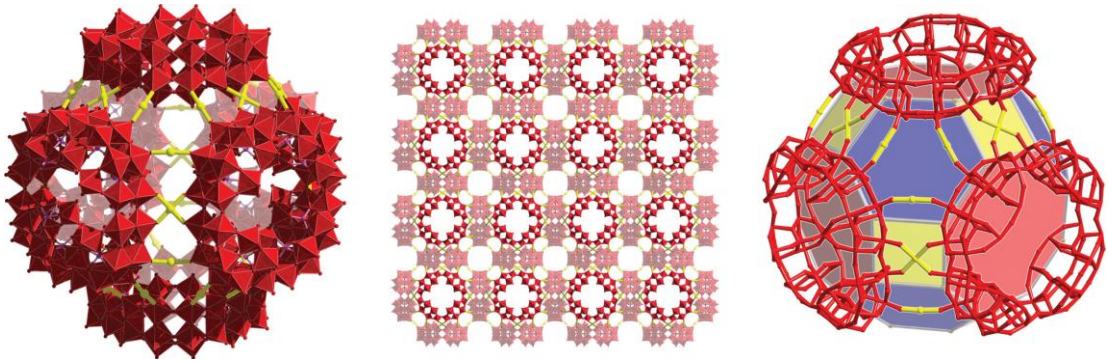

Figure 1. 7. a) Crystal packing of $[Mn_8(H_2O)_{48}P_8W_{48}O_{184}]^{242-}$ along the crystallographic an axis, b) packing of manganese-linked $\{P_8W_{48}O_{184}\}^{40-}$ clusters around a truncated cuboctahedron, and c) WO_6 (red polyhedron), O (red sphere), Mn (yellow sphere), P (pink sphere).

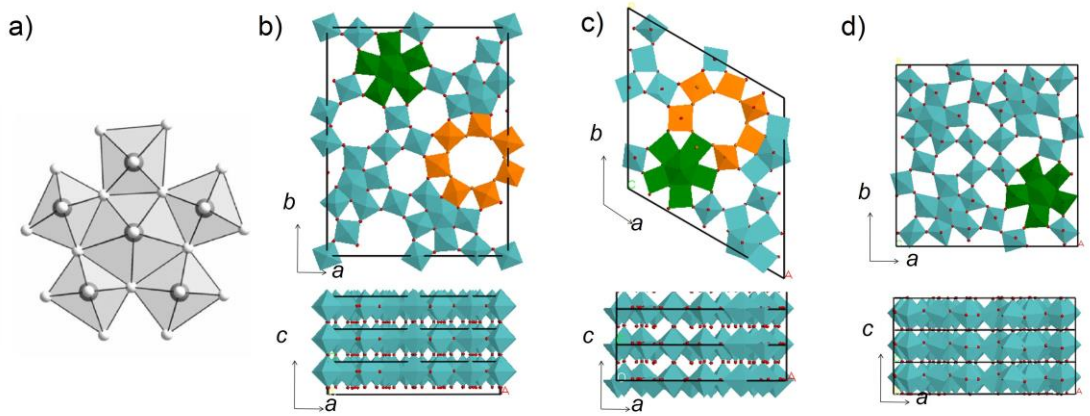

Figure 1. 8. Polyhedral representations of a) pentagonal unit, b) orthorhombic Mo–V oxide, c) trigonal Mo–V oxide, and d) tetragonal Mo–V oxide, $Mo(V)O_6$ (color octahedron), oxygen (red sphere).

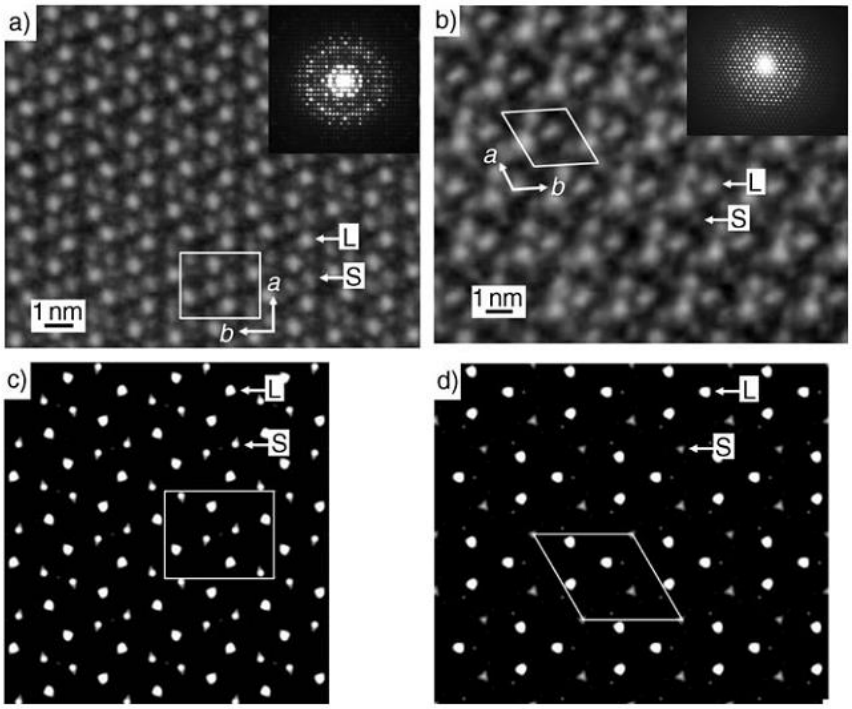

Figure 1. 9. HRTEM images and selected-area electron diffraction (SAED) patterns (insets) of a) orthorhombic Mo–V oxide, b) trigonal Mo–V oxide viewed along the [001] direction as well as the corresponding simulate contrast for c) orthorhombic Mo–V oxide calculated for a crystal thickness close to 24 nm and a defocus value $\Delta f = -130$ nm and d) trigonal Mo–V oxide calculated for a crystal thickness close to 20 nm and a defocus value $\Delta f = -155$ nm. L and S indicate large and small spots, respectively.

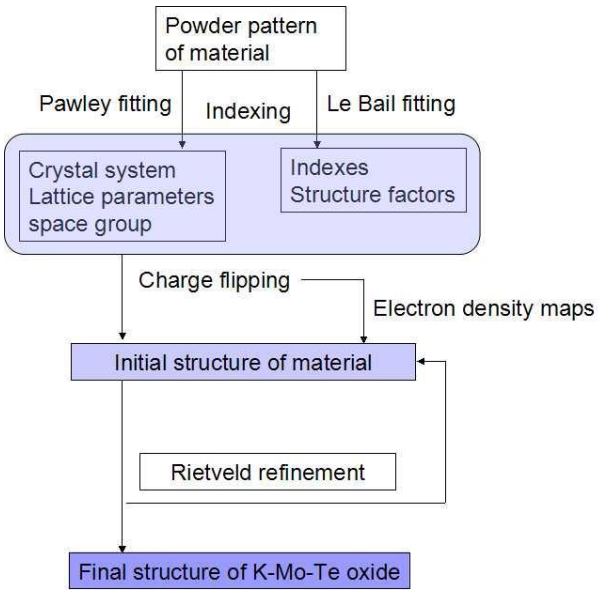

Figure 1. 10. The general process of structure determination with powder diffraction.

Table 1. 1. Reported ε-Keggin POMs.

Formula of POM moiety	Central site	Surrounding site	Capping site	Ref.
$[PMo_{12}O_{36}(OH)_4\{La(H_2O)_4\}]$	P	Mo	La	30,65
$[Mo_{12}O_{39}(OH)_{10}H_2\{Ni(H_2O)_3\}_4]$	-	Mo	Ni	66,67
$[Mo_{12}O_{39}(OH)_{10}H_2\{Co(H_2O)_3\}_4]$	-	Mo	Co	67,68
$[Mo_{12}O_{39}(OH)_{10}H_2\{Mn(H_2O)_3\}_4]$	-	Mo	Mn	67
$[Mo_{12}O_{39}(OH)_{10}H_2\{Cu(H_2O)_3\}_4]$	-	Mo	Cu	67
$[NiMo_{12}O_{40}\ \{Ni(H_2O)\}_4]$	Ni	Mo	Ni	69
$[MoMo_{12}O_{40}\{C_5Me_5Rh\}_8]$	Mo	Mo	Rh	70
$[PMo_{12}O_{40}\{Zn\}_4]$	P	Mo	Zn	13,71
$[PMo_{12}O_{38}(OH)_2\{Sm(H_2O)_5\}_4]$	P	Mo	Sm	29
$[PMo_{12}O_{38}(OH)_2\{Eu(H_2O)_5\}_4]$	P	Mo	Eu	29
$[PMo_{12}O_{38}(OH)_2\{Nd(H_2O)_5\}_4]$	P	Mo	Nd	29
$[PMo_{12}O_{38}(OH)_2\{Tb\ (H_2O)_5\}_4]$	P	Mo	Tb	29
$[GeMo_{12}O_{40}\{Ni\}_4]$	Ge	Mo	Ni	72
$[AlAl_{12}O_{40}]$	Al	Al	-	73
$[VV_{12}O_{40}\{Bi\}_4]$	V	V	Bi	74
$[HKV_{12}O_{27}(AsO_4)_4]$		V	As	75,76
$[H_6KV_{12}O_{27}(VO_4)(PO_3CH_3)_3]$	V	V	P	75

Table 1. 2. Examples of POM-macrocation materials.

Formula	macrocation	POM anion	Ref.
$K_2[Cr_3O(OOCH)_6(4\text{-etpy})_3]_2[\alpha\text{-}SiW_{12}O_{40}]$	$[Cr_3O(OOCH)_6(4\text{-etpy})_3]$	$[\alpha\text{-}SiW_{12}O_{40}]$	77
$K_2[Cr_3O(OOCH)_6(4\text{-etpy})_3]_2[\alpha\text{-}SiW_{12}O_{40}]$	$[Cr_3O(OOCH)_6(4\text{-etpy})_3]$	$[\alpha\text{-}SiW_{12}O_{40}]$	78
$Cs_5[Cr_3O(OOCH)_6(H_2O)_3][\alpha\text{-}CoW_{12}O_{40}]$	$[Cr_3O(OOCH)_6(H_2O)_3]$	$[\alpha\text{-}CoW_{12}O_{40}]$	79,80
$K_3[Cr_3O(OOCH)_6(H_2O)_3][\alpha\text{-}SiW_{12}O_{40}]$	$[Cr_3O(OOCH)_6(H_2O)_3]$	$[\alpha\text{-}SiW_{12}O_{40}]$	80,81
$[Co(tacn)_2][\ \alpha\text{-}PW_{12}O_{40}]$	$Co(tacn)_2$	$[\ \alpha\text{-}PW_{12}O_{40}]$	82
$[Co(tacn)_2]_2[\alpha\text{-}SiV_2W_{10}O_{40}]$	$Co(tacn)_2$	$[\alpha\text{-}SiV_2W_{10}O_{40}]$	82
$[Ni(tacn)_2]_2[\alpha\text{-}SiW_{12}O_{40}]$	$[Ni(tacn)_2]$	$[\alpha\text{-}SiW_{12}O_{40}]$	82
$[Ni(tacn)_2]_2[\alpha\text{-}SiV_2W_{10}O_{38}(OH)_2]$	$[Ni(tacn)_2]$	$[\alpha\text{-}SiV_2W_{10}O_{38}(OH)_2]$	82
$Rb_4[Cr_3O(OOCH)_6(H_2O)_3][\alpha\text{-}BW_{12}O_{40}]$	$[Cr_3O(OOCH)_6(H_2O)_3]$	$[\alpha\text{-}BW_{12}O_{40}]$	83
$K_3[Cr_3O(OOCH)_6(H_2O)_3][\alpha\text{-}SiW_{12}O_{40}]$	$[Cr_3O(OOCH)_6(H_2O)_3]$	$[\alpha\text{-}SiW_{12}O_{40}]$	83
$Na_2[Cr_3O(OOCH)_6(H_2O)_3][\alpha\text{-}PW_{12}O_{40}]$	$[Cr_3O(OOCH)_6(H_2O)_3]$	$[\ \alpha\text{-}PW_{12}O_{40}]$	83
$K_{1.5}[Cr_3O(OOCH)_6(C_5H_5N)_3]_2[Cr_3O(OOCH)_6(C_5H_5N)(CH_3OH)_2]_{0.5}[\alpha\text{-}SiW_{12}O_{40}]$	$[Cr_3O(OOCH)_6(C_5H_5N)_3]$and $[Cr_3O(OOCH)_6(C_5H_5N)(CH_3OH)_2]$	$[\alpha\text{-}SiW_{12}O_{40}]$	19
$K_2[Cr_3O(OOCH)_6(mepy)_3]_2[\alpha\text{-}SiW_{12}O_{40}]$	$[Cr_3O(OOCH)_6(mepy)_3]$	$[\alpha\text{-}SiW_{12}O_{40}]$	84

Table 1. 3. Examples of POM@MOF materials.

Material	POM	MOF	Ref.
$[Cu_3(C_9H_3O_6)_2]_4[\{(CH_3)_4N\}_4CuPW_{11}O_{39}H]$	$[CuPW_{11}O_{39}]$	$Cu_3(BTC)_2$	85
PTA/MIL-101	$[PW_{12}O_{40}]$	MIL-101	12,86–88
$\{[Ag_2(trz)_2][Ag_{24}(trz)_{18}]\}[PW_{12}O_{40}]_2$	$[PW_{12}O_{40}]$	$[Ag_2(trz)_2][Ag_{24}(trz)_{18}]$	89,90
$\{[Ln(H_2O)_4(pdc)]_4\}[XMo_{12}O_{40}]$	$[XMo_{12}O_{40}]$,X=La,Ce, Nd	$[Ln(H_2O)_4(pdc)]_4$	91
$\{[Co_4(dpdo)_{12}](PMo_{12}O_{40})_3\}$	$[PMo_{12}O_{40}]$	$[Co_4(dpdo)_{12}]$	92
$Cu_3(BTC)_2[XW_{12}O_{40}]$	$[XW_{12}O_{40}]$,X=P, Si	$Cu_3(BTC)_2$	93–100
$[Co(bpdo)_3]_2[PW_{12}O_{40}]$	$[PW_{12}O_{40}]$	$[Co(bpdo)_3]$	28
$[PW_{11}O_{40}]$/MIL-101	$[PW_{11}O_{40}]$	MIL-101	101
$[Cu_3(bpy)_5]_2[H_2SiW_{11}O_{39}]$	$[H_2SiW_{11}O_{39}]$	$Cu_3(bpy)_5$	102
$Ln_4(pdc)_4[SiW_{12}O_{40}]$	$[SiW_{12}O_{40}]$	$Ln_4(pdc)_4$	27
$Cu_3(bpy)_5]PW_{12}O_{40}$	$[PW_{12}O_{40}]$	$Cu_3(bpy)_5$	24

Table 1. 4. Examples of POMOF materials.

Organic linker	POM unit	Ref.
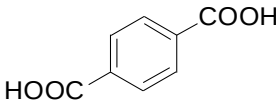	[ε-$PMo_{12}O_{36}(OH)_4Zn_4$]	13
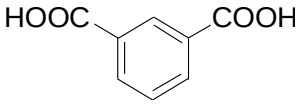	[ε-$PMo_{12}O_{36}(OH)_4Zn_4$]	103
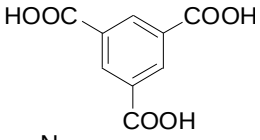	[ε-$PMo_{12}O_{36}(OH)_4Zn_4$]	71
	[ε-$PMo_{12}O_{37}(OH)_3Zn_4$]	71
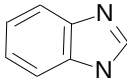	[ε-$PMo_{12}O_{37}(OH)_3Zn_4$]	71
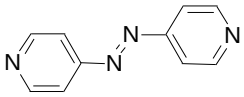	[ε-$PMo_{12}O_{37}(OH)_3Zn_4$]	103
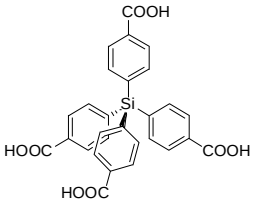	[ε-$PMo_{12}O_{36}(OH)_4\{La(H_2O)_4\}_4$]	104

Chapter 2. Synthesis of a well-crystallized Mo–V–Bi oxide and single crystal analysis of Mo–V–Bi oxide

2.1. Introduction

Polyoxometalates (POMs) are anionic metal oxide clusters of early transition metals such as molybdenum, vanadium, and tungsten. These materials have been widely applied to various fields such as catalysis, photocatalysis, materials science, magnetism, biology, and medicine. [1–6]

Crystalline solids based on POMs with porosity are of great interest, because properties of POMs such as redox and acidic properties can be combined with pore-based properties such as size selective adsorption of molecules and ions. A classical example of porous POM materials was microporous and/or mesoporous cesium or ammonium salts of α-Keggin-type POMs. [4,7–10] The porosity of the materials was derived from aggregation of nanometer-size crystallites of POMs, and the pores were present between the crystallites. Controlling of the pores was an important factor for enhancing catalytic activity of these materials.

Recently, new approaches to form porous POMs have attracted much attention. Mizuno's group successfully developed a method to use large cation molecules (macrocations) to synthesize porous POMs. The large cation molecules, which were composed of three chromium cations and six organic carboxylate such as $[Cr_3O\{RCO_2\}_6L_3]^+$ (L = ligand), and POMs formed crystalline materials with intrinsic micropores in their crystal structure. [11–16] Pore properties were tunable by selection of organic moiety, metals, and/or POMs, and selective adsorption and catalytic reaction in the pores have been achieved.

Another new approach is assembly of POMs to form microporous complex metal oxides. [17–19] The author has succeeded to synthesize orthorhombic and trigonal Mo–V oxides by assembly of pentagonal $[(Mo)Mo_5O_{21}]^{6-}$ polyoxomolybdate units of giant POMs, $\{Mo_{132}\}$ [20] or $\{Mo_{72}V_{30}\}$, [21] with other MoO_6 and VO_6 octahedra. The microporosity of the materials was resulted from 7-member-ring channels of octahedra. Thus formed Mo–V oxides were redox active and showed outstanding catalytic activity for selective oxidations of light alkanes, [22–24] acrolein, [25] and alcohols. [26,27] Furthermore,

the microporous properties were reversibly tunable by redox treatment. [28] Recently, the orthorhombic Mo–V oxide was applied as high capacity electrode materials for rechargeable lithium batteries. [29]

There have been a few reports on inorganic POM-based frameworks. [30–32] Linking of POM units with metal ions formed the frameworks with internal spaces. However, some organic molecules and/or ions occupied the spaces and were difficult to be removed, and the pore of these materials could not be opened.

Another example of POM-based frameworks was achieved by using POMs as building blocks for construction of metal organic frameworks (so-called POMOFs). [4,33–36] In POMOF materials, the ε-isomer of Keggin-type POMs is an ideal building block because ε-Keggin POMs have a truncated tetrahedral shape (T_d) with four hexagonal faces that can coordinate to metal ions (capping metal ions), such as Ni, Cu, Co, Bi, and La, by three oxygen atoms on one of the hexagonal faces (Figure 2. 1). [36–40] The capping metal ions can be coordinated by multi-dentate organic ligands that bridge the ε-Keggin POMs to form POMOFs. [34] However, the organic linkers result in materials with low oxidative and thermal stabilities, and the materials therefore cannot survive under harsh conditions. [34] Thus, no porosity was found in POMOFs due to molecules occupying the pores that cannot be removed without framework collapse. [34] A more inventive way would be to use metal ions to bridge ε-Keggin POMs without any organic linkers. So far, no example has been reported following this strategy.

Here, the author report the first all-inorganic microporous material based on ε-Keggin-type POM (ε-$VMo_{9.4}V_{2.6}O_{40}$, designated as Mo–V–Bi oxide), in which intrinsic micropores could be opened. These POM units were connected by Bi^{III} ions to form a three-dimensional (3D) network. Mo–V–Bi oxide had a 3D pore system like Faujasite FAU-type zeolites (Faujasite) [41] and showed zeolitic-like properties such as selective molecule adsorption.

Moreover, Mo–V–Bi oxide contained mostly octahedral coordinating metals and can be called “Octahedral Molecular Sieves (OMSs)”. Two kinds of OMSs have been

reported, the family of microporous Todorokite-type Mn and Fe oxides [42,43] and Mo–V mixed oxides, [19,28] and both of these have one-dimensional channels as with ZSM-12 MTW-type (ZMS-12) zeolites. [44] Mo–V–Bi oxide is the third member of OMSs, and the 3D pore system is new in OMS materials.

2.2. Experimental

2.2.1. Material preparation

$(NH_4)_6Mo_7O_{24}\cdot 4H_2O$ (8.828 g, 50 mmol based on Mo) was dissolved in 110 mL of water. $VOSO_4\cdot 5H_2O$ (3.219 g, 12.5 mmol) was dissolved in 110 mL of water. After the solids had been dissolved, the solution of $VOSO_4\cdot 5H_2O$ was poured into the solution of $(NH_4)_6Mo_7O_{24}\cdot 4H_2O$. After stirring at room temperature for 3 min, $Bi(OH)_3$ (0.438 g, 1.67 mmol) was added. Then the mixture was stirred for 7 min followed by N_2 bubbling for 10 min. The mixture was introduced into a 300-mL Teflon liner of a stainless-steel autoclave with the help of 20 mL of water. A Teflon sheet (4 m × 0.1 m × 0.1 mm) was inserted into the liner. The autoclave was placed in an oven heated at 448 K for 48 h. After the autoclave had been cooled down, the black solid on the bottom of the liner was transferred into centrifuge tubes with the help of water (200 mL) and separated by centrifugation (2000 rpm, 3 min). The collected solids were dispersed in water (200 mL) and separated by centrifugation (2000 rpm, 3 min). This washing process was repeated 6 times. The obtained solid was dried at 353 K overnight. Then 0.45 g of Mo–V–Bi oxide (yield: 3.3% based on Mo) was obtained. FT-IR (KBr pellets, ν/cm^{-1}): 1620, 1402, 991, 955, 856, 813, 718, 698, 642, and 546 cm^{-1}. Elemental Analysis: Calcd for $Bi_2Mo_{9.4}V_{3.6}N_{2.8}O_{47.2}H_{26.5}$: Bi, 17.98; Mo, 38.80; V, 7.89; N, 1.68; H, 1.15, Found: Bi, 18.45; Mo, 38.41; V, 7.51; N, 1.66; H, 0.97.

2.2.2. Crystal growth

Low concentration of the precursor, long synthesis time, and seed were applied to obtain a large single crystal for single crystal X-ray analysis. An aqueous solution (110

mL) of $(NH_4)_6Mo_7O_{24}\cdot 4H_2O$ (7.062 g, 40 mmol based on Mo) was mixed with 110 mL of an aqueous solution of $VOSO_4\cdot 5H_2O$ (2.575 g, 10 mmol). After stirring at room temperature for 3 min, $Bi(OH)_3$ (0.438 g, 1.67 mmol) was added, and synthesized Mo–V–Bi oxide (100 mg) was added as a seed. Then the mixture was stirred for 7 min followed by N_2 bubbling for 10 min. The mixture was introduced into a 300-mL Teflon liner of a stainless-steel autoclave with the help of 20 mL of water, and a Teflon sheet (4 m $\times$ 0.1 m $\times$ 0.1 mm) was inserted into the liner. The autoclave had been heated at 448 K for 96 h. After the autoclave was cooled down to room temperature, the black solid on the bottom of the liner was transferred into centrifuge tubes with the help of 200 mL of water and separated by centrifugation (2000 rpm, 3 min). The collected solids were dispersed in water (200 mL) and separated by centrifugation (2000 rpm, 3 min.). This washing process was repeated six times, and the obtained solid was dried at 353 K overnight. The obtained solid was used as a seed again. After repeating this crystal growth procedure four times, the crystal of Mo–V–Bi oxide was large enough for single crystal analysis.

2.2.3. Calcination

The synthesized Mo–V–Bi oxide (1 g) was placed in a glass tube in a furnace and heated at 2 K/min to 623 K under N_2 (50 mL/min) and then maintained for 2 h at 623 K.

2.2.4. Characterization

Redox titration: The concentration of $KMnO_4$ solution was determined by using $H_2C_2O_4$ as a standard compound. $H_2C_2O_4\cdot 2H_2O$ (0.1157 g) was dissolved in 30 mL of water, followed by acidification with 15 mL of 16% H_2SO_4. Titration was performed at 343-358 K. The concentration of $KMnO_4$ was 0.04848 mol/L. Then Mo–V–Bi oxide (0.2867 g) was dissolved in 40 mL of 50% of H_2SO_4 that was degassed by N_2 bubbling in a 100-mL beaker. A Horiba D-52 pH meter with a metal (ORP) electrode was used to detect the potential of the Mo–V–Bi oxide solution. The solution of Mo–V–Bi oxide

was titrated with the standard solution of $KMnO_4$ at room temperature. Measured potential was plotted against amount of $KMnO_4$ solution. Molecule (CO_2, CH_4, C_2H_6, and C_3H_8) adsorption was performed on Mo–V–Bi oxide by a BELSORP MAX (BEL Japan Inc.) sorption analyzer at 298 K. The samples were evacuated at 573 K for 2 h before the measurement. Nitrogen isotherms were obtained by a BELSORP MAX (BEL Japan Inc.) sorption analyzer at 77 K. Surface area was calculated by the BET method using an adsorption branch, and pore distribution was estimated by the SF method using an adsorption branch. The samples were evacuated at 573 K for 2 h before the measurement. Powder X-ray diffraction (XRD) patterns were obtained on RINT2200 (Rigaku) with Cu Kα radiation (tube voltage: 40 kV, tube current: 20 mA). Scanning electron microscopy (SEM) images were obtained with an HD-2000 (HITACHI). Transmission electron microscopy (TEM) images were taken with a 200 kV TEM (JEOL JEM-2010F). Carbon was deposited on the sample prior to TEM observation to reduce charging-up of the sample. Fourier transform infrared spectroscopy (FT-IR) was carried out on a PARAGON 1000 (Perkin Elmer). Thermal analysis (TG-DTA) was performed on Thermo Plus, TG8120 (Rigaku). Temperature-programmed desorption mass spectrometry (TPD-MS) measurements were carried out from 313 K to 893 K at a heating rate of 10 K min^{-1} under helium (flow rate: 50 mL min^{-1}). The Mo–V–Bi oxide sample was set between two layers of quartz wool. A TPD apparatus (BELJAPN, Inc.) equipped with a quadrupole mass spectrometer (M-100QA; Anelva) was used to detect NH_3 (m/z = 16), H_2O (m/z = 18), O_2 (m/z = 32), and N_2 (m/z = 28). X-ray photoelectron spectroscopy (XPS) was performed on a JPS-9010MC (JEOL). The spectrometer energies were calibrated using the C 1s peak at 284.8 eV. Elemental compositions were determined by an inductive coupling plasma (ICP-AES) method (ICPE-9000, Shimadzu). CHN elemental composition was determined at Instrumental Analysis Division, Equipment Management Center, Creative Research Institution, Hokkaido University.

2.2.5. Computer-based simulation

All computer-based simulation was performed using Materials Studio v 6.1.0 (Accelrys Software Inc.). Rietveld analysis [45] of a powder XRD pattern was performed using "Reflex" tool in Materials studio. The lattice parameter and pattern parameters were refined by Pawley refinement based on the structure data obtained by single crystal structure analysis. Connolly surfaces, solvent surfaces, free space of Mo–V–Bi oxide, and volume of an C_2H_6 molecule were simulated by "Atom Volume & Surfaces" program in Materials Studio. The diameters of the cage and the channel were estimated from the Connolly surfaces of the cage and the channel with Connolly radius of 1 Å, and the shortest values were presented. [46] The theoretical accessible space of Mo–V–Bi oxide (without ammonium cations and water) was obtained by solvent surface calculation with solvent radius of 1.4 Å. [46] The volume of an C_2H_6 molecule was obtained by Connolly surface calculation with Connolly radius of 1 Å.

2.2.6. Single crystal analysis

Since the crystals that had been grown were still too small for the diffractometer in the laboratory system, data collection was performed on a high-precision diffractometer installed in the SPring-8 BL40XU beamline. [47,48] The synchrotron radiation emitted from helical undulator was monochromated by using a Si(111) channel cut monochromator and focused with a Fresnel zone plate. A Rigaku Saturn724 CCD detector was used. The measurement was performed at 100 (2) K. An empirical absorption correction based on Fourier series approximation was applied. The data were corrected for Lorentz and polarization effects. The structure was solved by direct methods and refined by full-matrix least-squares (SHELX-97), [49] where the unweighted and weighted agreement factors of $R = \Sigma||F_o| - |F_c||/\Sigma|F_o|$ ($I > 2.00\sigma(I)$) and $wR = [\Sigma w(Fo^2 - Fc^2)^2/\Sigma w(Fo^2)^2]^{1/2}$, respectively, were used. Nitrogen atoms of ammonium cations were modeled as oxygen atoms because nitrogen atoms could not be distinguished from oxygen atoms. Oxygen atoms of water in Mo–V–Bi oxide were

refined isotropically, and other atoms were refined anisotropically. Total amounts of water and ammonium cations estimated by elemental analysis were slightly larger than those obtained by single crystal structure analysis. This is because the difference in the crystal sample and bulk sample. The sample for elemental analysis may contain surface waters. Crystallographic data of Mo–V–Bi oxide was listed in Table 2. 1. Anisotropic displacement ellipsoids were presented in Figure 2. 2. Metal-oxygen bond lengths, atom coordinates and atom occupancies are summarized in Table 2. 2 and Table 2. 3, respectively. CIF files are available in Supplementary Information. CSD-425857 contains the crystallographic data for Mo–V–Bi oxide (data available from CrysDATA@FIZ-Karlsruhe.de).

2.3. Results and discussion

2.3.1. Synthesis and structure characterization

Hydrothermal reaction of $(NH_4)_6Mo_7O_{24}\cdot 4H_2O$, $VOSO_4\cdot 5H_2O$, and $Bi(OH)_3$ produced crystalline Mo–V–Bi oxide, the powder XRD pattern of which is presented in Figure 2. 3a. SEM images showed that the resulting solids were polyhedral crystals that were too small (less than 1 μm in one dimension) to perform single crystal structure analysis (Figure 2. 4a). Therefore, crystal growth experiments were performed using the synthesized Mo–V–Bi oxide as a seed in the reaction mixture. After repeating the crystal growth procedure, crystals of Mo–V–Bi oxide large enough (~5 μm in one diameter) for single crystal analysis were obtained (Figure 2. 4b).

Single crystal structure analysis and elemental analysis (Mo: V: Bi = 9.4: 3.6: 2) of the as-prepared Mo–V–Bi oxide revealed that the building block of Mo–V–Bi oxide was an ε-Keggin-type polyoxovanadomolybdate, ε-$VMo_{9.4}V_{2.6}O_{40}$, that was formed by one central VO_4 tetrahedron surrounded by twelve distorted MO_6 (M = Mo or V) octahedra (Figure 2. 1). The central atom of this POM was a four-fold coordinated vanadium with bond length of V-O being 1.76(2) for Mo–V–Bi oxide. Bond valence sum (BVS) calculation revealed that valence of the central V was 5+, which is often

observed in polyoxometalate compounds. [40,50] Four edge-sharing M_3O_{13} (M = Mo or V) units were anchored to this tetrahedral VO_4 to form the ε-Keggin POM. Disordering of the molybdenum and vanadium atoms in the surrounding twelve positions was detected, as has been often observed in polyoxomolybdates [51] and Mo–V-based complex metal oxides. [17] Three oxygen atoms in each hexagonal face of the POM coordinated to Bi, and an adjacent POM supplied three oxygen atoms in the hexagonal face to the Bi to form a diamond-like 3D framework (Figure 2. 5). The bond length of Bi-O was 2.355(12) for Mo–V–Bi oxide, and BVS calculations revealed that the valence of the Bi linker was 3+.

The powder X-ray diffraction pattern of Mo–V–Bi oxide was similar to the simulated pattern obtained by using crystal data from single crystal structure analysis (Figure 2. 3). Furthermore, there were no additional peaks in the experimental data, indicating that the powder sample of Mo–V–Bi oxide was pure.

Figure 2. 6 shows a comparison of the generated polyhedral image and the high-resolution transmission electron microscopy (HRTEM) image of Mo–V–Bi oxide along the 1 0 1 direction. The HRTEM revealed a characteristic face-centered cubic lattice image for Mo–V–Bi oxide. Ordering of the rhombic black and white spots in the HRTEM image was exactly the same as the ordering of ε-$VMo_{9.4}V_{2.6}O_{40}$ building blocks and pores. The unit cell lengths and distances of the (1 1 1) plane were obtained from the HRTEM image: 19.7 Å and 11.4 Å, respectively.

The oxidation states of the metal elements were studied by X-ray photoelectron spectroscopy (XPS) (Figure 2. 7), which indicated that reduced states of molybdenum (Mo^V) and vanadium (V^{IV}) existed, and the oxidation state of bismuth was 3+. Furthermore, XPS showed that 25% of the molybdenum and 50% of the vanadium were Mo^V and V^{IV}, respectively. The total reduced metal content (molybdenum and vanadium) was 32%. Manganometric redox titration also confirmed that ca. 28% of the total metal (molybdenum and vanadium) was reduced (Figure 2. 8). Partial reduction was in good agreement with other reported ε-Keggin POM molecules. In the case of

[ε-$Mo^{VI}Mo^{V}_{12}O_{40}(C_5Me_5Rh^{III})_8]^{2+}$, [52] [$\varepsilon$-$P^{V}Mo^{V}_{8}Mo^{VI}_{4}O_{36}(OH)_4\{La^{III}(H_2O)_4\}_4]^{5+}$, [38] and [$\varepsilon$-$H_2Mo^{V}_{12}O_{30}(OH)_{10}\{Ni^{II}(H_2O)_3\}_4]$, [37] all or part of the surrounding twelve metal ions are reduced. Thus, the detailed formula of the ε-Keggin POM framework was [ε-$V^{V}_{1.0}Mo^{V}_{2.3}Mo^{VI}_{7.1}V^{IV}_{1.8}V^{V}_{0.8}O_{40}Bi^{III}_{2}]^{3.7-}$.

There were cages and channels in Mo–V–Bi oxide. A cage was comprised of ten ε-$VMo_{9.4}V_{2.6}O_{40}$ building blocks that were connected by Bi^{III} ions (Figure 2. 9a and b). The internal diameter of the cage was ca. 7.7 Å. One cage was tetrahedrally connected with four other adjacent cages by four channels (Figure 2. 9c and d). The diameter of the channel was ca. 3.4 Å. The cages and channels constructed a periodical 3D pore system for Mo–V–Bi oxide in a tetrahedral fashion. In one direction, the tunnel of the micropore was not straight but in a zigzag-like fashion (Figure 2. 9e and S3), which is new in OMSs.

Single crystal structure analysis of Mo–V–Bi oxide revealed that there were two types of sites for water or NH_4^+ (ten sites per one ε-$VMo_{9.4}V_{2.6}O_{40}$ unit). One was in the cage and the other was in the channel. Nitrogen (represented NH_4^+) could not be distinguished from oxygen (represented H_2O) by single crystal analysis (Figure 2. 9e). An FT-IR spectrum of Mo–V–Bi oxide showed the presence of water (1620 cm^{-1}) and NH_4^+ (1402 cm^{-1}) together with bands at 991, 955, 856, 813, 718, 698, 642, and 546 cm^{-1}, which were attributed to the framework. The amount of NH_4^+ was estimated by elemental analysis to be ca. 2.8 for one ε-Keggin POM. Therefore, the detailed formula can be expressed as $(NH_4)_{2.8}H_{0.9}[\varepsilon$-$V^{V}_{1.0}Mo^{V}_{2.3}Mo^{VI}_{7.1}V^{IV}_{1.8}V^{V}_{0.8}O_{40}Bi^{III}_{2}] \cdot 7.2H_2O$.

The NH_4^+ and H_2O in Mo–V–Bi oxide were removable by heat treatment. TG-DTA of Mo–V–Bi oxide indicated that there were two weight losses; one was between ca. 310 and 490 K and the other was between ca. 580 and 710 K (Figure 2. 10). Temperature programmed desorption (TPD) analysis revealed that the first weight loss corresponded to desorption of water and NH_3 and that the second weight loss corresponded to desorption of water, NH_3, and N_2 (Figure 2. 10). N_2 was produced by decomposition of NH_4^+. Total weight loss from room temperature to 773 K was ca.

7.8%, which was in accord with the total amount of NH_4^+ and water estimated by elemental analysis. TPD results showed that there were two kinds of NH_4^+ in the material. One NH_4^+, which had a strong interaction with the framework, desorbed at 633 K (peak top) and is denoted as NH_4^+(S). The other, which had a relatively weak interaction with the framework, desorbed at 443 K (peak top) and is denoted as NH_4^+(W). These results indicated that NH_4^+ and water co-occupied two different positions in the as-synthesized material; one was in the cage and the other was in the channel. Total NH_4^+ amount estimated by TPD was slightly less than NH_4^+ amount estimated by elemental analysis, because some NH_4^+ were released as N_2.

2.3.2. Microporosity

The NH_4^+ and water was removed by calcination (2 K/min, 623 K for 2 h, N_2 flow rate of 50 mL/min) without structural collapse (Figure 2. 11). However, further heating (calcination at 673 K) caused the framework of Mo–V–Bi oxide to collapse (Figure 2. 11). The nitrogen adsorption-desorption isotherm of calcined Mo–V–Bi oxide was best described as a type I isotherm, indicating that Mo–V–Bi oxide was a microporous material (Figure 2. 12 8a and b black). The BET surface area and pore volume of this material was calculated to be 60 m^2/g and 0.0202 cm^3/g, respectively, which are similar to those of other reported POM-based porous materials. The pore size distribution curve (obtained by the SF method) showed that the average diameter of the micropores was 5.5 Å, attributed to the cages and channels in the framework (Figure 2. 12). The powder XRD pattern of the material after adsorption measurement showed that the structure of the material did not change, indicating that the framework was stable under the measurement conditions.

Mo–V–Bi oxide selectively adsorbed different molecules depending on the size of the molecule (Figure 2. 13). The size of the channel (3.4 Å) of Mo–V–Bi oxide was similar to that of C (3.4 Å) and O (3.04 Å) atoms. Therefore, the straight molecules (CO_2, CH_4, and C_2H_6), in which skeleton atoms (C and O) were in a straight line, were

able to pass the channel and adsorbed in the material. C_3H_8 whose carbon skeleton was bent and larger than the channel was not adsorbed. Interestingly, Mo–V–Bi oxide adsorbed C_2H_6 at low pressure from 0.002 kPa to 0.06 kPa (type I isotherm, Figure 2. 13). The theoretical accessible space of a cage (49.84 $Å^3$) was similar to the volume of an C_2H_6 (47.28 $Å^3$) molecule, so that C_2H_6 could fit in the cage, which may be the reason for the type I adsorption of C_2H_6.

2.4. Conclusion

The first all-inorganic Keggin-type polyoxometalate-based microporous material with intrinsically ordered open micropores, Mo–V–Bi oxide, was successfully synthesized and characterized. Structure characterization showed that the material constructed by assembly of ε-Keggin POMs with Bi^{III} ions in a tetrahedral fashion. Heat treatment could remove the existing NH_4^+ and H_2O from the material to open the 3D micropores. The 3D micropore system of Mo–V–Bi oxide was result from cages and channels in the material. Mo–V–Bi oxide exhibited zeolite-like properties such as molecule adsorption. POMs have a diversity of elements and can incorporate other metals in the structure. The author believe our results will open a door for production of new porous materials based on ε-Keggin-type POM building blocks with tunable properties.

References

(1) Special thematic issue on polyoxometalates. *Chem. Rev.* **1998**, *98*, 1–390.

(2) Special thematic issue on polyoxometalates. *Chem. Soc. Rev.* **2012**, *41*, 7325–7648.

(3) Long, D.-L.; Tsunashima, R.; Cronin, L. *Angew. Chem. Int. Ed.* **2010**, *49*, 1736–1758.

(4) Kamiya, Y.; Sadakane, M.; Ueda, W. Heteropoly Compounds. In *Comprehensive Inorganic Chemistry II*; Reedijk, J., Poeppelmeier, K., Ed.; Oxford: Elsevier, 2013; Vol. 7, pp. 185–204.

(5) Song, J.; Luo, Z.; Britt, D. K.; Furukawa, H.; Yaghi, O. M.; Hardcastle, K. I.; Hill, C. L. *J. Am. Chem. Soc.* **2011**, *133*, 16839–16846.

(6) Sun, C.-Y.; Liu, S.-X.; Liang, D.-D.; Shao, K.-Z.; Ren, Y.-H.; Su, Z.-M. *J. Am. Chem. Soc.* **2009**, *131*, 1883–1888.

(7) Mizuno, N.; Misono, M. *Chem. Rev.* **1998**, *98*, 199–218.

(8) Taylor, D. B.; McMonagle, J. B.; Moffat, J. B. *J. Colloid Interface Sci.* **1985**, *108*, 278–284.

(9) Okamoto, K.; Uchida, S.; Ito, T.; Mizuno, N. *J. Am. Chem. Soc.* **2007**, *129*, 7378–7384.

(10) Inumaru, K. *Catal. Surv. Asia* **2006**, *10*, 151–160.

(11) Uchida, S.; Mizuno, N. *Coord. Chem. Rev.* **2007**, *251*, 2537–2546.

(12) Eguchi, R.; Uchida, S.; Mizuno, N. *J. Phys. Chem. C* **2012**, *116*, 16105–16110.

(13) Eguchi, R.; Uchida, S.; Mizuno, N. *Angew. Chem. Int. Ed.* **2012**, *51*, 1635–1639.

(14) Jiang, C.; Lesbani, A.; Kawamoto, R.; Uchida, S.; Mizuno, N. *J. Am. Chem. Soc.* **2006**, *128*, 14240–14241.

(15) Kawamoto, R.; Uchida, S.; Mizuno, N. *J. Am. Chem. Soc.* **2005**, *127*, 10560–10567.

(16) Uchida, S.; Hikichi, S.; Akatsuka, T.; Tanaka, T.; Kawamoto, R.; Lesbani, A.; Nakagawa, Y.; Uehara, K.; Mizuno, N. *Chem. Mater.* **2007**, *19*, 4694–4701.

(17) Sadakane, M.; Yamagata, K.; Kodato, K.; Endo, K.; Toriumi, K.; Ozawa, Y.; Ozeki, T.; Nagai, T.; Matsui, Y.; Sakaguchi, N.; Pyrz, W. D.; Buttrey, D. J.; Blom, D. A.; Vogt, T.; Ueda, W. *Angew. Chem. Int. Ed.* **2009**, *48*, 3782–3786.

(18) Sadakane, M.; Endo, K.; Kodato, K.; Ishikawa, S.; Murayama, T.; Ueda, W. *Eur. J. Inorg. Chem.* **2013**, 1731–1736.

(19) Sadakane, M.; Kodato, K.; Kuranishi, T.; Nodasaka, Y.; Sugawara, K.; Sakaguchi, N.; Nagai, T.; Matsui, Y.; Ueda, W. *Angew. Chem. Int. Ed.* **2008**, *47*, 2493–2496.

(20) Müller, A.; Krickemeyer, E.; Bögge, H.; Schmidtmann, M.; Peters, F. *Angew. Chem. Int. Ed.* **1998**, *37*, 3359–3363.

(21) Müller, A.; Todea, A. M.; van Slageren, J.; Dressel, M.; Bögge, H.; Schmidtmann, M.; Luban, M.; Engelhardt, L.; Rusu, M. *Angew. Chem. Int. Ed.* **2005**, *44*, 3857–3861.

(22) Konya, T.; Katou, T.; Murayama, T.; Ishikawa, S.; Sadakane, M.; Buttrey, D.; Ueda, W. *Catal. Sci. & Technol.* **2013**, *3*, 380–387.
(23) Kubo, J.; Watanabe, N.; Ueda, W. *Chem. Eng. Sci.* **2008**, *63*, 1648–1653.
(24) Watanabe, N.; Ueda, W. *Ind. Eng. Chem. Res.* **2006**, *45*, 607–614.
(25) Sadakane, M.; Watanabe, N.; Katou, T.; Nodasaka, Y.; Ueda, W. *Angew. Chem. Int. Ed.* **2007**, *46*, 1493–1496.
(26) Wang, F.; Ueda, W. *Catal. Today* **2009**, *144*, 358–361.
(27) Wang, F.; Ueda, W. *Topics in Catal.* **2008**, *50*, 90–97.
(28) Sadakane, M.; Ohmura, S.; Kodato, K.; Fujisawa, T.; Kato, K.; Shimidzu, K.; Murayama, T.; Ueda, W. *Chem. Commun.* **2011**, *47*, 10812–10814.
(29) Kaveevivitchai, W.; Jacobson, A. J. *Chem. Mater.* **2013**, *25*, 2708–2715.
(30) Liu, D.; Lu, Y.; Tan, H.-Q.; Chen, W.-L.; Zhang, Z.-M.; Li, Y.-G.; Wang, E.-B. *Chem. Commun.* **2013**, 3673–3675.
(31) Mitchell, S. G.; Streb, C.; Miras, H. N.; Boyd, T.; Long, D.-L.; Cronin, L. *Nature Chem.* **2010**, *2*, 308–312.
(32) Mitchell, S. G.; Boyd, T.; Miras, H. N.; Long, D.-L.; Cronin, L. *Inorg. Chem.* **2011**, *50*, 136–143.
(33) Mandic, S.; Healey, M. R.; Gotthardt, J. M.; Alley, K. G.; Gable, R. W.; Ritchie, C.; Boskovic, C. *Eur. J. Inorg. Chem.* **2013**, 1631–1634.
(34) Nohra, B.; El Moll, H.; Rodriguez Albelo, L. M.; Mialane, P.; Marrot, J.; Mellot-Draznieks, C.; O'Keeffe, M.; Biboum, R. N.; Lemaire, J.; Keita, B.; Nadjo, L.; Dolbecq, A. *J. Am. Chem. Soc.* **2011**, *133*, 13363–13374.
(35) Rodriguez-Albelo, L. M.; Rabdel Ruiz-Salvador, A.; Sampieri, A.; Lewis, D. W.; Gomez, A.; Nohra, B.; Mialane, P.; Marrot, J.; Secheresse, F.; Mellot-Draznieks, C.; Biboum, R. N.; Keita, B.; Nadjo, L.; Dolbecq, A. *J. Am. Chem. Soc.* **2009**, *131*, 16078–16087.
(36) Dolbecq, A.; Mialane, P.; Secheresse, F.; Keita, B.; Nadjo, L. *Chem. Commun.* **2012**, 8299–8316.
(37) Muller, A.; Beugholt, C.; Kogerler, P.; Bogge, H.; Bud'ko, S.; Luban, M. *Inorg. Chem.* **2000**, *39*, 5176–5177.
(38) Mialane, P.; Dolbecq, A.; Lisnard, L.; Mallard, A.; Marrot, J.; Secheresse, F. *Angew. Chem. Int. Ed.* **2002**, *41*, 2398–2401.
(39) Sloboda-Rozner, D.; Neimann, K.; Neumann, R. *J. Mol. Catal. A: Chem.* **2007**, *262*, 109–113.
(40) Tucher, J.; Nye, L. C.; Ivanovic-Burmazovic, I.; Notarnicola, A.; Streb, C. *Chem. Eur. J.* **2012**, *18*, 10949–10953.
(41) Baur, W. H. *Am. Mineral.* **1964**, *49*, 697–704.
(42) Suib, S. L. *Acc. Chem. Res.* **2008**, *41*, 479–487.
(43) Suib, S. L. *J. Mater. Chem.* **2008**, *18*, 1623–1631.
(44) Fyfe, C. A.; Gies, H.; Kokotailo, G. T.; Marler, B.; Cox, D. E. *J. Phys. Chem.* **1990**, *94*, 3718–3721.

(45) Young, R. A. *The Rietveld Method*; Young, R. A., Ed.; Oxford University Press: Oxford, 1995.
(46) Ryu, J.; Park, R.; Kim, D.-S. *J. Comput. Sci. Technol.* **2006**, *21*, 225–260.
(47) Yasuda, N.; Fukuyama, Y.; Toriumi, K.; Kimura, S.; Takata, M. In *AIP Conference Proceedings*; Garrett, R., Gentle, I., Nugent, K., Wilkins, S., Ed.; 2010; Vol. 1234, pp. 147–150.
(48) Yasuda, N.; Murayama, H.; Fukuyama, Y.; Kim, J.; Kimura, S.; Toriumi, K.; Tanaka, Y.; Moritomo, Y.; Kuroiwa, Y.; Kato, K.; Tanaka, H.; Takata, M. *J. Synchrotron Rad.* **2009**, *16*, 352–357.
(49) Sheldrick, G. M. *SHELX-97, Program for Crystal Structure Analysis*; Universität Göttingen: Germany, 1997.
(50) Zhang, Q.-Z.; Lu, C.-Z.; Yang, W.-B.; Wu, C.-D.; Yu, Y.-Q.; Yan, Y.; Liu, J.-H.; He, X. *J. Clust. Sci.* **2003**, *14*, 381–390.
(51) Zang, X.; Tan, H.; Wu, Q.; Li, Y.; Li, Y.; Wang, E. *Inorg. Chem. Commun.* **2010**, *13*, 471–474.
(52) Chae, K.; Day, V. W.; Eberspacher, T. A. *Inorg. Chem.* **1992**, *8*, 3187–3189.

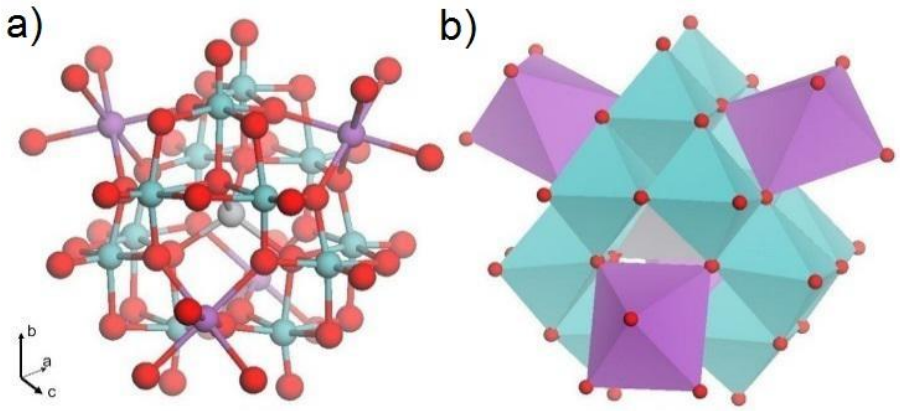

Figure 2. 1. Representations of ε-$VMo_{9.4}V_{2.6}O_{40}$ Keggin core with capping Bi^{III} ions a) ball-and-stick representation and b) polyhedral representation. central V (gray), Bi (purple), Mo or V (blue), O (red).

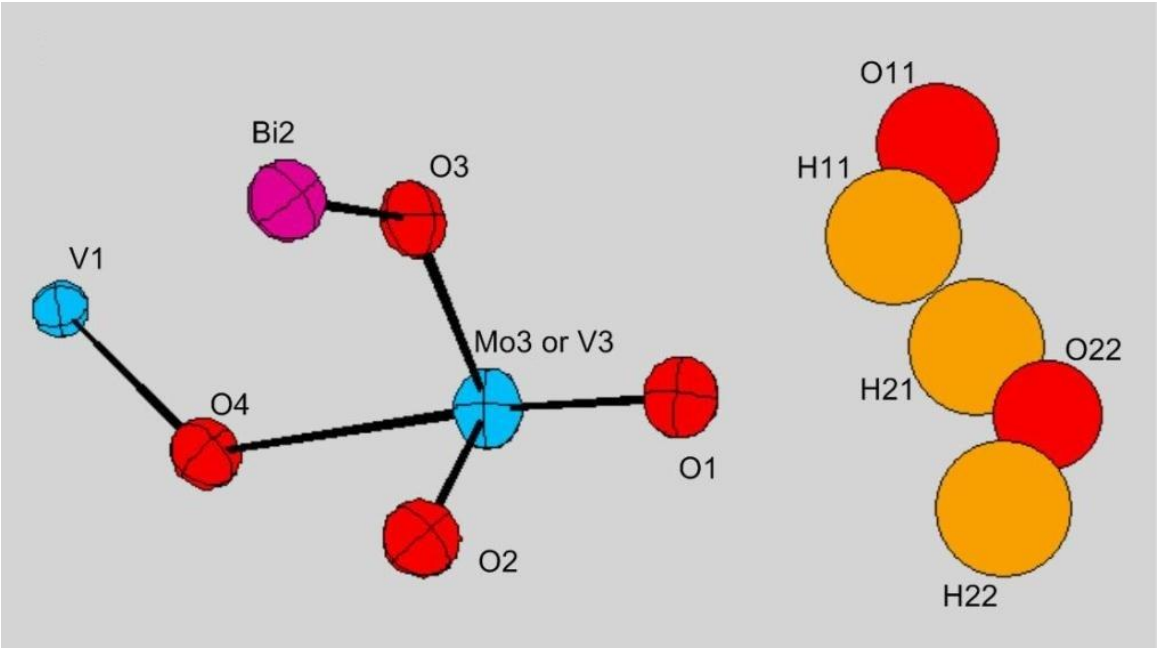

Figure 2. 2. Anisotropic displacement ellipsoids of Mo–V–Bi oxide structure by single crystal structure analysis as-synthesized Mo–V–Bi oxide.

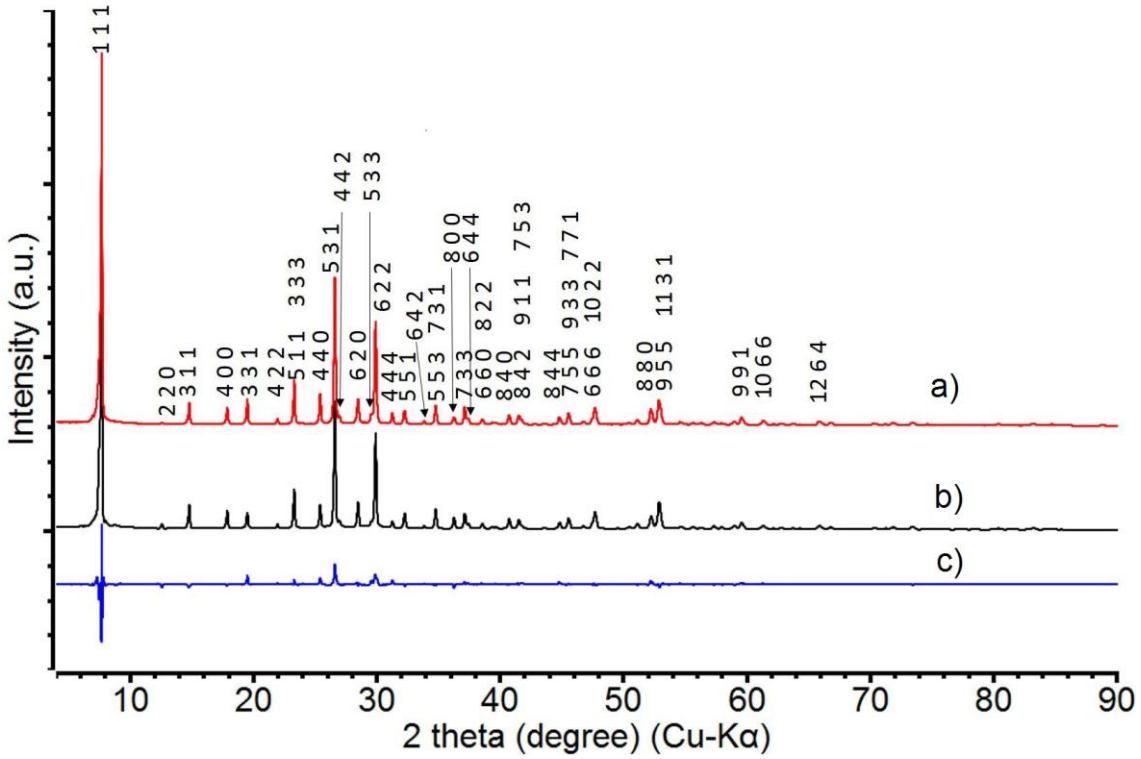

Figure 2. 3. Comparison of a) the experimental XRD pattern with b) simulated pattern using structure data obtained by single crystal structure analysis with lattice parameter refinement (a = 19.79 Å, R_{wp} = 10.49%), and c) difference of experimental pattern and simulated pattern.

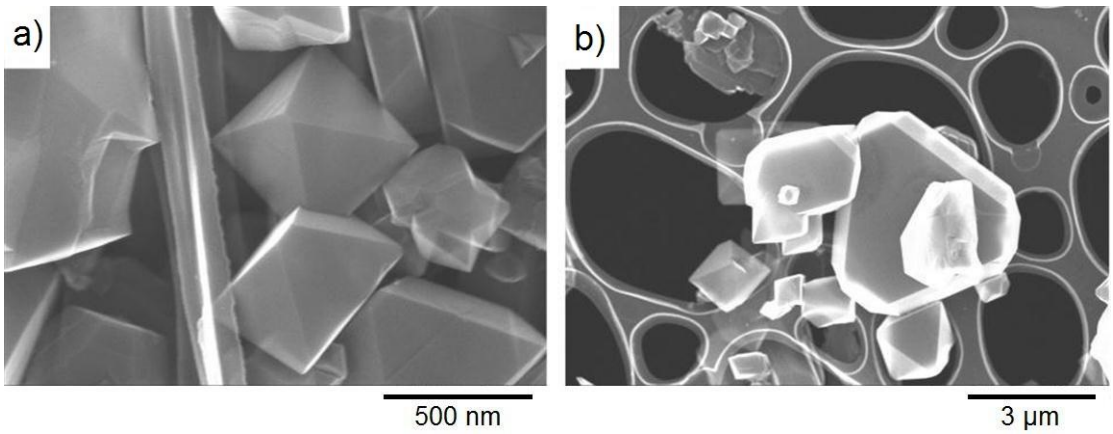

Figure 2. 4. SEM images of a) Mo–V–Bi oxide and b) large Mo–V–Bi oxide crystal for single crystal analysis.

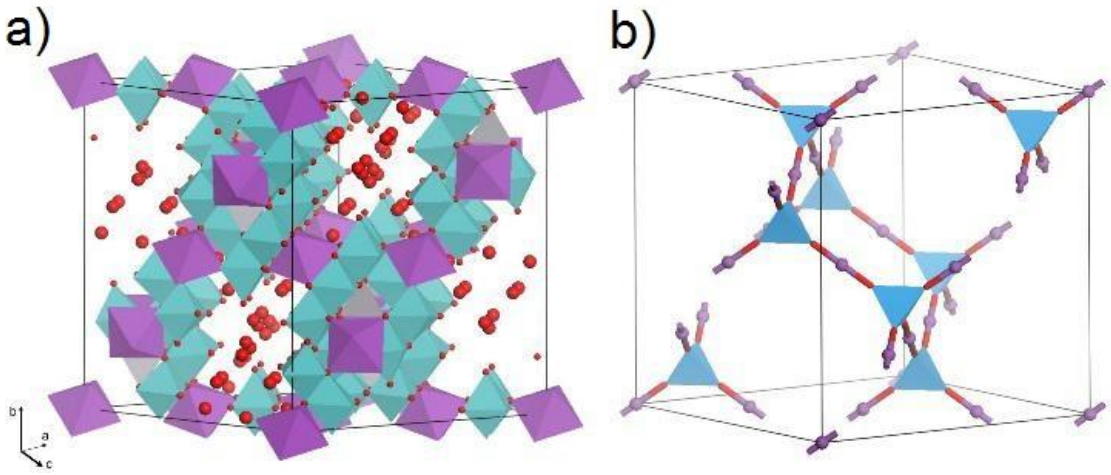

Figure 2. 5. a) Polyhedral representations of Mo–V–Bi oxide, central VO_4: (gray tetrahedron), BiO_6 (purple octahedron), $Mo(V)O_6$ (light blue octahedra), O (red sphere) and b) schematic representation of Mo–V–Bi oxide, POM unit (blue tetrahedron), Bi (purple sphere).

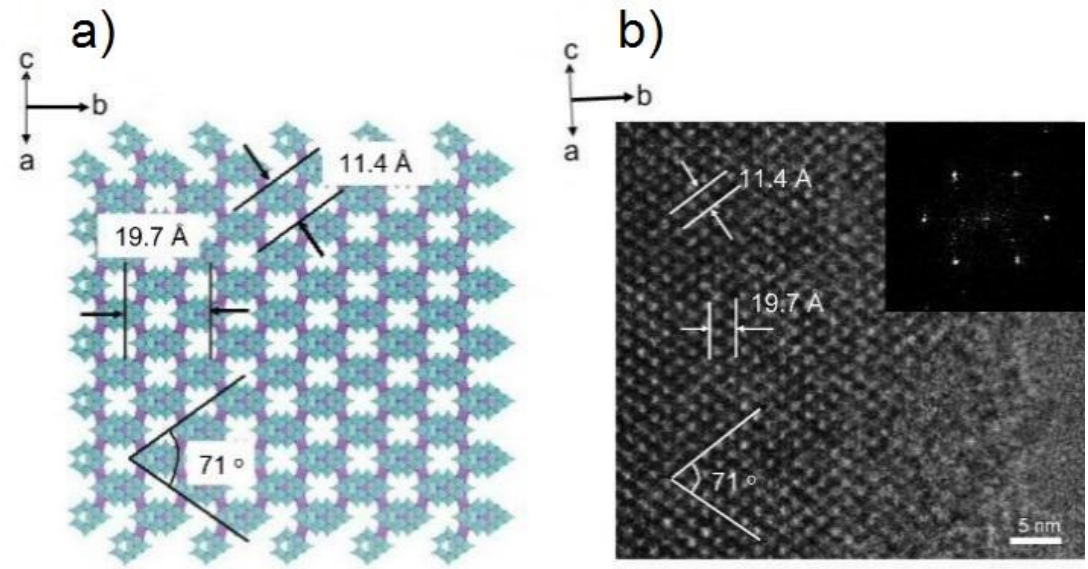

Figure 2. 6. Comparison of polyhedral representation of Mo–V–Bi oxide with HRTEM a) Polyhedral representation and b) HRTEM image (insert: power spectrum) of Mo–V–Bi oxide, viewed along the 1 0 1 direction. Mo–V–Bi oxide was not so stable under TEM condition, and an amorphous-like part was produced during observation.

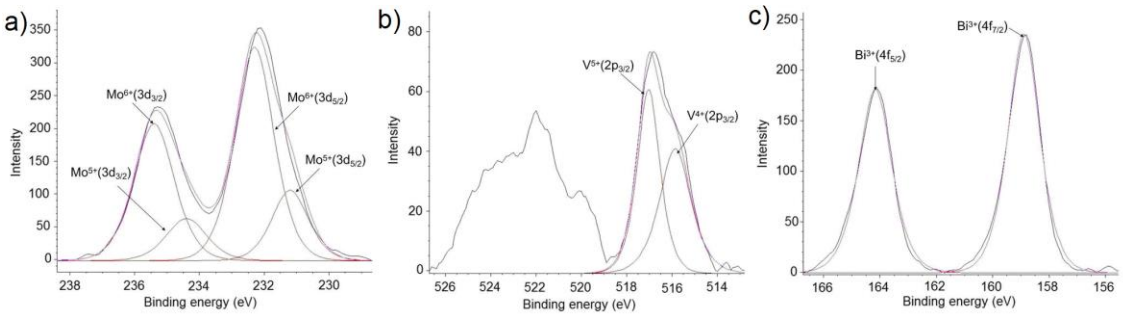

Figure 2. 7. XPS and curve fitting results of Mo–V–Bi oxide of a) Molybdenum, Mo^{6+}/Mo^{5+} = 3, b) vanadium, V^{5+}/V^{4+} = 1, and c) bismuth, blue: experimental data, purple: sum of every simulated peak, red: simulated peak.

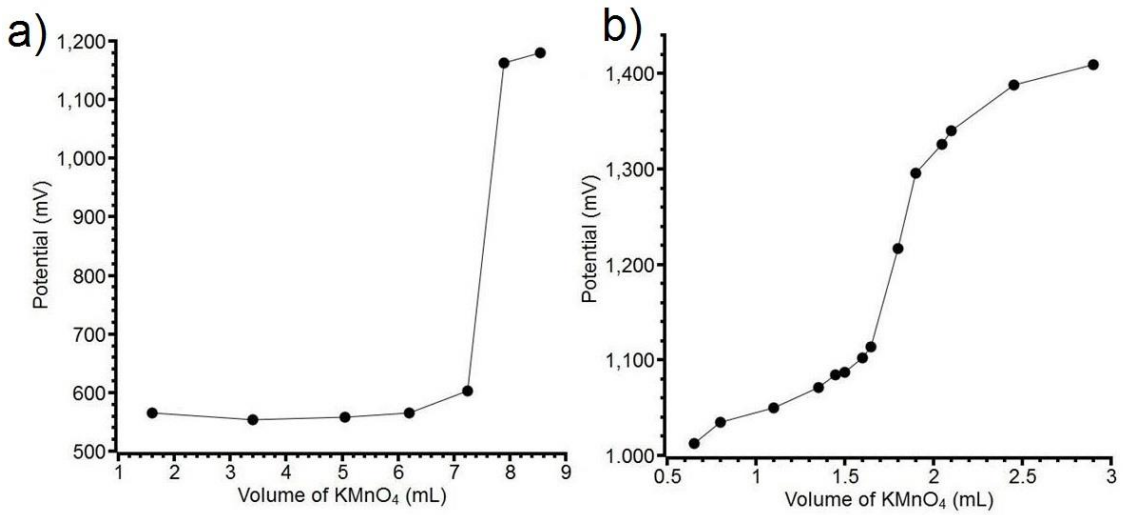

Figure 2. 8. Manganometric redox titration curves of a) $H_2C_2O_4 \cdot 2H_2O$ and b) Mo–V–Bi oxide.

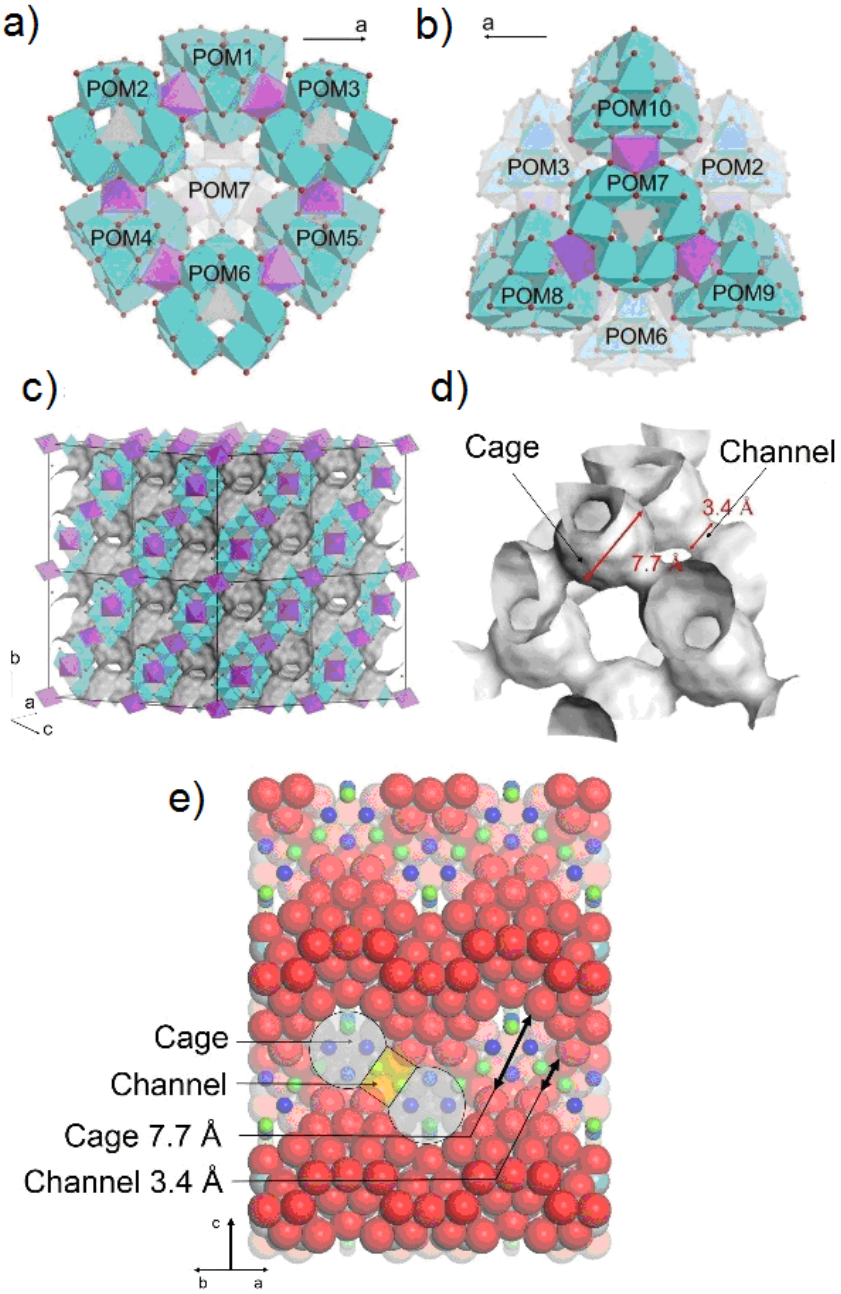

Figure 2. 9. Polyhedral representations of a) a front image of the cage, b) a back image of the cage, c) filling representation of the pore system with framework, gray curved surface described the morepores, d) filling representation of the pore system without framework and linkage of a cage by channels, gray curved surface described the morepores, central VO_4 (gray tetrahedron), BiO_6 (purple octahedron), $Mo(V)O_6$ (blue octahedron), O (red sphere), and e) CPK (Corey, Pauling, and Koltun) representations of the (1 1 0) plane of Mo–V–Bi oxide, N or O in cage (blue sphere), N or O in channel (green sphere).

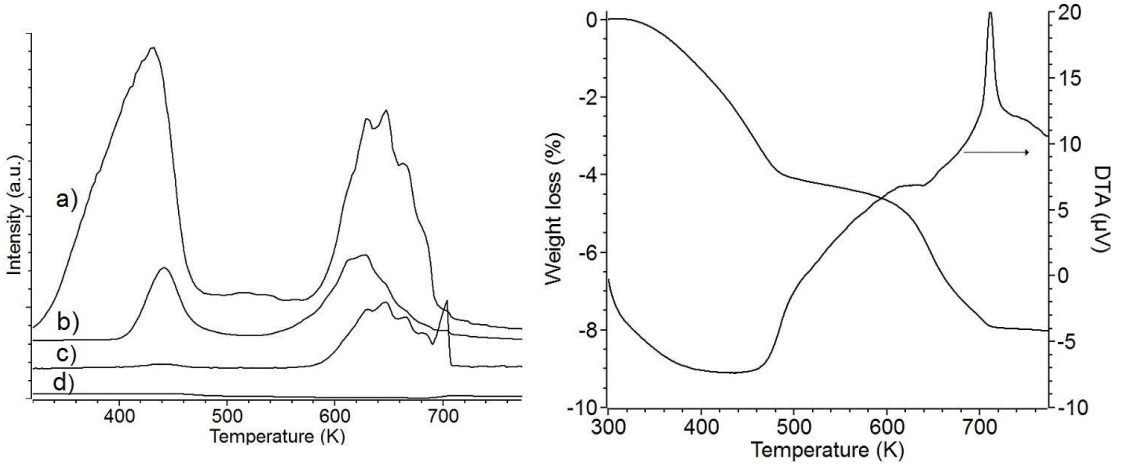

Figure 2. 10. (left) TPD of as-synthesized Mo–V–Bi oxide a) m/z = 18 for H_2O b) m/z = 16 for NH_3, c) m/z = 28 for N_2, and d) m/z = 32 for O_2, (right) TG-DTA of as-synthesized Mo–V–Bi oxide.

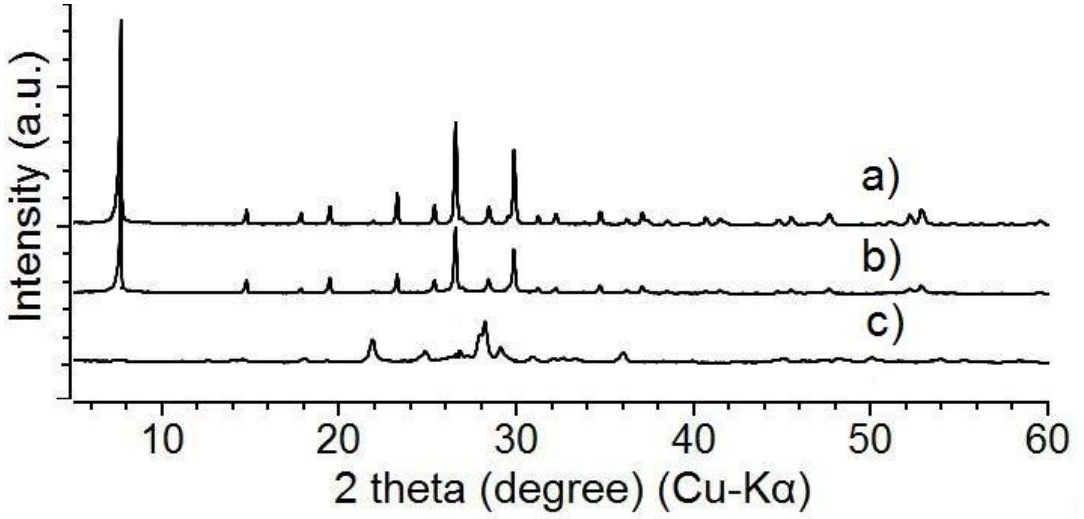

Figure 2. 11. XRD patterns of a) as-synthesized Mo–V–Bi oxide, b) Mo–V–Bi oxide calcined at 623 K, c) Mo–V–Bi oxide calcined at 673 K.

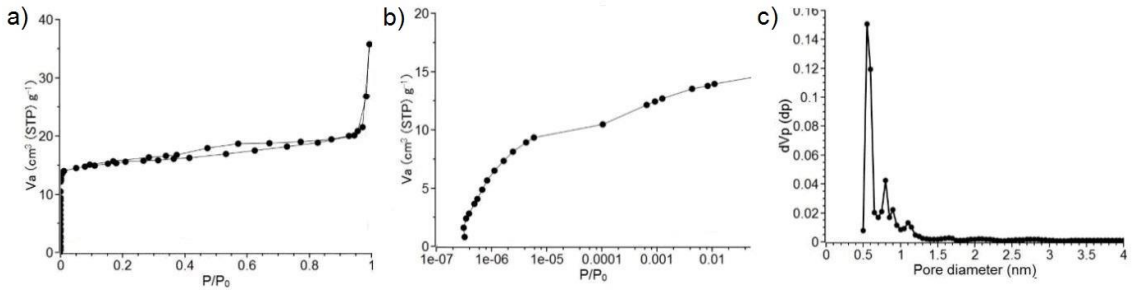

Figure 2. 12. Nitrogen adsorption-desorption isotherms a) p/p_0: 0 - 1, b) low p/p_0 range, and c) Pore size distribution of calcined Mo–V–Bi oxide using the SF method.

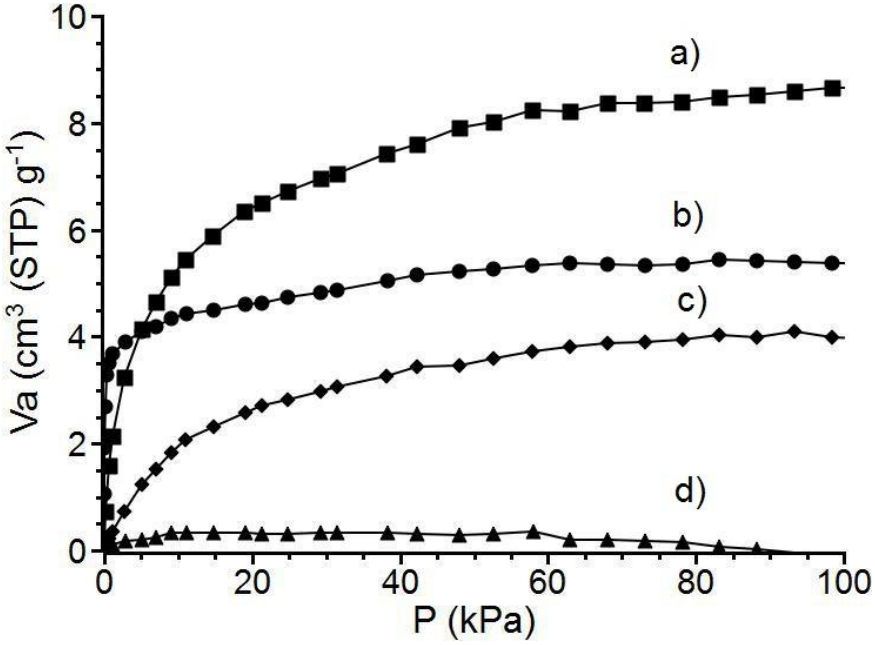

Figure 2. 13. Molecule adsorption isotherms of Mo–V–Bi oxide a) carbon dioxide, b) ethane, c) methane, and d) propane.

Table 2. 1. Crystallographic data of Mo–V–Bi oxide.

	Mo–V–Bi oxide
Formula	$H_{14.10}Bi_2Mo_{9.4}O_{47.05}V_{3.6}$
*M*r	2270.19
Crystal system	Cubic
Space group	$Fd\bar{3}m$
a (Å)	19.662(3)
V (Å^3)	7600.9(18)
T (K)	100(2)
Z	8
ρ_{calcd} (g·cm^{-3})	3.968
F_{000}	8273
λ (Å)	0.83077
μ (mm^{-1})	14.593
Measured reflections	3748
Unique reflections	372
$R1(I > 2\sigma(I))$	0.0580
w*R*2(all data)	0.1552
GOF	1.091

Table 2. 2. Atom position and occupancy from single crystal analysis of as-synthesized Mo–V–Bi oxide.

Atom	X	y	Z	Occupancy
V1	0.125	0.125	0.125	1
Bi2	0	0	0	1
V3	-0.04998(8)	0.07102(6)	0.17898(6)	0.22
Mo3	-0.04998(8)	0.07102(6)	0.17898(6)	0.78
O1	-0.1328(6)	0.0637(5)	0.1863(5)	1
O2	-0.0205(4)	-0.0205(4)	0.1733(6)	1
O3	-0.0387(6)	0.0802(4)	0.0802(4)	1
O4	0.0735(6)	0.0735(6)	0.1765(6)	1
O11	-0.260(3)	0.125	0.125	0.93(12)
H11	-0.235(4)	0.0998(4)	0.1502(4)	0.93(12)
O22	-0.287(7)	0.037(7)	0.213(7)	0.36(13)
H21	-0.262(7)	0.062(7)	0.188(7)	0.12(4)
H22	-0.262(7)	0.012(7)	0.238(7)	0.36(13)

Table 2. 3. Metal-oxygen bond lengths from single crystal analysis of as-synthesized Mo–V–Bi oxide.

	Bond length of Mo–V–Bi oxide (Å)
V1-O4	1.76(2)
Bi2-O3	2.355(12)
M3-O1	1.640(12)
M3-O2	1.894(5)
M3-O3	1.964(8)
M3-O4	2.428(12)

M includes V and Mo

Table 2. 4. Refined parameters and agreement factor of Rietveld analysis for as-synthesized Mo–V–Bi oxide.

Lattice parameter	
$a = b = c$ (Å)	19.79
$\alpha = \beta = \gamma$ (degree)	90
Agreement factors	
R_{wp}	10.49%
$R_{wp(w/o\ bck)}$	16.74%
R_p	7.88%
Pattern parameter	
Peak shape	
Function	Tomandl pseudo-voigt
FWHM	U = 0.35170, V = -0.14267, W = 0.02721
Profile parameter	N_A = 0.98930, N_B = -0.01099, N_C = 0.17914
Line shift	
Instrument geometry	Bragg-Brentano
Zero point	-0.28700
Shift#1	0.20214
Shift#2	0.09717
Correction:	
Method	Berar-Baldinozzi
Parameter	P1 = -0.63029, P2 = -0.01626, P3 = 1.09433, P4 = -0.01116
Background coefficients	Polynomial = 100
Preferred orientation	
March-Dollase	R0 = 0.71439

Chapter 3. Synthesis of X–Mo–Y oxide (X = NH_4^+ or Na^+, Y = Zn, Mn, Fe, or Co) and their structure analysis with powder XRD patterns

3.1. Introduction

One of the important properties of POMs is diversity of the elements in the structures, and it is desirable for many kinds of elements to be able to be incorporated in the structures of ε-Keggin POM-based 3D frameworks and their properties such as stability, ion-exchange property, acidity, redox properties, magnetic properties, and pore properties to be easily tuned.

From single crystal analysis, Mo–V–Bi oxide is comprised of ε-Keggin units with bismuth linkers. There are four sites in the material. Surrounding site, central site, and linker site are in the framework, and cation site is in the void space surrounded by the framework (Figure 3. 1).

Here, the author describe the synthesis and structure characterization of other new members of all-inorganic ε-Keggin POM-based 3D frameworks, which were comprised of ε-Keggin polyoxomolybdates with metal ions (Zn, Mn, Fe, and Co), $Na_{1.5}H_{11.4}[\varepsilon\text{-}Zn^{II}Mo^{V}_{10.9}Mo^{VI}_{1.1}O_{40}\{Zn^{II}\}_2]$, $(NH_4)_{1.5}H_{8.5}[Zn^{II}Mo^{VI}_4Mo^{V}_8O_{40}\{Zn^{II}_2\}]$, $Na_2H_{10.8}[Mn^{II}_{0.6}Mo^{VI}_2Mo^{V}_{10}O_{40}\{Mn^{II}_2\}]$, $(NH_4)_{2.1}H_{7.5}[\varepsilon\text{-}Mn^{II}_{0.2}Mo^{V}_6Mo^{VI}_6O_{40}\{Mn^{II}\}_2]$, $(NH_4)_2H_{8.1}[\varepsilon\text{-}Fe_{0.6}Mo^{V}_9Mo^{VI}_3O_{40}\{Fe\}_2]$, and $(NH_4)_{1.7}H_{6.3}[\varepsilon\text{-}CoMo^{V}_8Mo^{VI}_4O_{40}\{Co\}_2]$, denoted as Na–Mo–Zn oxide, NH_4–Mo–Zn oxide, Na–Mo–Mn oxide, NH_4–Mo–Mn oxide, NH_4–Mo–Fe oxide, and NH_4–Mo–Co oxide, respectively. Structures of the materials were determined by powder X-ray diffraction, FT-IR, XPS, and elemental analysis. Structure analysis indicated that the materials were constructed with ε-Keggin polyoxomolybdates and metal ions (Zn, Mn, Fe, and Co). It was found that the existing guest molecules can be partly removed by heat treatment. The chemical composition of the material can be easily tuned by applying different starting materials. Our results showed that the structure of the ε-Keggin POM-based 3D frameworks could be easily modified, and these four sites could be occupied with different metal ions (or species).

3.2. Experimental

3.2.1. Materials and synthesis

All chemicals were reagent grade and used as supplied and house made distilled water was used throughout.

Synthesis of Na–Mo–Zn oxide. $Na_2MoO_4 \cdot 2H_2O$ (2.823 g, 11.7 mmol based on Mo) was dissolved in 40 mL of distilled water. Metal Mo (0.2 g, 2.1 mmol) and $ZnCl_2$ (0.453 g, 3.3 mmol) were added to the mixture sequentially, followed by adjusting pH to 4.8 with 1 M of H_2SO_4. The mixture was introduced into a 50-mL Teflon liner of a stainless-steel autoclave. The autoclave was placed in an oven heated at 448 K for 24 h. After the autoclave was cooled down to room temperature, the mixture was moved to 100 mL-beaker. For solid recovery, 60 mL of water was added to the beaker, and the beaker was placed at room temperature for 5 min and up-most 50% of the suspension was collected by filtration. The recovery process was repeated for 3 times. The resulting solid was washed with 10 mL of water for 3 times and dried at 353 K overnight. 0.28 g of Na–Mo–Zn oxide (Yield: 14% based on Mo) were obtained. Elemental Analysis: Calcd for Calcd for $Na_{1.5}Zn_3Mo_{12}O_{45}H_{21.4}$: Zn, 9.24; Mo, 54.22; Na, 1.62; H, 1.02, Found: Zn, 9.63; Mo, 54.14; Na, 1.54; H, 1.18.

Synthesis of NH_4–Mo–Zn oxide. $(NH_4)_6Mo_7O_{24} \cdot 4H_2O$ (2.060 g, 11.7 mmol based on Mo) was dissolved in 40 mL of distilled water. Metal Mo (0.2 g, 2.1 mmol) and $ZnCl_2$ (0.453 g, 3.3 mmol) were added to the mixture sequentially, followed by adjusting pH to 4.8 with 1 M of H_2SO_4. The mixture was introduced into a 50-mL Teflon liner of a stainless-steel autoclave. The autoclave was placed in an oven heated at 448 K for 24 h with rotation. After the autoclave was cooled down to room temperature, the mixture was moved to 100 mL-beaker. For solid recovery, 60 mL of water was added to the beaker, and the beaker was placed at room temperature for 5 min and up-most 50% of the suspension was collected by filtration. The recovery process was repeated for 3 times. The resulting solid was washed with 10 mL of water for 3 times and dried at 353 K overnight. 1.09 g of NH_4–Mo–Zn oxide (Yield: 53% based on Mo) were obtained. Elemental Analysis: Calcd for $N_{1.5}Zn_3Mo_{12}O_{46}H_{26.5}$: Zn, 9.21; Mo, 54.03; N, 0.99; H, 1.24, Found: Zn, 9.25; Mo, 53.95; N, 1.02; H, 1.22.

Synthesis of Na–Mo–Mn oxide. $Na_2MoO_4 \cdot 2H_2O$ (2.823 g, 11.7 mmol based on Mo) was dissolved in 40 mL of distilled water. Metal Mo (0.2 g, 2.1 mmol) and MnO (0.235 g, 3.3 mmol) were added to the mixture sequentially (pH value was 4.8.). The mixture was introduced into a 50-mL Teflon liner of a stainless-steel autoclave. The autoclave was placed in an oven heated at 448 K for 24 h. After the autoclave was cooled down to room temperature, the mixture was moved to 100 mL-beaker. For solid recovery, 60 mL of water was added to the beaker, and the beaker was placed at room temperature for 5 min and up-most 50% of the suspension was collected by filtration. The recovery process was repeated for 3 times. The resulting solid was washed with 10 mL of water for 3 times and dried at 353 K overnight. 0.94 of Na–Mo–Mn oxide (Yield: 46% based on Mo) were obtained. Elemental Analysis: Calcd for $Na_2Mn_{2.6}Mo_{12}O_{47}H_{24.8}$: Mn, 6.75; Mo, 54.39; Na, 2.17; H, 1.17, Found: Mn, 6.65; Mo, 54.84; Na, 2.29; H, 1.08.

Synthesis of NH_4–Mo–Mn oxide. $(NH_4)_6Mo_7O_{24} \cdot 4H_2O$ (2.060 g, 11.7 mmol based on Mo) was dissolved in 40 mL of distilled water. Metal Mo (0.2 g, 2.1 mmol) and MnO (0.235 g, 3.3 mmol) were added to the mixture sequentially (pH value was 4.8.). The mixture was introduced into a 50-mL Teflon liner of a stainless-steel autoclave. The autoclave was placed in an oven heated at 448 K for 24 h. After the autoclave was cooled down to room temperature, the mixture was moved to 100 mL-beaker. For solid recovery, 60 mL of water was added to the beaker, and the beaker was placed at room temperature for 5 min and up-most 50% of the suspension was collected by filtration. The recovery process was repeated for 3 times. The resulting solid was washed with 10 mL of water for 3 times and dried at 353 K overnight. 0.32 g of NH_4–Mo–Mn oxide (Yield: 16% based on Mo) were obtained. Elemental Analysis: Calcd for $N_{1.7}Mn_{2.2}Mo_{12}O_{46}H_{26.3}$: Mn, 5.88; Mo, 56.02; N, 1.16; H, 1.28, Found: Mn, 5.91; Mo, 56.45; N, 1.62; H, 1.23.

Synthesis of NH_4–Mo–Fe oxide. $(NH_4)_6Mo_7O_{24} \cdot 4H_2O$ (2.060 g, 11.7 mmol based on Mo) was dissolved in 40 mL of distilled water. Metal Mo (0.2 g, 2.1 mmol) and

Fe_3O_4 (0.258 g, 1.1 mmol) were added to the mixture sequentially (pH of 5.1). The mixture was introduced into a 50-mL Teflon liner of a stainless-steel autoclave. The autoclave was placed in an oven heated at 448 K for 48 h with rotation (~1 rpm). After the autoclave had been cooled down to room temperature, the mixture was placed in a 100-mL beaker. For solid recovery, 60 mL of water was added to the beaker, and the beaker was kept at room temperature for 5 min. Then the upper 50% part of the suspension was collected by filtration. The recovery process was repeated 3 times. The resulting solid was washed with 10 mL of water 3 times and dried at 353 K overnight. Then 0.87 g of NH_4–Mo–Fe oxide (yield: 44% based on Mo) was obtained. Elemental Analysis: Calcd for $N_2Fe_{2.6}Mo_{12}O_{43}H_{22.1}$: Fe, 7.11; Mo, 56.36; N, 1.37; H, 1.08, Found: Fe, 7.14; Mo, 56.46; N, 1.29; H, 1.00.

Synthesis of NH_4–Mo–Co oxide. $(NH_4)_6Mo_7O_{24}$ $4H_2O$ (2.060 g, 11.7 mmol based on Mo) was dissolved in 40 mL of distilled water. Metal Mo (0.2 g, 2.1 mmol) and Co_3O_4 (0.258 g, 3.3 mmol) were added to the mixture sequentially (pH value was 4.8.). The mixture was introduced into a 50-mL Teflon liner of a stainless-steel autoclave. The autoclave was placed in an oven heated at 448 K for 48 h with rotation. After the autoclave was cooled down to room temperature, the mixture was moved to 100 mL-beaker. For solid recovery, 60 mL of water was added to the beaker, and the beaker was placed at room temperature for 5 min and up-most 50% of the suspension was collected by filtration. The recovery process was repeated for 3 times. The resulting solid was washed with 10 mL of water for 3 times and dried at 353 K overnight. 0.32 g of NH_4-Mo–Co oxide (Yield: 16% based on Mo) were obtained. Elemental Analysis: Calcd for $N_{1.7}Co_3Mo_{12}O_{41}H_{17.1}$: Co, 8.65; Mo, 56.32; N, 1.16; H, 0.84, Found: Co, 8.79; Mo, 56.96; N, 1.31; H, 1.20.

3.2.2. Characterization

Nitrogen adsorption isotherm was obtained by a BELSORP MAX (BEL Japan Inc.) sorption analyzer at 77 K. Surface area was calculated by the BET method using

adsorption branch. Outer surface area and pore volume were calculated by the t-plot method. The samples of Na–Mo–Zn oxide, NH_4–Mo–Zn oxide, Na–Mo–Mn oxide, NH_4–Mo–Mn oxide, NH_4–Mo–Fe oxide, and NH_4–Mo–Co oxide were evacuated at 473 K for 2.5 h before the measurement. Powder X-ray diffraction (XRD) pattern was obtained on RINT2200 (Rigaku) with Cu Kα radiation (tube voltage: 40 kV, tube current: 20 mA). Scanning electron microscopy (SEM) images were obtained with HD-2000 (HITACHI). Transmission electron microscopy (TEM) images were taken with a 200 kV TEM (JEOL JEM-2100F). Fourier transform infrared (FT-IR) was carried out on PARAGON 1000, Perkin Elmer. Raman spectra were recorded with Renishaw inVia Raman Microscope. Temperature-programmed desorption mass spectrometry (TPD-MS) measurements were carried out from 313 K to 893 K at a heating rate of 10 K min^{-1} under helium (flow rate: 50 mL min^{-1}). Samples were set up between two layers of quartz wool. A TPD apparatus (BEL Japan, Inc.) equipped with a quadrupole mass spectrometer (M-100QA; Anelva) was used to detect NH_3 (m/z = 16) and H_2O (m/z = 18). For TPD-MS measurements of the materials after heat treatment, the samples were heated at 473 K under high vacuum for 2.5 h in TPD instrument before the measurements. X-ray photoelectron spectroscopy (XPS) was performed on a JPS-9010MC (JEOL). The spectrometer energies were calibrated using the C 1s peak at 284.8 eV. Elemental compositions were determined by an inductive coupling plasma (ICP-AES) method (ICPE-9000, Shimadzu). CHN elemental composition was determined at Instrumental Analysis Division, Equipment Management Center, Creative Research Institution, Hokkaido University.

3.2.3. Structure determination and computer-based simulation

The structures of Na–Mo–Zn oxide, NH_4–Mo–Zn oxide, Na–Mo–Mn oxide, NH_4–Mo–Mn oxide, NH_4–Mo–Fe oxide, and NH_4–Mo–Co oxide were determined by powder X-ray diffraction. Powder XRD patterns were recorded on RINT2200 (Rigaku) with Cu Kα radiation (tube voltage: 40 kV, tube current: 40 mA, scan speed: 1

degree/min, step: 0.01 degree). First, the powder XRD pattern was indexed by programs, such as DICVOL06 [1] and X-cell, [2] which gave the same result. After performing Pawley refinement, the most reasonable space group was obtained. Then, Le Bail method [3] was applied for intensity extraction with EdPCR program. The initial structure was solved by a charge flipping algorithm. [4] The positions and types of heavy metal atoms (Mo, Zn, Mn, Fe, and Co) were obtained by analyzing the generated electron density maps. Most of the oxygen atoms and cations were assigned according to the residual peaks, which were indicated by the charge flipping algorithm.

The initial structures of Na–Mo–Zn oxide, NH_4–Mo–Zn oxide, Na–Mo–Mn oxide, NH_4–Mo–Mn oxide, NH_4–Mo–Fe oxide, and NH_4–Mo–Co oxide were refined by powder XRD Rietveld refinement. [5] The lattice parameters and pattern parameters of the material were refined by Pawley refinement first. Then, isotropical temperature factors were given for every atom in the initial structure. Rietveld analysis was started with the initial model of the material and lattice parameters and pattern parameters from Pawley refinement. Every atom position was refined. Occupancy of atoms in framework was fixed without further refinement and occupancies of atoms in micropores were refined with consideration of elemental analysis results. Finally, the pattern parameters were refined again for obtaining the lowest R_{wp} value.

Material modeling, X-cell program, Pawley refinement, and Rietveld refinement were performed with Materials Studio v6.1.0 package (Accelrys Software Inc.). DICVOL06 and EdPCR were carried out with Fullprof package. The charge flipping algorithm was performed with superflip in Jana2006 and electron density maps were generated with Chimera 1.8.1.

Connolly surfaces and free space of POM-based materials were simulated by "Atom Volume & Surfaces" program in Materials Studio. The diameters of the cage and the channel were estimated from the Connolly surfaces of the cage and the channel with Connolly radius of 1 Å, [6] and the shortest values were presented.

3.3. Results and discussion

3.3.1. Material preparation

Novel POM-based crystalline metal oxides, Na–Mo–Zn oxide, NH_4–Mo–Zn oxide, Na–Mo–Mn oxide, NH_4–Mo–Mn oxide, NH_4–Mo–Fe oxide, and NH_4–Mo–Co oxide, were synthesized under hydrothermal conditions. To obtain these materials, three main starting materials were needed: molybdenum source, reducing agent, and linker metal ions. Ammonium heptamolybdate or sodium molybdate was used as a molybdenum source. $VOSO_4$ (in the case of Mo–V–Bi oxide) or metal molybdenum was used as a reducing agent. Linker metal source could be metal oxides or metal salts. After hydrothermal reaction at 448 K for 24~48 hours, the POM-based crystalline metal oxides were obtained. The crude solids after hydrothermal reaction were not pure, and thus purification processes were necessary to get pure materials. The settlement method was applied to isolate the impurities from the materials. After purification, pure materials were obtained.

3.3.2. Structure characterizations of Na–Mo–Zn oxide, NH_4–Mo–Zn oxide, Na–Mo–Mn oxide, NH_4–Mo–Mn oxide, NH_4–Mo–Fe oxide, and NH_4–Mo–Co oxide

Powder XRD profiles of Na–Mo–Zn oxide, NH_4–Mo–Zn oxide, Na–Mo–Mn oxide, NH_4–Mo–Mn oxide, NH_4–Mo–Fe oxide, and NH_4–Mo–Co oxide were similar to that of Mo–V–Bi oxide with slight shift of 2 theta and different intensity ratio (Figure 3. 2), and XRD pattern indexing and Pawley refinement showed that these three materials were cubic system with the same space group of *Fd*-3*m* and similar lattice parameters (Table 3. 1). FT-IR spectra of the POM-based materials were quite similar (Figure 3. 3). Na–Mo–Zn oxide, NH_4–Mo–Zn oxide, Na–Mo–Mn oxide, NH_4–Mo–Mn oxide, NH_4–Mo–Fe oxide, and NH_4–Mo–Co oxide had octahedral morphologies which were similar to that of Mo–V–Bi oxide (Figure 3. 4). Therefore, the author consider the basic structures of all the materials were similar to that of Mo–V–Bi oxide. The structure of Mo–V–Bi oxide has been determined by single crystal analysis, [7] which showed that the

material was comprised of ε-Keggin POM units, ε-$VMo_{9.4}V_{3.6}O_{40}$, with Bi^{III} linker (Figure 3. 2). A V–O tetrahedron was surrounded by twelve M–O (M = Mo and V) octahedra to form the ε-Keggin-type POM which was linked by Bi^{III} to form a diamond-like framework. There were four sites for metal occupation in the materials. Surrounding site, central site, and linker site were in framework, and cation site in the materials was in the void space surrounded by framework.

The SEM images (Figure 3. 4) of the six materials of Na–Mo–Zn oxide, NH_4–Mo–Zn oxide, Na–Mo–Mn oxide, NH_4–Mo–Mn oxide, NH_4–Mo–Fe oxide, and NH_4–Mo–Co oxide showed that these materials were too small to perform single crystal analysis (100-200 nm in one diameter). Therefore, structure analysis based on powder X-ray diffraction was carried out.

For Na–Mo–Zn oxide, NH_4–Mo–Zn oxide, and NH_4–Mo–Co oxide, the result of the charge flipping algorithm revealed three most intensive peaks of electron density map with the intensity order of surrounding metal site > central metal site ~ linking metal site (Figure 3. 5 and Table 3. 2). Elemental analysis of the Mo–M (M = Zn or Co) oxide revealed that ratio of Mo: M (M = Zn or Co) was 12: 3. From these results, the author assigned that Zn or Co was present in central and linking metal sites and Mo was present in the surrounding metal site. In the case of Na–Mo–Mn oxide, NH_4–Mo–Mn oxide, and NH_4–Mo–Fe oxide the most intensive two peaks of electron density map corresponds to the surrounding metal site and linking metal site where intensity of the surrounding metal site was much higher than that of the linking metal site (Figure 3. 5d-f). A weak peak was found at the central metal site, which indicated that the position was occupied partly or with light atoms. Elemental analysis of Na–Mo–Mn oxide and NH_4–Mo–Mn oxide revealed that ratio of Mo: Mn was 12: 2.6 and 12: 2.2 and of NH_4–Mo–Fe oxide revealed that ratio of Mo: Fe was 12: 2.6. From these results, the author assigned that Mo was present in the surrounding metal site, Mn or Fe was present in the linking metal site. The central metal site of Na–Mo–Mn oxide and NH_4–Mo–Mn oxide was occupied by Mn with 0.6 and 0.2 of occupancy, respectively,

and the central metal site was occupied by Fe with 0.6 of occupancy for NH_4–Mo–Fe oxide. Other sites in the six materials were assigned to be oxygen atoms of the Keggin-unit, countercations, and oxygen atoms of water.

The initial structures of Na–Mo–Zn oxide, NH_4–Mo–Zn oxide, Na–Mo–Mn oxide, NH_4–Mo–Mn oxide, NH_4–Mo–Fe oxide, and NH_4–Mo–Co oxide were refined with Rietveld refinement. Figure 3. 6 shows the simulated powder XRD patterns of the six materials. The R_{wp} values of Rietveld refinement for the six materials were listed in Table 3. 1, which were quite low. The results of Rietveld analysis and elemental analysis demonstrated that the POM building blocks of Na–Mo–Zn oxide, NH_4–Mo–Zn oxide, Na–Mo–Mn oxide, NH_4–Mo–Mn oxide, NH_4–Mo–Fe oxide, and NH_4–Mo–Co oxide were ε-Keggin POMs, ε-$ZnMo_{12}O_{40}$, ε-$ZnMo_{12}O_{40}$, ε-$Mn_{0.6}Mo_{12}O_{40}$, ε-$Mn_{0.2}Mo_{12}O_{40}$, ε-$Fe_{0.6}Mo_{12}O_{40}$, and ε-$CoMo_{12}O_{40}$, respectively (Figure 3. 7a). Twelve MoO_6 octahedra surrounded a MO_4 (M = Zn, Mn, Fe, and Co) tetrahedron to form the ε-Keggin cores, which were connected by metal ions (M = Zn, Mn, Fe, and Co) in a tetrahedral fashion to form a 3D framework (Figure 3. 7b). In the case of other ε-Keggin POMs, there were four capping metal ions for one ε-Keggin POM. [8–11] In case of ε-Keggin POM-based complex metal oxides, capping metal ions connected the POM units.

FT-IR spectra (Figure 3. 3) of Na–Mo–Zn oxide, NH_4–Mo–Zn oxide, Na–Mo–Mn oxide, NH_4–Mo–Mn oxide, NH_4–Mo–Fe oxide, and NH_4–Mo–Co oxide were similar to those of other ε-Keggin polyoxomolybdates, [ε-$Mo_{12}O_{40}Ni_4(H_2O)$] [8] and [ε-$Mo_{12}O_{40}Co_4(H_2O)$]. [12] The [ε-$Mo_{12}O_{40}Ni_4(H_2O)$] and [ε-$Mo_{12}O_{40}Co_4(H_2O)$] were composed of ε-Keggin polyoxomolybdate, [ε-$H_2Mo^{VI}_xMo^{V}_{12-x}O_{40}$], and four Ni^{2+} or Co^{2+} on the hexagonal surfaces of ε-Keggin polyoxomolybdate. These results confirmed that surrounding metal sites in the ε-Keggin cores were mostly occupied by Mo in the materials.

High-resolution transmission electron microscopy (HRTEM) images were obtained to further confirm the structures of the six materials. Figure 3. 8 showed a comparison

of HRTEM images of the materials. HRTEM showed clear lattice images for the materials, illustrating that the materials were well-ordered sub-micrometer-sized single crystals. Layers could be observed in TEM images, which were corresponding to the (1 1 1) plane of the materials. The layer distances from TEM images were 11.3, 11.3, 11.4, 11.4, 11.1, and 11.2 Å for Na–Mo–Zn oxide, NH_4–Mo–Zn oxide, Na–Mo–Mn oxide, NH_4–Mo–Mn oxide, NH_4–Mo–Fe oxide, and NH_4–Mo–Co oxide, which were in good agreement with the results from crystal structures of the materials.

The oxidation states of the metal elements in the POM-based complex metal oxides were studied by X-ray photoelectron spectroscopy (XPS), the resulting profiles of which were presented in Figure 3. 9 and Figure 3. 10. The oxidation states of metal elements were calculated by curving fitting of XPS profiles, and the results were shown in Table 3. 3. In all materials, the surrounding 12 molybdenum were mostly reduced, which was similar to other ε-Keggin polyoxomolybdates. [8,10,13] The ratio of Mo^{V} : Mo^{VI} is from 1 to 0.1. For linker metals and central metals, zinc and manganese in Na–Mo–Zn oxide, NH_4–Mo–Zn oxide, Na–Mo–Mn oxide, and NH_4–Mo–Mn oxide were Zn^{II} and Mn^{II}. In the case of NH_4–Mo–Fe oxide and NH_4–Mo–Co oxide, the ratio of Fe^{II}/Fe^{III} and $Co^{II/}Co^{III}$ were 0.5. The detailed chemical formulas of these six POM units were estimated as $[\varepsilon\text{-}Zn^{II}Mo^{V}_{10.9}Mo^{VI}_{1.1}O_{40}\{Zn^{II}\}_2]^{12.9-}$, $[Zn^{II}Mo^{VI}_4Mo^{V}_8O_{40}\{Zn^{II}_2\}]^{10-}$, $[Mn^{II}_{0.6}Mo^{VI}_2Mo^{V}_{10}O_{40}\{Mn^{II}_2\}]^{12.8-}$, $[\varepsilon\text{-}Mn^{II}_{0.2}Mo^{V}_6Mo^{VI}_6O_{40}\{Mn^{II}\}_2]^{9.6-}$, $[\varepsilon\text{-}Fe_{0.6}Mo^{V}_9Mo^{VI}_3O_{40}\{Fe\}_2]^{10.1-}$, and $[\varepsilon\text{-}Co^{II}_3Mo^{V}_8Mo^{VI}_4O_{40}]^{10-}$.

The presence of water and ammonium cation in the POM-based materials was confirmed by FT-IR analysis. FT-IR spectra (Figure 3. 3) of NH_4–Mo–Zn oxide, NH_4–Mo–Mn oxide, NH_4–Mo–Fe oxide, and NH_4–Mo–Co oxide showed the peak maximums at 1628 cm^{-1} and 1401 cm^{-1}, which corresponded to water and NH_4^+, respectively. In the case of sodium type materials, Na–Mo–Zn oxide and Na–Mo–Mn oxide, peak at 1630 cm^{-1} that corresponded to water was observed. The cationic species of Na–Mo–Zn oxide and Na–Mo–Mn oxide was Na^+, which resulted from the starting

agent of $Na_2MoO_4{\cdot}2H_2O$. The amount of cationic species (NH_4^+ and Na^+) and water were estimated by elemental analysis. Therefore, the detailed formulas of Na–Mo–Zn oxide, NH_4–Mo–Zn oxide, Na–Mo–Mn oxide, NH_4–Mo–Mn oxide, NH_4–Mo–Fe oxide, and NH_4–Mo–Co oxide were $Na_{1.5}H_{11.4}[\varepsilon\text{-}Zn^{II}Mo^{V}_{10.9}Mo^{VI}_{1.1}O_{40}\{Zn^{II}\}_2]\ 5H_2O$, $(NH_4)_{1.5}H_{8.5}[Zn^{II}Mo^{VI}_4Mo^{V}_8O_{40}\{Zn^{II}_2\}]\ 6H_2O$ $Na_2H_{10.8}[Mn^{II}_{0.6}Mo^{VI}_2Mo^{V}_{10}O_{40}\{Mn^{II}_2\}]\ 7H_2O$, $(NH_4)_{2.1}H_{7.5}[\varepsilon\text{-}Mn^{II}_{0.2}Mo^{V}_6Mo^{VI}_6O_{40}\{Mn^{II}\}_2]\ 4H_2O$, $(NH_4)_2H_{8.1}[\varepsilon\text{-}Fe_{0.6}Mo^{V}_9Mo^{VI}_3O_{40}\{Fe\}_2]\ 3H_2O$, and $(NH_4)_{1.7}H_{8.3}[\varepsilon\text{-}Co^{II}_3Mo^{V}_8Mo^{VI}_4O_{40}]\ H_2O$.

Cages and channels existed in the materials. One cage was surrounded by ten ε-Keggin POM units with metal ion linkers (Bi, Zn, Mn, Fe, and Co ions). The cages were connected with channels in a tetrahedral fashion to form a periodical 3 D pore system as FAU-type zeolites (Faujasite) do. The sizes of the cages were estimated from the Connolly surfaces (see details in experimental part) to be around 7.7 Å, and the sizes of the channels were estimated to be around 3 Å. The pore systems of these materials were unique. In one direction, the tunnel of the pore was not straight but in a zig-zag fashion (Figure 3. 7). The present NH_4^+ (or Na^+) and water occupied the cages and channels in the as-synthesized materials.

3.3.3. Heat treatment

Temperature programmed desorption-mass spectroscopy (TPD-MS) analysis showed that the water and NH_4^+ in the materials desorbed under heat treatment (Figure 3. 11). *m*/*z* = 16 and *m*/*z* = 18 were attributed to the signals of NH_3 and water. In chapter 2, TPD-MS (*m*/*z* = 16) showed that Mo–V–Bi oxide had two NH_4^+ desorption processes, when the temperature was increased to 873 K. One NH_4^+ had weak interaction with framework, which desorbed at 433 K and the other had strong interaction with framework and desorbed at 633 K. [7] NH_4–Mo–Zn oxide, NH_4–Mo–Mn oxide, NH_4–Mo–Fe oxide, and NH_4–Mo–Co oxide only showed a peak maximum at 600~650

K in TPD profiles (m/z = 16), which indicated only one kind of NH_4^+ in the frameworks of the materials. Na–Mo–Zn oxide and Na–Mo–Zn oxide did not have any NH_4^+ in structure, so no signal of m/z = 16 was found in TPD profiles. For water desorption, TPD profiles of these six materials showed two main water desorption processes. The one desorbed at 350~500 K was attributed to weakly bound water, and the other desorbed at 500~700 K was attributed to strongly bound water.

The guest molecules, ammonia and water, in the as-synthesized POM-based materials could be removed by sufficient heat treatment conditions without structure decomposition. Mo–V–Bi oxide was calcined at 623 K for 2 h under nitrogen atmosphere followed by treated at 573 K for 2.5 h under high vacuum (see chapter 2 in detail). Na–Mo–Zn oxide, NH_4–Mo–Zn oxide, Na–Mo–Mn oxide, NH_4–Mo–Mn oxide, NH_4–Mo–Fe oxide, and NH_4–Mo–Co oxide were treated at 473 K for 2.5 h under high vacuum. Most of the guest molecules occupying the cages and the channels were removed by heat treatment without collapse of the structures (Figure 3. 12).

Nitrogen adsorption-desorption measurement of calcined Mo–V–Bi oxide at 623 K showed a characteristic type I isotherm, which demonstrates that the material was a microporous material. Na–Mo–Zn oxide, NH_4–Mo–Zn oxide, Na–Mo–Mn oxide, NH_4–Mo–Mn oxide, NH_4–Mo–Fe oxide, and NH_4–Mo–Co oxide were heated at 473 K for 2.5 h under high vacuum, which mostly removed the NH_3 and water, before adsorption measurement. The result showed the micropores of the materials were also opened, although the adsorbed volume of N_2 on the materials was lower than that on Mo–V–Bi oxide (Figure 3. 13). Surface areas were calculated using the BET method to be 37 m^2/g, 45 m^2/g, 22 m^2/g, 27 m^2/g, 20 m^2/g, and 32 m^2/g for the six materials (Table 3. 4). The highest BET surface area mainly resulted from the highly opened micropores of Mo–V–Bi oxide. The less opened micropores of Na–Mo–Zn oxide, NH_4–Mo–Zn oxide, Na–Mo–Mn oxide, NH_4–Mo–Mn oxide, NH_4–Mo–Fe oxide, and NH_4–Mo–Co oxide might be caused by the remaining NH_4^+ and Na^+, which would block micropores and decrease the pore volume of the materials. After nitrogen gas adsorption

experiments, the recovered samples were tested with powder XRD, which showed the same profile to that of the sample before measurement, indicating that the structures were stable during the experiments.

3.4. Conclusion

Six new ε-Keggin polyoxomolybdate-based 3D framework materials, cubic Na–Mo–Zn oxide, NH_4–Mo–Zn oxide, Na–Mo–Mn oxide, NH_4–Mo–Mn oxide, NH_4–Mo–Fe oxide, and NH_4–Mo–Co oxide, have been successfully synthesized and characterized. In these metal oxides, ε-Keggin polyoxomolybdate with twelve molybdenum atoms were linked by metal ions to form 3D diamond-like frameworks. These oxides were thermally less stable than previously reported Mo–V–Bi oxide. Our results, indicating that variety of transition metals can be incorporated in the ε-Keggin polyoxomolybdate-based materials, open a door for development of ε-Keggin polyoxomolybdate-based 3D framework materials as functional materials such as ion-exchange materials, catalyst materials, adsorption materials, and magnetic materials.

References

(1) Boultif, A.; Louer, D. *J. Appl. Crystallogr.* **2004**, *37*, 724–731.

(2) Neumann, M. A. *J. Appl. Crystallogr.* **2003**, *36*, 356–365.

(3) Le Bail, A. *Powder Diffr.* **2008**, *23*, S5–S12.

(4) Palatinus, L.; Chapuis, G. *J. Appl. Crystallogr.* **2007**, *40*, 786–790.

(5) Young, R. A. *The Rietveld Method*; Young, R. A., Ed.; Oxford University Press: Oxford, 1995.

(6) Deok-Soo Kim Joonghyun Ryu Rhohun Park *J. Comput. Sci. & Technol.* **2006**, *21*, 255–260.

(7) Zhang, Z.; Sadakane, M.; Murayama, T.; Izumi, S.; Yasuda, N.; Sakaguchi, N.; Ueda, W. *Inorg. Chem.* **2014**, *53*, 903–911.

(8) Muller, A.; Beugholt, C.; Kogerler, P.; Bogge, H.; Bud'ko, S.; Luban, M. *Inorg. Chem.* **2000**, *39*, 5176–5177.

(9) Sloboda-Rozner, D.; Neimann, K.; Neumann, R. *J. Mol. Catal. A: Chem.* **2007**, *262*, 109–113.

(10) Mialane, P.; Dolbecq, A.; Lisnard, L.; Mallard, A.; Marrot, J.; Secheresse, F. *Angew. Chem. Int. Ed.* **2002**, *41*, 2398–2401.

(11) Tucher, J.; Nye, L. C.; Ivanovic-Burmazovic, I.; Notarnicola, A.; Streb, C. *Chem. Eur. J.* **2012**, *18*, 10949–10953.

(12) Ellern, A.; Kögerler, P. *Acta Crystallogr. C.* **2012**, *68*, i17–i19.

(13) Rodriguez-Albelo, L. M.; Rabdel Ruiz-Salvador, A.; Sampieri, A.; Lewis, D. W.; Gomez, A.; Nohra, B.; Mialane, P.; Marrot, J.; Secheresse, F.; Mellot-Draznieks, C.; Biboum, R. N.; Keita, B.; Nadjo, L.; Dolbecq, A. *J. Am. Chem. Soc.* **2009**, *131*, 16078–16087.

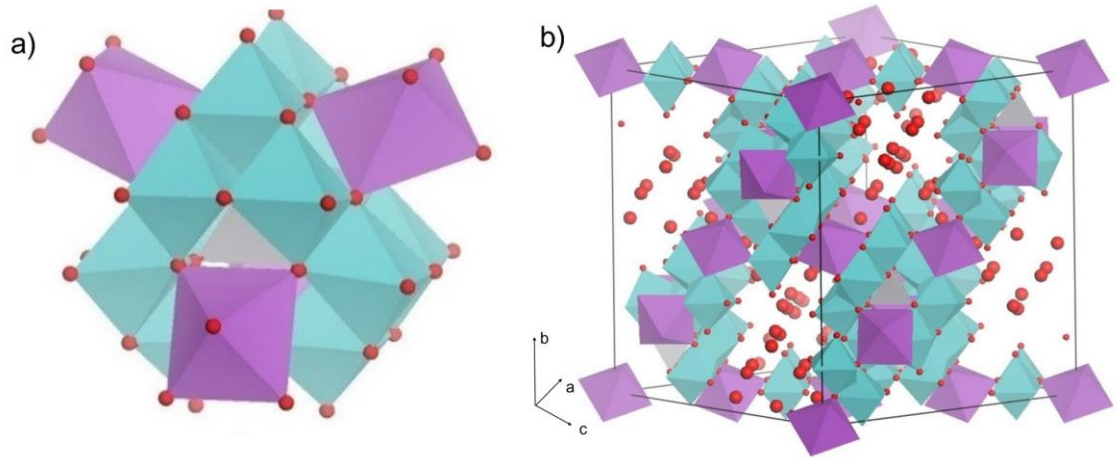

Figure 3. 1. Polyhedral representations of a) ε-Keggin POM unit and b) unit cell of the material, central site (gray tetrahedron), surrounding site (blue octahedron), linker site (purple octahedron), cation site (big red sphere in b)).

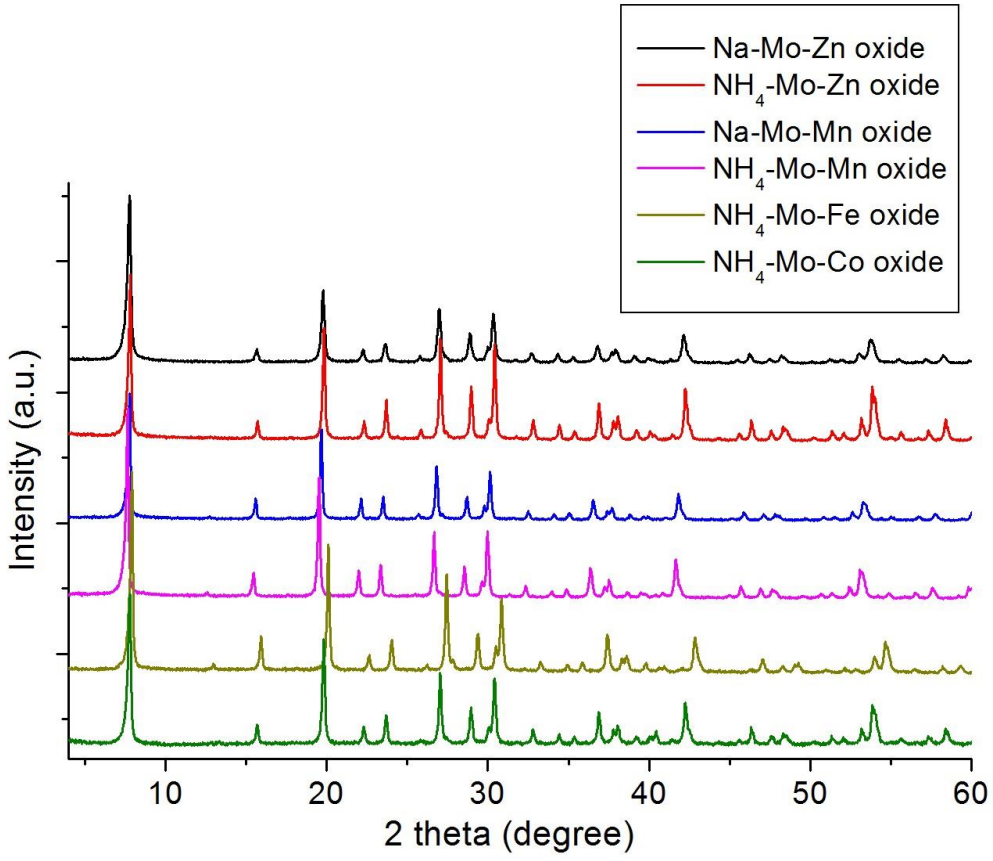

Figure 3. 2. Powder XRD patterns of Na–Mo–Zn oxide, NH_4–Mo–Zn oxide, Na–Mo–Mn oxide, NH_4–Mo–Mn oxide, NH_4–Mo–Fe oxide, and NH_4–Mo–Co oxide.

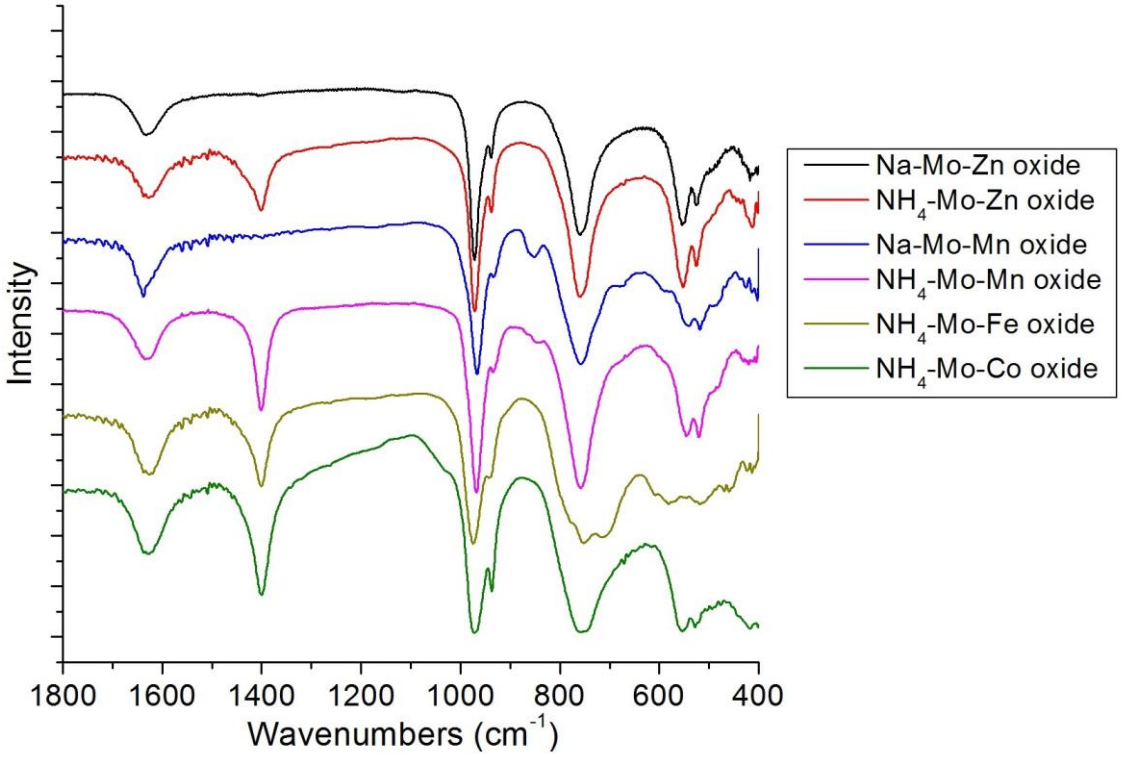

Figure 3. 3. FT-IR spectra of Na–Mo–Zn oxide, NH_4–Mo–Zn oxide, Na–Mo–Mn oxide, NH_4–Mo–Mn oxide, NH_4–Mo–Fe oxide, and NH_4–Mo–Co oxide.

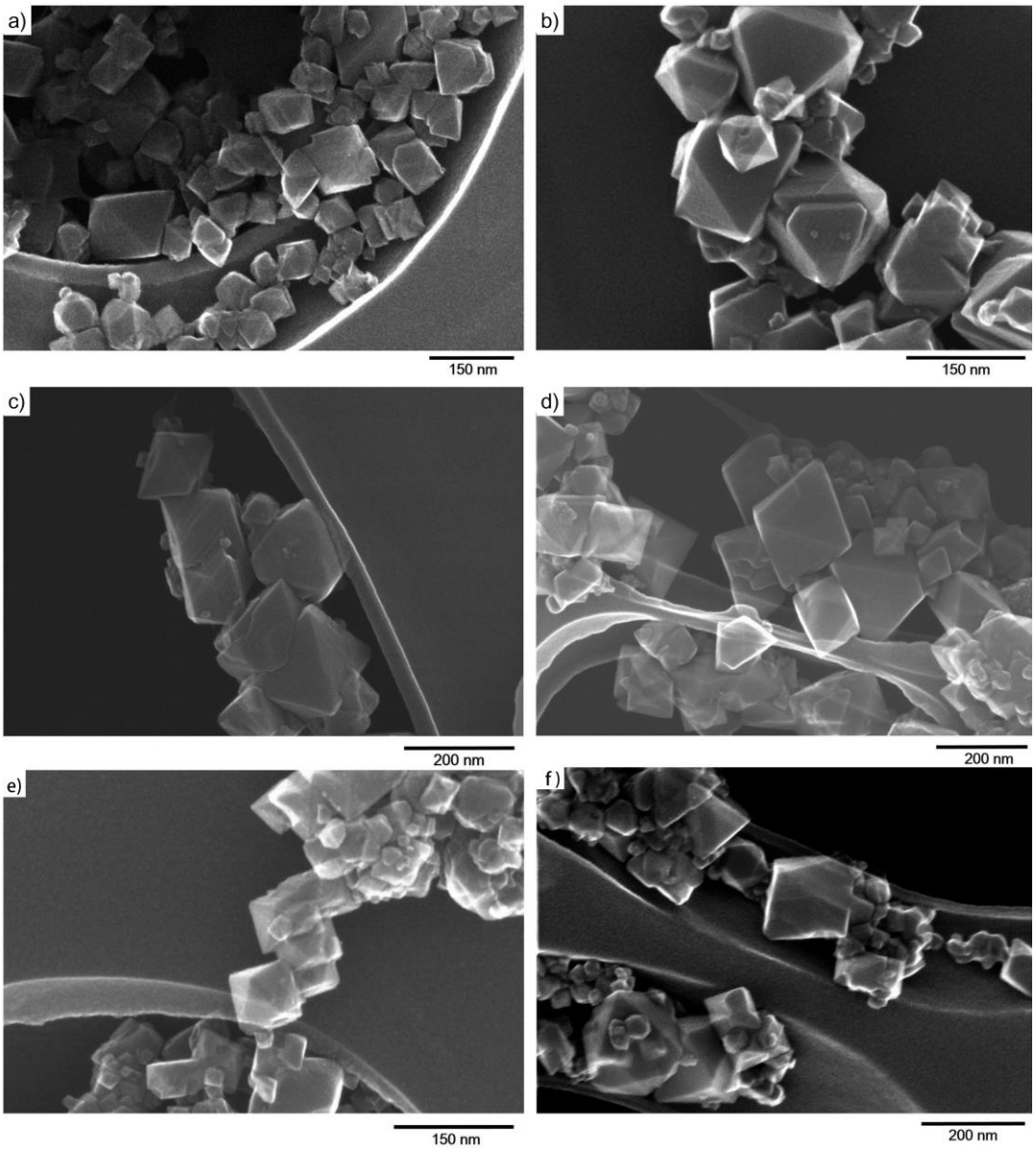

Figure 3. 4. SEM images of a) Na–Mo–Zn oxide, b) NH_4–Mo–Zn oxide, c) Na–Mo–Mn oxide, d) NH_4–Mo–Mn oxide, e) NH_4–Mo–Fe oxide, and f) NH_4–Mo–Co oxide.

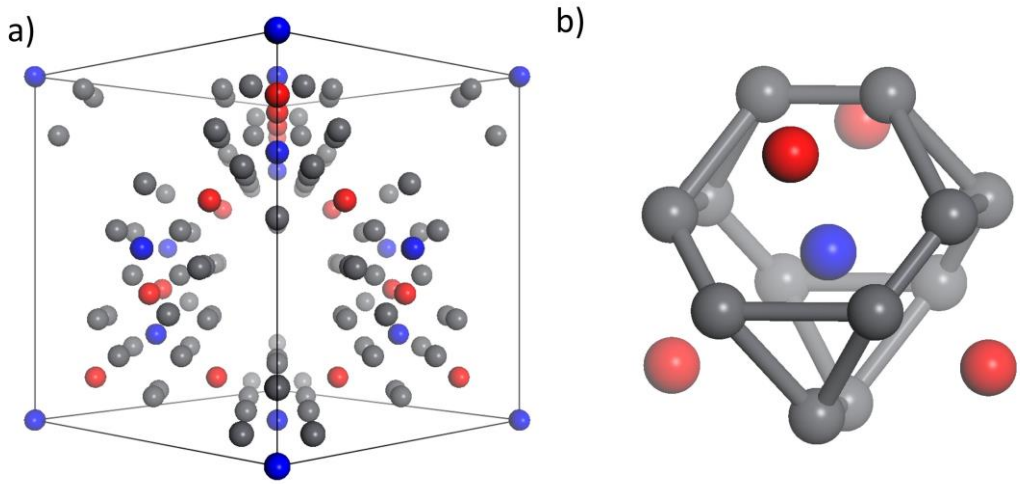

Figure 3. 5. Schematic representations of the charge flipping algorithm results, a) electron density map from the charge flipping method showing the positions of the intensive peaks: surrounding metal sites (grey sphere), linking metal sites (red sphere), central metal sites (blue sphere) in an unit cell and b) an ε-Keggin unit with 4 linking metal sites.

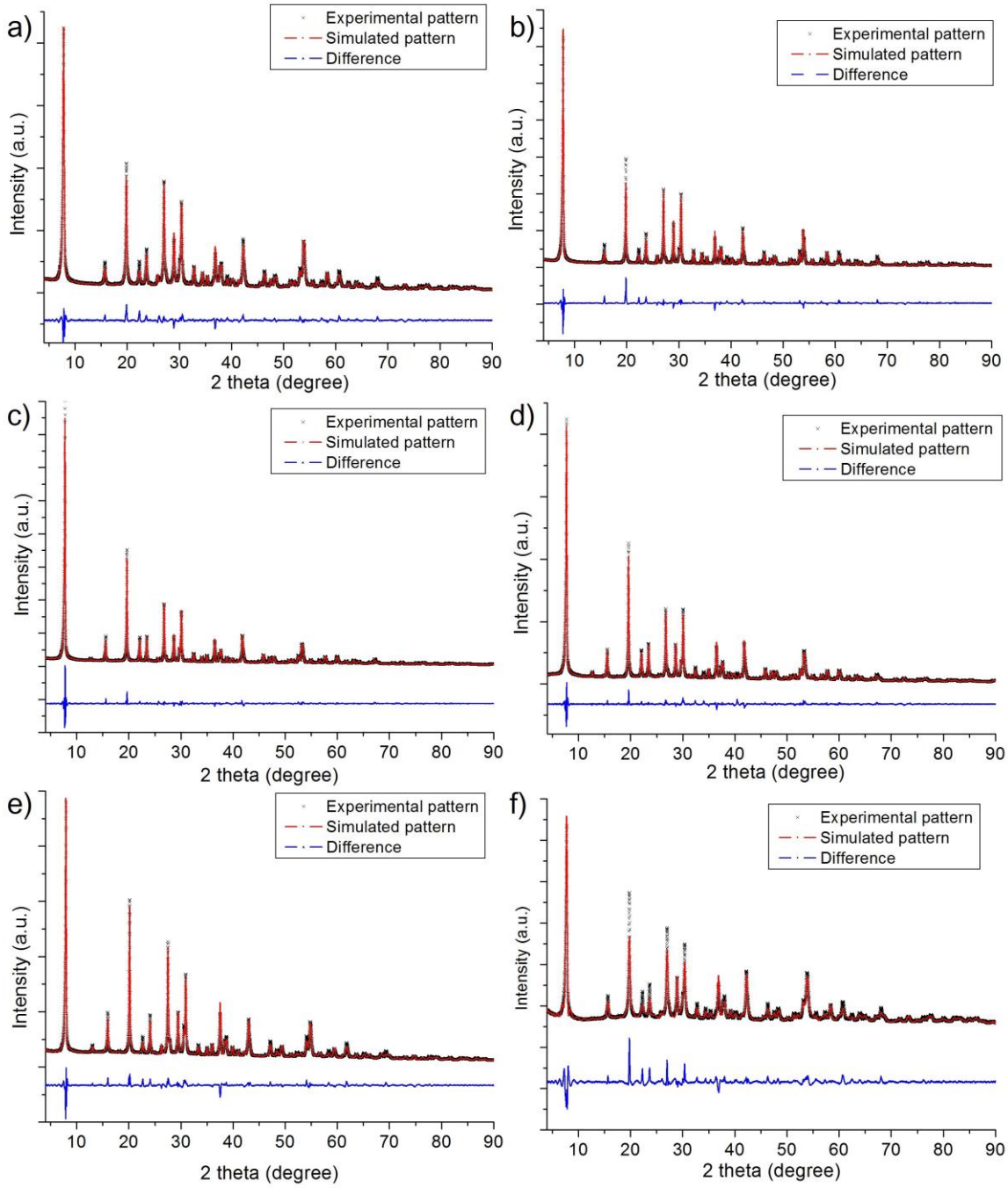

Figure 3. 6. Comparison of simulated powder XRD patterns from Rietveld analysis with experimental patterns: a) Na–Mo–Zn oxide, b) NH_4–Mo–Zn oxide, c) Na–Mo–Mn oxide, d) NH_4–Mo–Mn oxide, e) NH_4–Mo–Fe oxide, and f) NH_4–Mo–Co oxide.

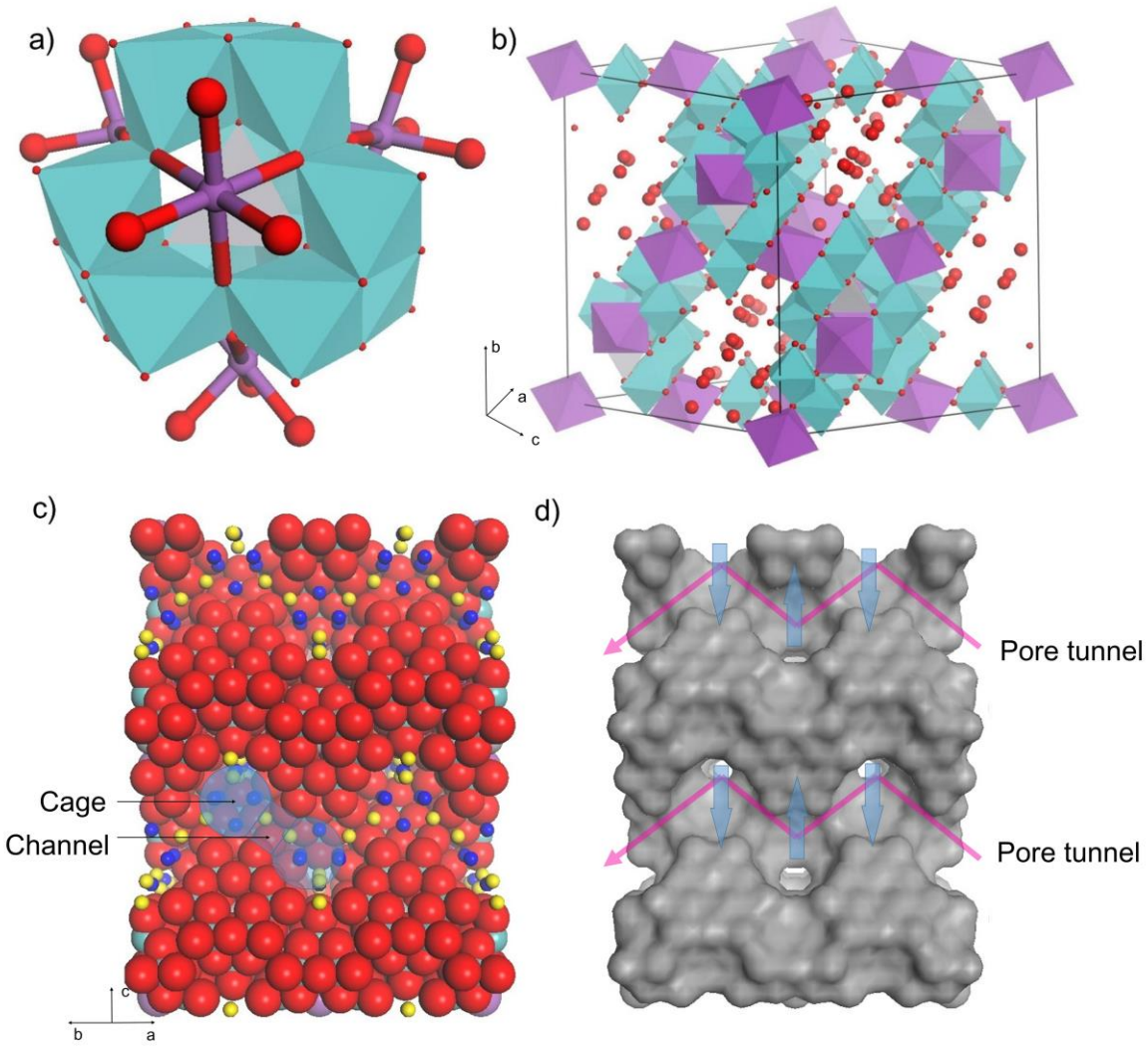

Figure 3. 7. Polyhedral representations of a) ε-Keggin POM with capping metal ions, b) an unit cell, surrounding MoO_6 (blue octahedron), central MO_4 (grey tetrahedron), metal ion linkers (purple octahedron), oxygen (red sphere), c) CPK (Corey, Pauling, and Koltun) representations of (110) plane, framework oxygen (red sphere), species in channel (yellow sphere), species in cages (deep blue sphere), and d) Connolly surface of the materials in (110) plane, pink arrow described the pore tunnel along the (110) plane, blue arrow described the pore tunnel perpendicular to the (110) plane.

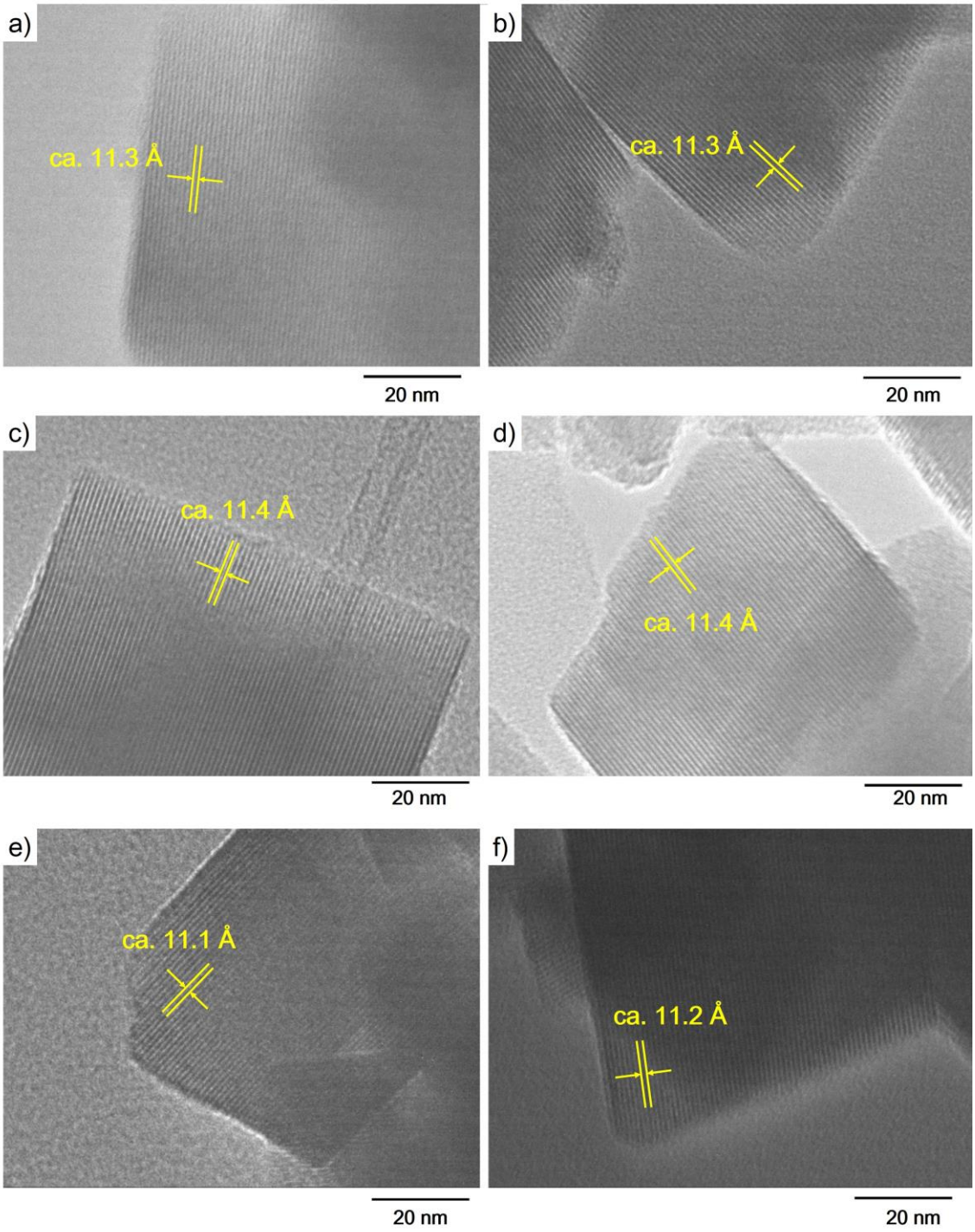

Figure 3. 8. HRTEM images of a) Na–Mo–Zn oxide, b) NH_4–Mo–Zn oxide, c) Na–Mo–Mn oxide, d) NH_4–Mo–Mn oxide, e) NH_4–Mo–Fe oxide, and f) NH_4–Mo–Co oxide.

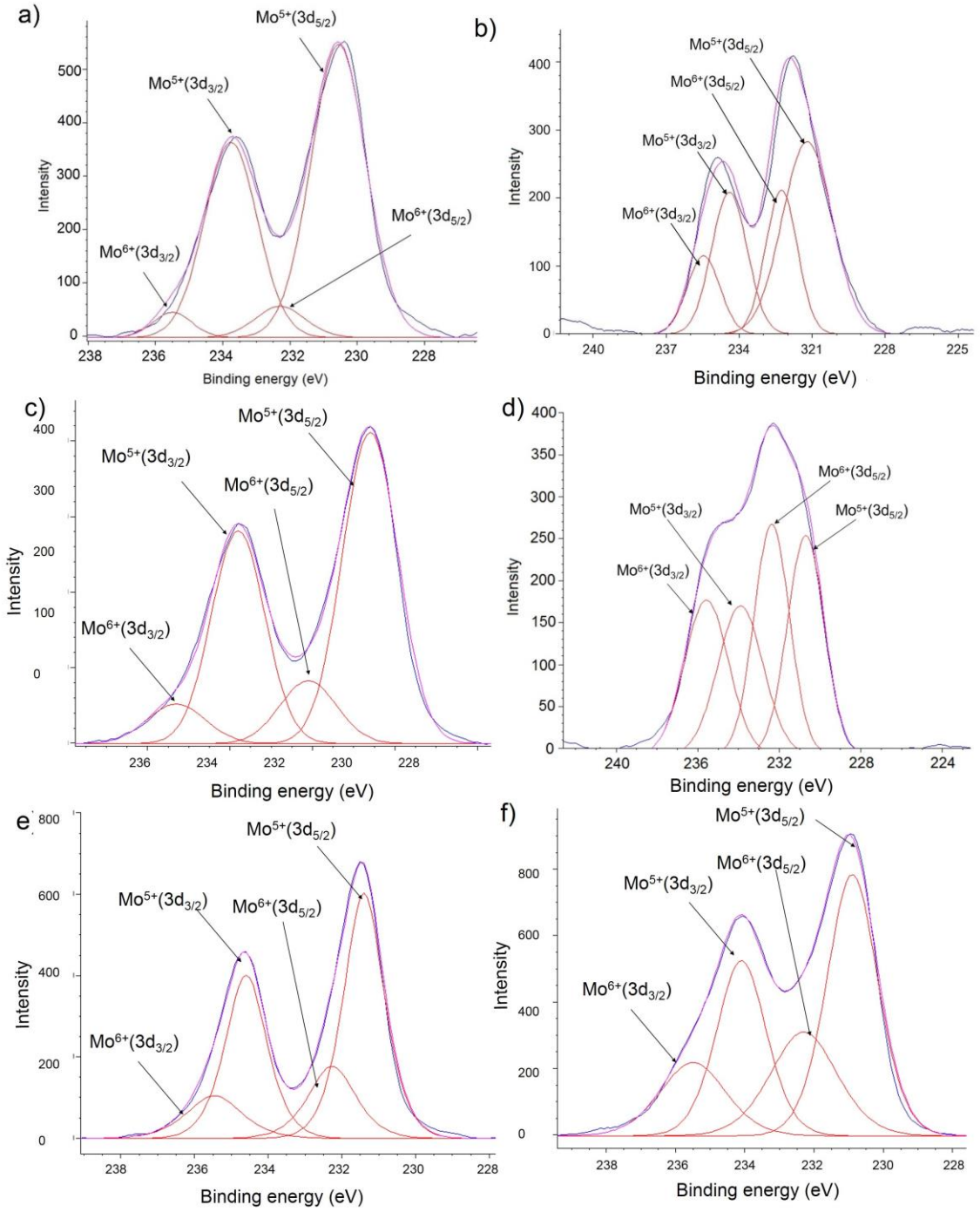

Figure 3. 9. XPS spectra of Mo of a) Na–Mo–Zn oxide, b) NH_4–Mo–Zn oxide, c) Na–Mo–Mn oxide, d) NH_4–Mo–Mn oxide, e) NH_4–Mo–Fe oxide, and f) NH_4–Mo–Co oxide.

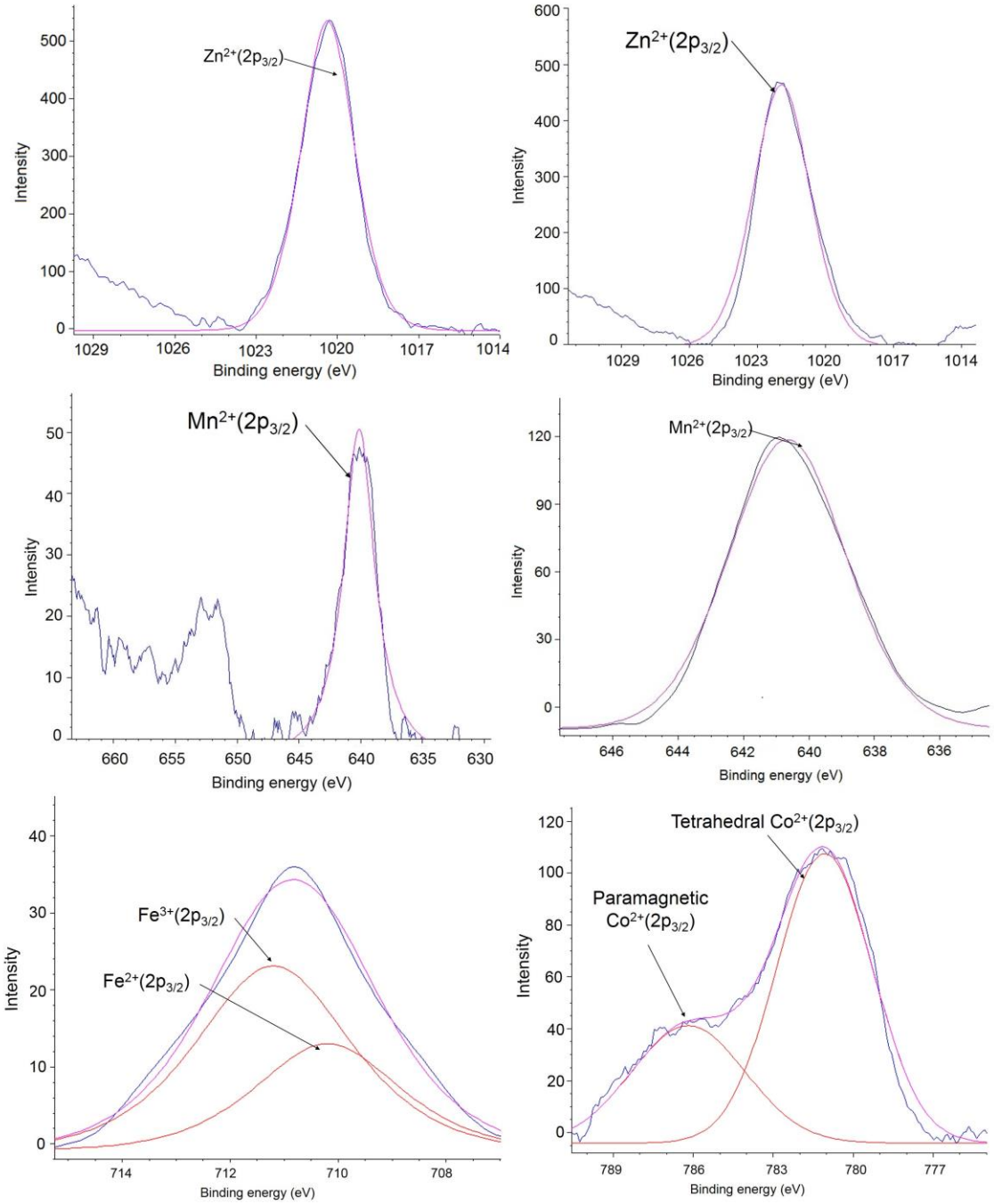

Figure 3. 10. XPS spectra of other metals in the materials of a) Na–Mo–Zn oxide, b) NH_4–Mo–Zn oxide, c) Na–Mo–Mn oxide, d) NH_4–Mo–Mn oxide, e) NH_4–Mo–Fe oxide, and f) NH_4–Mo–Co oxide.

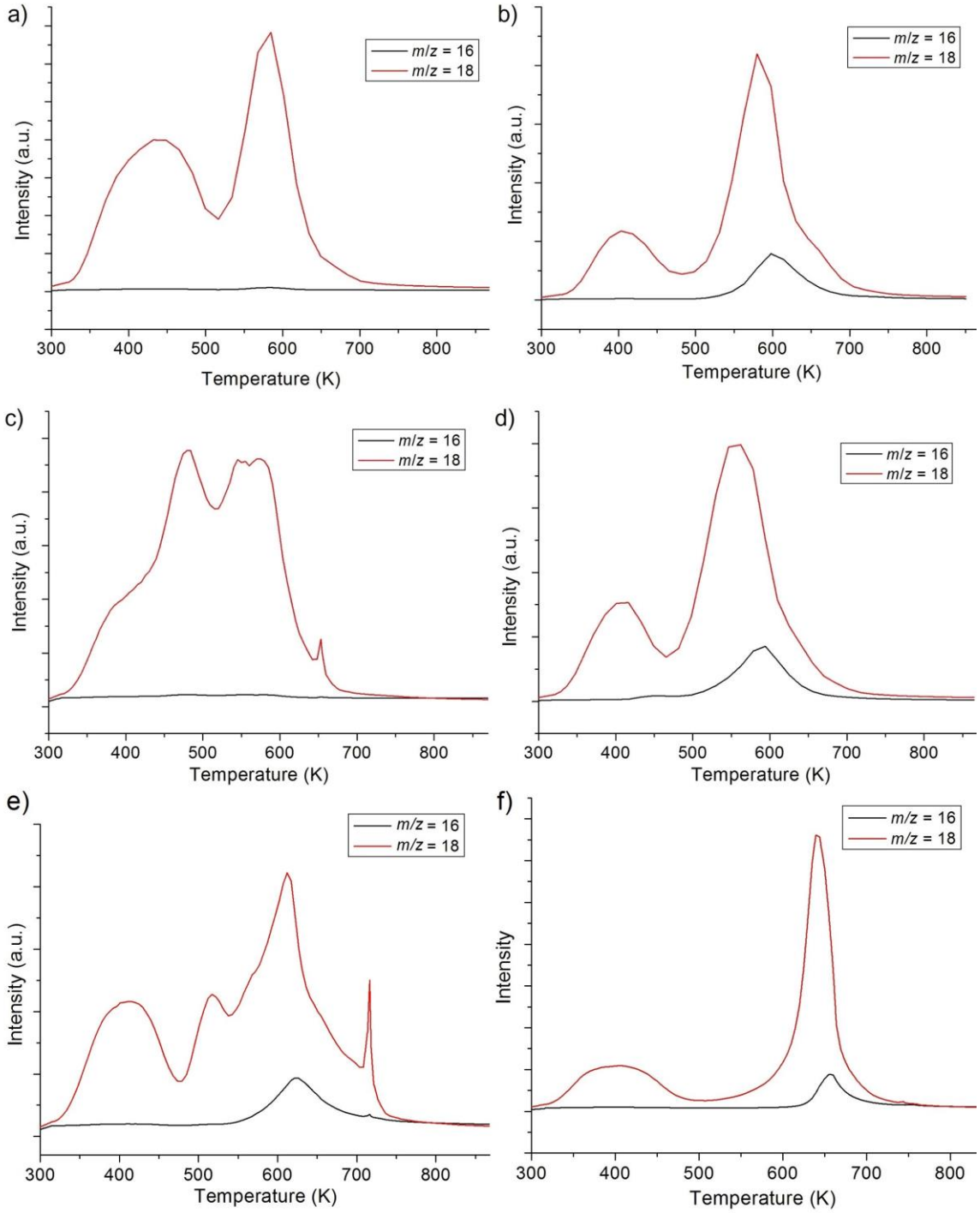

Figure 3. 11. TPD profiles of a) Na–Mo–Zn oxide, b) NH_4–Mo–Zn oxide, c) Na–Mo–Mn oxide, d) NH_4–Mo–Mn oxide, e) NH_4–Mo–Fe oxide, and f) NH_4–Mo–Co oxide

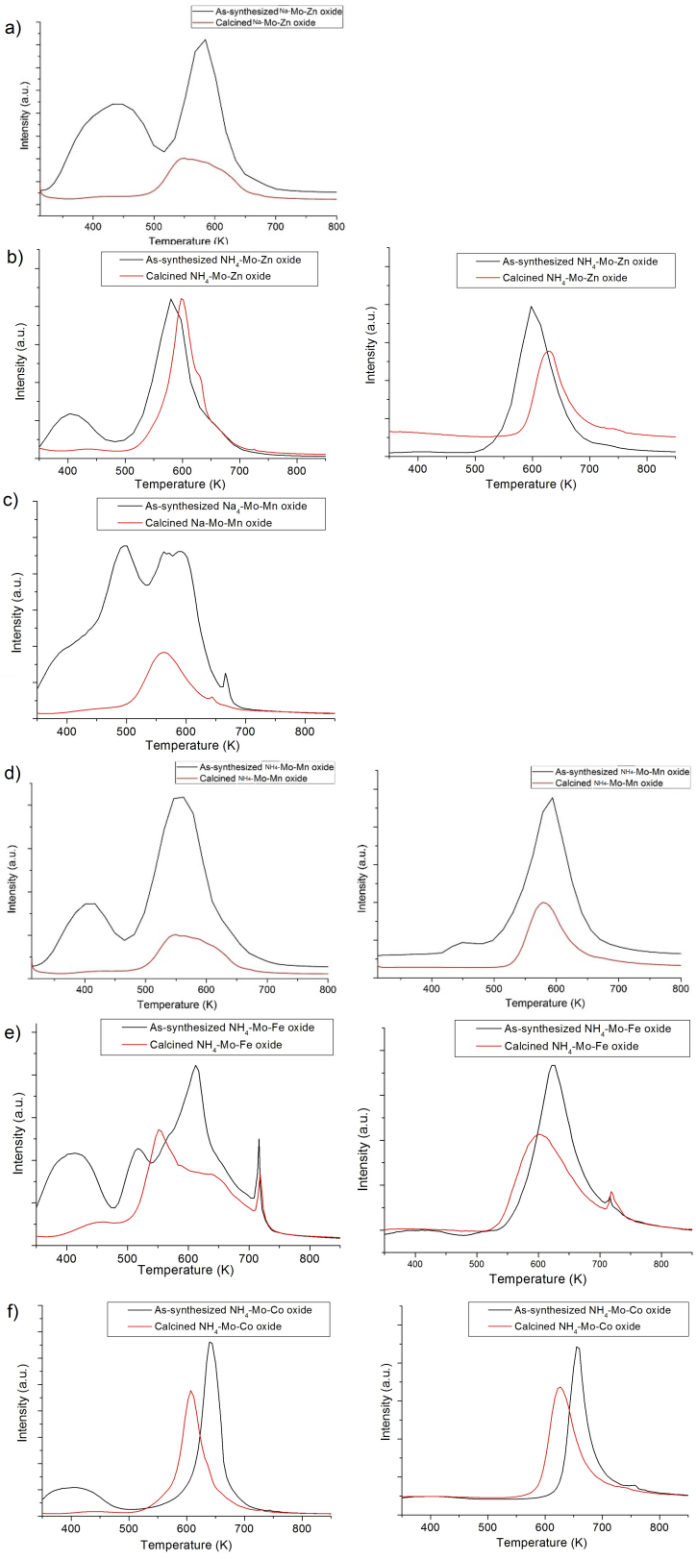

Figure 3. 12. Comparison of TPD profiles of the material before and after calcination: a) Na–Mo–Zn oxide, b) NH_4–Mo–Zn oxide, c) Na–Mo–Mn oxide, d) NH_4–Mo–Mn oxide, e) NH_4–Mo–Fe oxide, and f) NH_4–Mo–Co oxide, left m/z = 18 (water) and right m/z = 16 (NH_3).

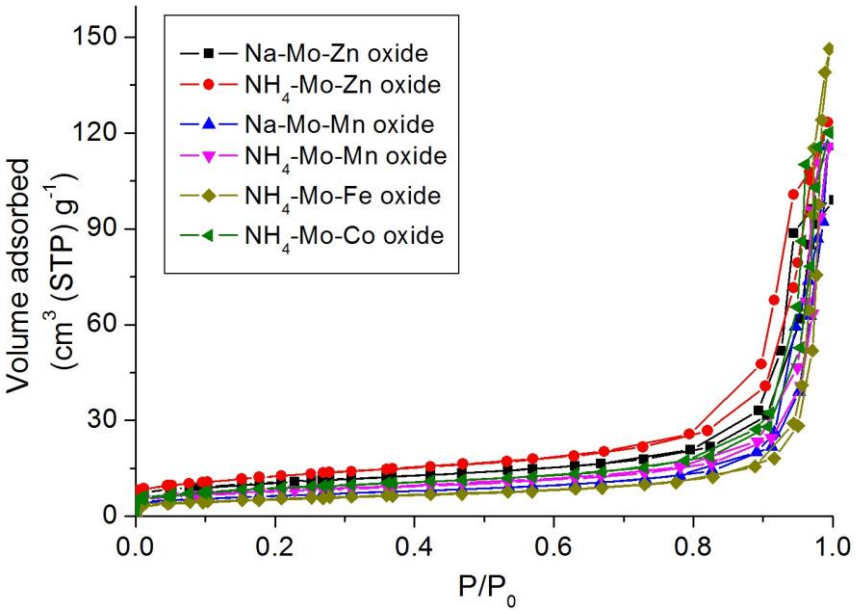

Figure 3. 13. Nitrogen gas adsorption isotherms Na–Mo–Zn oxide, NH_4–Mo–Zn oxide, Na–Mo–Mn oxide, NH_4–Mo–Mn oxide, NH_4–Mo–Fe oxide, and NH_4–Mo–Co oxide.

Table 3. 1. Refined parameters and agreement factor of Rietveld analysis for Mo–Zn oxide and Mo–Mn oxide.

	Na–Mo–Zn oxide	NH_4–Mo–Zn oxide	Na–Mo–Mn oxide	NH_4–Mo–Mn oxide	NH_4–Mo–Fe oxide	NH_4–Mo–Co oxide
crystal system	Cubic	cubic	cubic	cubic	cubic	cubic
space group	$Fd\bar{3}m$	$Fd\bar{3}m$	$Fd\bar{3}m$	$Fd\bar{3}m$	$Fd\bar{3}m$	$Fd\bar{3}m$
$a = b = c$ (Å)	19.4675	19.4533	19.7047	19.6578	19.1347	19.4358
$\alpha = \beta = \gamma$ (degree)	90	90	90	90	90	90
V (Å^3)	7377.86	7361.73	7650.85	7596.34	7005.92	7341.88
R_{wp}	7.10%	8.66%	6.14%	6.19%	5.66%	5.93%
$R_{wp(w/o\ bck)}$	12.09%	14.42%	11.59%	11.92%	13.76%	25.52%
R_p	5.35%	6.26%	4.43%	4.66%	4.06%	3.87%

Table 3. 2. Results from the charge flipping method and assignment of heavy atoms for ε-Keggin POM-based materials.

	Na–Mo–Zn oxide	NH_4–Mo–Zn oxide	Na–Mo–Mn oxide	NH_4–Mo–Mn oxide	NH_4–Mo–Fe oxide	NH_4–Mo–Co oxide
			Peak intensity			
Surrounding site	22.87	9.48	16.67	20.55	8.25	7.58
Linking site	11.74	7.56	5.96	9.16	3.21	2.62
Central site	12.69	6.51	1.93	1.25	1.69	1.97
			Assignment			
Surrounding site	Mo	Mo	Mo	Mo	Mo	Mo
Linking site	Zn	Zn	Mn	Mn	Fe	Co
Central site	Zn	Zn	Mn	Mn	Fe	Co

Table 3. 3. valence of metal ions in the materials from XPS spectra curving fitting.

	Mo^{V}: Mo^{VI}	X (= Zn, Mn, Fe, and Co)
Na–Mo–Zn oxide	1: 10	Zn^{II}
NH_4–Mo–Zn oxide	4: 8	Zn^{II}
Na–Mo–Mn oxide	2: 10	Mn^{II}
NH_4–Mo–Mn oxide	1: 1	Mn^{II}
NH_4–Mo–Fe oxide	3: 9	Fe^{II}: Fe^{III} = 1: 2
NH_4–Mo–Co oxide	4: 8	Co^{II}

Table 3. 4. Surface area and pore volume from nitrogen gas adsorption experiments.

	BET surface area (m^2/g)	Outer surface area (m^2/g)	Pore volume (cm^3/g)
Na–Mo–Zn oxide	37	27	0.0075
NH_4–Mo–Zn oxide	45	35	0.0044
Na–Mo–Mn oxide	22	16	0.0028
NH_4–Mo–Mn oxide	27	21	0.0051
NH_4–Mo–Fe oxide	20	16	0.0034
NH_4–Mo–Co oxide	32	24	0.0058

BET surface area was calculated with the BET method. Outer surface area and pore volume was calculated with the t-plot method.

Chapter 4. Investigation of the formation process of zeolite-like 3D frameworks constructed by ε-Keggin-type polyoxometalates with binding metal ions and preparation of a nano-crystal

4.1. Introduction

The formation process of Mo–V–Bi oxide (Figure 4. 1) has not been understood. Moreover, the yield of Mo–V–Bi oxide is low (3% based on Mo after purification), which should be improved for further investigations of this material. Furthermore, in the viewpoint of applications, size of material is also of importance, and many examples are presented that nanometer-sized materials show superior properties to that of the bulk materials. Some applications of materials depend not only on the ability of control the chemical structure of materials but also their microstructure, size, and morphology. [1–4]

In this chapter, the author described in detail the conditions for synthesis of Mo–V–Bi oxide. The crystal size of the resulting Mo–V–Bi oxide was found to be highly dependent on the starting materials and could be controlled by altering the solubility of the starting materials. Nanometer-sized Mo–V–Bi oxide crystallites, denoted as nano-Mo–V–Bi oxide, could be formed by applying all soluble starting materials. The material formation mechanism was proposed on the basis of Raman spectra of the precursor solution during the synthesis, indicating the transformation of $\{Mo_{72}V_{30}\}$ [5] to ε-Keggin POM as building blocks of the material in solution.

4.2. Experimental

4.2.1. Synthesis of Mo–V–Bi oxide

$(NH_4)_6Mo_7O_{24}\cdot 4H_2O$ (denoted as AHM, 8.828 g, 50 mmol based on Mo) was dissolved in 110 mL of water. $VOSO_4\cdot 5H_2O$ (3.219 g, 12.5 mmol) was dissolved in 110 mL of water. After the solids were completely dissolved, the solution of $VOSO_4\cdot 5H_2O$ was poured into the solution of $(NH_4)_6Mo_7O_{24}\cdot 4H_2O$ quickly. After stirring at room temperature for 3 min, $Bi(OH)_3$ (0.438 g, 1.67 mmol) was added. Then the mixture was left to stir for 7 min followed by N_2 bubbling for 10 min. The mixture was introduced into a 300-mL Teflon liner of a stainless-steel autoclave with the help of 20 mL of water. A Teflon sheet (4 m × 0.1 m × 0.1 mm) was inserted into the liner. The autoclave was placed in an oven and heated at 448 K for 48 h. After the autoclave had been cooled

down to room temperature, Mo–V–Bi oxide formed on the bottom of the liner. For purification, the Teflon sheet was removed carefully, on which most of the impurity of Mo–V oxide was formed. Then, the solid on bottom was filtrated by two pieces of cotton sheets. The filtrate that contained Mo–V–Bi oxide was transferred into centrifugation tubes with the help of 200 mL of water and separated by centrifugation (2000 rpm, 3 min). Solid on the bottom of centrifugation tube was collected and then the solid was dispersed in water (200 mL) and separated by centrifugation (2000 rpm, 3 min). This washing process was repeated 6 times, and the obtained solid was dried at 353 K overnight. 0.45 g of Mo–V–Bi oxide (yield: 3.3% based on Mo) was obtained.

4.2.2. Synthesis of nano-Mo–V–Bi oxide with high yield

$Bi(NO_3)_3\ 5H_2O$ (0.68 g, 1.40 mmol) was dissolved in a solution (1.7 mL) of glycerol and water with the volume ratio of 1 : 1. $(NH_4)_6Mo_7O_{24}\ 4H_2O$ (1.471 g, 8.33 mmol based on Mo) was dissolved in 20 mL of water. $VOSO_4\ 5H_2O$ (0.5365 g, 2.08 mmol) was dissolved in 20 mL of water. After the solids had been completely dissolved, the solution of $VOSO_4\ 5H_2O$ was rapidly poured into the solution of $(NH_4)_6Mo_7O_{24}\ 4H_2O$. After stirring at room temperature for 3 min, $Bi(NO_3)_3$ solution was added. Then the mixture was stirred for 7 min. The pH of the precursor was adjusted to 3.7 with 28% of ammonia aqueous solution. After the mixture was purged by N_2 for 10 min, the mixture was introduced into a 50-mL Teflon liner of a stainless-steel autoclave. The autoclave was placed in an oven with rotation equipment and heated at 448 K for 48 h with rotation (~1 rpm). After the autoclave had been cooled down to room temperature, black solid was collected by filtration, washed with 20 mL of water 3 times, and dried at 353 K overnight. 0.506 g of Mo–V–Bi oxide (yield: 22% based on Mo) was obtained.

4.2.3. Synthesis of $\{Mo_{72}V_{30}\}$ with sodium and potassium cations (K–Na–$\{Mo_{72}V_{30}\}$) with ammonium cation (NH_4–$\{Mo_{72}V_{30}\}$)

K–Na–{$Mo_{72}V_{30}$} was obtained according to a previous paper. [6] FT-IR (KBr pellet): 1629 (water), 1190, 1131, 1054, 966, 794, 632, 580, 453 cm^{-1}. NH_4–{$Mo_{72}V_{30}$} was synthesized according to the previous paper with slight modification. Briefly, $(NH_4)_6Mo_7O_{24}\cdot 4H_2O$ (4.38 g, Mo: 24.8 mmol) was dissolved in 50 mL of water. NH_4VO_3 (2.49 g, 21.3 mmol) was dissolved in 80 mL of water at 100 ^oC. After the temperature of NH_4VO_3 solution was cooled under, NH_4VO_3 solution was added into $(NH_4)_6Mo_7O_{24}\cdot 4H_2O$ solution. Then pH was adjusted to 2 using H_2SO_4 (1 M), followed by treated with $N_2H_6SO_4$ (0.9 g, 6.9 mmol). The solution was stirred at room temperature for 3 h and then was left standing at room temperature for 24 h. The resulting solid was collected by filtration and washed with water 3 times, and dried at room temperature. FT-IR (KBr pellet): 1626 (water), 1405 (ammonium cation), 1198, 1123, 1053, 963, 789, 633, 577, 450 cm^{-1}. FT-IR data of the resulting solids are quite in good agreement with the reported data, indicating K–Na–{$Mo_{72}V_{30}$} and NH_4–{$Mo_{72}V_{30}$} were successfully synthesized.

4.2.4. Synthesis of Mo–V–Bi oxide using POM of {$Mo_{72}V_{30}$}

Briefly, 1.691 g of K–Na–{$Mo_{72}V_{30}$} or NH_4–{$Mo_{72}V_{30}$} was dissolved in 40 mL of water. $Bi(NO_3)_3\cdot 5H_2O$ (0.68 g, 1.40 mmol) was dissolved in a solution (1.7 mL) of glycerol and water with the volume ratio of 1 : 1. $Bi(NO_3)_3\cdot 5H_2O$ solution was added into {$Mo_{72}V_{30}$} solution, and the mixture was stirred for 10 min. Then pH of the solution was adjusted to 3.4 with 28% of ammonia aqueous solution. After the mixture was purged by N_2 for 10 min, the mixture was heated at 373 K for 2.5 h with stirring. The resulting solid was collected with filtration.

4.2.5. Characterization

Nitrogen gas adsorption isotherms were obtained by a BELSORP MAX (BEL Japan Inc.) sorption analyzer at 77 K. Surface area was calculated with the BET method. The materials were evacuated at 573 K for 2.5 h before measurement. Powder X-ray

diffraction (XRD) patterns were obtained on RINT2200 (Rigaku) with Cu Kα radiation (tube voltage: 40 kV, tube current: 20 mA). Scanning electron microscopy (SEM) images were obtained with HD-2000 (HITACHI). Transmission electron microscopy (TEM) images were taken with a 200 kV TEM (JEOL JEM-2100F). Fourier transform infrared (FT-IR) analysis was carried out on PARAGON 1000, Perkin Elmer. Raman spectra were recorded with a Renishaw inVia Raman Microscope. Elemental compositions were determined by an inductive coupling plasma (ICP-AES) method (ICPE-9000, Shimadzu). Crystallite size was calculated from the most intensive powder diffraction peak (the peak at 7.6 degree) with the MID Jade 7 software package by using the Scherrer equation.

4.3. Results and discussion

4.3.1. Preparation of Mo–V–Bi oxide

Well-crystallized Mo–V–Bi oxide was synthesized by a hydrothermal reaction of $(NH_4)_6Mo_7O_{24}{\cdot}4H_2O$, $VOSO_4{\cdot}5H_2O$, and $Bi(OH)_3$. After the hydrothermal synthesis, the powder XRD pattern of the resulting material showed that the crude material in the autoclave was not pure, which was a mixture of Mo–V–Bi oxide and orthorhombic Mo–V oxide (Figure 4. 2a), Orthorhombic Mo–V oxide was synthesized by a hydrothermal synthesis of AHM and $VOSO_4$, and it was constructed by connecting pentagonal POM units with metal-oxygen octahedra in a-b plane that grown in c-axis (Figure 4. 1). Therefore, purification processes were essential to obtain pure material of Mo–V–Bi oxide. Mo–V–Bi oxide tended to form on the bottom of the Teflon liner, and a material formed on the Teflon sheet inserted in the Teflon liner was orthorhombic Mo–V oxide (Figure 4. 2b). [7] Most of the orthorhombic Mo–V oxide could be removed by removal of the Teflon sheet, and the rest of the orthorhombic Mo–V oxide on the bottom was removed by filtration with cotton and centrifugation. Mo–V–Bi oxide was separated from the orthorhombic Mo–V oxide, because of the shape difference of these oxides. Orthorhombic Mo–V oxide, which had a rod-like shape, [7] attached to the cotton,

whereas Mo–V–Bi oxide, which had an octahedral shape, easily passed through the cotton (Figure 4. 3a), and thus Mo–V–Bi oxide could be separated from orthorhombic Mo–V oxide with cotton. Centrifugation was also an effective method for separating the Mo–V–Bi oxide. After centrifugation, Mo–V–Bi oxide tended to settle on the bottom of the centrifugation tube (Figure 4. 2c) and orthorhombic Mo–V oxide was still dispersed in the solution. After the purification process, pure well-crystallized Mo–V–Bi oxide was obtained (Figure 4. 2c).

The effects of synthesis conditions of Mo–V–Bi oxide were investigated by altering synthesis conditions including reaction time, reaction temperature, concentration of the precursor, pH value of the precursor, and starting materials. All the synthesis conditions were summarized in Table 4. 1 and the powder XRD patterns of the resulting compounds were shown in Figure 4. 4. Formation of Mo–V–Bi oxide was affected by synthesis time. Reaction time more than 4 hour was necessary to obtain Mo–V–Bi oxide (Table 4. 1, entries 1-4, Figure 4. 4a-d) at 448 K. After 4 hours' reaction, only Mo–V–Bi oxide had been formed, and no orthorhombic Mo–V oxide had been formed, indicating that Mo–V–Bi oxide formed faster than orthorhombic Mo–V oxide. Low temperature (293 K) was not suitable for formation of Mo–V–Bi oxide (Table 4. 1, entry 5, Figure 4. 4e), and Mo–V–Bi oxide formed at high temperatures (373~448 K, Table 4. 1, entries 1, 6-7, Figure 4. 4a,f-g). A hydrothermal reaction at 373 K produced only Mo–V–Bi oxide, and orthorhombic Mo–V oxide was not produced. Mo–V–Bi oxide was prepared under different concentrations of the precursors, and too low concentration was not good for Mo–V–Bi oxide (Table 4. 1, entries 1, 8-11, Figure 4. 4a, h-k). The suitable pH value range for Mo–V–Bi oxide was from 2 to 5, and Mo–V–Bi oxide did not form at pH value higher than 5 and lower than 2 (Table 4. 1, entries 12-15, Figure 4. 4a, l-o). It has been reported that orthorhombic Mo–V oxide was produced in solution with pH value between ca. 2.7 to 3.4, and trigonal Mo–V oxide and hexagonal Mo–V oxide were produced in solution with pH value of 2. [8] Only Mo–V–Bi oxide was produced from the solution with pH value from 2 to 5. These

results indicated that Mo–V–Bi oxide could be produced under wider conditions than could orthorhombic Mo–V oxide.

In the case of molybdenum sources, potassium molybdate and sodium molybdate were not suitable to yield Mo–V–Bi oxide (Table 4. 1, entries 16-17, Figure 4. 4p-q) despite pH values being between 2 and 5. For vanadium sources, using $VOSO_4$ $5H_2O$ was essential for Mo–V–Bi oxide, and other vanadium contained materials could not produce the material (Table 4. 1, entries 18-20, Figure 4. 4r-t). Vanadium and molybdenum in Mo–V–Bi oxide were partially reduced, and $VOSO_4$ $5H_2O$ acted also as a reducing reagent. Therefore, NH_3VO_3 and $NaVO_3$ were not suitable vanadium sources. VO_2 was not suitable for production of Mo–V–Bi oxide, the reason of which was in a later section.

Several bismuth sources were tested for synthesis of Mo–V–Bi oxide, and all of these could produce Mo–V–Bi oxide (Table 4. 1, entries 1, 21-24, Figure 4. 4u-x). A reaction with $Bi(NO_3)_3$ $5H_2O$ produced Mo–V–Bi oxide as well as hexagonal Mo–V oxide without formation of orthorhombic Mo–V oxide. Interestingly, powder diffraction peaks of Mo–V–Bi oxide produced by synthesis using $Bi(NO_3)_3$ were broader than those of Mo–V–Bi oxide produced by using other Bi sources (Figure 4. 4x), indicating that smaller crystals of Mo–V–Bi oxide were produced by $Bi(NO_3)_3$. The crystallite size calculated with the Scherrer equation to be 1000, 625, 755, 805, and 396 Å for the materials from $Bi(OH)_3$, Bi_2O_3, BiOCl, $Bi_2(SO_4)_3$, and $Bi(NO_3)_3$, respectively. Solubility of the bismuth compounds was tested, which was shown in Table 4. 2. Solubility of $Bi(NO_3)_3$ was remarkably higher than that of other bismuth compounds. High concentration of Bi^{III} ion in solution was favored for production of Mo–V–Bi oxide, and crystallite size of the produced Mo–V–Bi oxide was smaller than those produced with other insoluble Bi sources (Table 4. 1, entries 21-24). Orthorhombic Mo–V oxide and hexagonal Mo–V oxide formed whichever bismuth compounds were used for synthesis, indicating that Mo and V were excess in the synthesis system.

The influence of solubility of the starting materials in water on the crystallinity of

the resulting materials was studied. The author found that the use of the dynamic hydrothermal method (the autoclave being rotated during hydrothermal synthesis) for material synthesis, which was expected to make the reaction precursor uniformly and thus yielded uniform products, [9] and increasing the amount of bismuth species was expected to consume the excess Mo and V in solution. Table 4. 3 and Figure 4. 5 showed Mo–V–Bi oxide synthesized from different starting materials with different solubility (Solubility of every material is listed in Table 4. 2.). The powder diffraction peaks of the resulting materials were sharp, when the system contained one insoluble material, such as H_2MoO_4 and $Bi(OH)_3$ (Table 4. 3, entries 1~4). Using all soluble starting materials (AHM, $VOSO_4 \cdot 5H_2O$, and $Bi(NO_3)_3 \cdot 5H_2O$) formed a material with broad powder diffraction peaks, indicating the worse crystallinity of the resulting material (entry 5). The crystal size of the material estimated with the Scherrer equation showed that the material synthesized from all soluble starting materials was smaller (entry 5) than that obtained from insoluble starting materials (entries 1~4).

4.3.2. Synthesis and characterization of nanometer-sized Mo–V–Bi oxide

By using $Bi(NO_3)_3$, the author could prepare Mo–V–Bi oxide with hexagonal Mo–V oxide (Table 4. 1, entry 24). Addition of a certain amount of glycerol that increased the solubility of $Bi(NO_3)_3$ (Table 4. 2) and increasing the amount of bismuth source (Mo: V: Bi = 4: 1: 0.673) further suppressed the side-reactions and produced mostly pure Mo–V–Bi oxide (Table 4. 3, entry 5 and Figure 4. 5e). Without glycerol the there was a by-product XRD peak being observed (Table 4. 3, entry 6 and Figure 4. 5f). Using the rotation synthesis method was expected to have uniform particle of Mo–V–Bi oxide. The broad powder diffraction peaks indicated smaller particle of Mo–V–Bi oxide, denoted as nano-Mo–V–Bi oxide. Nano-Mo–V–Bi oxide could be obtained with high yield (22% based on Mo) compared with the yield of the material obtained by using $Bi(OH)_3$ (3% based on Mo).

Powder XRD patterns (Figure 4. 5) and FT-IR spectra (Figure 4. 6) of

well-crystallized Mo–V–Bi oxide and nano-Mo–V–Bi oxide confirmed that the basic structure of nano-Mo–V–Bi oxide was the same as that of well-crystallized Mo–V–Bi oxide. SEM images of nano-Mo–V–Bi oxide and Mo–V–Bi oxide (Figure 4. 3) showed that size of nano-Mo–V–Bi oxide (20~50 nm in one diameter) was much smaller than that of Mo–V–Bi oxide (1 μm in one diameter). Clear lattice images of Mo–V–Bi oxide and nano-Mo–V–Bi oxide could be observed by high-resolution TEM. A HRTEM image of Mo–V–Bi oxide showed that the layer distance of the (111) plane was 11.4 Å (Figure 4. 7a), which was in accordance with results of structure analysis. [10] Nano-Mo–V–Bi oxide exhibited polyhedral nanometer-sized crystals with the size around 50 nm in one diameter in HRTEM. Layer of (111) plane of nano-Mo–V–Bi oxide could also be observed in HRTEM image, demonstrating that they were well-ordered nanometer-sized single crystallites (Figure 4. 7b).

Crystal size of Mo–V–Bi oxide affected the properties of the material. Nitrogen adsorption isotherms of Mo–V–Bi oxide and nano-Mo–V–Bi oxide were shown in Figure 4. 8, illustrating that both materials were microporous materials. Amounts of nitrogen gas uptake at very low relative pressure less than 0.05 of Mo–V–Bi oxide and nano- Mo–V–Bi oxide were similar, indicating that both oxides had similar volumes of micropores. However, nitrogen gas uptake of nano-Mo–V–Bi oxide continued to increase with increasing the relative pressure, indicating that nano-Mo–V–Bi had a larger external surface area. The surface areas of Mo–V–Bi oxide and nano-Mo–V–Bi oxide were calculated to be 60 m^2/g and 75 m^2/g, respectively. The external surface area of the materials were calculated by the t-plot method to be 20 m^2/g and 48 m^2/g for Mo–V–Bi oxide and nano-Mo–V–Bi oxide, respectively. An obvious hysteresis in the N_2 adsorption isotherm of nano-Mo–V–Bi oxide was observed in the relative pressure range of 0.6~1.0, which was ascribed to mesopores of the material from particle aggregation.

4.3.3. Formation mechanism

It was found that Mo–V–Bi oxide could be obtained by heating the precursor mixture at 373 K in a flask under atmospheric conditions. Therefore, the formation mechanism of Mo–V–Bi oxide was studied using a solution containing the starting materials with composition of Mo: V: Bi = 4: 1: 0.67 at 373 K in a flask with stirring. The solution of the system was monitored by Raman spectra during the synthesis (Figure 4. 9). When $(NH_4)_6Mo_7O_{24}\cdot 4H_2O$ and $VOSO_4\cdot 5H_2O$ was mixed in glycerol-water solution, A Raman spectrum with a band top of 880 cm^{-1}, typically corresponding to ball-type molybdovanadate $\{Mo_{72}V_{30}\}$, was observed. [11] It has been reported that mixing $(NH_4)_6Mo_7O_{24}\cdot 4H_2O$ and $VOSO_4\cdot 5H_2O$ in an aqueous solution spontaneously produced $\{Mo_{72}V_{30}\}$ which then produced orthorhombic Mo–V oxide under hydrothermal conditions. When $Bi(NO_3)_3$ was added to the solution of $(NH_4)_6Mo_7O_{24}\cdot 4H_2O$ and $VOSO_4\cdot 5H_2O$ and then heated for 7~15 min, a new band ascribed to [ε-$VMo_{9.4}V_{2.6}O_{40}$] at 820 cm^{-1} appeared. Furthermore, Raman analysis indicated that heating of the solution of $(NH_4)_6Mo_7O_{24}\cdot 4H_2O$ and $VOSO_4\cdot 5H_2O$ did not produce the Raman band at 820 cm^{-1} (Figure 4. 10).

The formation process of Mo–V–Bi oxide was proposed. After mixing $(NH_4)_6Mo_7O_{24}\cdot 4H_2O$ with $VOSO_4\cdot 5H_2O$ in aqueous solution, $\{Mo_{72}V_{30}\}$ formed immediately. Addition of $Bi(NO_3)_3$ and heating produced ε-Keggin POMs, which transferred from $\{Mo_{72}V_{30}\}$, and the ε-Keggin POMs assembled in a tetrahedral fashion with Bi^{III} ions to form the nucleus of Mo–V–Bi oxide (Figure 4. 11).

To confirm the transformation of $\{Mo_{72}V_{30}\}$ anion, $\{Mo_{72}V_{30}\}$ with ammonium cation [12] (denoted as NH_4–$\{Mo_{72}V_{30}\}$) was reacted with $Bi(NO_3)_3$. NH_4–$\{Mo_{72}V_{30}\}$ (1.691 g) was mixed with $Bi(NO_3)_3$ (0.68 g) in water-glycerol solution (1.7 mL), which was heated at 373 K for 150 min. The XRD pattern and FT-IR spectra of the resulting solid indicated that the solid synthesized from NH_4–$\{Mo_{72}V_{30}\}$ was Mo–V–Bi oxide (Figure 4. 12). These results indicated that $\{Mo_{72}V_{30}\}$ was transformed to ε-Keggin POMs that assembled with Bi^{III} ions to yield Mo–V–Bi oxide, and formation of $\{Mo_{72}V_{30}\}$ anion in precursor was important for the material. In the case using VO_2 as

vanadium source, Raman spectrum indicated that {$Mo_{72}V_{30}$} did not form in precurosr solution (Figure 4. 13), and thus Mo–V–Bi oxide could not be obtained (Table 4. 1, entry 20). Interestingly, using {$Mo_{72}V_{30}$} with sodium and potassium ions (denoted as K–Na–{$Mo_{72}V_{30}$}) could not yield Mo–V–Bi oxide, indicating that Na^+ and K^+ were not suitable cations for Mo–V–Bi oxide synthesis, and that might be a reason that K_2MoO_4 and Na_2MoO_4 were not suitable starting materials for synthesis of Mo–V–Bi oxide (Table 4. 1, entries 16 and 17).

In the synthesis system of well-crystallized Mo–V–Bi oxide (Table 4. 2, entry 1), small amount of bismuth source was used (Mo: V: Bi = 4: 1: 0.134). After consuming all bismuth ions, the excess {$Mo_{72}V_{30}$} formed Mo–V oxide under hydrothermal condition. [8,11]

4.4. Conclusion

In summary, the formation of Mo–V–Bi oxide was investigated and the suitable synthesis condition of Mo–V–Bi oxide was confirmed. It was found that solubility of the starting materials affected the crystal size of the resulting material. Soluble starting materials produced nanometer-sized Mo–V–Bi oxide (nano-Mo–V–Bi oxide). Crystal size of Mo–V–Bi oxide affected the property of Mo–V–Bi oxide such as adsorption property that was enhanced by decreasing the crystal size. The formation mechanism was studied with Raman spectroscopy, indicating the transformation of {$Mo_{72}V_{30}$} to ε-Keggin POM units in solution, which acted as building blocks for the material.

References

(1) Wee, L. H.; Lohe, M. R.; Janssens, N.; Kaskel, S.; Martens, J. A. *J. Mater. Chem.* **2012**, *22*, 13742–13746.

(2) Guo, H.; Zhu, Y.; Wang, S.; Su, S.; Zhou, L.; Zhang, H. *Chem. Mater.* **2012**, *24*, 444–450.

(3) Ma, M.; Zacher, D.; Zhang, X.; Fischer, R. A.; Metzler-Nolte, N. *Cryst. Growth Des.* **2011**, *11*, 185–189.

(4) Ishikawa, S.; Yi, X.; Murayama, T.; Ueda, W. *Appl. Catal. A Gen.* **2013**, *474*, 10–17.

(5) Müller, A.; Todea, A. M.; van Slageren, J.; Dressel, M.; Bögge, H.; Schmidtmann, M.; Luban, M.; Engelhardt, L.; Rusu, M. *Angew. Chem. Int. Ed.* **2005**, *44*, 3857–3861.

(6) Botar, B.; Kögerler, P.; Hill, C. L. *Chem. Commun.* **2005**, 3138–3140.

(7) Sadakane, M.; Kodato, K.; Kuranishi, T.; Nodasaka, Y.; Sugawara, K.; Sakaguchi, N.; Nagai, T.; Matsui, Y.; Ueda, W. *Angew. Chem. Int. Ed.* **2008**, *47*, 2493–2496.

(8) Sadakane, M.; Endo, K.; Kodato, K.; Ishikawa, S.; Murayama, T.; Ueda, W. *Eur. J. Inorg. Chem.* **2013**, 1731–1736.

(9) Li, X.; Wang, Z.; Zheng, J.; Shao, S.; Wang, Y.; Yan, Y. *Chinese J. Catal.* **2011**, *32*, 217–223.

(10) Zhang, Z.; Sadakane, M.; Murayama, T.; Izumi, S.; Yasuda, N.; Sakaguchi, N.; Ueda, W. *Inorg. Chem.* **2014**, *53*, 903–911.

(11) Sadakane, M.; Yamagata, K.; Kodato, K.; Endo, K.; Toriumi, K.; Ozawa, Y.; Ozeki, T.; Nagai, T.; Matsui, Y.; Sakaguchi, N.; Pyrz, W. D.; Buttrey, D. J.; Blom, D. A.; Vogt, T.; Ueda, W. *Angew. Chem. Int. Ed.* **2009**, *48*, 3782–3786.

(12) Sahiro, K.; Ide, Y.; Sano, T.; Sadakane, M. *Mater. Res. Bull.* **2005**, *48*, 4157–4162.

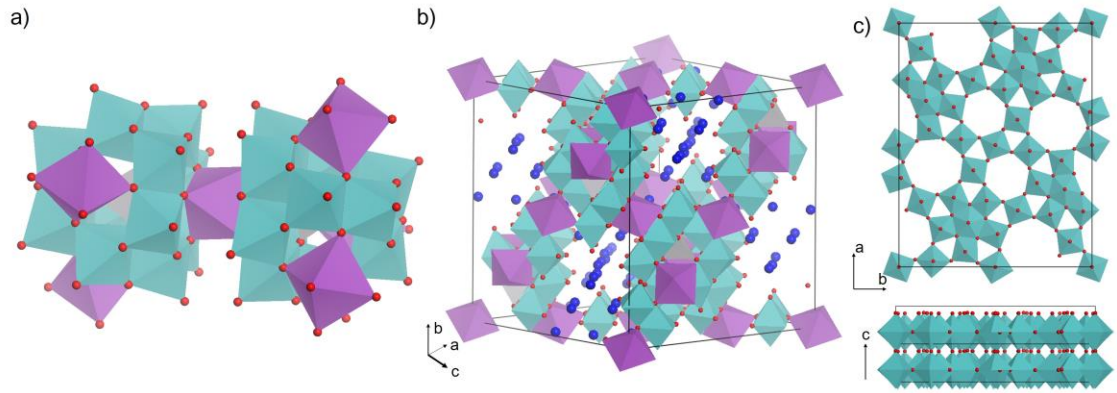

Figure 4. 1. Polyhedral representations of a) ε-Keggin units and their connection, b) unit cell of Mo–V–Bi oxide, and c) orthorhombic Mo–V oxide, Mo or V in surrounding sites (blue octahedron), central VO_4 (gray octahedron), BiO_6 (purple octahedron), cation or water (deep blue sphere), O (red sphere).

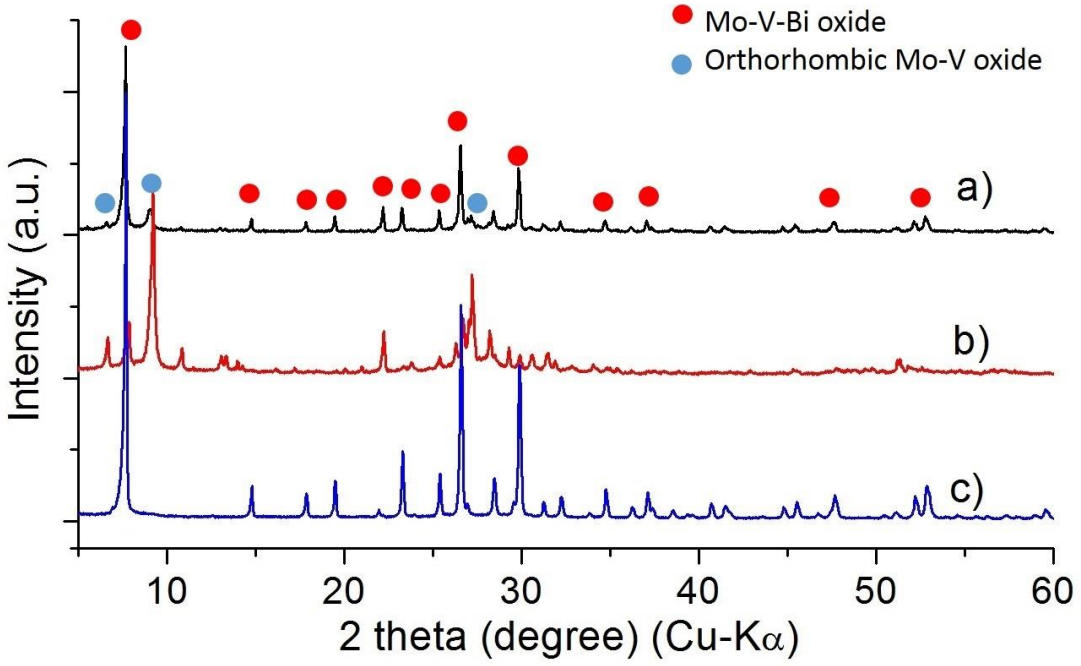

Figure 4. 2. XRD patterns of a) crude solid of Mo–V–Bi oxide, b) the solid of orthorhombic Mo–V oxide collected on the Teflon sheet, and c) the solid of Mo–V–Bi oxide collected on bottom.

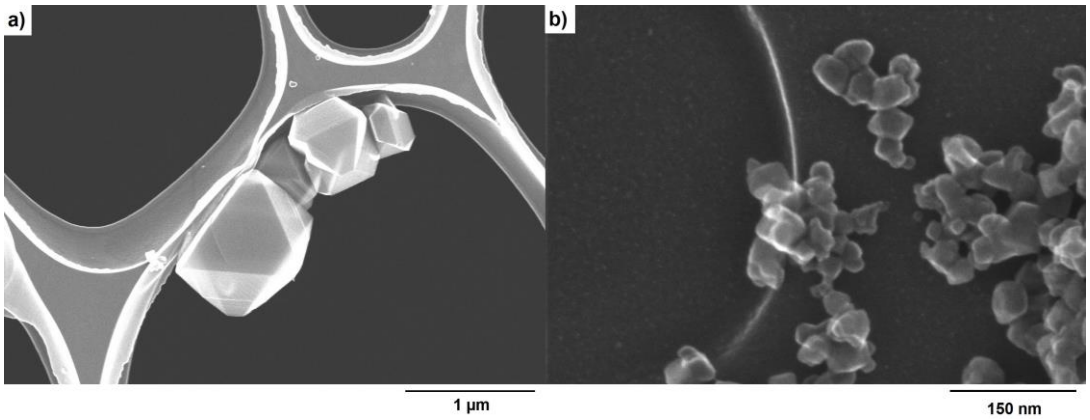

Figure 4. 3. SEM images of a) Mo–V–Bi oxide and b) nano-Mo–V–Bi oxide.

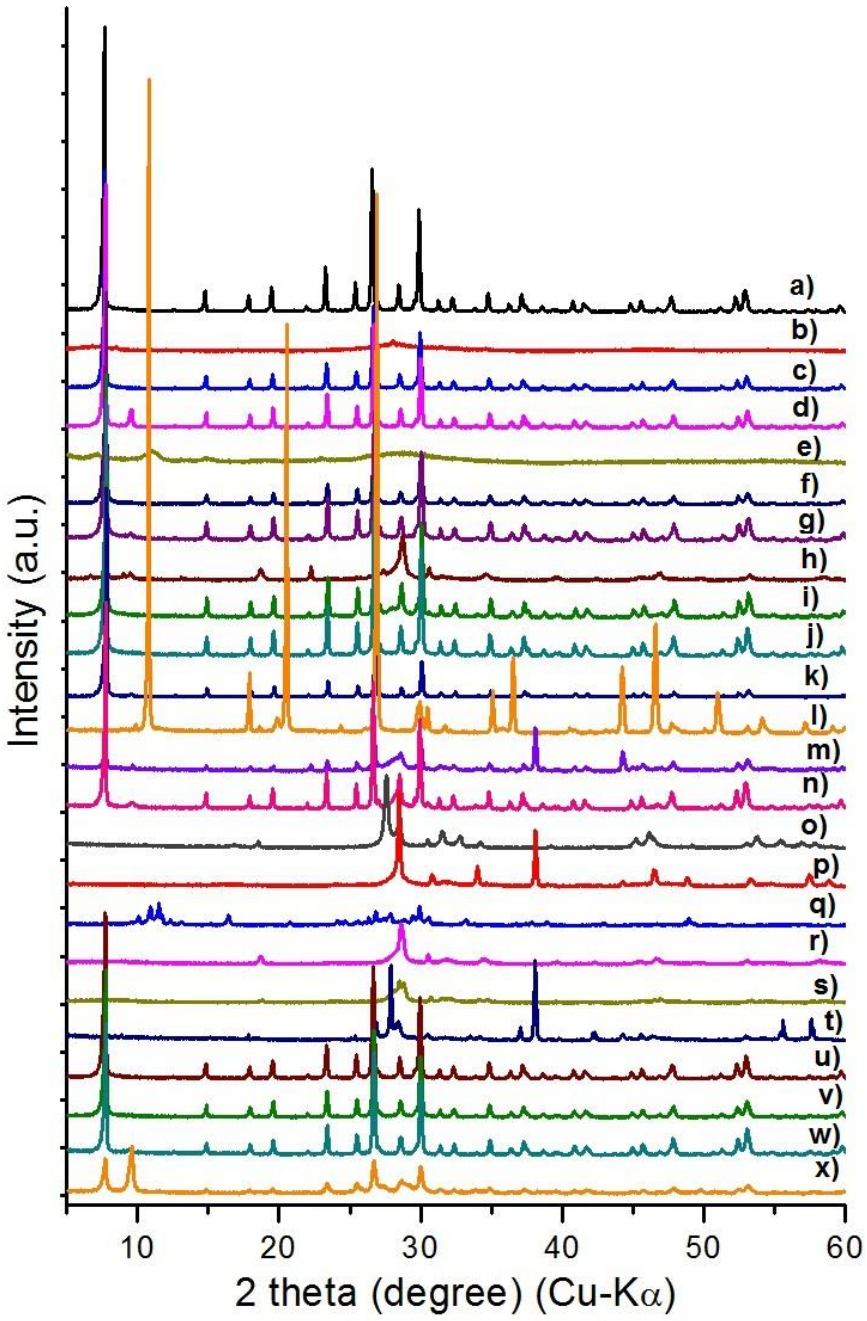

Figure 4. 4. XRD patterns of resulting materials synthesized under different conditions described in Table 1, a) entry 1, b) entry 2, c) entry 3, d) entry 4, e) entry 5, f) entry 6, g) entry 7, h) entry 8, i) entry 9, j) entry 10, k) entry 11, l) entry 12, m) entry 13, n) entry 14, o) entry 15, p) entry 16, q) entry 17, r) entry 18, s) entry 19, t) entry 20, u) entry 21, v) entry 22, w) entry23, and x) entry24, peak around 9 degree is ascribed to hexagonal Mo–V oxide.

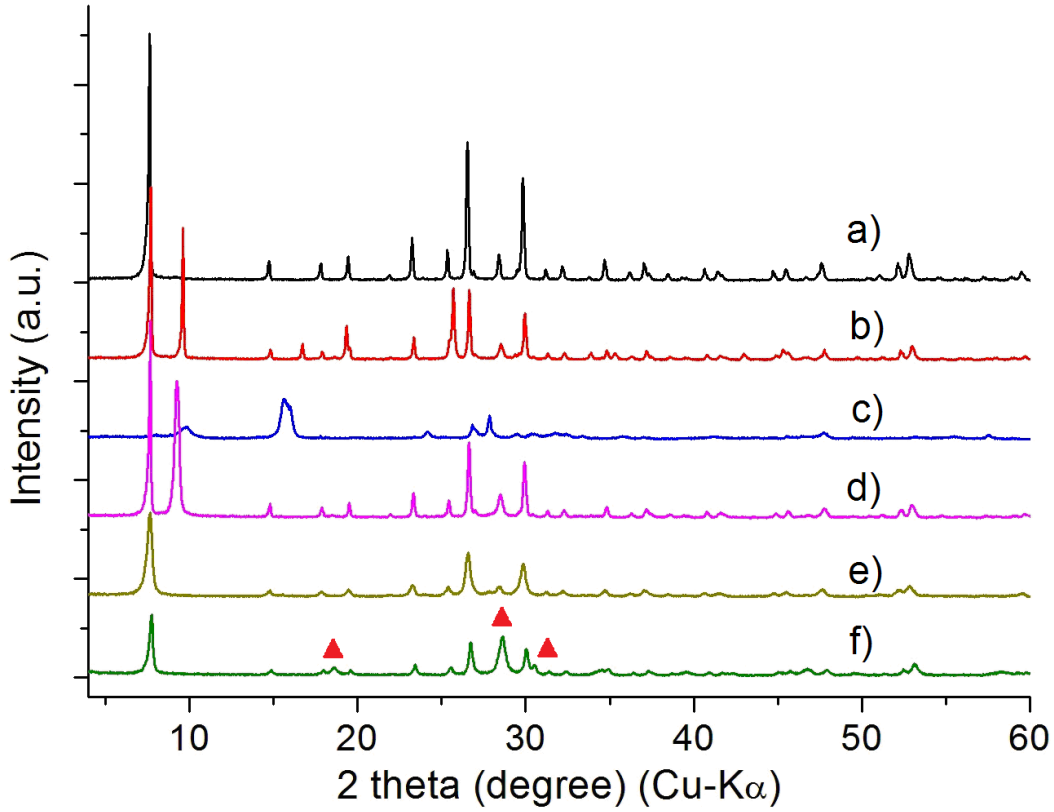

Figure 4. 5. Powder XRD patterns of Mo–V–Bi oxide formed under conditions in Table 2 a) Table 2 entry 1, b) Table 2 entry 2, c) Table 2 entry3, d) Table 2 entry 4, e) Table 2 entry 5, and f) Table 2 entry 6, red triangle shows the impurity peaks.

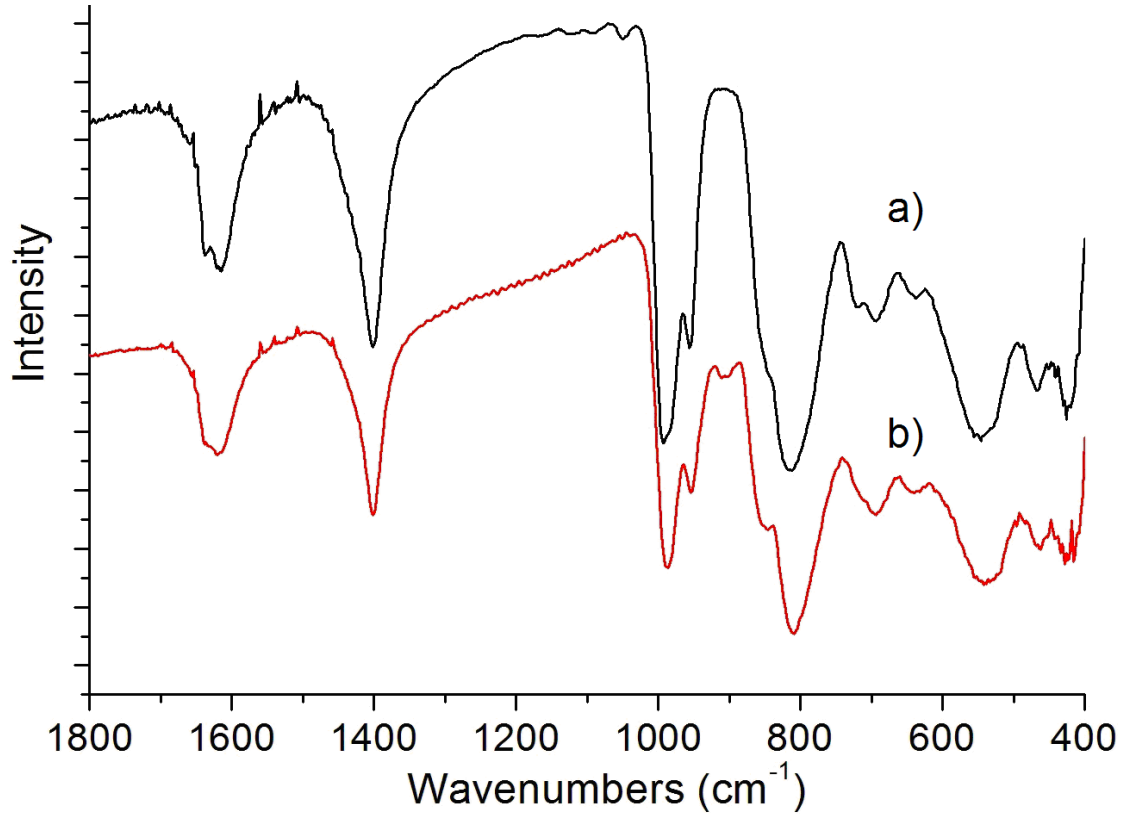

Figure 4. 6. FT-IR spectra of a) Mo–V–Bi oxide and b) nano-Mo–V–Bi oxide.

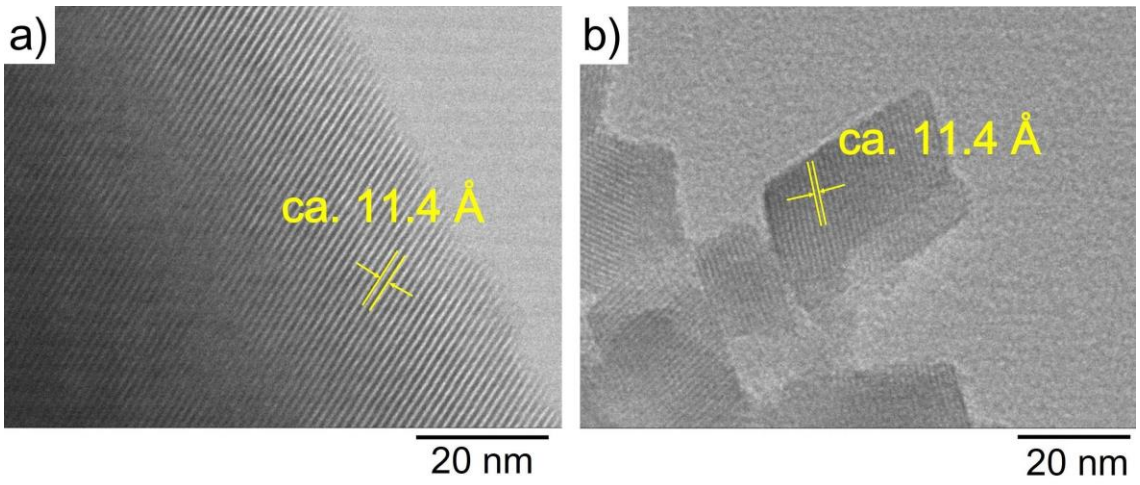

Figure 4. 7. TEM images of a) Mo–V–Bi oxide and b) nano-Mo–V–Bi oxide.

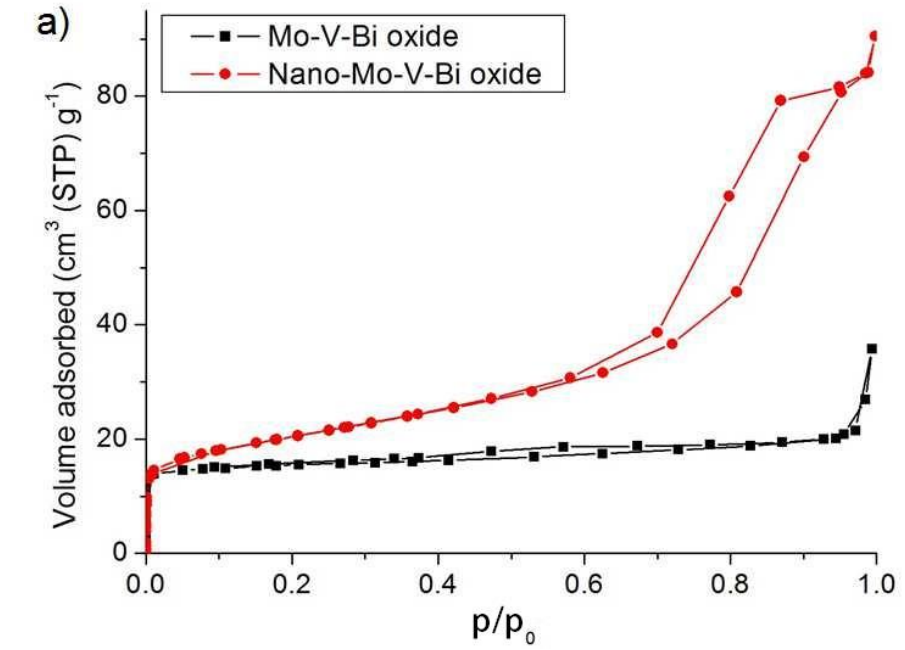

Figure 4. 8. Nitrogen adsorption-desorption isotherms of Mo–V–Bi oxide and nano-Mo–V–Bi oxide.

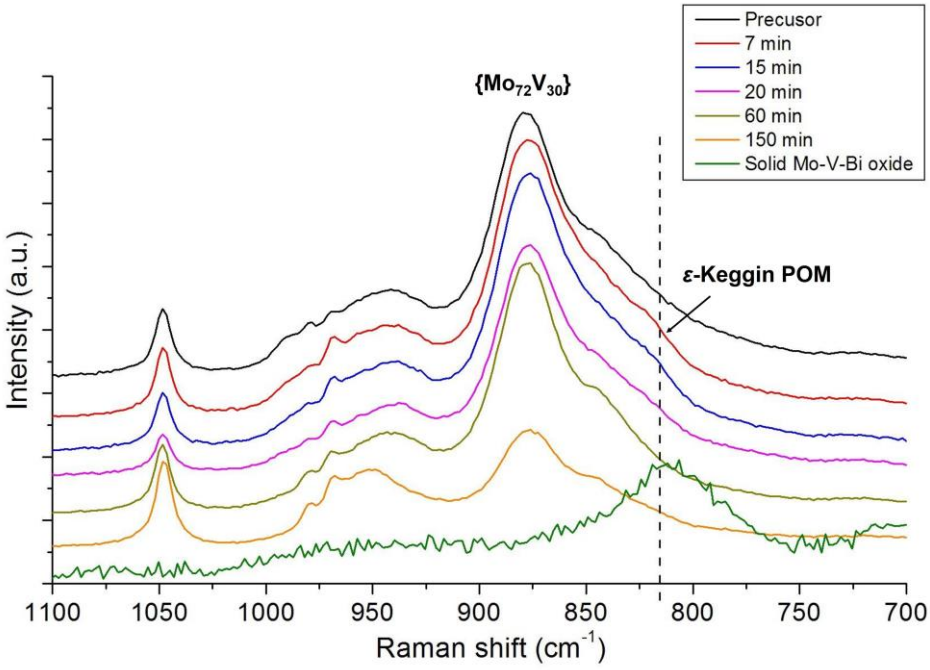

Figure 4. 9. Raman spectra of Mo–V–Bi oxide precursor solution and solid, synthesis conditions: $(NH_4)_6Mo_7O_{24}$ $4H_2O$, 8.33 mmol based on Mo, $VOSO_4$ $5H_2O$, 2.08 mmol, $Bi(NO_3)_3$ $5H_2O$, 1.40 mmol, 40 mL of water, pH 3.4, reaction temperature 373 K.

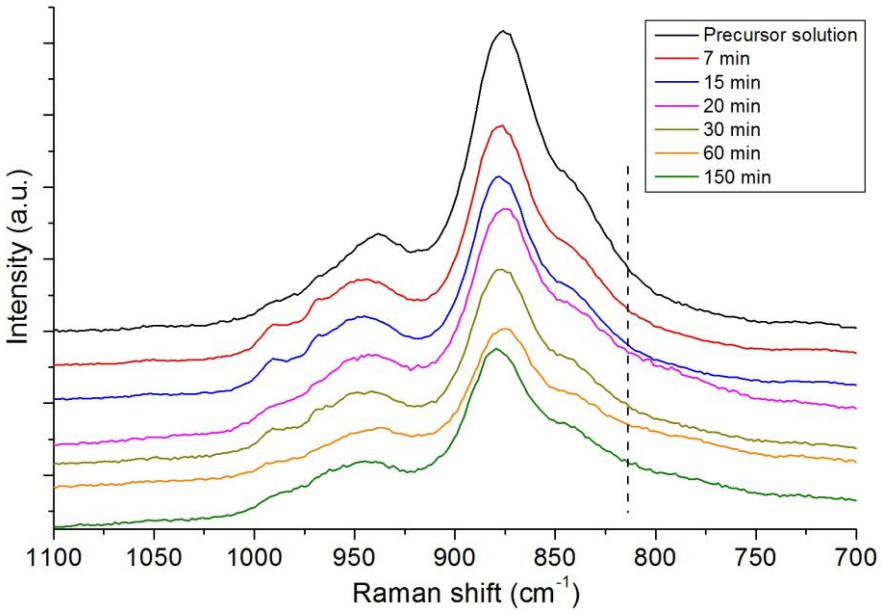

Figure 4. 10. Raman spectra of solution of $(NH_4)_6Mo_7O_{24}\cdot 4H_2O$ and $VOSO_4\cdot 5H_2O$, $(NH_4)_6Mo_7O_{24}\cdot 4H_2O$, 8.33 mmol based on Mo, $VOSO_4\cdot 5H_2O$, 2.08 mmol, 40 mL of water, pH 3.4, temperature, 373 K.

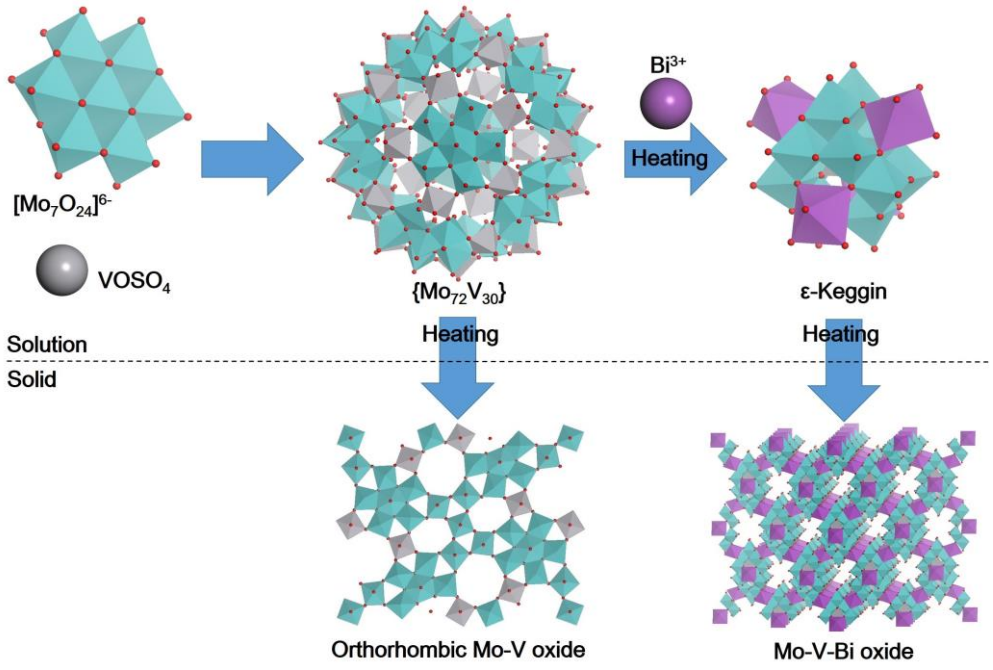

Figure 4. 11. Formation pathway of Mo–V–Bi oxide and orthorhombic Mo–V oxide, MoO_6 or MoO_7 (blue polyhedron), VO_6 (gray octahedron), BiO_6 (purple octahedron), O (red sphere).

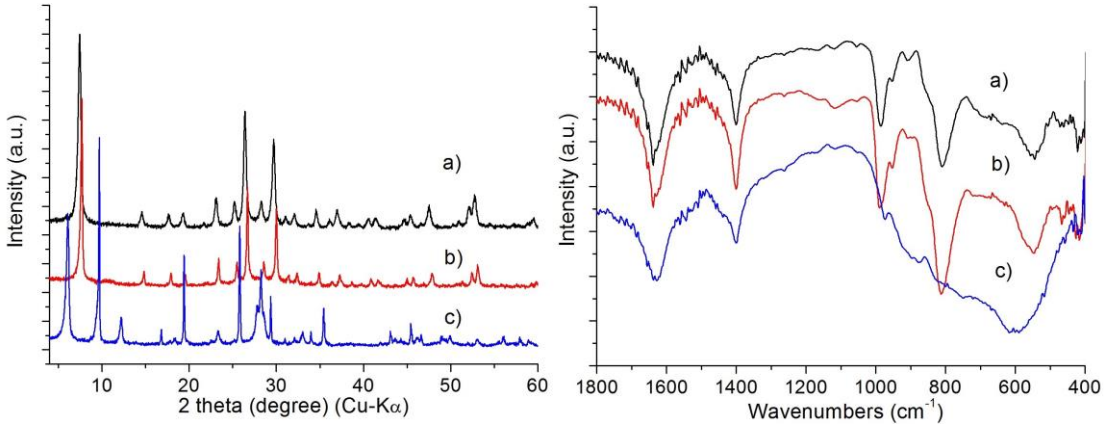

Figure 4. 12. (left) XRD patterns and (right) FT-IR spectra of a) $(NH_4)_6Mo_7O_{24}$ $4H_2O$: 8.33 mmol based on Mo, $VOSO_4$ $5H_2O$: 2.08 mmol, 1.4 mmol of $Bi(NO_3)_3$ $5H_2O$ in 1.7 mL of water-glycerol (1:1), 40 mL of water, 373 K, 150 min, pH was adjusted to 3.4. b) NH_4–$\{Mo_{72}V_{30}\}$: 1.691 g, 1.4 mmol of $Bi(NO_3)_3$ $5H_2O$ in 1.7 mL of water-glycerol (1:1), 40 mL of water, 373 K, 150 min, pH was adjusted to 3.4. c) K–Na–$\{Mo_{72}V_{30}\}$:1.691 g, 1.4 mmol of $Bi(NO_3)_3$ $5H_2O$ in 1.7 mL of water-glycerol (1:1), 40 mL of water, 373 K, 150 min, pH was adjusted to 3.4.

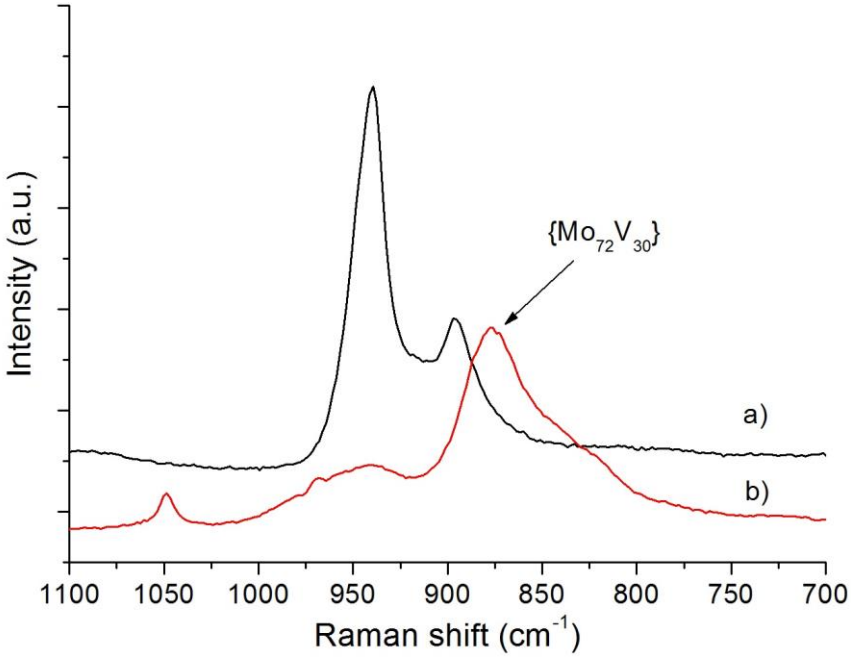

Figure 4. 13. a) Raman spectrum of the solution: $(NH_4)_6Mo_7O_{24}$ $4H_2O$: 8.33 mmol based on Mo, VO_2: 2.08 mmol, 40 mL of water, pH of 3.4, 373 K, 10 min. b) Raman spectrum of the solution: $(NH_4)_6Mo_7O_{24}$ $4H_2O$: 8.33 mmol based on Mo, $VOSO_4$ $5H_2O$: 2.08 mmol, $Bi(NO_3)_3$ $5H_2O$: 1.40 mmol, 40 mL of water, pH of 3.4, 373 K, 15 min.

Table 4. 1. Synthesis conditions of Mo–V–Bi oxide. [a)]

entry	Mo	V	Bi	pH	Time (h)	Temp. (K)	Conc. (M) [b)]	Product [c)]	Orthorhombic-Mo–V Oxide
1	AHM [d)]	$VOSO_4$	$Bi(OH)_3$	3.45	48	448	0.208	Y	Y
2	AHM	$VOSO_4$	$Bi(OH)_3$	3.45	1	448	0.208	N	N
3	AHM	$VOSO_4$	$Bi(OH)_3$	3.45	4	448	0.208	Y	N
4	AHM	$VOSO_4$	$Bi(OH)_3$	3.45	120	448	0.208	Y	Y
5	AHM	$VOSO_4$	$Bi(OH)_3$	3.45	48	293	0.208	N	N
6	AHM	$VOSO_4$	$Bi(OH)_3$	3.45	48	373	0.208	Y	N
7	AHM	$VOSO_4$	$Bi(OH)_3$	3.45	48	423	0.208	Y	Y
8	AHM	$VOSO_4$	$Bi(OH)_3$	3.40	48	448	0.104	N	Y
9	AHM	$VOSO_4$	$Bi(OH)_3$	3.40	48	448	0.125	Y	Y
10	AHM	$VOSO_4$	$Bi(OH)_3$	3.43	48	448	0.166	Y	Y
11	AHM	$VOSO_4$	$Bi(OH)_3$	3.44	48	448	0.187	Y	Y
12	AHM	$VOSO_4$	$Bi(OH)_3$	1.03	48	448	0.208	N	N
13	AHM	$VOSO_4$	$Bi(OH)_3$	2.07	48	448	0.208	Y	N
14	AHM	$VOSO_4$	$Bi(OH)_3$	4.92	48	448	0.208	Y	N
15	AHM	$VOSO_4$	$Bi(OH)_3$	6.39	48	448	0.208	N	N
16	Na_2MoO_4	$VOSO_4$	$Bi(OH)_3$	3.38	48	448	0.208	N	N
17	K_2MoO_4	$VOSO_4$	$Bi(OH)_3$	3.41	48	448	0.208	N	N
18	AHM	NH_4VO_3	$Bi(OH)_3$	3.55	48	448	0.208	N	N
19	AHM	$NaVO_3$	$Bi(OH)_3$	3.35	48	448	0.208	N	N
20	AHM	VO_2	$Bi(OH)_3$	3.48	48	448	0.208	N	N
21	AHM	$VOSO_4$	Bi_2O_3	3.42	48	448	0.208	Y	Y
22	AHM	$VOSO_4$	BiOCl	3.42	48	448	0.208	Y	Y
23	AHM	$VOSO_4$	$Bi_2(SO_4)_3$	3.38	48	423	0.208	Y	Y
24	AHM	$VOSO_4$	$Bi(NO_3)_3$	3.32	48	448	0.208	Y	N

[a)] Mo source: 50 mmol based on Mo, V source: 12.5 mmol, Bi source: 1.67 mmol, 240 mL of water, the purification method was in experimental section, [b)] concentration of Mo sources were based on Mo, Mo: V: Bi was 4: 1: 0.134, [c)] N: Mo–V–Bi oxide did not form, Y: Mo–V–Bi oxide formed, [d)] AHM: $(NH_4)_6Mo_7O_{24}{\cdot}4H_2O$, corresponding powder XRD patterns of the materials were in Figure 4. 4. The value of pH was adjusted by H_2SO_4 (1M).

Table 4. 2. The solubility of bismuth compounds determined by elemental analysis. [a)]

entry	Materials	Material amount (mmol based on metal)	Water amount (mL)	Ion concentration (mmol/L)
1	$Bi(OH)_3$	0.281	40	2.54×10^{-5}
2	Bi_2O_3	0.281	40	4.93×10^{-5}
3	BiOCl	0.281	40	0
4	$Bi_2(SO_4)_3$	0.281	40	0.0288
5	$Bi(NO_3)_3$	0.281	40	5.41
6	$Bi(NO_3)_3$	1.402	40	7.91
7 [b)]	$Bi(NO_3)_3$	1.402	40	9.98
8 [c)]	AHM	8.33	40	208
9 [c)]	$VOSO_4$	2.08	40	52
10	H_2MoO_4	8.33	40	3.75
11	VO_2	2.08	40	0.33

[a)] Materials were added into water and stirred for 10 min. The solutions were filtered with membrane filter before ICP measurement. [b)] 0.85 mL of glycerol was added into 40 mL of water. [c)] AHM and $VOSO_4$ can be dissolved completely in this condition and theoretical values are shown.

Table 4. 3. Synthesis of POM-based microporous materials with different starting materials. [a)]

Entry	Mo source	V source	Bi source	Materials	Crystallite size (Å)
1 [b)]	AHM	$VOSO_4$	*$Bi(OH)_3$	Y	>1000
2	*H_2MoO_4	$VOSO_4$	$Bi(NO_3)_3$	Y	>1000
3	AHM	*VO_2	$Bi(NO_3)_3$	N	-
4	AHM	$VOSO_4$	*$Bi(OH)_3$	Y	>1000
5 [c)]	AHM	$VOSO_4$	$Bi(NO_3)_3$	Y	243
6	AHM	$VOSO_4$	$Bi(NO_3)_3$	Y	387

[a)] Synthesis conditions: 8.33 mmol of Mo source based on Mo, 2.08 mmol of V source, 1.4 mmol of Bi source, 40 mL of water, 448 K, 48 h, pH was adjusted to 3.4 by H_2SO_4 (1M), rotation (~1 rpm). The crystallite size of the material was calculated by Scherrer equation with MID Jade 7. [b)] AHM: 50 mmol based on Mo, V source: 12.5 mmol, Bi source: 1.67 mmol, 240 mL of water, the purification method was in experimental section. [c)] 0.85 mL of glycerol was added.

Chapter 5. Selective molecule adsorption in the polyoxometalate-based microporous materials

5.1. Introduction

Carbon dioxide separation is currently important in the viewpoint of industrial processes and environmental protection, which is rapidly developed in several decades. [1–4] Generally, there are two kinds of materials for carbon dioxide separation based on different separation mechanism. First type of materials for carbon dioxide adsorption is on the basis of chemisorption, such as calcium oxide and amine solution. [3] These materials can easily separate carbon dioxide from methane, but they possess significant disadvantages such as toxicity, corrosiveness, and high energy for regeneration. The second kinds of material for carbon dioxide separation, such as zeolites and metal-organic frameworks (MOFs), [1,2,4,5] based on physical-sorption are considered to have higher application potential because of environmentally friendly and economically feasible techniques.

The important property of POM-based microporous material is its high chemical composition diversity, which allows different kinds of elements to be incorporated in the material. There are four main sites in the materials, surrounding metal site, center metal site, linker site, and cation site (Figure 5. 1). The elements in all sites here can be altered, and the properties of the materials are easily tuned.

Herein, the author demonstrated the adsorption property of the materials. The materials of Mo–Zn oxide with different cations (NH_4^+ and Na^+) species were synthesized. The materials showed selective adsorption property for small molecules. Carbon dioxide and methane adsorption in the materials could be tuned by altering countercations from ammonium cation to sodium cation. Carbon dioxide separation efficiency could be remarkably enhanced by incorporating Na^+ in the material. Carbon dioxide-methane co-adsorption experiment showed that the materials were able to be used as a good material for molecule separation. For the first time, Na−Mo−Zn oxide was successfully used as a material for gas chromatographic separation of carbon dioxide and methane at 363 K.

5.2. Experimental

5.2.1. Adsorption experiments

The materials of Na−Mo−Zn oxide and NH_4−Mo−Zn oxide were evacuated before the measurement to form calcined Na−Mo−Zn oxide and NH_4−Mo−Zn oxide, denoted as Cal−Na−Mo−Zn oxide and Cal−NH_4−Mo−Zn oxide. All of the materials were evacuated at 473 K for 2.5 h before the measurement. Molecule (carbon dioxide, methane, ethane, and propane) adsorption was performed on the materials by a BELSORP MAX (BEL Japan Inc.) sorption analyzer at 278 K, 288 K, and 298 K.

5.2.2. Adsorption isotherm-based calculation

The mono-component adsorption isotherms of carbon dioxide and methane were fitted with dual-site Langmuir-Freundlich model, which gave the functions:

$$q = \frac{q_1 b_1 p^{n1}}{1 + b_1 p^{n1}} + \frac{q_2 b_2 p^{n2}}{1 + b_2 p^{n2}}$$

Here, q was adsorbed amount, and p was pressure. q_1, q_2, b_1, b_2, n_1, and n_2 were fitting parameters.

The adsorption enthalpy was calculated with Clausius-Clapeyron equation.

$$\frac{\mathrm{d}\ln p}{\mathrm{d}T} = \frac{\Delta H}{RT^2}$$

Here, p was pressure, T was temperature, and ΔH was adsorption enthalpy.

CO_2 selectivity was calculated with the following equation. [41]

$S_{CO_2} = (x_{CO_2}/y_{CO_2})/(x_{CH_4}/y_{CH_4})$

y_{CO_2}: mole fraction of component CO_2 in gas phase; y_{CH_4}: mole fraction of component CH_4 in gas phase; x_{CO_2}: mole fraction of component CO_2 in adsorbed phase; x_{CH_4}: mole fraction of component CH_4 in adsorbed phase

5.2.3. Gas chromatographic (GC) separation of carbon dioxide and methane

GC separation of a gas mixture of carbon dioxide and methane using a column packed with Cal−Na−Mo−Zn oxide was performed with a Shimadzu GC-8A system equipped with a thermal conductivity detector. Na−Mo−Zn oxide was well ground and screened with a mesh (aperture: 150 μm), and about 20 mL of Na−Mo−Zn oxide was densely packed into a column (length: 1m, inner diameter: 3 mm). The fresh column of Na−Mo−Zn oxide was treated at 473 K by introducing a carrier gas of nitrogen for 2.5 h to remove the original water in the material and open the micropores of the material. The gas mixture (carbon dioxide: methane = 1: 1) was injected, and the separation was carried out at 363 K.

5.3. Results and discussion

Mo–Zn oxide with ammonium cation and sodium cation, denoted as NH_4–Mo–Zn oxide and Na–Mo–Zn oxide, were synthesized for the investigation of molecule adsorption. Structure analysis of NH_4–Mo–Zn oxide and Na–Mo–Zn oxide was described in chapter 3. The structures of NH_4–Mo–Zn oxide and Na–Mo–Zn oxide were basically the same. The frameworks of both materials were comprised of the ε-Keggin POM of [ε-$ZnMo_{12}O_{40}$] and Zn^{II} ion linker. The difference of the oxides was the cation species. NH_4–Mo–Zn oxide had ammonium cation, and Na–Mo–Zn oxide had sodium cation. The structure information of the materials is listed in Table 5. 1. Changing countercation species in the structure was expected to have influence on the adsorption properties of the materials. After heat treatment at 473 K for 2.5 h, water and ammonia would desorb from NH_4–Mo–Zn oxide, and micropores of the material could be opened. Protons would be generated in the calcined material by removal of ammonia to make charge balance. In the case of Na–Mo–Zn oxide, sodium cation could not be removed by heat treatment and would retain in the calcined sample. The amount of sodium ions in the materials of Na–Mo–Zn oxide was less that the number of cages and channels in the materials, so the sodium ions would not block the aperture of the microspores of the materials.

5.3.1. General molecule adsorption

Microspores of Cal−Na–Mo–Zn oxide and Cal−NH_4–Mo–Zn oxide were opened by removal of occupied guest molecules with calcination under nitrogen gas without collapse of the structures (see chapter 3 for details). Nitrogen gas adsorption measurements at 77 K indicated that the materials were microporous materials with BET surface areas of 37 and 45 cm^3/g, respectively. The external surface area of the material was calculated with the t-plot method for Cal−Na–Mo–Zn oxide and Cal−NH_4–Mo–Zn oxide to be 27 and 35, respectively. BET surface area and external surface area of the materials were similar. See detailed information in chapter 3.

The adsorption properties of Cal−Na–Mo–Zn oxide and Cal−NH_4–Mo–Zn oxide were further studied by small molecule adsorption. It was found that the materials adsorbed different kinds of small molecules based on the size of the molecules. Figure 5. 2 displays the adsorption isotherms of methane, carbon dioxide, ethane, and propane in the materials at 298 K. The results indicated that the materials adsorbed small molecules of methane, carbon dioxide, and ethane, whereas a larger molecule of propane was not adsorbed by both materials. The author assumed that the size of the channel (3.4 Å) of the material was close to the size of atom (3.0 for oxygen and 3.4 for carbon). Therefore, straight molecules, such as methane, carbon dioxide, and ethane, of which the skeleton atoms distributed linearly, were adsorbed by the materials. A larger molecule (propane) with bent carbon skeleton could not be adsorbed in the materials.

For Cal−Na–Mo–Zn oxide, about 1.84 of carbon dioxide, 0.86 methane, and 1.04 ethane per one POM unit were adsorbed by the material. For Cal−NH_4–Mo–Zn oxide, about 1.44 carbon dioxide, 0.89 methane, and 0.99 ethane per one POM unit were adsorbed by the material (Table 5. 2). Pre-treatment was very important process to active the materials and open the micropores of the materials, although the occupied cations/molecules were difficult to be removed completely (see chapter 3 for details). However, some cations that blocked the micropores originally could be removed by

current pre-treatment process. Uncalcined sample of Cal−Na–Mo–Zn oxide showed very low adsorption capacity of carbon dioxide, which demonstrated that heat treatment was necessary for opening the micropores (Figure 5. 3).

5.3.2. Carbon dioxide and methane adsorption and separation

In the purpose of carbon dioxide separation from methane, the materials were expected to have remarkably different adsorption properties of carbon dioxide and methane. The author would like to use Cal−Na–Mo–Zn oxide and Cal−NH_4–Mo–Zn oxide for investigation of carbon dioxide and methane selective adsorption.

The isotherms of carbon dioxide for Cal−Na–Mo–Zn oxide and Cal−NH_4–Mo–Zn oxide were interesting (Figure 5. 2). Carbon dioxide uptake on both materials sharply increased at low pressure range (< 1 kPa), which indicated that both Mo–Zn oxides had strong interaction with carbon dioxide, and showed high carbon dioxide adsorption capacity (20~15 mL at 100 kPa). In the case of methane adsorption, methane uptake in low pressure range increased gently (10 mL at 100 kPa), indicating that the materials showed relative weak interaction with methane. Both Mo–Zn oxides could adsorb carbon dioxide at low pressure (< 1 kPa), whereas it cannot adsorb methane at so low pressure (< 1 kPa). This indicated that the materials can be used as for carbon dioxide capture from carbon dioxide-methane mixed gas.

The materials adsorbed both carbon dioxide and methane at room temperature. From the isotherms of carbon dioxide and methane, the materials seemed to adsorb more carbon dioxide than methane (Figure 5. 2a-d). Carbon dioxide and methane adsorption was performed on the materials of Cal−Na–Mo–Zn oxide and Cal−NH_4–Mo–Zn oxide at 278, 288, and 298 K (Figure 5. 4 - Figure5. 7). When adsorption temperature decreased, the adsorbed amount increased. The isotherms of carbon dioxide and methane were fitted with dual-site Langmuir-Freundlich model, and the fitting parameters were listed in Table 5. 3 - Table 5.7. The resulting R^2 values of the fitting processes were close to 1, indicating that simulated data by dual-site

Langmuir-Freundlich model was fit with experimental isotherms. The adsorbed amount dependent adsorption entropy was calculated with Clausius-Clapeyron equation, which is shown in Figure 5. 8. The adsorption heat of carbon dioxide and methane for Cal−Na–Mo–Zn oxide was calculated to be 46~65 kJ/mol and 18~30 kJ/mol, respectively. The adsorption heat of carbon dioxide and methane on Cal−NH_4–Mo–Zn oxide was calculated to be 35~45 kJ/mol and 25~30 kJ/mol, respectively. The adsorption heat of carbon dioxide for both materials was higher than that of methane for them. The results of adsorption heat calculation indicated that the materials strongly interacted with carbon dioxide while weakly interacted with methane.

Interestingly, it was noticed that carbon dioxide adsorption property of Cal−Na–Mo–Zn oxide and Cal−NH_4–Mo–Zn oxide was very different. In the case of carbon dioxide adsorption, Cal−Na–Mo–Zn oxide revealed much higher adsorption capacity than that of Cal−NH_4–Mo–Zn oxide at low pressure (< 1 kPa), which was ascribed to the adsorption in micropores of the materials (Figure 5. 2a, b). Thus, introduction of sodium in the materials promoted the carbon dioxide adsorption of the materials. On the other hand, the materials of Cal−Na–Mo–Zn oxide and Cal−NH_4–Mo–Zn oxide adsorbed methane molecule. It was found that the adsorption behavior were very similar. For both Mo–Zn oxides, 10 cm^3/g of gas molecule could be adsorbed. Sodium ion did not affect the adsorption of methane in the materials.

With consideration of the structures of Cal−Na–Mo–Zn oxide and Cal−NH_4–Mo–Zn oxide, it was found that the difference between these two materials was cation species. Adsorption entropy of carbon dioxide (Figure 5. 8) for Cal−Na–Mo–Zn oxide (46~65 kJ/mol) appeared higher than that for NH_4–Mo–Zn oxide (35~45 kJ/mol), indicating that Na^+ in the material enhanced interaction of carbon dioxide with the frameworks. In the case of methane adsorption, adsorption heat of Na–Mo–Zn oxide (18~30 kJ/mol) and Cal−NH_4–Mo–Zn oxide (25~30 kJ/mol) were almost the same, which suggested that cation species would not affect the adsorption of methane.

5.5.3. Monte Carlo simulation

A primitive cell of Cal–Na–Mo–Zn oxide contained 2 POM units of [$ZnMo_{12}O_{40}$] with 2 cages, 23 protons and 3 Na ions. Assuming that Na ions were located in two cages of the material, one cage contains two Na ions (cage A) and another cage contains the rest one Na (cage B) (Figure 5. 9a). Monte Carlo simulation was performed on Cal–Na–Mo–Zn oxide to estimate affinity of CO_2 with Na^+ ions. CO_2 was loaded one by one during the simulation. It was found that the first CO_2 was located in cage A, and the second CO_2 was located in cage B (Figure 5. 9b and c). Cage A contained more Na, indicating CO_2 interacted with sodium strongly. Adsorption energy estimated by Monte Carlo simulation for O_2 in cage A (Figure 5. 9b) and CO_2 in cage B (Figure 5. 9 c) were 53 and 41 kJ/mol, which was similar to the trend of adsorption enthalpy of CO_2 in the material, indicating that the proposed adsorbed structure was correct. In the case of CH_4, CH_4 was firstly filled in cage B, which was because cage B had more space, and CH_4 had weak electrostatic interaction with Na ion (Figure 5. 9d and e). Adsorption energy from Monte Carlo simulation for CH_4 in both sites are the same of 24 kJ/mol, which also indicated CH_4 would not interacted with Na ion.

5.3.4. Separation experiment

The CO_2 is widely existed gas in landfill gas. CO_2 selective adsorption from CO_2/CH_4 mixture is of great importance for improvement of the gas quality. Co-adsorption experiments were carried out on Cal−Na–Mo–Zn oxide and Cal−NH_4–Mo–Zn oxide under both high (125.2 and 127.5 kPa of equilibrium total pressures) and low pressure (1.5 and 1.6 kPa of equilibrium total pressures) at 298 K. The initial ratio of CO_2 and CH_4 was 40: 60. According to the individual adsorption isotherms, under low pressure range, the materials might show high separation efficiency of CO_2.

Equilibrium total pressure, total adsorbed amount, CO_2 and CH_4 partial pressure,

and CO_2 and CH_4 adsorbed amount were presented in Figure 5. 10. In high pressure condition, both materials adsorbed more CO_2 than CH_4. When the materials continued to be left under mixed gas pressure, they further adsorbed CO_2, while CH_4 desorbed from the material (Figure 5. 10a,c), supporting that adsorbed CH_4 was partly replaced by CO_2. Moreover, Cal–Na–Mo–Zn oxide (14 cm^3/g at the fifth co-adsorption equilibrium) tended to adsorb more CO_2 compared with Cal–NH_4–Mo–Zn oxide (10 cm^3/g at the fifth co-adsorption equilibrium). In low pressure condition, both materials adsorbed similar amount of CO_2 and CH_4. With prolonging the adsorption process, Cal–Na–Mo–Zn oxide further adsorbed CO_2 and concurrently desorbed CH_4, while Cal–NH_4–Mo–Zn oxide adsorbed both CH_4 and CO_2 (Figure 5. 10b,d).

CO_2 selectivity of final equilibrium (5th data in Table 5. 7) for the material was calculated and summarized in Table 5. 1. Both oxides showed high selectivity of CO_2 under low pressure range compared with adsorption under high pressure. Cal–Na–Mo–Zn oxide showed higher selectivity of CO_2 adsorption than that of Cal–NH_4–Mo–Zn oxide under both high and low pressure. Co-adsorption experiments demonstrated that Cal–Na–Mo–Zn oxide had better performance of CO_2 adsorption than Cal–NH_4–Mo–Zn oxide.

Furthermore, Na–Mo–Zn oxide was successfully applied to gas chromatographic separation of CO_2 from CO_2/CH_4 mixture. The gas mixture (CO_2: CH_4 = 1: 1) was injected into a gas chromatograph equipped with a column filled with Na–Mo–Zn oxide. As shown in Figure 5. 11, CH_4 and CO_2 were separated within a few minutes at 363 K. The peak of CO_2 appeared slower and was broader than that of CH_4, indicating that the material had stronger interaction with CO_2 than with CH_4.

5.4. Conclusion

The materials of Cal−Na–Mo–Zn oxide and Cal−NH_4–Mo–Zn oxide could adsorb small molecules including carbon dioxide, ethane and methane. Both oxides selectively adsorbed carbon dioxide from the carbon dioxide/methane mixture, because the

materials showed high adsorption capacity of carbon dioxide than that of methane. Cal−Na–Mo–Zn oxide showed stronger interaction with carbon dioxide than NH_4–Mo–Zn oxide, while for methane, both oxides showed similar interaction. Co-adsorption experiment showed that selectivity of carbon dioxide in Cal−Na–Mo–Zn oxide was higher than that on Cal−NH_4–Mo–Zn oxide. Cal−Na–Mo–Zn oxide was unitized as a material for GC separation of carbon dioxide and methane.

References

(1) Sumida, K.; Rogow, D. L.; Mason, J. A; McDonald, T. M.; Bloch, E. D.; Herm, Z. R.; Bae, T.-H.; Long, J. R. *Chem. Rev.* **2012**, *112*, 724–81.

(2) Férey, G.; Serre, C.; Devic, T.; Maurin, G.; Jobic, H.; Llewellyn, P. L.; De Weireld, G.; Vimont, A.; Daturi, M.; Chang, J.-S. *Chem. Soc. Rev.* **2011**, *40*, 550–62.

(3) Kierzkowska, A. M.; Pacciani, R.; Müller, C. R. *ChemSusChem* **2013**, *6*, 1130–48.

(4) Li, J.-R.; Ma, Y.; McCarthy, M. C.; Sculley, J.; Yu, J.; Jeong, H.-K.; Balbuena, P. B.; Zhou, H.-C. *Coord. Chem. Rev.* **2011**, *255*, 1791–1823.

(5) Wickramaratne, N. P.; Jaroniec, M. *ACS Appl. Mater. Interfaces* **2013**, *5*, 1849–55.

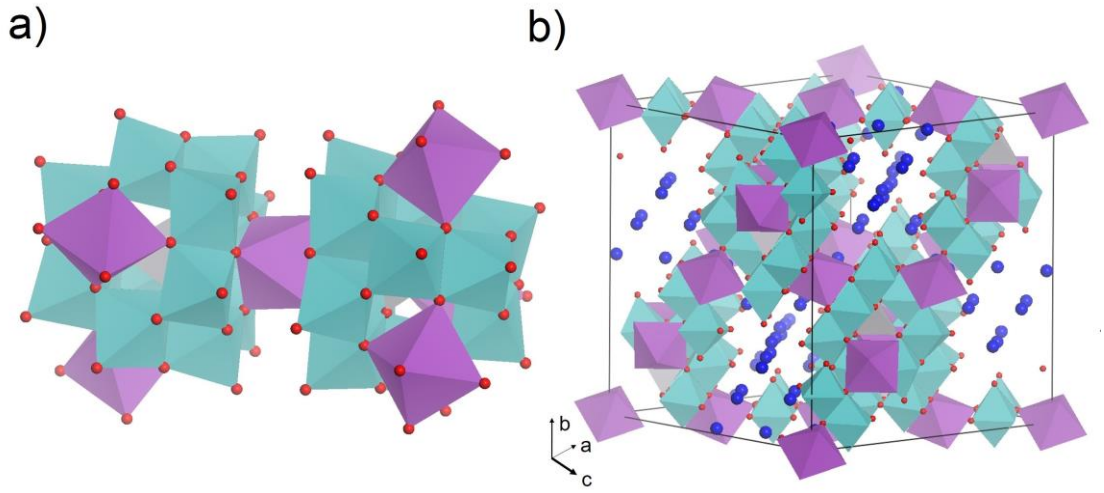

Figure 5. 1. Polyhedral representations of a) ε-Keggin units and their connection and b) unit cell of Mo–V–Bi oxide, $Mo(V)O_6$ octahedron (blue octahedron), VO_4 tetrahedron (gray tetrahedron), BiO_6 octahedron (purple octahedron), cation or water (deep blue sphere), and O (red sphere).

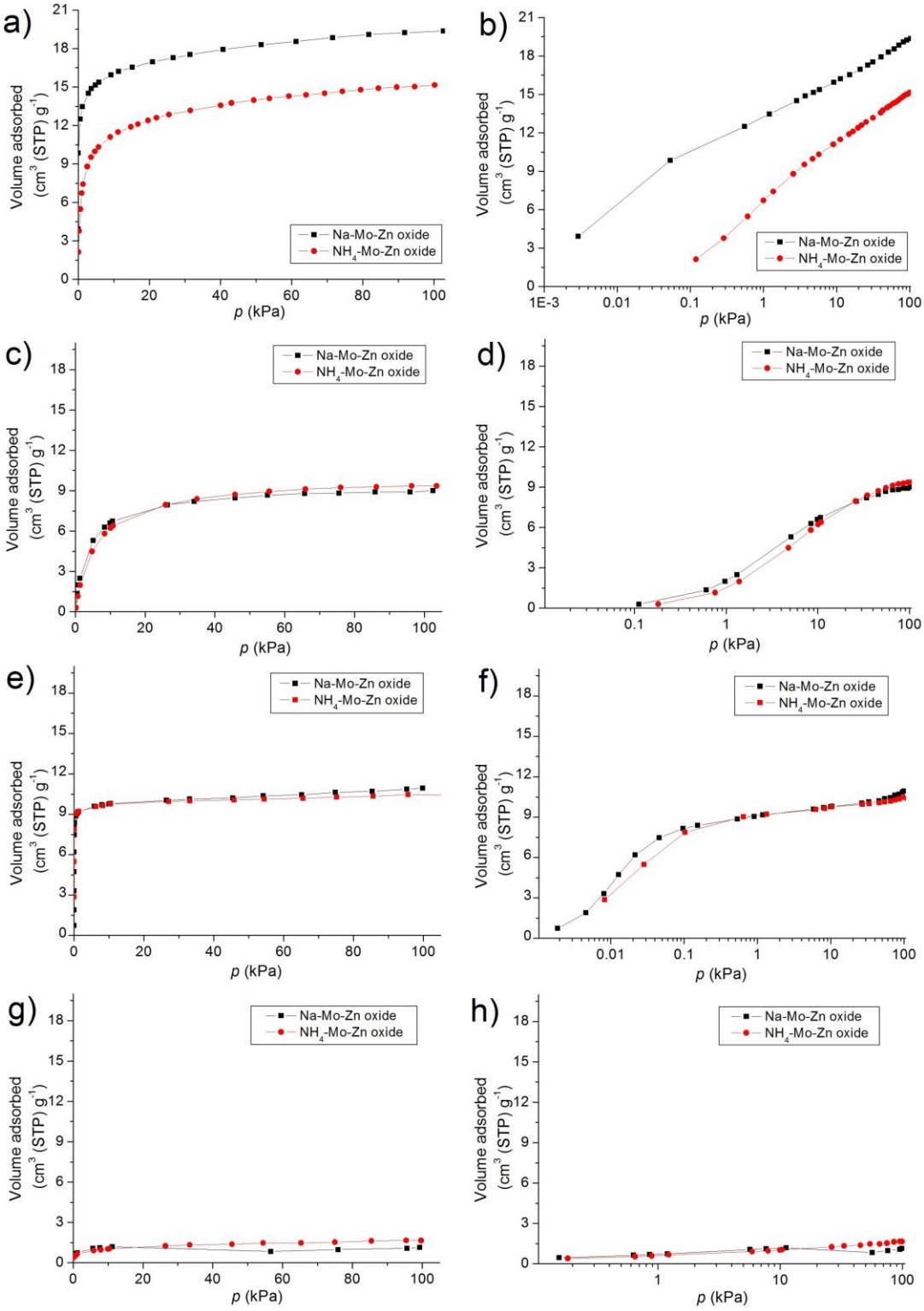

Figure 5. 2. Molecule adsorption isotherms of a) carbon dioxide, b) carbon dioxide (low pressure), c) methane, d) methane (low pressure), e) ethane, f) ethane (low pressure), g) propane, and h) propane (low pressure) for different materials.

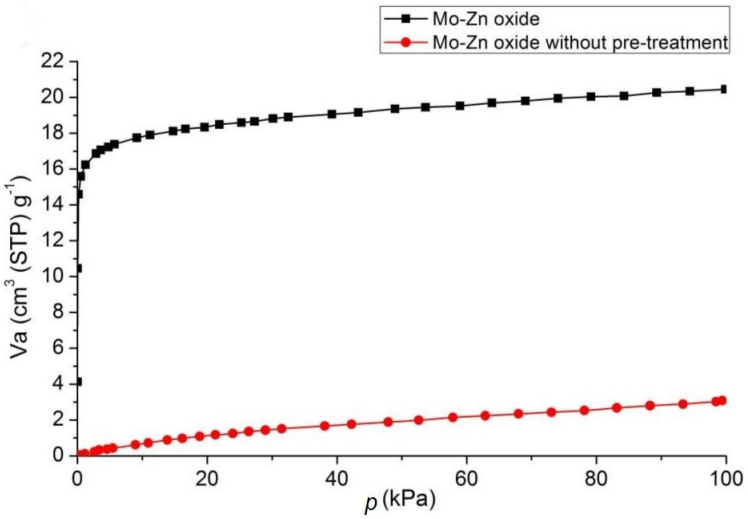

Figure 5. 3. Adsorption isotherms of Na–Mo–Zn oxide with and without pre-treatment.

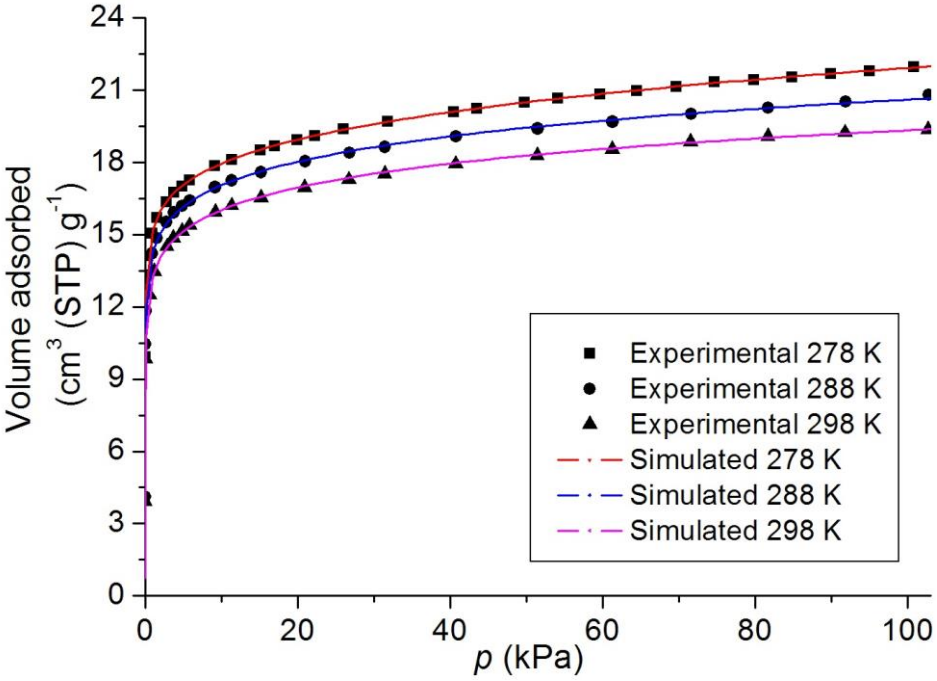

Figure 5. 4. Carbon dioxide adsorption in Na–Mo–Zn oxide at different temperatures and Langmuir-Freundlich fitting.

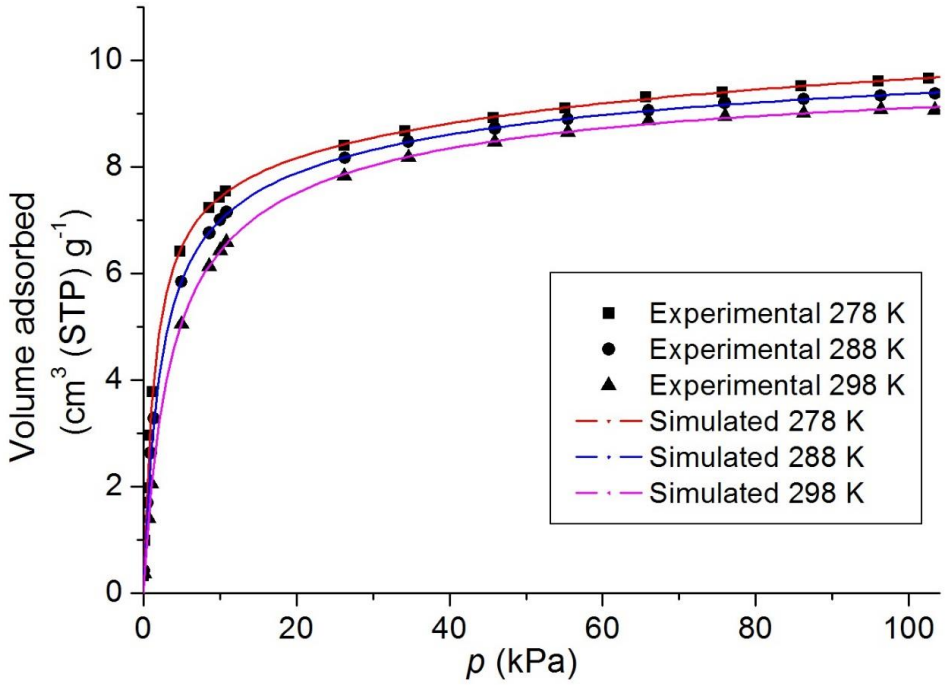

Figure 5. 5. Methane adsorption in Na–Mo–Zn oxide at different temperatures and Langmuir-Freundlich fitting.

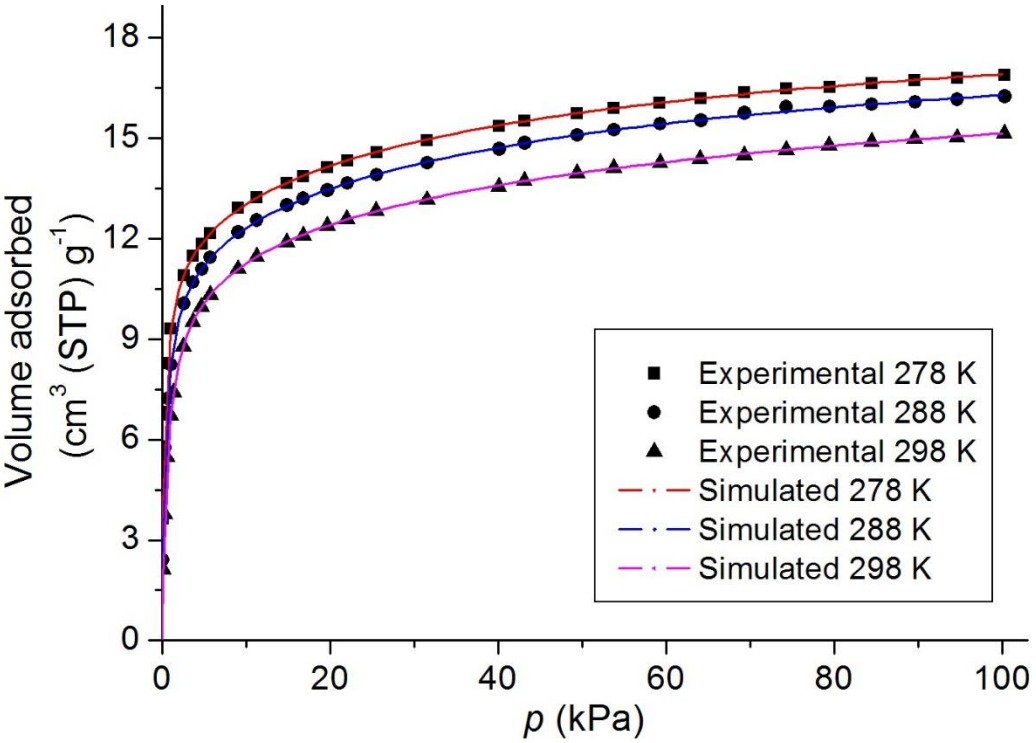

Figure 5. 6. Carbon dioxide adsorption in NH_4–Mo–Zn oxide at different temperatures and Langmuir-Freundlich fitting.

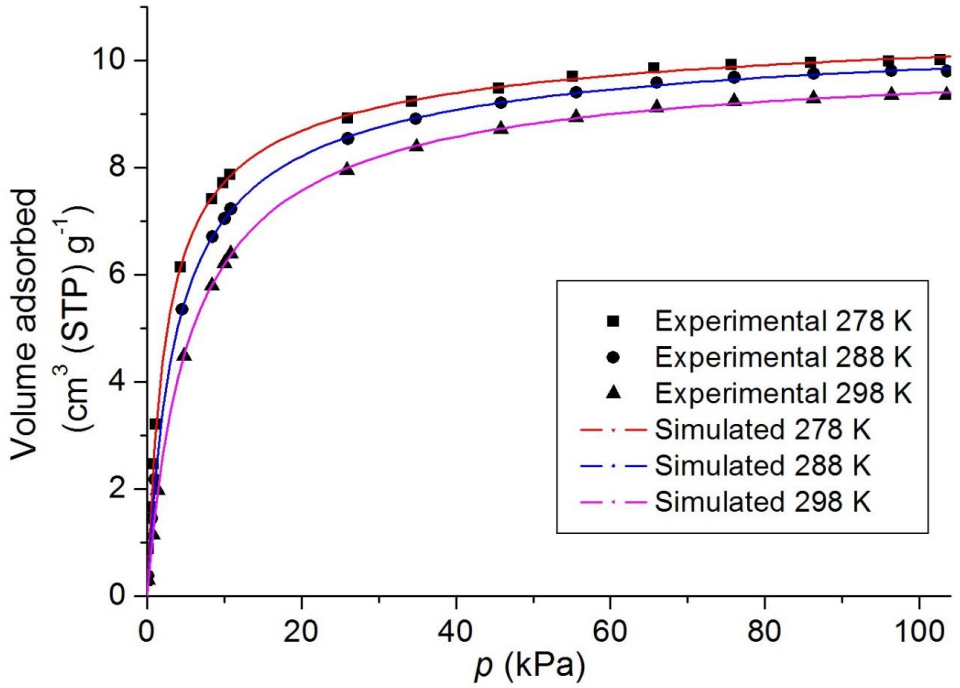

Figure 5. 7. Methane adsorption in NH_4–Mo–Zn oxide at different temperatures and Langmuir-Freundlich fitting.

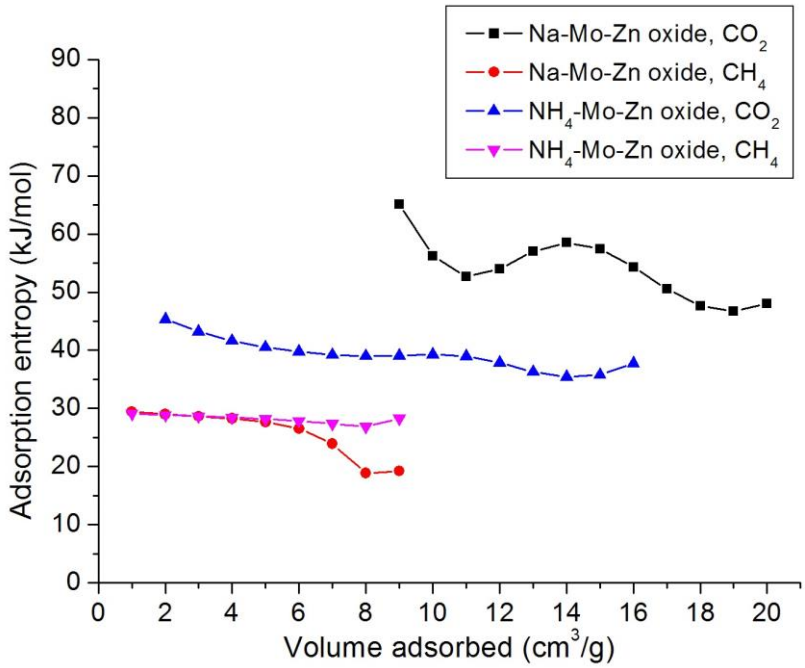

Figure 5. 8. Adsorption enthalpy of carbon dioxide and methane calculated with the Clausius-Clapeyron equation.

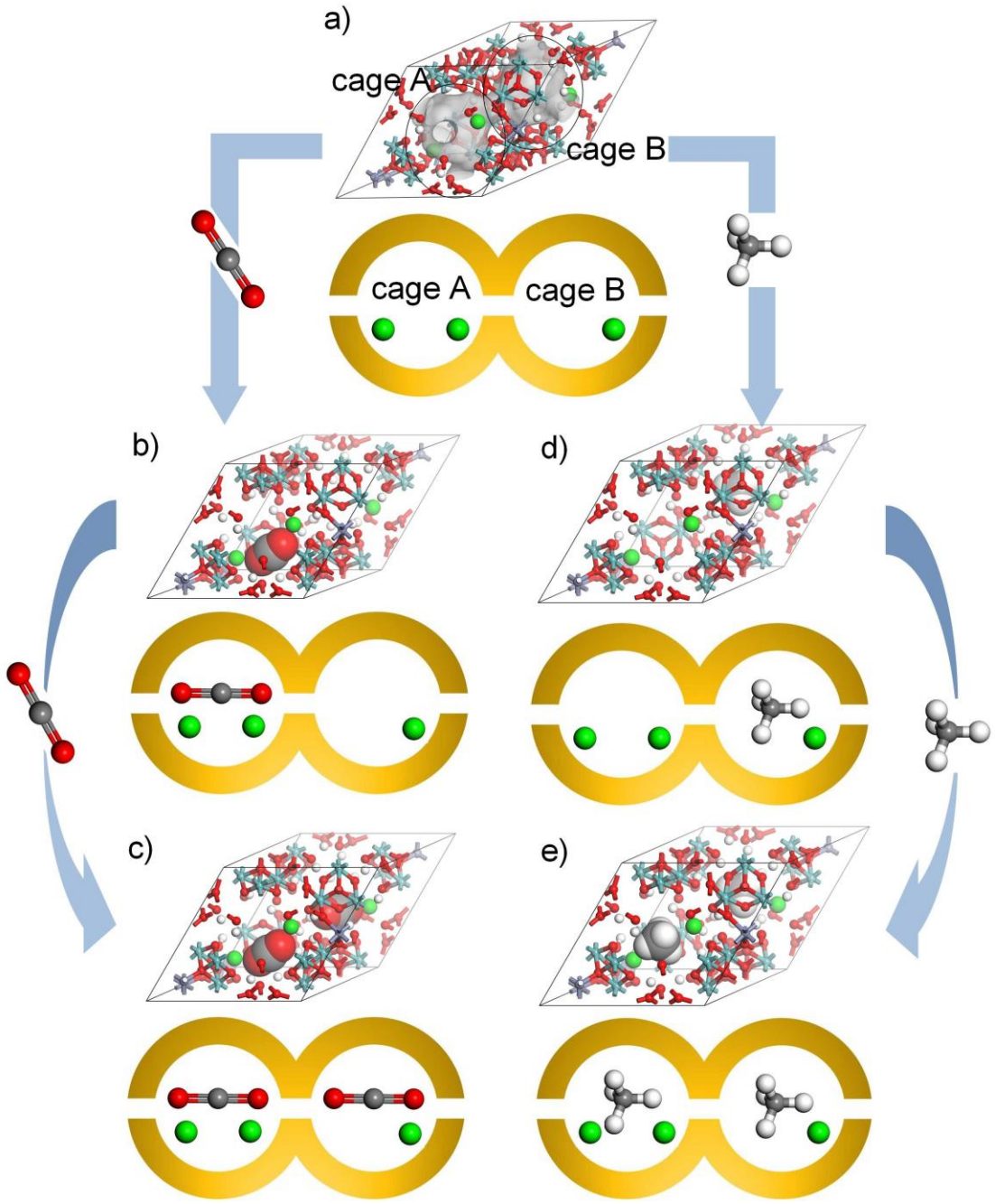

Figure 5. 9. Representations of adsorbed structures of Na–Mo–Zn oxide from Monte Carlo simulation, up: ball-and-stick representations, down: schematic representations. a) primitive cell with cage A and cage B, b) Na–Mo–Zn oxide adsorbed first CO_2, c) Na–Mo–Zn oxide adsorbed second CO_2, d) Na–Mo–Zn oxide adsorbed first CH_4, and e) Na–Mo–Zn oxide adsorbed second CH_4, blue sphere: Mo, purple sphere: Zn, red sphere: O, white sphere: H, black sphere: C, and green sphere: Na.

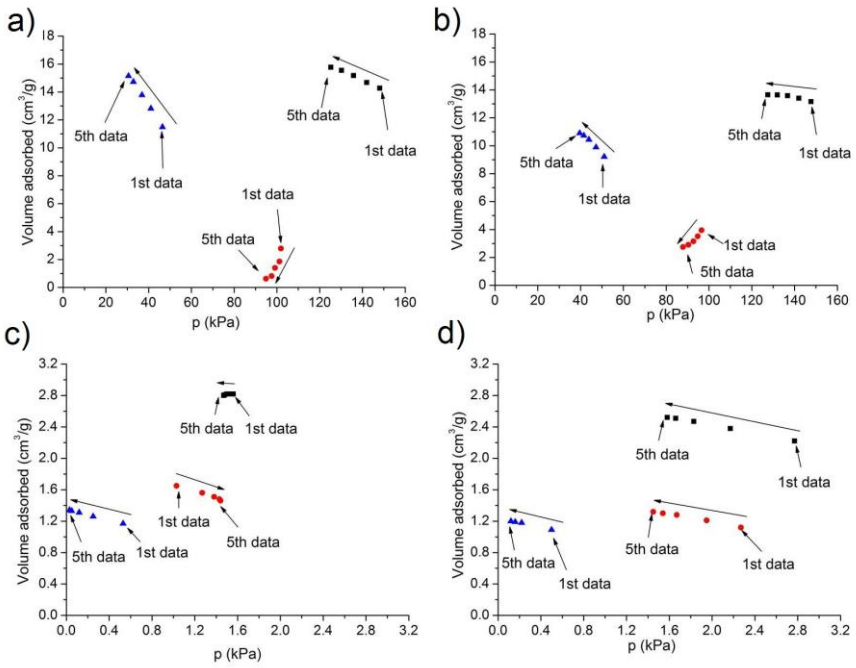

Figure 5. 10. CO_2/CH_4 co-adsorption results of a) Na–Mo–Zn oxide at high pressure b) Na–Mo–Zn oxide at low pressure, c) NH_4–Mo–Zn oxide at high pressure, and d) NH_4–Mo–Zn oxide at low pressure, black square: system total pressure (x-aixs) and adsorbed amount (y-axis), red cycle: CH_4 partial pressure (x-axis) and adsorbed amount (y-aixs), blue triangle: CO_2 partial pressure (x-axis) and adsorbed amount (y-axis).

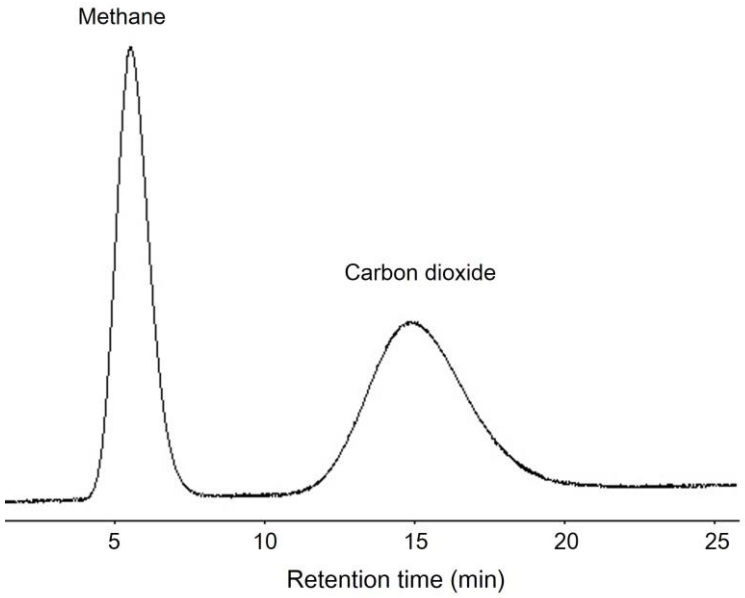

Figure 5. 11. Gas chromatograms of gas mixture of carbon dioxide and methane separated on a column of Na–Mo–Zn oxide.

Table 5. 1. The detailed structure information of Na–Mo–Zn oxide and NH_4–Mo–Zn oxide.

	Na–Mo–Zn oxide	NH_4–Mo–Zn oxide
a (Å)	19.4675	19.4533
α (°)	90	90
Crystal system	Cubic	Cubic
Space group	$Fd\bar{3}m$	$Fd\bar{3}m$
POM unit	$ZnMo_{12}O_{40}$	$ZnMo_{12}O_{40}$
Linker ions	Zn	Zn
Central ions	Zn	Zn
Surrounding sites	Mo	Mo
Cations	Na^+	NH_4^+
Formula	$Na_{1.5}H_{10.5}[ZnMo_{12}O_{40}\{Zn_2\}]$	$Na_{1.5}H_{10.5}[ZnMo_{12}O_{40}\{Zn_2\}]$

Table 5. 2. The numbers of small molecules per one POM unit adsorbed in the materials.

	POM unit	CO_2	CH_4	C_2H_6	C_3H_8
Na–Mo–Zn oxide	$ZnMo_{12}O_{40}$	1.84	0.86	1.04	0.11
NH_4–Mo–Zn oxide	$ZnMo_{12}O_{40}$	1.44	0.89	0.99	0.16

Table 5. 3. Langmuir-Freundlich fitting parameters of carbon dioxide adsorption in Na–Mo–Zn oxide at different temperature.

	278 K	288 K	298K
q1	20.80056	8.68786	7.07908
b1	2.51436	61.15111	107.04572
n1	0.22578	0.7852	1
q2	18.5472	53.50337	32.73628
b2	0.01685	0.12043	0.23647
n2	0.58338	0.18823	0.20134
R^2	0.99997	0.99958	0.99975

Table 5. 4. Langmuir-Freundlich fitting parameters of methane adsorption in Na–Mo–Zn oxide at different temperature.

	278 K	288 K	298K
q1	8.15089	8.00455	7.85594
b1	0.71534	0.48415	0.31888
n1	0.98438	1	1
q2	2.99718	2.38219	2.02925
b2	0.01172	0.01794	0.02742
n2	0.99998	1	1
R^2	0.99998	0.99997	0.99991

Table 5. 5. Langmuir-Freundlich fitting parameters of carbon dioxide adsorption in NH_4–Mo–Zn oxide at different temperature.

	278 K	288 K	298K
q1	11.69525	11.4436	8.87547
b1	3.01139	2.16161	0.0501
n1	0.76212	0.82124	0.70284
q2	8.32908	7.72081	10.29691
b2	0.05374	0.03957	1.56268
n2	0.76015	0.82922	0.86657
R^2	0.99994	0.99988	0.99997

Table 5. 6. Langmuir-Freundlich fitting parameters of methane adsorption in NH_4–Mo–Zn oxide at different temperature.

	278 K	288 K	298K
q1	1.29993	1.62354	8.69241
b1	0.04517	0.02378	0.45642
n1	0.92089	0.99907	1
q2	8.82744	8.97993	2.36074
b2	0.19609	0.29819	0.06047
n2	0.99951	1	0.74746
R^2	0.99989	0.99993	0.99994

Table 5. 7. Carbon dioxide and methane co-adsorption in Na–Mo–Zn oxide and NH_4–Mo–Zn oxide.

Entry	Material	Total pressure (p_e) (kPa)	Ratio in gas phase (%)		Ratio in adsorbed phase (%)		Sel.
			CO_2	CH_4	CO_2	CH_4	
1	Na–Mo–Zn oxide	1.5	1.7	98.3	47.4	52.6	52
2	Na–Mo–Zn oxide	125.2	24.4	75.6	96.0	4.0	75
3	NH_4–Mo–Zn oxide	1.6	7.8	92.2	47.7	52.3	11
4	NH_4–Mo–Zn oxide	127.5	31.0	69.0	79.8	20.2	9

Chapter 6. Ion-exchange property and catalytic activity of polyoxometalate-based microporous complex metal oxides

6.1. Introduction

The ε-Keggin POM-based 3D frameworks offer one advantage that their chemical composition can be easily changed without collapse of their basic structures. The countercation in the materials can be easily replaced by other cation species in aqueous solution, as zeolites do. Properties of the materials are expected to be tuned by changing chemical compositions of the materials.

In this chapter, the author demonstrated the ion-exchange property of the materials of Mo–V–Bi oxide, Na–Mo–Zn oxide, and NH_4–Mo–Mn oxide. The materials after ion-exchange process were characterized with powder XRD, FT-IR, TPD, and elemental analysis, which illustrated that the original cations could be successfully exchanged with other cations. The position of exchanged cation (K^+) in K–Mo–V–Bi oxide was determined with single crystal analysis, while cations (Rb^+) in Rb–Mo–Zn oxide and Rb–Mo–Mn oxide were determined with Rietveld refinement. It was found that the micropores of Mo–V–Bi oxide were blocked after replacement of the original ammonium cation with K^+.

6.2. Experimental

6.2.1. Ion-exchange

Preparation details of Mo–V–Bi oxide, Na–Mo–Zn oxide, and NH_4–Mo–Mn oxide were in chapter 2 and chapter 3.

As-synthesized Mo–V–Bi oxide, Na–Mo–Zn oxide, and NH_4–Mo–Mn oxide (0.3 g) was dispersed in 15 mL of water that contained KCl (0.0455 g), LiCl (0.0259 g), NaCl (0.0367 g), RbCl (0.074 g) or CsCl (0.103 g). The mixture was stirred at 353 K for 6 h. The resulting solids were collected by filtration, washed with water (3 × 10 mL), and dried at 353 K overnight. To get proton-exchange samples, 0.5 mL of HCl (36%) was dissolved in 14.5 mL of water, and 0.3 g of Mo–V–Bi oxide, Na–Mo–Zn oxide, and NH_4–Mo–Mn oxide was added to the solution. The mixture was stirred for 6 h at 353 K. The solids were recovered by filtration, washed with water (3 × 10 mL), and dried at

353 K overnight. The ion-exchanged materials were designated as M–Mo–V–Bi oxide, M–Mo–Zn oxide, and M–Mo–Mn oxide (M = H, Li, Na, K, Rb, or Cs).

To obtain a large crystal of K–Mo–V–Bi oxide for single crystal analysis, the large crystal of as-synthesized Mo–V–Bi oxide (50 mg) was dispersed in 2.5 mL of water followed by addition of KCl (7.6 mg). The mixture was heated at 353 K for 6 h. The solid was recovered by centrifugation, washed with water three times, and dried at 353 K overnight.

Elemental Analysis:

H–Mo–V–Bi oxide Calcd for $Bi_2Mo_{9.4}V_{3.6}N_{2.1}O_{47.2}H_{24.4}$. Bi, 18.08; Mo, 39.00; V, 7.93; N, 1.27; H, 1.06, Found: Bi, 18.13; Mo, 39.11; V, 7.54; N, 1.29; H, 0.98.

Li–Mo–V–Bi oxide Calcd for $Li_{0.2}Bi_2Mo_{9.4}V_{3.6}N_{2.6}O_{47.2}H_{25.7.}$ Bi, 18.00; Mo, 38.84; V, 7.90; Li, 0.06; N, 1.57; H, 1.11, Found: Bi, 18.55; Mo, 38.41; V, 7.68; Li, 0.05; N, 1.48; H, 0.94.

Na–Mo–V–Bi oxide Calcd for $Na_{0.6}Bi_2Mo_{9.4}V_{3.6}N_{2.2}O_{47.2}H_{24.1}$. Bi, 17.96; Mo, 38.75; V, 7.88; Na, 0.59; N, 1.32; H, 1.04, Found: Bi, 18.51; Mo, 38.69; V, 7.44; Na, 0.58; N, 1.05; H, 0.86.

K–Mo–V–Bi oxide Calcd for $K_{1.9}Bi_2Mo_{9.4}V_{3.6}N_{0.9}O_{46.1}H_{16.5}$: Bi, 17.83; Mo, 38.47; V, 7.82 K, 3.17; N, 0.54; H, 0.70, Found: Bi, 18.03; Mo, 38.27; V, 7.42; K 3.15; N, 0.42; H, 0.67.

Rb–Mo–V–Bi oxide Calcd for $Rb_{2.1}Bi_2Mo_{9.4}V_{3.6}N_{0.7}O_{47.2}H_{18.1}$: Bi, 16.95; Mo, 36.58; V, 7.44; Rb, 7.28; N, 0.40; H, 0.73, Found: Bi, 16.58; Mo, 37.21; V, 7.52; Rb 7.12; N, 0.20; H, 0.53.

Cs–Mo–V–Bi oxide Calcd for $Cs_2Bi_2Mo_{9.4}V_{3.6}N_{0.8}O_{47.2}H_{18.5}$. Bi, 16.36; Mo, 35.31; V, 7.18; Cs, 10.41; N, 0.44; H, 0.73, Found: Bi, 16.81; Mo, 34.97; V, 6.89; Cs, 10.49; N, 0.21; H, 0.57.

H–Mo–Zn oxide, Calcd for $Na_{0.6}Zn_3Mo_{12}O_{45}H_{22.3}$: Zn, 9.32; Mo, 54.73; Na, 0.66; H, 1.07. Found: Zn, 9.18; Mo, 54.98; Na, 0.67; H, 1.38.

Li–Mo–Zn oxide, Calcd for $Li_{0.7}Na_{0.8}Zn_3Mo_{12}O_{45}H_{21.4}$: Li, 0.23; Zn, 9.29; Mo, 54.51; Na, 0.87; H, 1.15. found: Li, 0.07; Zn, 9.19; Mo, 54.88; Na, 0.72; H, 1.19.

NH_4–Mo–Zn oxide, Calcd for $Na_{0.1}N_{1.4}Zn_3Mo_{12}O_{45}H_{27}$: Na, 0.11; Zn, 9.27; Mo, 54.40; N, 0.93; H, 1.29. found: Na, 0.08; Zn, 9.32; Mo, 54.37; N, 1.19; H, 1.45.

K–Mo–Zn oxide, Calcd for $K_{1.4}Na_{0.1}Zn_3Mo_{12}O_{45}H_{21.4}$: K, 2.55; Zn, 9.14; Mo, 53.65; Na, 0.11; H, 1.01. found: K, 2.31; Zn, 9.26; Mo, 53.43; Na, 0.07; H, 1.16.

Rb–Mo–Zn oxide, Calcd for $Rb_{1.3}Na_{0.2}Zn_3Mo_{12}O_{45}H_{21.4}$: Rb, 5.04; Zn, 8.90; Mo, 52.22; Na, 0.21; H, 0.98. found: Rb, 5.02; Zn, 8.93; Mo, 52.02; Na, 0.07; H, 1.10.

Cs–Mo–Zn oxide, Calcd for $Cs_{1.5}Zn_3Mo_{12}O_{45}H_{21.4}$: Cs, 8.71; Zn, 8.57; Mo, 50.31; Na, 0; H, 0.94. found: Cs, 8.73; Zn, 8.67; Mo, 50.47; Na, 0; H, 1.01.

H–Mo–Mn oxide, Calcd for $N_{1.7}Mn_{2.2}Mo_{12}O_{43}H_{20.7}$: Mn, 6.03; Mo, 57.43; N, 1.19; H, 1.04. Found: Mn, 5.78; Mo, 57.75; N, 0.95; H, 1.47.

Li–Mo–Mn oxide, Calcd for $Li_{0.1}N_{2.0}Mn_{2.2}Mo_{12}O_{43}H_{21.5}$: Li, 0.03; Mn, 6.01; Mo, 57.26; N, 1.39; H, 1.08. found: Li, 0.04; Mn, 6.12; Mo, 57.15; N, 1.28; H, 1.47.

Na–Mo–Mn oxide, Calcd for $Na_{0.4}N_{1.7}Mn_{2.2}Mo_{12}O_{43}H_{20.3}$: Na, 0.46; Mn, 6.00; Mo, 57.18; N, 1.18; H, 1.02. found: Na, 0.52; Mn, 5.89; Mo, 56.99; N, 1.20; H, 1.38.

K–Mo–Mn oxide, Calcd for $K_{1.4}N_{0.7}Mn_{2.2}Mo_{12}O_{43}H_{16.3}$: K, 2.68; Mn, 5.92; Mo, 56.41; N, 0.48; H, 0.80. found: K, 2.63; Mn, 6.37; Mo, 56.53; N, 0.38; H, 1.16.

Rb–Mo–Mn oxide, Calcd for $Rb_{1.5}N_{0.6}Mn_{2.2}Mo_{12}O_{43}H_{15.9}$: Rb, 6.07; Mn, 5.72; Mo, 54.49; N, 0.40; H, 0.76. found: Rb, 6.03; Mn, 5.81; Mo, 54.55; N, 0.12; H, 1.07.

Cs–Mo–Mn oxide, Calcd for $Cs_{1.4}N_{0.7}Mn_{2.2}Mo_{12}O_{44}H_{18.3}$: Cs, 8.49; Mn, 5.52; Mo, 52.56; N, 0.45; H, 0.84. found: Cs, 8.65; Mn, 5.44; Mo, 52.65; N, 0.17; H, 1.08.

6.2.2. Single crystal analysis of K–Mo–V–Bi oxide

Since the crystals that had been grown were still too small for the diffractometer in the laboratory system, data collection was performed on a high-precision diffractometer installed in the SPring-8 BL40XU beamline. [1,2] The synchrotron radiation emitted from helical undulator was monochromated by using a Si(111) channel cut monochromator

and focused with a Fresnel zone plate. A Rigaku Saturn724 CCD detector was used. The measurement was performed at 100 (2) K. An empirical absorption correction based on Fourier series approximation was applied. The data were corrected for Lorentz and polarization effects. The structure was solved by direct methods and refined by full-matrix least-squares (SHELX-97), [3] where the unweighted and weighted agreement factors of $R = \Sigma||F_o| - |F_c||/\Sigma|F_o|$ ($I > 2.00\sigma(I)$) and $wR = [\Sigma w(Fo^2 - Fc^2)^2/\Sigma w(Fo^2)^2]^{1/2}$, respectively, were used. Position of K in the structure of K–Mo–V–Bi oxide was determined from differential Fourier map. Nitrogen atoms of ammonium cations were modeled as oxygen atoms because nitrogen atoms could not be distinguished from oxygen atoms. Oxygen atoms of water in Mo–V–Bi oxide were refined isotropically, and other atoms were refined anisotropically. The sample for elemental analysis may contain surface waters. Anisotropic displacement ellipsoids were presented in Figure 6. 1. The atom position, occupancy, and bond length were listed in Table 6. 1 and Table 6. 2.

6.2.3. Characterization

Nitrogen gas adsorption isotherms were obtained by a BELSORP MAX (BEL Japan Inc.) sorption analyzer at 77 K. Surface area was calculated with the BET method. The materials were evacuated at 573 K for 2.5 h before measurement. Powder X-ray diffraction (XRD) patterns were obtained on RINT2200 (Rigaku) with Cu Kα radiation (tube voltage: 40 kV, tube current: 20 mA). Fourier transform infrared (FT-IR) analysis was carried out on PARAGON 1000, Perkin Elmer. A TPD apparatus (BEL Japan, Inc.) equipped with a quadrupole mass spectrometer (M-100QA; Anelva) was used to detect NH_3 (m/z = 16) and H_2O (m/z = 18). For TPD-MS measurements of the materials after heat treatment, the samples were heated at 473 K under high vacuum for 2.5 h in TPD instrument before the measurements. Elemental compositions were determined by an inductive coupling plasma (ICP-AES) method (ICPE-9000, Shimadzu). CHN elemental composition was determined at Instrumental Analysis Division, Equipment Management Center, Creative Research Institution, Hokkaido University.

6.3. Results and discussion

6.3.1. Ion-exchange property of Mo–V–Bi oxide

The ammonium cation in the micropores of Mo–V–Bi oxide was exchangeable with other cations in aqueous solution, such as H^+, Li^+, Na^+, K^+, Rb^+, and Cs^+. The powder XRD patterns and FT-IR spectra showed that the basic structure of ion-exchanged Mo–V–Bi oxide did not change (Figure 6. 2 and Figure 6. 3). In chapter 2, we demonstrated that there were two different ammonium cations in Mo–V–Bi oxide. Weakly bound ammonium cation desorbed at low temperature, denoted as NH_4^+(W), and strongly bound ammonium cation desorbed at high temperature, denoted as NH_4^+(S). Table 6. 3 summarizes the formulas and amounts of NH_4^+(S) and NH_4^+(W) after ion-exchange estimated by elemental analysis and TPD, respectively. Moreover, TPD profiles (*m*/z = 16 for NH_3) of exchanged Mo–V–Bi oxide indicated that small cations such as H^+, Li^+, and Na^+ selectively replaced the weakly bound ammonium cation NH_4^+(W), whereas large K^+, Rb^+, and Cs^+ cations selectively replaced the strongly bound ammonium cation NH_4^+(S) (Figure 6. 4).

In K–Mo–V–Bi oxide, in which only NH_4^+(S) was exchanged, ca. 1.9 NH_4^+ per one ε-$VMo_{9.4}V_{2.6}O_{40}$ building block were exchanged with K^+. In the case of H–Mo–V–Bi oxide, in which only NH_4^+(W) was exchanged, ca. 0.7 NH_4^+ per one ε-$VMo_{9.4}V_{2.6}O_{40}$ building block were exchanged with H^+. From this result, the author estimated the ratio of NH_4^+(W) and NH_4^+(S) to be ca. 0.7-0.9 : 1.9-2.1. Single crystal analysis of K–Mo–V–Bi oxide revealed that 89% of K^+ selectively occupied the channel and that the rest 11% of K^+, NH_4^+, and H_2O occupied the cage in K–Mo–V–Bi oxide (Figure 6. 5). Therefore, the author speculate that K^+ replaced NH_4^+ in the channel and that the NH_4^+(S) was located in the channel and NH_4^+(W) was located in the cage. K^+ blocked the micropores of Mo–V–Bi oxide and could not be removed by calcination. The material lost microporosity with decrease in BET surface area (4.4 m^2/g) after ion-exchange with K^+ (Figure 6. 6).

6.3.2. Activity as an acid catalyst

The calcined Mo–V–Bi oxide (20 mg) and 10 mmol of benzyl alcohol were added to a reaction tube. Some cotton (50 mg) was set at the uppermost part of the tube to adsorb the water generated during the reaction. The reaction tube was heated at 403 K for 3 h. After the temperature had cooled to room temperature, the cotton was removed, and 4 mmol of tridecane and 10 mL of acetone were added to the reaction tube. The mixture was stirred at room temperature for 5 min. Yield, conversion, and selectivity were measured by GC-FID. Catalyst recovery: The catalyst was recovered by centrifugation (5 min, 3000 rpm), washed with 5 mL of acetone 3 times, and dried at 353 K overnight. Filtration experiment: 20 mg of calcined Mo–V–Bi oxide, 10 mmol of benzyl alcohol, and 0.8 mmol of tridecane were added to a reaction tube. 50 mg of cotton was set at the uppermost part of the tube to adsorb the water generated during the reaction. The reaction tube was heated at 403 K. After reaction for 45 min, the material was removed using a syringe with a disposable syringe filter unit (PTFE, 0.2 μm) when the solution was still hot, and the filtrate kept on reacting. The reaction was monitored by GC.

Removal of NH_3 from NH_4^+(W) and NH_4^+(S) produced weak and strong H^+ acid sites on Mo–V–Bi oxide, respectively. Table 6. 4 shows results of catalytic performance of Mo–V–Bi oxide for benzyl alcohol etherification. Mo–V–Bi oxide without calcination was not active (Entry 1). Calcined Mo–V–Bi oxide showed catalytic activity (Entry 2). Mo–V–Bi oxide calcined at temperatures over 473 K (Entries 2 and 3) and proton-exchanged H–Mo–V–Bi oxide (Entry 4) showed catalytic activity. These results indicated that a weak acid had sufficient catalytic activity for this reaction. Filtration experiments (Figure 6. 7) showed that calcined Mo–V–Bi oxide was a heterogeneous catalyst. The material could be reused without loss of activity (Entry 5). Benzyl alcohol was larger than the pore size, thus the reaction occurred on the surface of Mo–V–Bi oxide.

6.3.3. Ion-exchange Property of Na–Mo–Zn oxide and NH_4–Mo–Mn oxide

Na–Mo–Zn oxide and NH_4–Mo–Mn oxide also showed selective ion-exchange properties. The countercations, NH_4^+ in NH_4–Mo–Mn oxide and Na^+ in Na–Mo–Zn oxide, were exchangeable with other cations. Various countercations, such as H^+, Li^+, Na^+, K^+, Rb^+, and Cs^+, were tested for ion-exchange with Na–Mo–Zn oxide and NH_4–Mo–Mn oxide. After ion-exchange process, the ion-exchanged samples were characterized by powder XRD (Figure 6. 8 and Figure 6. 9) and FT-IR (Figure 6. 10 and Figure 6. 11), which showed that all the characteristic peaks of Na–Mo–Zn oxide and NH_4–Mo–Mn oxide retained in the corresponding ion-exchanged materials and demonstrated that basic structures of the materials did not change. For K^+, Rb^+, and Cs^+ exchanged samples, powder XRD patterns revealed that the change of relative peak intensity for ion-exchanged samples were observed compared with those of as-synthesized samples, indicating cations were successfully introduced into the materials. Moreover, diffraction peaks shifted, especially after ion-exchange with Rb^+ and Cs^+, which implied the slight alteration of lattice parameters. For FT-IR spectra of the materials after ion-exchange, vibration peaks of POM moiety were unchanged, indicating high stability of the materials during ion-exchange process (Figure 6. 10 and Figure 6. 11). Decrease of NH_4^+ peaks in FT-IR spectra of Mo–Mn oxide also indicated that NH_4^+ was replaced by other countercations. Moreover, TPD profiles of ion-exchanged NH_4–Mo–Mn oxide showed that the ammonium cations were successfully replaced by other ions (Figure 6. 12).

Elemental analysis further confirmed that the cations were introduced into the materials of Na–Mo–Zn oxide and NH_4–Mo–Mn oxide, and the chemical formulas of ion-exchanged samples are summarized in Table 6. 5. The results showed that ion-exchange properties of the materials depended on the size of the ions. Large cations, such as K^+, Rb^+, and Cs^+, showed high ion-exchange capacity for both Na–Mo–Zn oxide and NH_4–Mo–Mn oxide. Small ions, H^+, Li^+, and Na^+, were not as efficient as the

large ions to replace the NH_4^+ or Na^+ in as-synthesized materials of Na–Mo–Zn oxide and NH_4–Mo–Mn oxide. Elemental analysis further showed that the amount of Mo, Zn, and Mn was kept constant after ion-exchange process, indicating that Mo, Zn, and Mn were in the frameworks of the materials.

The Rb-exchanged materials of Rb–Mo–Zn oxide and Rb–Mo–Mn oxide, powder diffraction peak intensity of which appealed remarkable differences from that of as-synthesized materials, were analyzed by Rietveld refinement to understand the position of Rb atom. Two models were set up for determination of Rb in the materials (Figure 6. 5). One was Rb located in channel and other was Rb located in cage. The position of Rb was determined by comparison of R_{wp} of corresponding models after Rietveld refinement. The results showed that the model with Rb atom located in channel showed lower R_{wp} value for both materials of Na–Mo–Zn oxide and NH_4–Mo–Mn oxide, which indicated the Rb atom located in channel (Figure 6. 13).

6.4. Conclusion

The POM-based complex metal oxides of Mo–V–Bi oxide, Na–Mo–Zn oxide, and NH_4–Mo–Mn oxide showed zeolite-like ion-exchange property. The original cations in the materials could be replaced by other ions in aqueous solution without change of their basic structure. Single crystal analysis was carried out to understand the exchange K^+ in Mo–V–Bi oxide, which suggested that K^+ was in channel. Rietveld analysis showed that the Rb^+ in Na–Mo–Zn oxide and NH_4–Mo–Mn oxide also occupied channel.

References

(1) Yasuda, N.; Fukuyama, Y.; Toriumi, K.; Kimura, S.; Takata, M. In *AIP Conference Proceedings*; Garrett, R., Gentle, I., Nugent, K., Wilkins, S., Ed.; 2010; Vol. 1234, pp. 147–150.

(2) Yasuda, N.; Murayama, H.; Fukuyama, Y.; Kim, J.; Kimura, S.; Toriumi, K.; Tanaka, Y.; Moritomo, Y.; Kuroiwa, Y.; Kato, K.; Tanaka, H.; Takata, M. *J. Synchrotron Rad.* **2009**, *16*, 352–357.

(3) Sheldrick, G. M. *SHELX-97, Program for Crystal Structure Analysis*; Universität Göttingen: Germany, 1997.

(4) Zhang, Z.; Sadakane, M.; Murayama, T.; Izumi, S.; Yasuda, N.; Sakaguchi, N.; Ueda, W. *Inorg. Chem.* **2014**, *53*, 903–911.

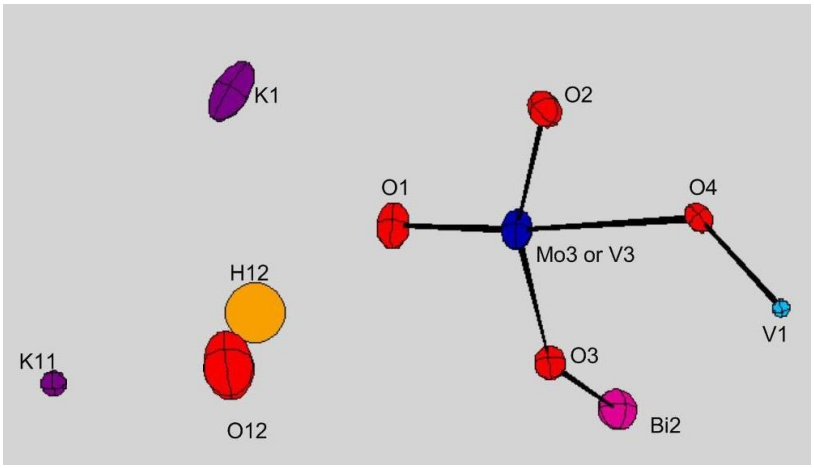

Figure 6. 1. Anisotropic displacement ellipsoids of Mo–V–Bi oxide structure by single crystal structure analysis as-synthesized Mo–V–Bi oxide.

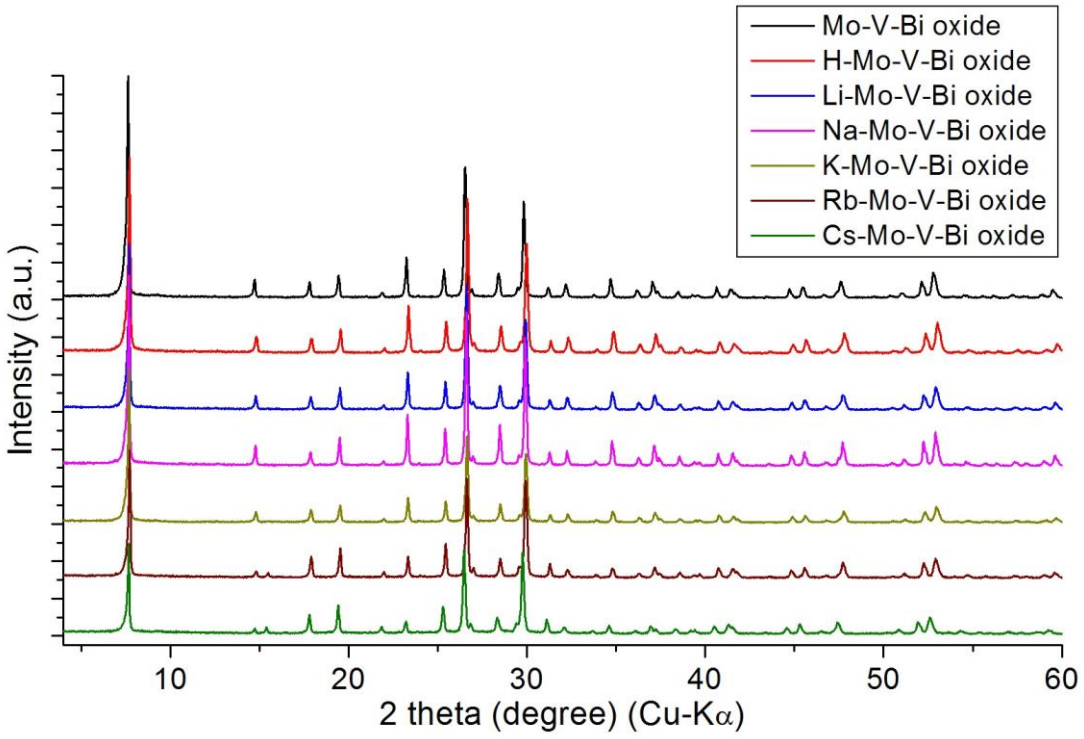

Figure 6. 2. Powder XRD patterns of ion-exchanged Mo–V–Bi oxides.

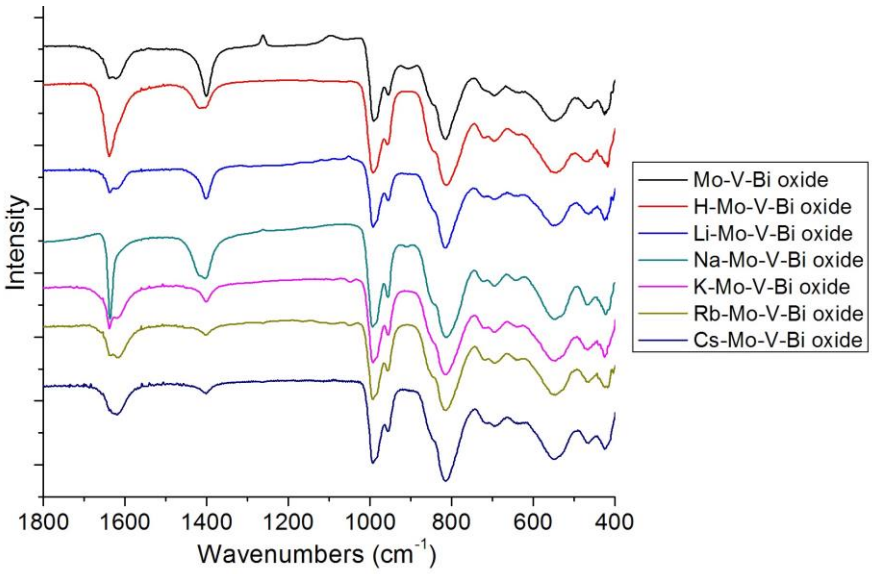

Figure 6. 3. FT-IR spectra of ion-exchanged Mo–V–Bi oxides.

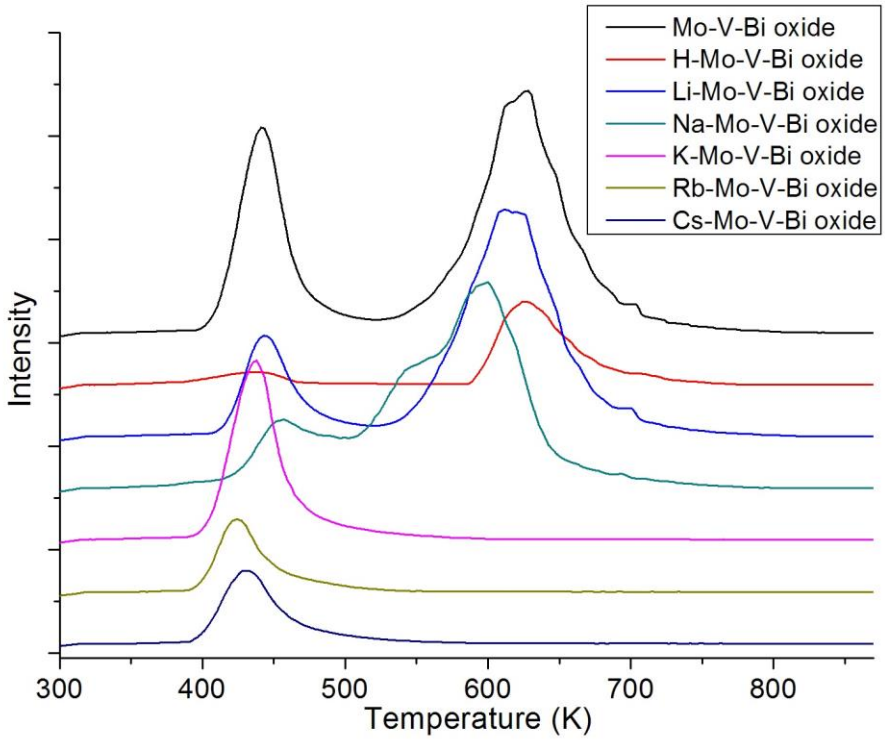

Figure 6. 4. TPD profiles (*m*/*z* = 16) of Mo–V–Bi oxides.

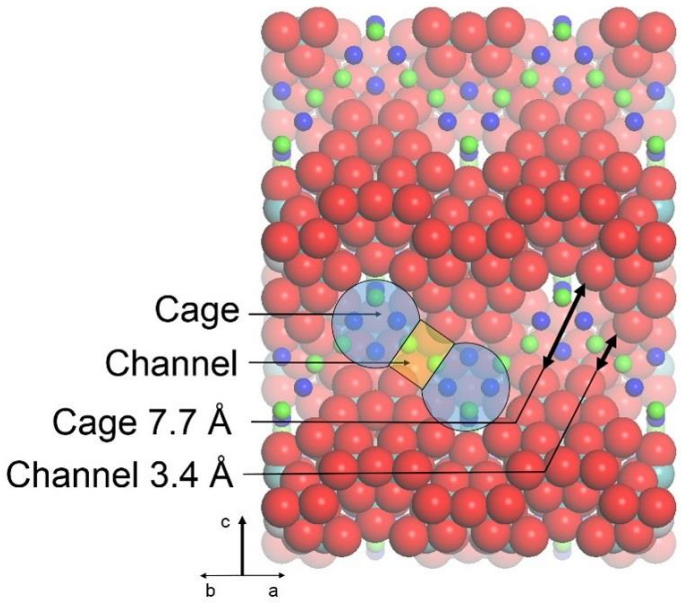

Figure 6. 5. CPK representation of (1 0 1) plane the POM-based material, framework oxygen (red sphere), species in cage (blue sphere), species in channel (green sphere).

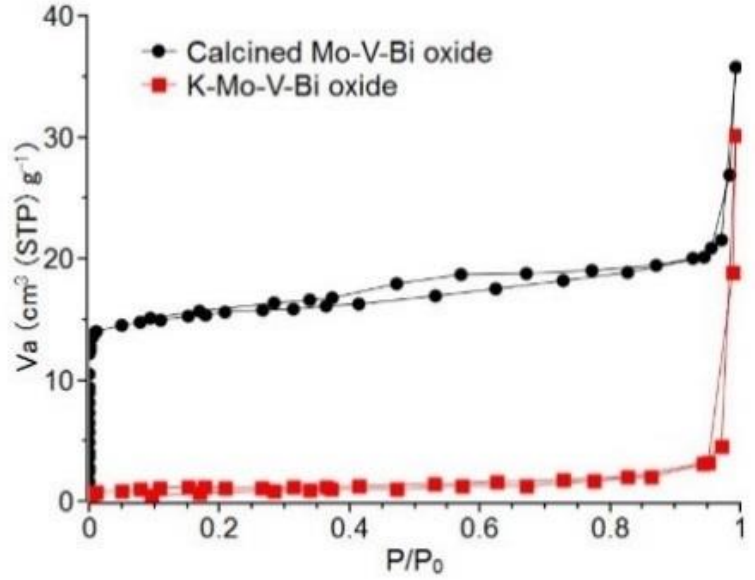

Figure 6. 6. Adsorption-desorption isotherms of Mo–V–Bi oxide and K–Mo–V–Bi oxide

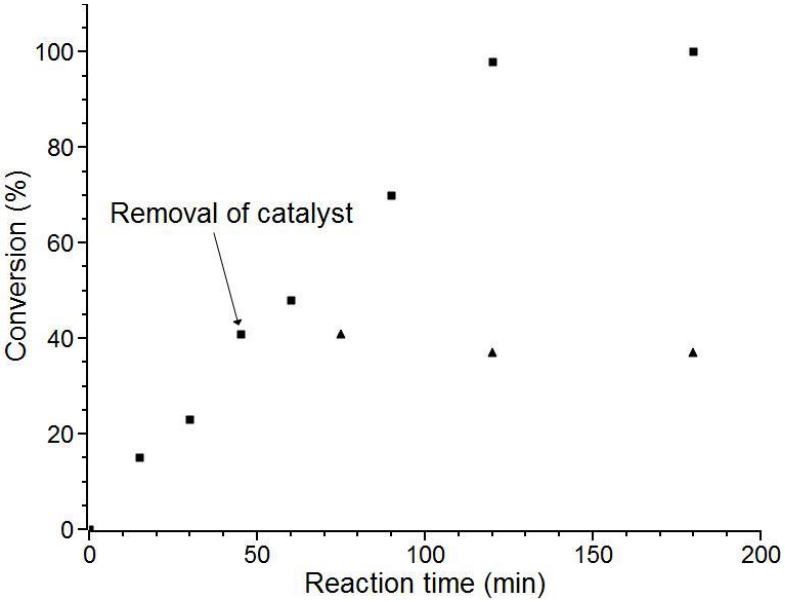

Figure 6. 7. Filtration experiment on calcined (at 623 K) Mo–V–Bi oxide. Squares presented the reaction with catalyst. Triangles presented the reaction after removal of catalyst.

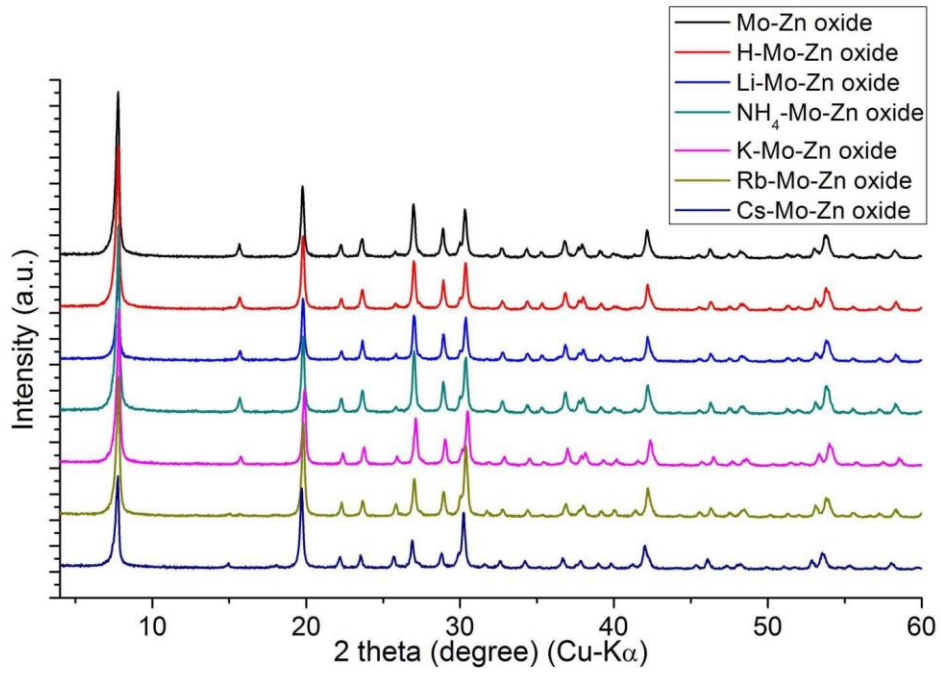

Figure 6. 8. Powder XRD patterns of ion-exchanged Na–Mo–Zn oxides.

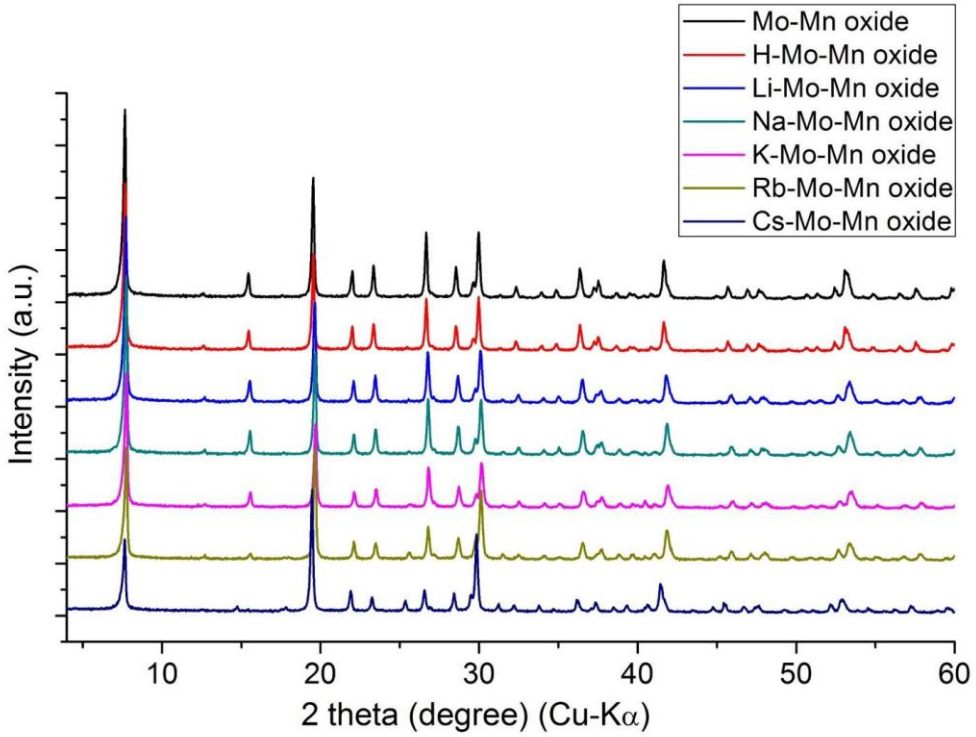

Figure 6. 9. Powder XRD patterns of ion-exchanged NH_4–Mo–Mn oxides.

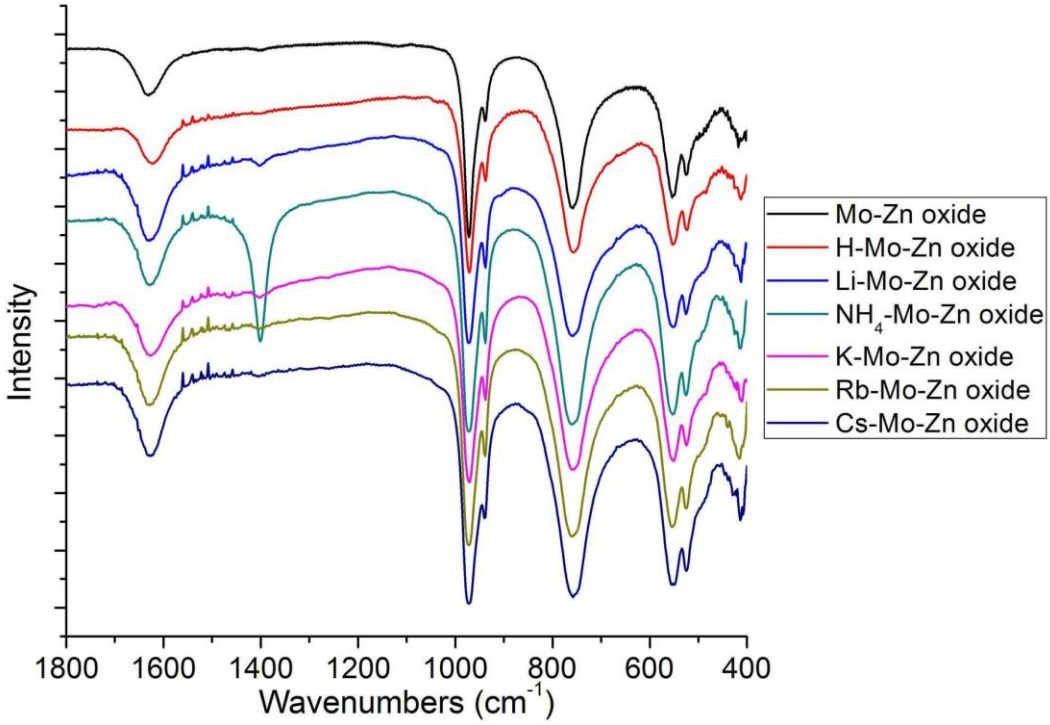

Figure 6. 10. FT-IR spectra of ion-exchanged Na–Mo–Zn oxides.

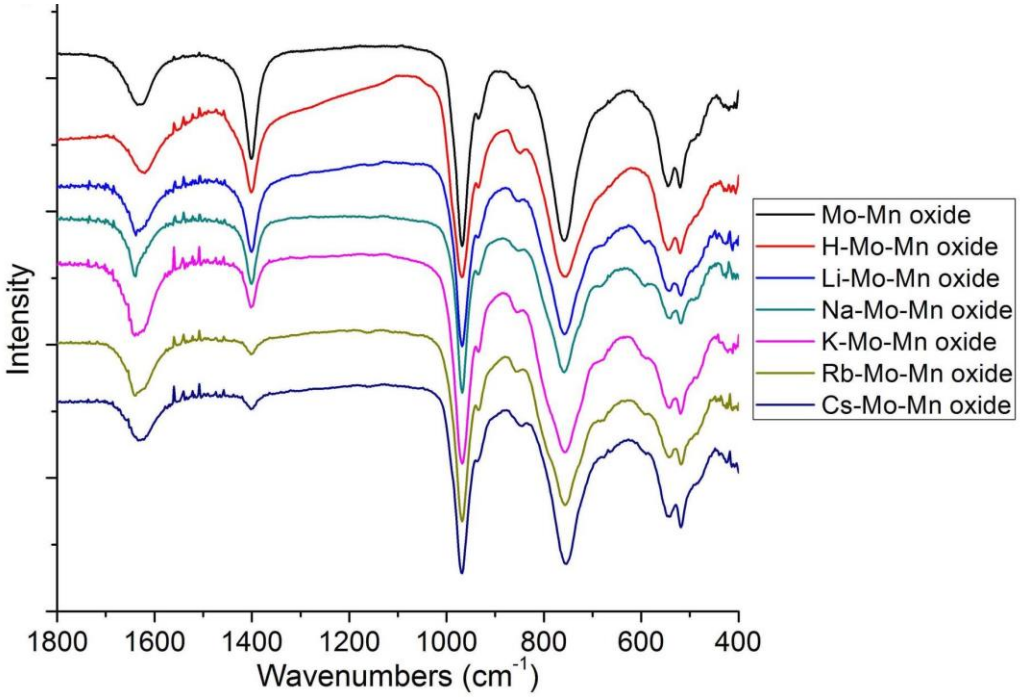

Figure 6. 11. FT-IR spectra of ion-exchanged NH_4–Mo–Mn oxides.

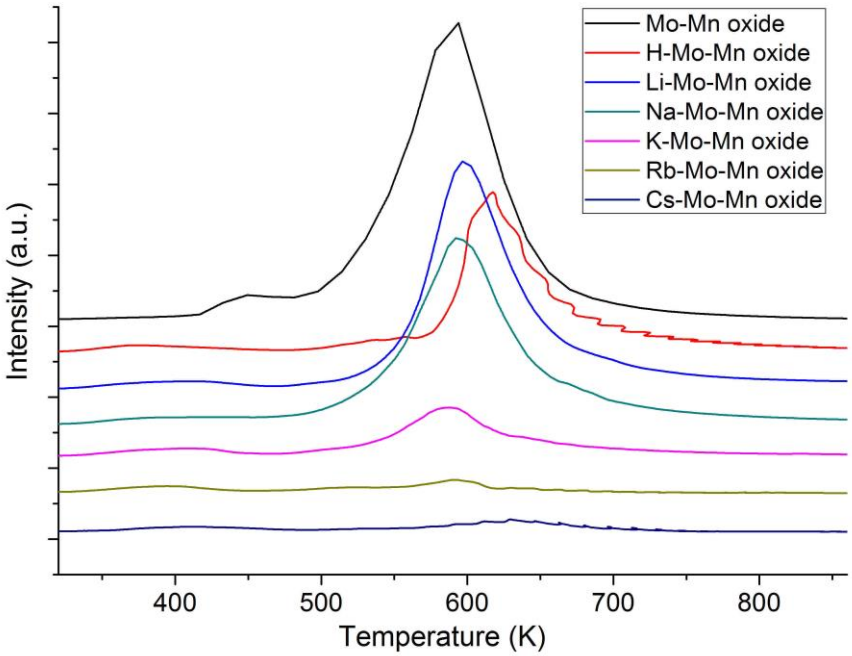

Figure 6. 12. TPD profiles (m/z = 16) of ion-exchanged NH_4–Mo–Mn oxides.

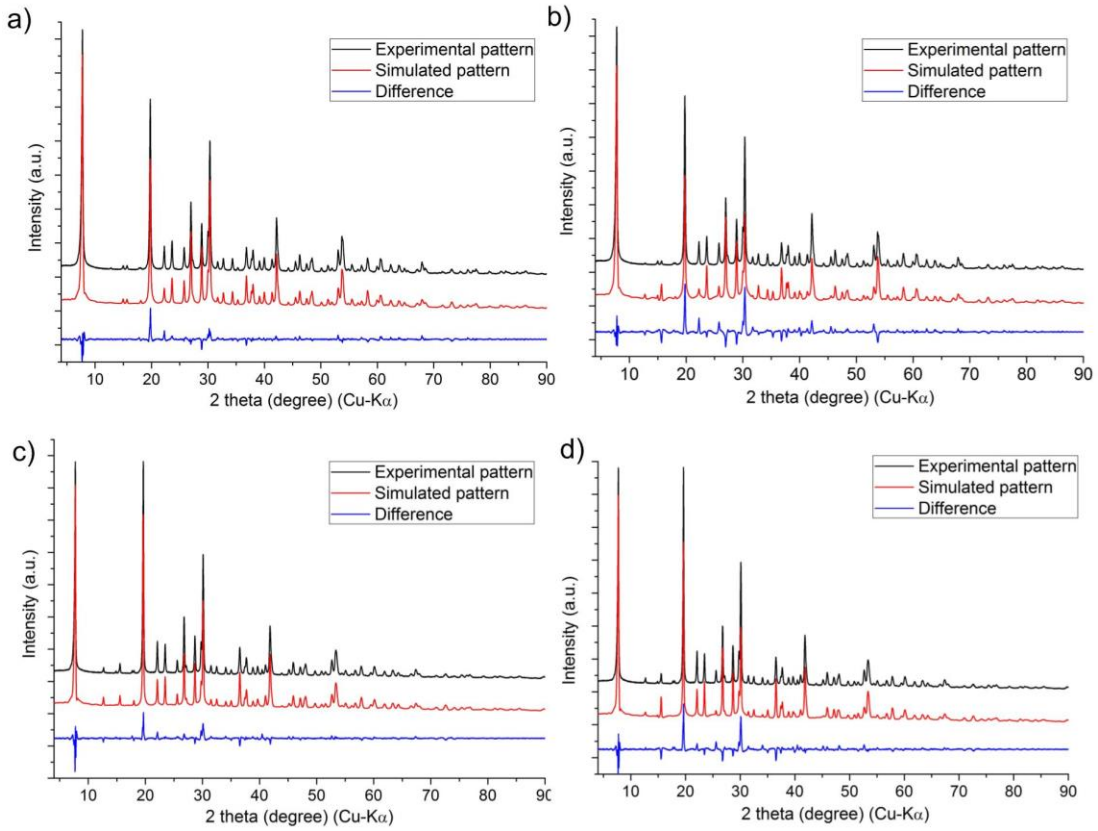

Figure 6. 13. Comparison of experimental pattern and simulated pattern with Rietveld refinement of Rb-exchanged materials a) Rb–Mo–Zn oxide Rb in channel, R_{wp} = 7.51%, b) Rb–Mo–Zn oxide Rb in cage, R_{wp} = 14.41%, c) Rb–Mo–Mn oxide Rb in channel, R_{wp} = 7.30%, and d) Rb–Mo–Mn oxide Rb in cage, R_{wp} = 12.01%.

Table 6. 1. Atom position and occupancy from single crystal analysis of K–Mo–V–Bi oxide.

Atom	X	y	Z	Occupancy
K1	0.2641(3)	-0.0141(3)	-0.2359(3)	0.401(12)
V1	0.125	0.125	0.125	1
Bi2	0	0	0	1
Mo3	0.17894(3)	0.07106(3)	-0.04996(5)	0.78
V3	0.17894(3)	0.07106(3)	-0.04996(5)	0.22
O1	0.1876(2)	0.0624(2)	-0.1341(3)	1
O2	0.2711(2)	0.0778(3)	-0.0211(2)	1
O3	0.0794(2)	0.0794(2)	-0.0383(3)	1
O4	0.1754(3)	0.0746(3)	0.0746(3)	1
K11	0.125	0.125	-0.375	0.173(18)
O12	0.125	0.125	-0.2548(8)	0.827(18)
H12	0.1502(4)	0.0998(4)	-0.234(2)	0.827(18)

Table 6. 2. Metal-oxygen bond lengths from single crystal analysis of K–Mo–V–Bi oxide.

	Bond length (Å)
V1-O4	1.719(9)
Bi2-O3	2.335(6)
M3-O1	1.674(6)
M3-O2	1.906(3)
M3-O3	1.980(4)
M3-O4	2.454(6)

M includes V and Mo

Table 6. 3. Changes in formulas of Mo–V–Bi oxide after ion-exchange.

Entry	Cation	Formula [a]	Amount of NH_4 per one ε-$VMo_{9.4}V_{2.6}O_{40}$ [b]	
			NH_4^+(W)	NH_4^+(S)
1	Before ion-exchange	$(NH_4)_{2.8}H_{0.9}[\varepsilon\text{-}VMo_{9.4}V_{2.6}O_{40}Bi_2]$	0.7	1.4
2	H^+	$(NH_4)_{2.1}H_{0.7}H_{0.9}[\varepsilon\text{-}VMo_{9.4}V_{2.6}O_{40}Bi_2]$	0	1.6
3	Li^+	$(NH_4)_{2.6}Li_{0.2}H_{0.9}[\varepsilon\text{-}VMo_{9.4}V_{2.6}O_{40}Bi_2]$	0.3	1.4
4	Na^+	$(NH_4)_{2.2}Na_{0.6}H_{0.9}[\varepsilon\text{-}VMo_{9.4}V_{2.6}O_{40}Bi_2]$	0.2	1.4
5	K^+	$(NH_4)_{0.9}K_{1.9}H_{0.9}[\varepsilon\text{-}VMo_{9.4}V_{2.6}O_{40}Bi_2]$	0.6	0
6	Rb^+	$(NH_4)_{0.7}Rb_{2.1}H_{0.9}[\varepsilon\text{-}VMo_{9.4}V_{2.6}O_{40}Bi_2]$	0.2	0
7	Cs^+	$(NH_4)_{0.8}Cs_{2.0}H_{0.9}[\varepsilon\text{-}VMo_{9.4}V_{2.6}O_{40}Bi_2]$	0.3	0

[a] Estimated by elemental analysis, [b] estimated by TPD.

Table 6. 4. Benzyl alcohol dehydration to form dibenzyl ether catalyzed by Mo–V–Bi oxide. [a]

Entry	Catalyst	Conv. (%)	Yield (%)	Sel. (%)
1	As-synthesized Mo–V–Bi oxide	3	3	100
2	Calcined Mo–V–Bi oxide at 623 K	95	94	99
3	Calcined Mo–V–Bi oxide at 473 K	92	91	99
4	H–Mo–V–Bi oxide	99	95	95 [b]
5	Recovered catalyst in Entry 2	100	97	97
6	Calcined Mo–V–Bi oxide at 673 K	98	91	93 [c]
7	No catalyst	5	0	0

[a] Reaction conditions: 20 mg of Mo–V–Bi oxide, 10 mmol of benzyl alcohol, 403 K, 3 h, after the reaction, 4 mmol of tridecane was added as an internal standard after reaction. [b] ca. 3% of benzaldehyde was formed. [c] ca. 4% of benzaldehyde was formed.

Table 6. 5. Chemical formulas of Na–Mo–Zn oxides and NH_4–Mo–Mn oxides.

	Formulas
As-synthesized Mo–Zn oxide	$Na_{1.5}H_{11.4}[\varepsilon\text{-}ZnMo_{12}O_{40}\{Zn\}_2]\cdot 5H_2O$
H–Mo–Zn oxide	$Na_{0.6}H_{12.3}[\varepsilon\text{-}ZnMo_{12}O_{40}\{Zn\}_2]\cdot 5H_2O$
Li–Mo–Zn oxide	$Li_{0.7}Na_{0.8}H_{11.4}[\varepsilon\text{-}ZnMo_{12}O_{40}\{Zn\}_2]\cdot 5H_2O$
NH_4–Mo–Zn oxide	$(NH_4)_{1.4}Na_{0.1}H_{11.4}[\varepsilon\text{-}ZnMo_{12}O_{40}\{Zn\}_2]\cdot 5H_2O$
K–Mo–Zn oxide	$K_{1.4}Na_{0.1}H_{11.4}[\varepsilon\text{-}ZnMo_{12}O_{40}\{Zn\}_2]\cdot 5H_2O$
Rb–Mo–Zn oxide	$Rb_{1.3}Na_{0.2}H_{11.4}[\varepsilon\text{-}ZnMo_{12}O_{40}\{Zn\}_2]\cdot 5H_2O$
Cs–Mo–Zn oxide	$Cs_{1.5}H_{11.4}[\varepsilon\text{-}ZnMo_{12}O_{40}\{Zn\}_2]\cdot 5H_2O$
As-synthesized Mo–Mn oxide	$(NH_4)_{2.1}H_{7.5}[\varepsilon\text{-}Mn_{0.2}Mo_{12}O_{40}\{Mn\}_2]\cdot 4H_2O$
H–Mo–Mn oxide	$(NH_4)_{1.7}H_{7.9}[\varepsilon\text{-}Mn_{0.2}Mo_{12}O_{40}\{Mn\}_2]\cdot 3H_2O$
Li–Mo–Mn oxide	$Li_{0.1}(NH_4)_{2.0}H_{7.5}[\varepsilon\text{-}Mn_{0.2}Mo_{12}O_{40}\{Mn\}_2]\cdot 3H_2O$
Na–Mo–Mn oxide	$Na_{0.4}(NH_4)_{1.7}H_{7.5}[\varepsilon\text{-}Mn_{0.2}Mo_{12}O_{40}\{Mn\}_2]\cdot 3H_2O$
K–Mo–Mn oxide	$K_{1.4}(NH_4)_{0.7}H_{7.5}[\varepsilon\text{-}Mn_{0.2}Mo_{12}O_{40}\{Mn\}_2]\cdot 3H_2O$
Rb–Mo–Mn oxide	$Rb_{1.5}(NH_4)_{0.6}H_{7.5}[\varepsilon\text{-}Mn_{0.2}Mo_{12}O_{40}\{Mn\}_2]\cdot 3H_2O$
Cs–Mo–Mn oxide	$Cs_{1.4}(NH_4)_{0.7}H_{7.5}[\varepsilon\text{-}Mn_{0.2}Mo_{12}O_{40}\{Mn\}_2]\cdot 4H_2O$

Chapter 7. One dimensional fully-inorganic complex metal oxides based on molybdenum and tellurium

7.1. Introduction

In the case of POM structure chemistry, the flexible metal-oxygen coordination, such as octahedral and tetrahedral coordination, leads to variety of structural derivative of POMs. There are many types of structures in the POMs, such as Keggin, Dowson, and sandwidage-type POM, which have been synthesized and structural characterized. POM molecules have been applied to assembly of POM-based materials, leading to plenty of applications in many fields, including adsorption, separation, and catalysis. POMs in solid state are ionic crystals, which were comprised of polyanions (primary structure), cations, water of crystallization, and other molecules (if any). [1] Polyanions are recognized as molecule-type structures, constructed from several metal-oxygen octahedra of tetrahedra.

Recently, some interesting unusual POM anions have been synthesized. It is found that molybdenum, tungsten, and vanadium can assemble to the metal-oxygen clusters with nanometer-sized scale. [2–22] The resulting materials are comprised of tens to hundreds of metal-oxygen octahedra, bipyramid or tetrahedral, which are much larger than ordinary polyanions (primary structure) such as Keggin. Various novel POM structures are found on the basis of POM materials, including ball-shaped POM and wheel-shaped POM. Even though the new POMs are interesting and impressive, polyanions are still recognized as molecule-type species with 0 dimension structure.

Herein, the author would like to present a new type of polyanion with 1D topology. The structure information of the material was obtained using powder X-ray diffraction combined with FT-IR analysis, UV-Vis, redox titration, and elemental analysis. A tellurium ion was surrounded by six molybdenum-oxygen octahedra, forming a hexagonal unit stacking in c-axis to form a column-type POM primary structure (polyanion). The crystal of the material was arranged by assembly of the columns in a hexagonal fashion. The material showed ion-exchange property, in which the ammonium cations could be replaced by other ions such as potassium ions. It was indicated that crystal structure of the material can be easily damaged without collapse

the POM anion structure of the material. This study indicated that polyanion can be high dimensional structures.

7.2. Experimental

7.2.1. Material preparation

The molybdenum and tellurium based material with ammonium cation was denoted as NH_4–Mo–Te oxide. $(NH_4)_6Mo_7O_{24}{\cdot}4H_2O$ (1.766 g, Mo: 10 mmol) was dissolved in 20 mL of water, followed by addition of 0.391 g of $Te(OH)_6$ into the $(NH_4)_6Mo_7O_{24}{\cdot}4H_2O$ solution to form solution A. Then $VOSO_4{\cdot}5H_2O$ (0.6438 g, 2.54 mmol) was dissolved in 20 mL of water to form solution B. Solution B was poured into solution A rapidly. The mixture was left at room temperature to stir for 10 min and degassed by N_2 bubbling for 10 min. The mixture was introduced into a 50-mL Telfon-liner of a stainless-steel autoclave, which was heated at 448 K for 24 h. After the autoclave had been cooled at room temperature, the resulting solid was recovered from the solution by filtration. The obtained solid was washed with 10 mL of water for 3 times and dried at 353 K overnight. Elemental Analysis: Calcd for $N_{1.9}Mo_6Te_1O_{23}H_{11.6}$: N, 2.40; Mo, 51.89; Te, 11.50; H, 1.05, Found: N, 2.49; Mo, 51.59; Te, 11.59; H, 1.22.

K–Mo–Te oxide: NH_4–Mo–Te oxide (0.3 g) was dispeased into 15 mL of water, followed by addition of 0.091 g of KCl. The mixture was stirred at 353 K for 6 h. The solid was recovered by filtration and washed with 10 mL of water for 3 times, and dried at 353 K overnight (K–Mo–Te oxide). Elemental Analysis: Calcd for $K_{1.8}N_{0.1}Mo_6Te_1O_{23.3}H_{4.4}$: K, 6.11; N, 0.12; Mo, 49.96; Te, 11.07; H, 0.38, Found: K, 6.28; N, 0.15; Mo, 50.24; Te, 11.21; H, 0.64.

Crystal growth. $(NH_4)_6Mo_7O_{24}{\cdot}4H_2O$ (1.766 g, Mo: 10 mmol) was dissolved in 20 mL of water, followed by adding 0.391 g of $Te(OH)_6$ into the $(NH_4)_6Mo_7O_{24}{\cdot}4H_2O$ solution to form solution A. Then $VOSO_4{\cdot}5H_2O$ (0.6438 g, 2.54 mmol) was dissolved in 20 mL of water to form solution B. Solution B was poured into solution A rapidly. The mixture was left at room temperature to stir for 10 min, and degassed by N_2 bubbling

for 10 min. The solution was sealed with a cap and left in a fridge for about 3 months. The well-crystallized NH_4–Mo–Te oxide was collected by centrifugation.

7.2.2. Characterization

Powder X-ray diffraction (XRD) pattern was obtained on RINT2200 (Rigaku) with Cu Kα radiation (tube voltage: 40 kV, tube current: 20 mA). The powder XRD patterns for structure analysis were collected on RINT2200 (Rigaku) with Cu Kα radiation (tube voltage: 40 kV, tube current: 40 mA). Scanning electron microscopy (SEM) images were obtained with HD-2000 (HITACHI). Transmission electron microscopy (TEM) images were taken with a 200 kV TEM (JEOL JEM-2100F). Fourier transform infrared (FT-IR) was carried out on PARAGON 1000, Perkin Elmer. Thermal analysis (TG-DTA) was performed on Thermo Plus, TG8120 (Rigaku). UV-vis spectra were obtained with JASCO V-570. Elemental compositions were determined by an inductive coupling plasma (ICP-AES) method (ICPE-9000, Shimadzu). CHN elemental composition was determined at Instrumental Analysis Division, Equipment Management Center, Creative Research Institution, Hokkaido University.

7.2.3. Redox titration

$H_2C_2O_4 \cdot 2H_2O$ (0.1031 g) was dissolved in 30 mL of water followed by adding 10 mL of H_2SO_4 (wt = 16%). Titration was performed at 343-358 K. The concentration of $KMnO_4$ was 0.04658 mol/L. Typically, NH_4–Mo–Te oxide was dissolved in the solution of Na_2CO_3 (0.3 g, 10 mL of water). After the NH_4–Mo–Te oxide dissolved completely, 40 mL of H_2SO_4 (1 M) was slowly added and 15 mL of H_2SO_4 (16%). The standard solution of $KMnO_4$ (4.45 mL) was added into the solution of NH_4–Mo–Te oxide and stirred at room temperature for 10 min. The solution was heated to 343-358 K. $H_2C_2O_4 \cdot 2H_2O$ aqueous solution titrate unreacted $KMnO_4$ in the solution of NH_4–Mo–Te oxide. Potential of the solution was monitored by a Horiba D-52 pH meter with a metal (ORP) electrode. Titration curves are in Figure 7. 1.

7.2.4. Structure analysis with powder diffraction data

The structures of NH_4–Mo–Te oxide and K–Mo–Te oxide were determined by powder X-ray diffraction. Powder XRD patterns of the materials were obtained from laboratory powder XRD instrument (tube voltage: 40 kV, tube current: 40 mA, scan speed: 1 degree/min, step: 0.01 degree). The powder XRD patterns of the materials were indexed to obtain crystal system and lattice parameters with the programs of X-cell and DICVOL06, which showed the same result for the materials. The unit cell was refined by Pawley refinement to get profile parameters. Structure factors were obtained by Le Bail method with EdPCR program. The initial structures of the materials were solved by a charge flipping algorithm. The results of the charge flipping algorithm were listed in Table 7. 1 and Table 7. 2.

The initial structures of the materials were refined by Rietveld refinement. Firstly, Pawley refinement was applied for refinement of the lattice parameters and pattern parameters of the materials. Then isotropical temperature factor of every atom was given without further refinement. Rietveld refinement was started with the initial models of the materials and lattice parameters and pattern parameters from Pawley refinement. The occupancy of the framework atoms were fixed without further refinement. The occupancy of the cations was carefully refined with consideration of elemental analysis. The position of atoms was refined. Finally, the pattern parameters were refined again to obtain the lowest R_{wp} value. Crystallographic parameters and Rietveld refinement parameters were in Table 7.3-7.8. DICVOL06 and EdPCR were performed with the Fullprof package. Material modeling, X-cell program, Pawley refinement, and Rietveld refinement were carried out with Materials Studio v6.1.0 package (Accelrys Software Inc.). The charge flipping algorithm was performed with the superflip program in Jana2006. Electron density maps were represented with Chimera 1.8.1.

7.2.5. Single crystal analysis

Since the crystals that had been grown were still too small for the diffractometer in the laboratory system, data collection was performed on a high-precision diffractometer installed in the SPring-8 BL40XU beamline. [23,24] The synchrotron radiation emitted from helical undulator was monochromated by using a Si(111) channel cut monochromator and focused with a Fresnel zone plate. A Rigaku Saturn724 CCD detector was used. The measurement was performed at 100 (2) K. An empirical absorption correction based on Fourier series approximation was applied. The data were corrected for Lorentz and polarization effects. The structure was solved by direct methods and refined by full-matrix least-squares (SHELX-97), [25] where the unweighted and weighted agreement factors of $R = \Sigma||F_o|-|F_c||/\Sigma|F_o|$ ($I > 2.00\sigma$ (I)) and wR = $[\Sigma w(Fo^2-Fc^2)^2/\Sigma w(Fo^2)^2]^{1/2}$, respectively, were used. Crystallographic data of Mo–V–Bi oxide was listed in Table 7. 4.

7.3. Results and discussion

7.3.1. Material synthesis

Hydrothermal synthesis of $(NH_4)_6Mo_7O_{24}\cdot 4H_2O$, $Te(OH)_6$, and $VOSO_4\cdot 5H_2O$ yielded a novel POM-based materials of NH_4–Mo–Te oxide. SEM images, listed in Figure 7. 2, exhibited that NH_4–Mo–Te oxide was a rod-like material with about 10 μm of length and about 0.3 μm of width. Element analysis confirmed that no vanadium was found in the material. Therefore, vanadium was not a building block for the material, and $VOSO_4\cdot 5H_2O$ only acted as a reducing agent to reduce other starting materials. Using other reducing agents, such as $H_2C_2O_4\cdot 2H_2O$, also produced the same material. Ion-exchange with potassium ion did not change the morphology of the material (Figure 7. 2a). After ion-exchange with potassium, K–Mo–Te oxide still revealed rod-like morphology (Figure 7. 2b). Powder XRD patterns of NH_4–Mo–Te oxide and K–Mo–Te oxide were listed in Figure 7. 3a, which showed similar diffraction patterns with slight peak shift and intensity difference, indicating that the basic structures of the materials were similar. FT-IR spectra (Figure 7. 3b) showed that the profiles of the materials were

similar to each other's, which also suggested the similarity of the structures. The peak at 1400 cm^{-1} decreased remarkably in K–Mo–Te oxide, indicating NH_4^+ was replaced by K^+.

7.3.2. Structure characterization

The crystal sizes of the materials synthesized with the hydrothermal method were too small in one diameter for single crystal analysis. The structures of NH_4–Mo–Te oxide and K–Mo–Te oxide were determined with powder X-ray diffraction. Diffraction peaks of both NH_4–Mo–Te oxide and K–Mo–Te oxide could be indexed with hexagonal cell and the lattice parameters of a = 12.45 Å, c = 3.94 Å and of a = 12.28 Å, c = 3.94 Å, respectively. The similar unit cells of the materials indicated the similar structures of the materials.

The structure factors of the materials were extracted by Le Bail fitting, and the initial structures of the NH_4–Mo–Te oxide and K–Mo–Te oxide were solved by the charge flipping algorithm, and then heavy metal distribution was known. The charge flipping algorithm generated the electron density maps for the materials, which exhibited that there were two sites, showing the most intensive peaks (Figure 7. 4a,b), which were denoted as surrounding site and center site. Six surrounding sites surrounded one center site, forming a hexagonal sub-building unit. Elemental analysis showed that the ratio of Mo/Te was 6. Heavy metal atoms, six Mo atoms and one tellurium, were assigned to these two sites with electron density maps after the charge flipping algorithm (Figure 7. 4c). However, molybdenum was very difficult to distinguish from tellurium with powder XRD pattern. For K–Mo–Te oxide, density of center site showed slight higher than that of surrounding site. This indicated that site may be occupied with tellurium and surrounding site may be occupied with molybdenum. In the case of NH_4–Mo–Te oxide, the charge flipping showed that there were two electron density maximum in the center site, which might be ascribed to disorder of the center metal ions. From the result, the author would like to ascribe the

surrounding site to be molybdenum and the central site to be tellurium. The positions of oxygen atoms of the framework, countercations, and water were assigned from residual peaks of the charge flipping algorithm. Some atom positions of framework oxygen and countercations were ambiguous from electron density maps after the charge flipping method, which were determined by Rietveld refinement.

The initial structures of NH_4–Mo–Te oxide and K–Mo–Te oxide were refined with Rietveld refinement. The resulting simulated patterns of the materials were quite similar to that of experimental data (Figure 7. 5). The R_{wp} value of NH_4–Mo–Te oxide and K–Mo–Te oxide were 7.17% and 5.20%, respectively, which indicated that the proposed structures were correct. Structure analysis showed that six metal-oxygen units surrounded one metal ion in a-b plane, which formed a units of $[TeMo_6O_{21}]$. The metal-oxygen pentagonal units were connected with each other with two edge sharing oxygen atoms (Figure 7. 6). The hexagonal units of $[TeMo_6O_{21}]$ stacked along c axis to form prismatic clusters. The columns assemble parallel in a hexagonal fashion to form the material. The columns were assembled by cations and water, which existed in the spaces between columns and interact with column weakly. It was found that the oxygen inside the hexagonal unit was disordered with occupancy of 0.5. A recent paper showed a molecule type $[TeMo_6O_{21}]$ POM was synthesized and characterized, which showed a very similar structure with our proposed structure, the FT-IR spectra of which were similar with the materials in the present work, indicating our structures were reasonable. [26]

Single crystal analysis was applied to confirm the structure of material. Large single crystal of NH_4–Mo–Te oxide was obtained by using low temperature condition for synthesis (see experimental). SEM image in Figure 7. 2a,c shows that NH_4–Mo–Te oxide synthesized with low temperature method was much larger than that with hydrothermal method. The basic structure of the material by using low temperature synthesis was the same with the material by using hydrothermal synthesis (Figure 7. 7). Single crystal analysis confirmed that the basic structure of the material from powder

diffraction data was correct.

Clear lattice images of NH_4–Mo–Te oxide and K–Mo–Te oxide were obtained by high-resolution TEM. TEM images clearly showed the (1 0 0) plane of the materials with the layer distance of 10 Å (Figure 7. 8). The layer of (0 0 1) was ambiguous in TEM image, which might be result from the unstable structure of the material against the electron beam. TEM images were in good agreement with crystal structures from structure analysis.

UV-vis spectra of the materials were obtained and presented in Figure 7. 9. From the spectra, no signal was found in the range from 500 to 600 nm in both cases of NH_4–Mo–Te oxide and K–Mo–Te oxide, which attributed to Mo^{V}, and this indicated at molybdenum ions in the materials was Mo^{VI}. The oxidation states of tellurium in the Mo–Te oxide were determined with redox titration. Most of the tellurium ions of NH_4–Mo–Te oxide were Te^{IV}. Tellurium ions in the K–Mo–Te oxide were partly oxidized during ion-exchange process. The ratio of Te^{VI}/Te^{IV} was proposed to be 1.86. The amount of ammonium cations and water in the materials were estimated with elemental analysis. According to the structure analysis, UV-Vis, and elemental analysis, the chemical formulas were estimated to be $(NH_4)_{1.9}[Te^{IV}_{0.95}Te^{VI}_{0.05}Mo^{VI}_{6}O_{21}]\cdot 2H_2O$ and $(NH_4)_{0.1}K_{1.8}[Te^{IV}_{0.65}Te^{VI}_{0.35}Mo^{VI}_{6}O_{21.3}]\cdot 2H_2O$ for NH_4–Mo–Te oxide and K–Mo–Te oxide, respectively.

7.3.3. Thermal stability

The existence of water and ammonium cations in the materials of NH_4–Mo–Te oxide and K–Mo–Te oxide was confirmed by FT-IR spectra (Figure 7. 3), which exhibited the signal at 1620 cm^{-1} for water and 1400 cm^{-1} for ammonium cations. After ion-exchange with K ion, the intensity of the peak at 1400 cm^{-1} decreased dramatically, indicating the replacement of ammonium cation with potassium ion. Thermal analysis (TG-DTA) under N_2 flow was performed to understand the guest molecules of water and ammonium cations desorbed from the materials (Figure 7. 10). In the case of

NH_4–Mo–Te oxide, there were two weight loss processes during heating. The first weight loss at 300~400 K was ascribed to desorption of water, and amount of weight loss was 3%. The second desorption process was at 400~800 K, and 4% of molecules (water and ammonium cation) was desorbed. For K–Mo–Te oxide, the 3% of mass was lost at 300~400 K. The ammonium amount in NH_4–Mo–Te oxide was estimated from TG was 4%, and H_2O was about 3%. The amount of water and ammonia estimated from TG-DTA well fitted the elemental analysis.

Ammonium cations (or K cations) and water held the column and stabilized the crystal structures of NH_4–Mo–Te oxide and K–Mo–Te oxide. After removal of ammonium and water, the material shrined gradually. XRD peak patterns of the materials showed that the peak at around eight degree shifted to high angle, indicating that distance between columns shortened (Figure 7. 11). The peak shifts were also observed in the peaks corresponding to a-b plane. In the case of the peak of (0 0 1) plane, no shift was observed, which demonstrated that calcination only affected distance between columns and did not affect the layer distance in one column (Figure 7. 11). The diffraction peaks of the material decreased and broaden, which indicated that the material was damaged during heating.

7.3.4. Separation of the nanowire

NH_4–Mo–Te oxide can be disassembled into thinner particle and even individual nanowires by dispersion in ethanol using ultrasound. The isolated nanowires were further characterized by atomic force microscope (AFM). AFM image of Mo–Te oxide after isolation experiments displayed tubular particle. Some very small particle can be found in AFM, and the thickness of the typical particles in Figure 7. 12 were ca. 1.2 nm and ca. 4.8 nm. The thickness of particle i was consistent with that of a single nanowire deduced from the crystallographic data of Mo–Te oxide, and the particle ii ascribed to the structure with four layers of nanowires. One possible structure was shown in Figure 7. 12. The width of the particle appeared much large than a single nanowire (1.2 nm), which resulted from the large cantilever of AFM. In the case of Mo–Se oxide, because the nanowires were shorter than that

of Mo–Te oxide, which were observed in AFM.

The size of the this ultrathin nanowire can be easily manipulated due to its 1D molecule structure. The property of the materials are expected to be tuned by altering size of the material. The materials are expected to be applied to many fields.

7.4. Conclusion

A new material based on molybdenum and tellurium was synthesized by hydrothermal method. The structure of the materials is determined by powder X-ray diffraction combined with FT-IR, redox titration, and elemental analysis. Single crystal analysis confirmed that the proposed structure of the material was correct. The material was comprised of $[TeMo_6O_{21}]_n$ hexagonal-shaped 1D tube with other water and cations.

References

(1) Mizuno, N.; Misono, M. *Chem. Rev.* **1998**, *98*, 199–218.

(2) Müller, A.; Todea, A. M.; van Slageren, J.; Dressel, M.; Bögge, H.; Schmidtmann, M.; Luban, M.; Engelhardt, L.; Rusu, M. *Angew. Chem. Int. Ed.* **2005**, *44*, 3857–3861.

(3) Müller, A.; Roy, S. *Eur. J. Inorg. Chem.* **2005**, *2005*, 3561–3570.

(4) Kortz, U.; Müller, A.; van Slageren, J.; Schnack, J.; Dalal, N. S.; Dressel, M. *Coord. Chem. Rev.* **2009**, *253*, 2315–2327.

(5) Schäffer, C.; Todea, A. M.; Bögge, H.; Petina, O. a; Rehder, D.; Haupt, E. T. K.; Müller, A. *Chem. Eur. J.* **2011**, *17*, 9634–9.

(6) Miiller, A.; Krickemeyer, E.; Meyer, J.; Bogge, H.; Peters, F.; Plass, W.; Diemann, E.; Dillinger, S.; Randerath, M.; Menke, C. *Angew. Chem. Int. Ed.* **1995**, *4*, 2122–2124.

(7) Müller, A.; Krickemeyer, E.; Bogge, H.; Schmidtmann, M.; Peters, F.; Menke, C.; Meyer, J. *Angew. Chem. Int. Ed.* **1997**, *36*, 483–486.

(8) Eda, K.; Iriki, Y.; Kawamura, K.; Ikuki, T.; Hayashi, M. *J. Solid State Chem.* **2007**, *180*, 3588–3593.

(9) Müller, A.; Kogerler, P.; Dress, A. W. M. *Coord. Chem. Rev.* **2001**, *222*, 193–218.

(10) Müller, A.; Diemann, E.; Kuhlmann, C.; Eimer, W.; Serain, C.; Tak, T.; Knöchel, A.; Pranzas, P. K. *Chem. Commun.* **2001**, 1928–1929.

(11) Yan, J.; Gao, J.; Long, D.-L.; Miras, H. N.; Cronin, L. *J. Am. Chem. Soc.* **2010**, *132*, 11410–11411.

(12) Müller, A.; Krickemeyer, E.; Dillinger, S.; Bögge, H.; Plass, W.; Proust, A.; Dloczik, L.; Menke, C.; Meyer, J.; Rohlfing, R. *Z. Anorg. Allg. Chem.* **1994**, 599–619.

(13) Todea, A. M.; Merca, A.; Bögge, H.; van Slageren, J.; Dressel, M.; Engelhardt, L.; Luban, M.; Glaser, T.; Henry, M.; Müller, A. *Angew. Chem. Int. Ed.* **2007**, *46*, 6106–6110.

(14) Müller, A.; Krickemeyer, E.; Bögge, H.; Schmidtmann, M.; Peters, F. *Angew. Chem. Int. Ed.* **1998**, 3359–3363.

(15) Müller, A.; Sarkar, S.; Shah, S.; Bögge, H.; Schmidtmann, M.; Kögerler, P.; Hauptfleisch, B.; Trautwein, A.; Schünemann, V. *Angew. Chem. Int. Ed.* **1999**, *38*, 3238–3241.

(16) Müller, A.; Serain, C. *Acc. Chem. Res.* **2000**, *33*, 2–10.

(17) Liu, T. *J. Am. Chem. Soc.* **2002**, *124*, 10942–10943.

(18) Xu, Z.-H.; Li, Y.-G.; Wang, E.-B.; Qin, C.; Wang, X.-L. *Inorg. Chem. Commun.* **2006**, *9*, 1315–1318.

(19) Todea, A. M.; Merca, A.; Bögge, H.; Glaser, T.; Pigga, J. M.; Langston, M. L. K.; Liu, T.; Prozorov, R.; Luban, M.; Schröder, C.; Casey, W. H.; Müller, A. *Angew. Chem. Int. Ed.* **2010**, *49*, 514–519.

(20) Schäffer, C.; Merca, A.; Bögge, H.; Todea, A. M.; Kistler, M. L.; Liu, T.; Thouvenot, R.; Gouzerh, P.; Müller, A. *Angew. Chem. Int. Ed.* **2009**, *48*, 149–153.
(21) Todea, A. M.; Merca, A.; Bögge, H.; Glaser, T.; Engelhardt, L.; Prozorov, R.; Luban, M.; Müller, A. *Chem. Commun.* **2009**, 3351–3353.
(22) Müller, A.; Das, S. K.; Fedin, V. P.; Krickemeyer, E.; Beugholt, C.; Bo, H.; Schmidtmann, M. *Z. Anorg. Allg. Chem.* **1999**, *625*, 1187–1192.
(23) Yasuda, N.; Fukuyama, Y.; Toriumi, K.; Kimura, S.; Takata, M. In *AIP Conference Proceedings*; Garrett, R., Gentle, I., Nugent, K., Wilkins, S., Ed.; 2010; Vol. 1234, pp. 147–150.
(24) Yasuda, N.; Murayama, H.; Fukuyama, Y.; Kim, J.; Kimura, S.; Toriumi, K.; Tanaka, Y.; Moritomo, Y.; Kuroiwa, Y.; Kato, K.; Tanaka, H.; Takata, M. *J. Synchrotron Rad.* **2009**, *16*, 352–357.
(25) Sheldrick, G. M. *SHELX-97, Program for Crystal Structure Analysis*; Universität Göttingen: Germany, 1997.
(26) Yang, D.; Li, S.; Ma, P.; Wang, J.; Niu, J. *Inorg. Chem.* **2013**, *52*, 14034–14039.

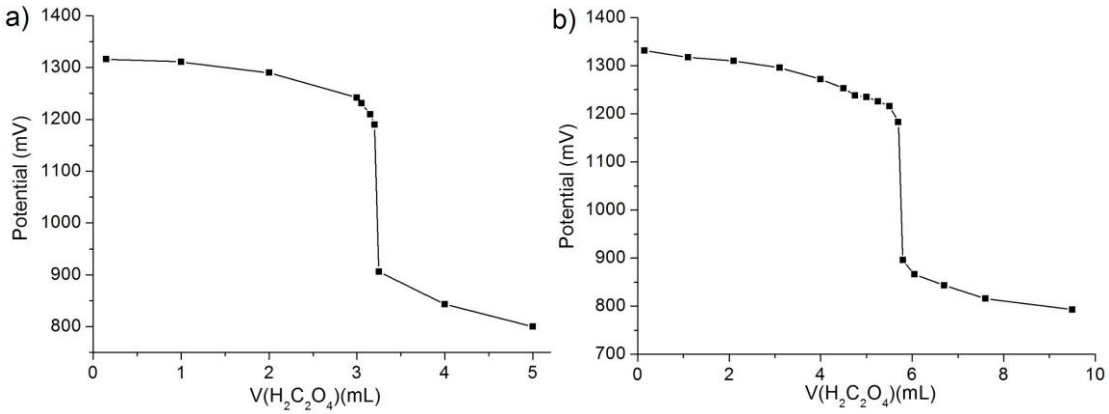

Figure 7. 1. Redox titration curve of a) NH_4–Mo–Te oxide and b) K–Mo–Te oxide.

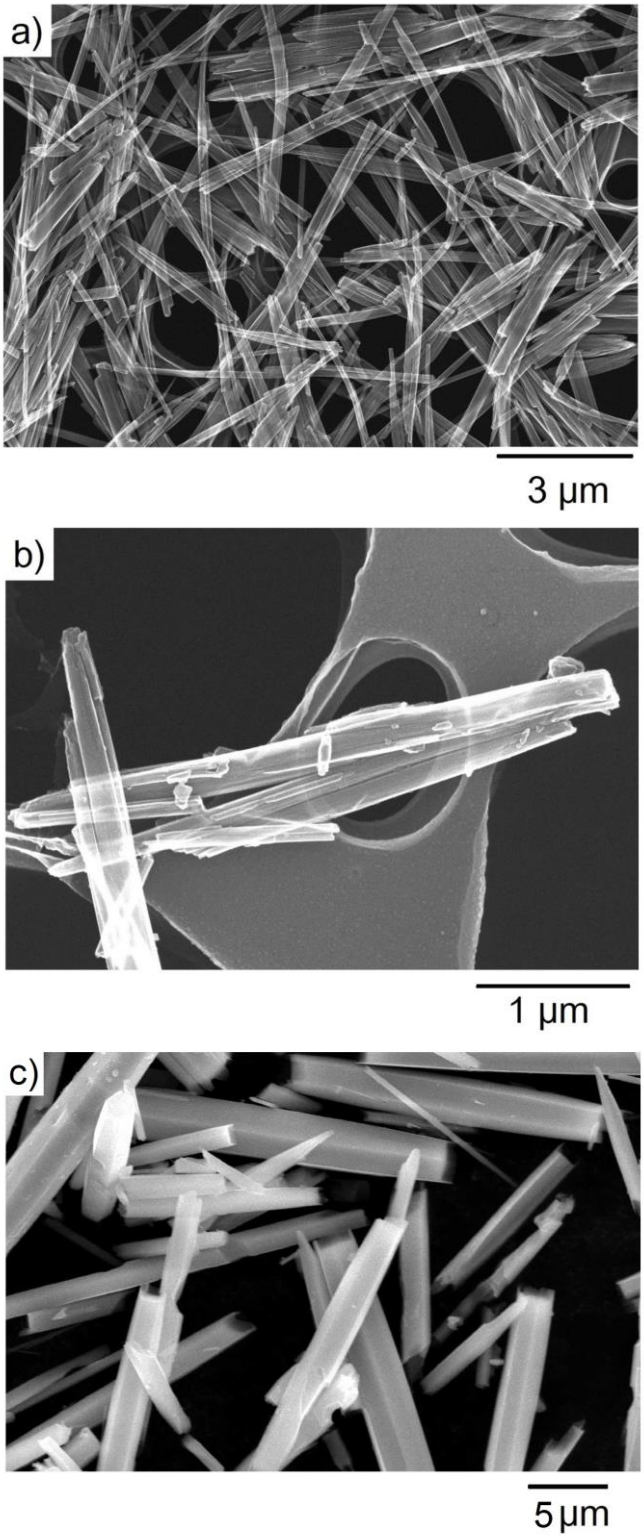

Figure 7. 2. SEM images of a) NH_4–Mo–Te oxide, b) K–Mo–Te oxide, and c) large crystal of NH_4–Mo–Te oxide.

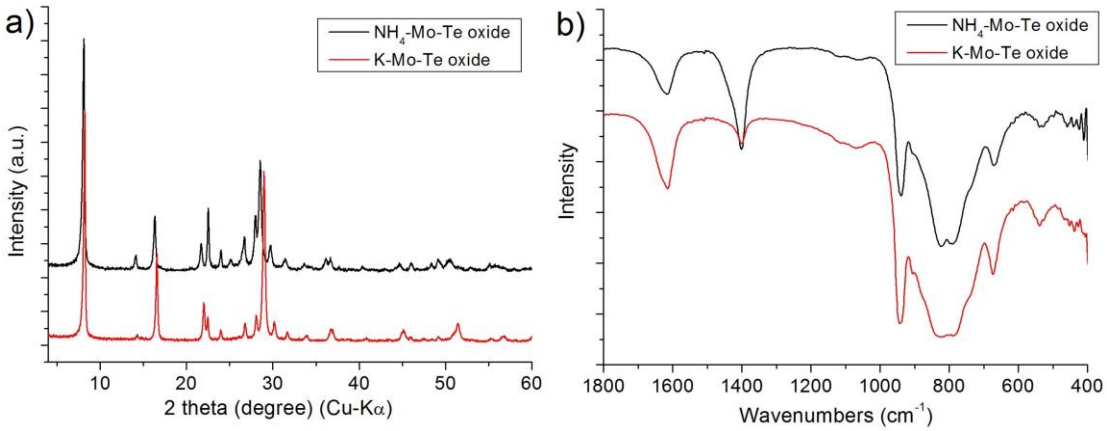

Figure 7. 3. a) XRD patterns and b) NH_4–Mo–Te oxide and K–Mo–Te oxide.

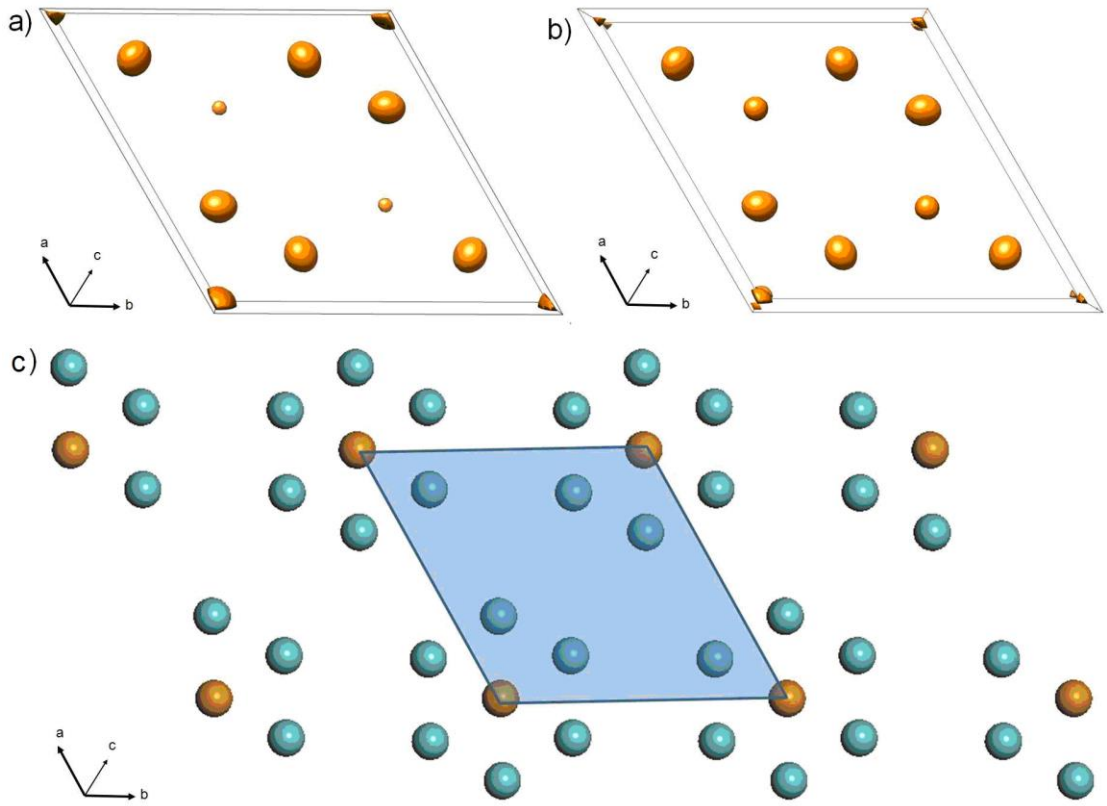

Figure 7. 4. Electron density map of a) K–Mo–Te oxide, b) NH_4–Mo–Te oxide, and c) heavy metal distribution, surrounding metal sites (blue sphere), center metal site (yellow sphere).

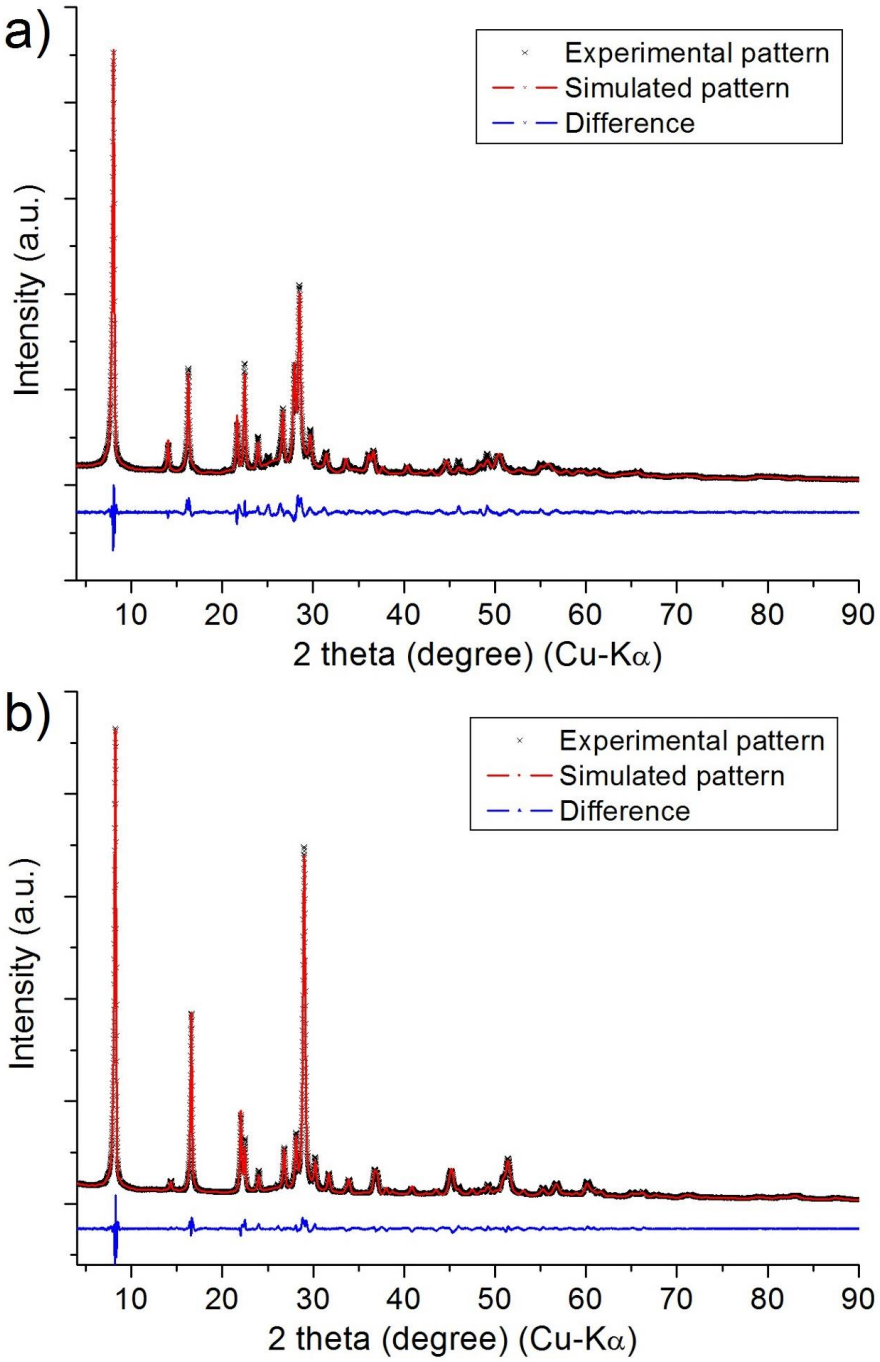

Figure 7. 5. Comparison of experimental XRD patterns with simulated XRD patterns using Rietveld method, a) NH_4–Mo–Te oxide, R_{wp} = 7.17% and b) K–Mo–Te oxide, R_{wp} = 5.20%.

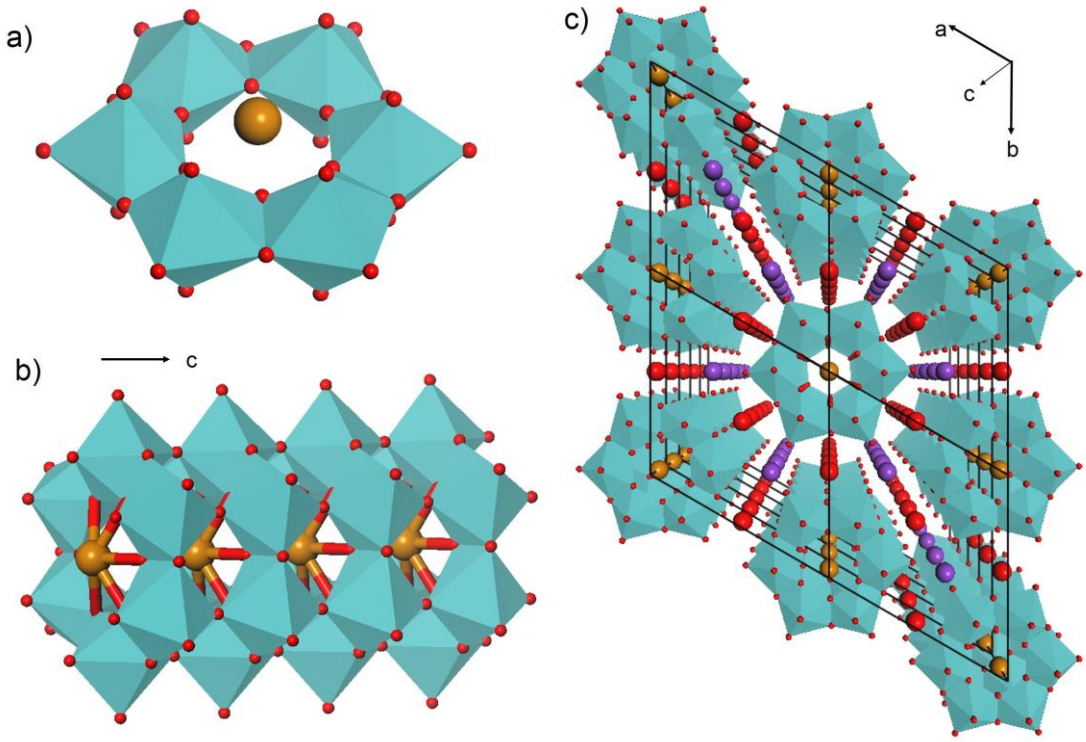

Figure 7. 6. Structure representations a) hexagonal unit of [$TeMo_6O_{21}$], b) column formed by stacking of hexagonal unit of [$TeMo_6O_{21}$], and c) unit cell (2 ×2 ×5) of Mo–Te oxide, surrounding site metal (Mo or Te) (blue polyhedron), center Te (yellow sphere), oxygen (red sphere), cation (NH_4^+ or K^+) (purple sphere).

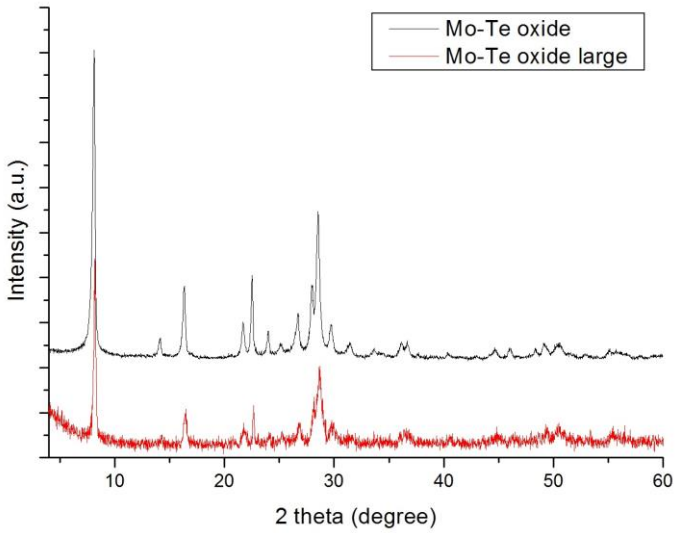

Figure 7. 7. XRD patterns of Mo-Te oxide.

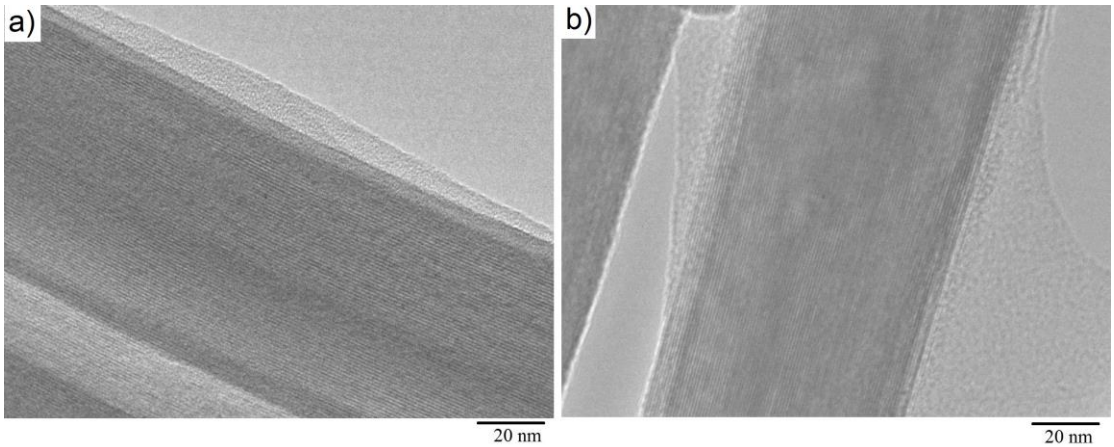

Figure 7. 8. TEM images of a) NH_4–Mo–Te oxide and b) K–Mo–Te oxide.

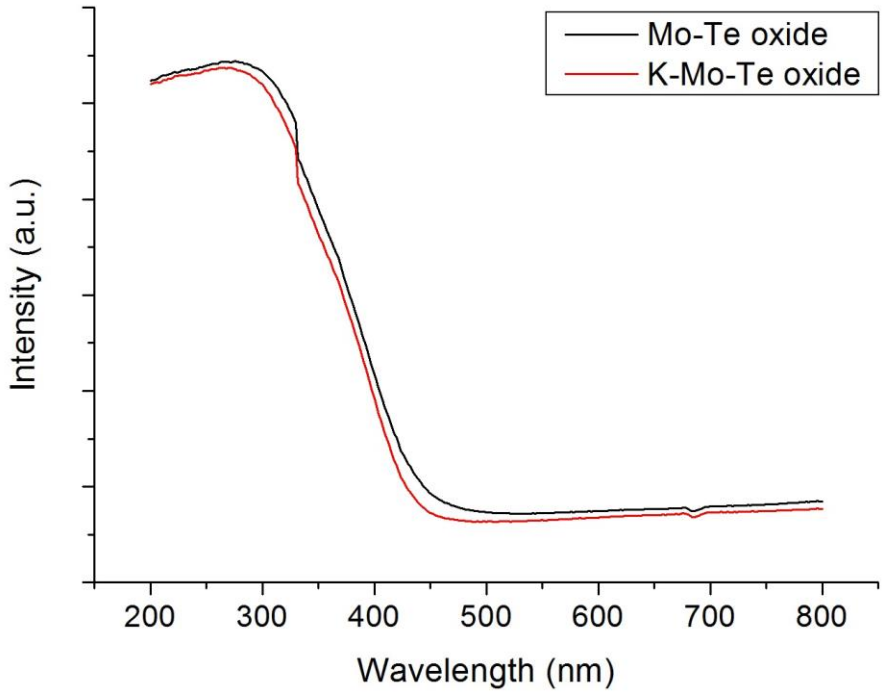

Figure 7. 9. UV-Vis spectra of NH_4–Mo–Te oxide and K–Mo–Te oxide.

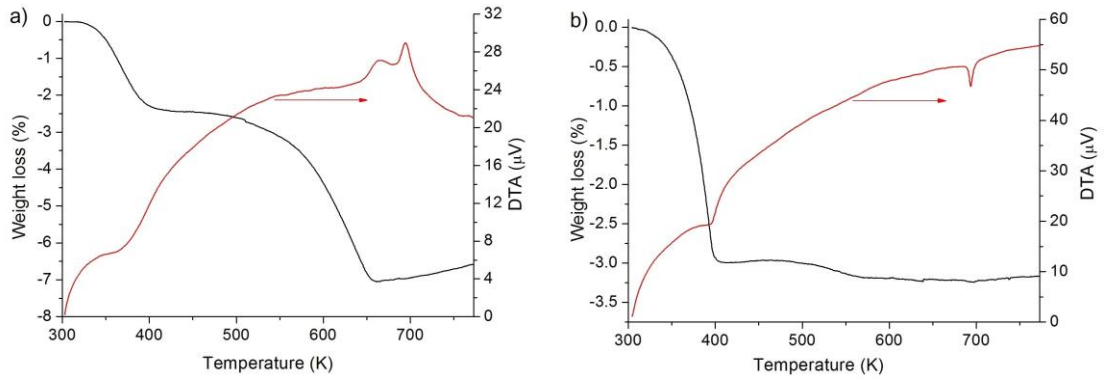

Figure 7. 10. TG-DTA of a) NH_4–Mo–Te oxide and b) K–Mo–Te oxide.

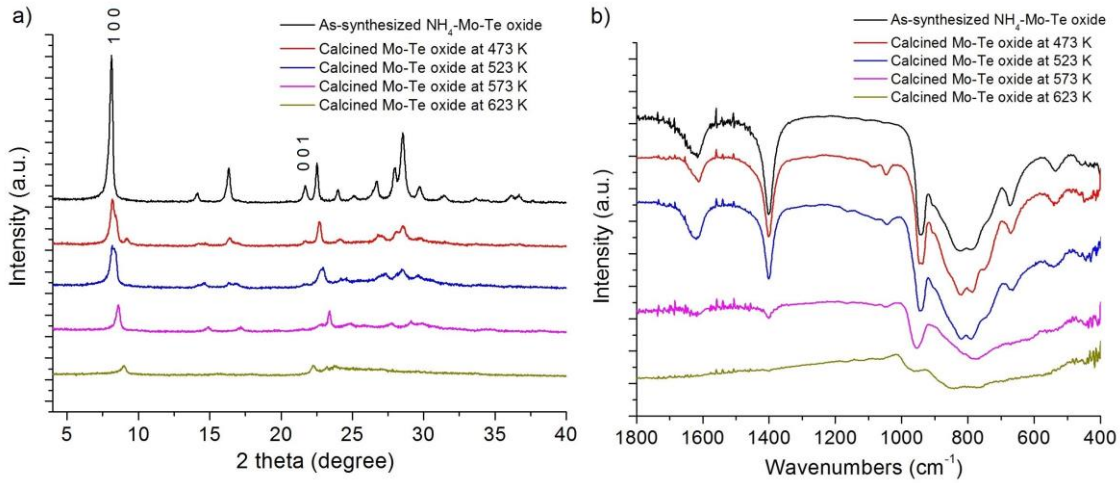

Figure 7. 11. a) Powder XRD patterns and b) FT-IR spectra of NH_4–Mo–Te oxide calcined at different temperature.

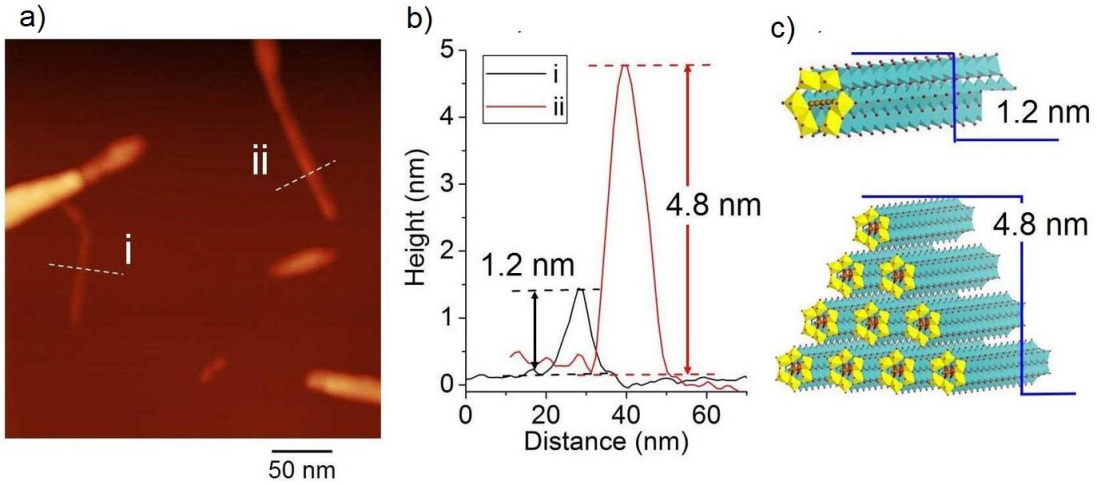

Figure 7. 12. a) AFM image of Mo-Te oxide, b) line profiles, and c) corresponding strutures.

Table 7. 1. Result of NH_4–Mo–Te oxide from the charge flipping method.

x	y	z	intensity	assignment
0	0	0.7912	50	Te
0.3376	0.1696	0.528	50.39	Mo
0	0	0.2975	25.32	Te
0.332	0.6653	0.8717	6.12	O (cation)
0.2595	-0.0012	0.5295	6.73	O (framework)
0.313	0.1591	0.9184	4.09	O (framework)
0.4995	0.2145	0.5256	4.49	O (framework)
0.3217	0.1603	0.1302	3.87	-
0.2337	-0.0011	0.0125	5.9	-
0.4994	0.2814	0.5242	4.32	-
0.2926	0.583	0.0205	4.01	O (cation)
0.4926	0.0016	0.9028	3.13	O (cation)

Table 7. 2. Result of K–Mo–Te oxide from the charge flipping method.

x	y	z	intensity	assignment
0	0	0.5572	82.27	Te
0.3281	0.1643	0.1853	74.62	Mo
0.3158	0.1582	0.6725	20.21	O (framework)
0.3333	0.668	0.1004	18.44	K
0.3333	0.668	0.6249	17.37	K
0.4933	0.2451	0.1573	13.56	O (framework)
0.0046	-0.0045	0.1275	6.24	-
0.3241	-4E-4	0.2118	7.44	O (framework)
0.45	-0.0013	0.8894	3.68	O (cation)
0.384	0.6174	0.8561	4.91	-
0.1568	0.576	0.1567	6.41	-
0.5	0	0.1906	4.67	O (cation)

Table 7. 3. Crystallographic information of NH_4–Mo–Te oxide and K–Mo–Te oxide from powder X-ray diffraction.

	NH_4–Mo–Te oxide	K–Mo–Te oxide
Crystal system	Hexagonal	Hexagonal
Space group	*P*6	*P*6
$a = b$ (Å)	12.4824	12.2820
c (Å)	3.9366	3.9404
$\alpha = \beta$ (degree)	90	90
γ (degree)	120	120
V (Å^3)	613.36	594.40
R_{wp}	7.17%	5.20%
$R_{wp(w/o\ bck)}$	13.73%	8.76%
R_p	5.54%	4.01%

Table 7. 4. Crystallographic data of NH_4–Mo–Te oxide.

	NH_4–Mo–Te oxide
Formula	$H_{14}N_2Mo_6O_{24}Te$
*M*r	1129.37
Crystal system	hexagonal
Space group	*P6*
a (Å)	12.56(3)
c (Å)	3.944(9)
$\alpha = \beta$ (degree)	90
γ (degree)	120
V (Å^3)	539(3)
T (K)	100(2)
Z	1
ρ_{calcd} (g·cm^{-3})	3.482
F_{000}	524
λ (Å)	0.78118
μ (mm^{-1})	6.182
Measured reflections	2903
Unique reflections	640
*R*1($I > 2\sigma(I)$)	0.0885
w*R*2(all data)	0.2467
GOF	0.851

Table 7. 5. Structure information of NH_4–Mo–Te oxide from Rietveld analysis.

atom	x	y	z	Uiso	occupancy
Mo1	0.32344	0.14912	0.19419	0.01	1
O2	0.31505	0.15056	0.72566	0.06	1
O3	0.4703	0.24013	0.20151	0.06	1
O4	0.32334	-0.00191	0.2294	0.06	1
O5	0.45521	-0.06414	0.61357	0.06	0.5
O6	0.14834	0.15491	0.24745	0.06	0.5
Te7	0	0	0.50102	0.01	1
O8	0.33333	0.66667	0.77013	0.06	0.91

Table 7. 6. Bond length of NH_4–Mo–Te oxide

Bond	Length (Å)
Mo1-O2	1.984
Mo1-O3	1.813
Mo1-O4	1.772
Mo1-O5	2.184
Mo1-O6	1.940

Table 7. 7. Structure information of K–Mo–Te oxide from Rietveld analysis.

atom	x	y	z	Uiso	occupancy
Mo1	0.33102	0.15887	0.19107	0.01	1
O2	0.31671	0.15094	0.68902	0.06	1
O3	0.50014	0.25727	0.22758	0.06	1
O4	0.32759	0.01319	0.21995	0.06	1
O5	0.5	0	0.63054	0.06	0.4
O6	0.16832	0.17541	0.30411	0.06	0.5
Te7	0	0	0.47504	0.01	1
K8	0.33333	0.66667	0.69786	0.03	0.95

Table 7. 8. Bond length of K–Mo–Te oxide

Bond	Length (Å)
Mo1-O2	1.848
Mo1-O3	1.603
Mo1-O4	1.890
Mo1-O5	2.168
Mo1-O6	1.973

Chapter 8. General conclusion

In chapter 1, the author reviewed the recent progress on POM-based material and structure determination with powder X-ray diffraction.

In chapter 2, the author presented the synthesis of a well-crystallized Mo–V–Bi oxide for single crystal analysis. A large single crystal of the material was obtained by repeating Mo–V–Bi oxide as a seed. Single crystal structure analysis combined with elemental analysis and oxidation state analysis showed that the material was comprised of ε-Keggin POM, [ε-$VMo_{9.4}V_{2.6}O_{40}$], with linking Bi ions. Cages and channels could be found in the material, which were surrounded by framework of the material. The cage was connected with the channels in a tetrahedral fashion to form a 3D pore system of the material. After removal of the guest molecules in the material, the material showed microporosity. Small molecules, such as N_2, CO_2, CH_4, and C_2H_6, were adsorbed in the material.

In chapter 3, the author demonstrated that the ε-Keggin POM-based complex metal oxides displayed high chemical composition diversity. Different kinds of transition metal ions, including Zn, Mn, Fe, and Co, could be incorporated in the material. Different complex metal oxides based on polyoxomolybdate were synthesized. The structures of the new materials were solved with powder diffraction data. Structure analysis showed that the materials were iso-structural materials of Mo–V–Bi oxide. TPD-MS measurement showed that the existing guest molecules were able to be removed by heat treatment.

In chapter 4, the author reported the investigation of synthesis and formation process on Mo–V–Bi oxide. Synthesis conditions of Mo–V–Bi oxide were studied in detail. It was found that size of the material was highly dependent on the starting materials. A nanometer-sized single crystal of Mo–V–Bi oxide was prepared by using all soluble starting materials. Crystal size of the material affected properties of the material, such as adsorption. Formation mechanism of Mo–V–Bi oxide was studied with Raman spectroscopy, indicating that a ε-Keggin POM, [ε-$VMo_{9.4}V_{2.6}O_{40}$], and a ball-shaped polyoxovanadomolybdate, {$Mo_{72}V_{30}$}, formed in precursor solution, which

transferred to Mo–V–Bi oxide and orthorhombic Mo–V oxide, respectively.

In chapter 5, adsorption properties of ε-Keggin POM-based complex metal oxide were investigated. Na–Mo–Zn oxide and NH_4–Mo–Zn oxide selectively adsorbed CO_2 in the CO_2/CH_4 mixture. The materials showed higher heat of adsorption for CO_2 than that for CH_4, which demonstrated that the materials strongly interacted with CO_2 while weakly with CH_4. Sodium ion could improve the interaction with CO_2. Co-adsorption experiments of CO_2/CH_4 indicated that Na–Mo–Zn oxide showed high CO_2 selectivity. Na–Mo–Zn oxide was successfully applied to gas chromatographic separation of CO_2 and CH_4.

In chapter 6, the author found that the ε-Keggin POM-based materials showed selective ion-exchange property. The ion-exchange experiments were carried out on Mo–V–Bi oxide, Na–Mo–Zn oxide, and NH_4–Mo–Mn oxide. Large cations showed high ion-exchange ability, while small cations showed low ion-exchange ability. The position of the cation species in Mo–V–Bi oxide was determined by single crystal analysis, which indicated that the cation was in channel site of the material.

In chapter 7, the first oxide molecular wire, Mo–Te oxide, was successfully synthesized, the structure of which was firstly determined with powder diffraction. Then a large crystal of the material was successfully prepared, and single crystal analysis confirmed that the proposed structure was correct. The material was constructed with nanowires in a hexagonal fashion. The molecular wire could be separated from the crystal easily.

In this thesis, the author found two types of new transition metal oxide. The first all-inorganic microporous POM-based material was synthesized and characterized. The author found that the new porous POM material shows zeolite-like properties including ion-exchange and molecule adsorption. Moreover, the chemical composition of the porous material can be easily tuned and different transition metal ions can be incorporated, which is superior to zeolite. The author also synthesized the first transition metal oxide molecular wire. A single molecular wire can be observed. Therefore, the

thesis opens a new door for developing transition metal oxides with new structures, including porous transition metal oxides and nanostructured transition metal oxides. The materials with interesting structures are expected to be applied in many fields.

Acknowledgment

This thesis is finished under Professor Wataru Ueda's supervision. Most of the researches presented in this thesis were conducted at Catalysis Research Center, Hokkaido University in three years (from October, 2011 to December 2014)

First of all, I would like to express my sincere thanks to Professor Ueda. His wide knowledge and patient guidance make me learn more when doing research. His discussion often provides important information to solve the problems and gives interesting ideas for further investigation. His encouragement also makes me recovered when I suffered from setback.

I also would like to thank Associate Professor Masahiro Sadakane in Hiroshima University. His kind help on structure analysis and manuscript preparation is very important to finish this thesis.

I also would like to thank Associate Professor Kenichi Shimizu and Assistant Professor Toru Murayama for his kind assistance on daily experiments and discussion.

I am grateful to Associate Professor Chen, Dr. Dummer, Mr. Nakamura, Ms. Omata, Mr. Konya, Mr. Ishikawa, and other members in Ueda Lab for their kind help, suggestion, and discussion.

I would like to thank Ministry of education, culture, sports, science and technology of Japan for financial support.

I would like to thank my father and mother. They are my strong shield all the time.

Finally, I would like to thank to my wife for taking care my daily life. She is my power source for doing everything.

Zhenxin Zhang